



The  
University  
Of  
Sheffield.

# **Lock-in Based Fibre-Optic Fluorimetric Sensors for Water- and Airborne Analytes**

**By:**

**Alhulw Alshammari**

A thesis submitted in partial fulfilment of the requirements for the degree of Doctor of  
Philosophy in Physics

Faculty of Science  
Department of Physics and Astronomy  
The University of Sheffield

**September 2020**

## ***Dedications***

*This thesis is dedicated to my parents for their continuous supplications and support, my brothers and sisters for their strong motivations, my wife for her unconditional support, my daughters and son*

## Acknowledgements

First and foremost, I would like to thank **Allah** almighty who has guided me throughout my PhD research.

I would like to thank my previous supervisor Dr. Martin Grell who retired last year for his support and gaudiness during the first two years and half of my PhD journey. I also would like to thank my previous co-supervisor Dr. Ashely Kadby for his advice and constructive feedback.

Special appreciation goes to my current supervisor Dr. Alan Dunbar for his unlimited support, encouragement, patience. I also extend my thanks to my co-supervisor Dr. Andrew Parnell for his supports and encouragements.

I am grateful to our collaborators Dr. Faiz Bukhari Mohd Suah and Dr. Syaza Atikah Nizar from (School of Chemical Sciences, University Sains Malaysia (USM)) who provided us a Morin derivative dye namely 'sodium salt of morin sulfonic acid', (NaMSA) that I used in our sensing application. I also extend my thank to our collaborator Dr. Mehboobali Pannipara who provided us a pyrazolyl chromene derivative (Probe 1) molecule that I also used in our sensing application.

I am grateful to Dr. Faleh Al-Jashaam, Dr. Anthony Ezeribe, Dr. Thomas Routledge, and Dr. Kyriacos Georgiou, Dr. Ali Alkorbi, Dr. Ibrahim Althobaiti, for their support during my PhD study and for supplying some samples. I would like to thank the technical staff in physics workshop of the University of Sheffield especially; Simon Dixon, and Mark who helped me to design refractive, PMMA cuvettes and gas-testing chamber that I used as part of our sensor.

Finally, I would like to thank my Lab team; Dr, Abraham Kirwa who designed the first generation (circuits plus LabVIEW code) of the used sensor, Dr. Abbad Al baroot, Nawal Alghamdi, and Zahrah Alqahtani for their help, support, and motivations.

I would like to thank Aljouf University for funding my PhD project.

## Published work and attended conferences

1. **Alshammari, A.H.**, Kirwa, A., Dunbar, A. and Grell, M., 2019. Adaptive and sensitive fibre-optic fluorimetric transducer for air-and water-borne analytes. *Talanta*, 199, pp.40-45. **(featured article)**: Outside Front Cover, *Analytica Chimica Acta*, Volume 1105, 2020, Page OFC, ISSN 0003-2670, [https://doi.org/10.1016/S0003-2670\(20\)30238-5](https://doi.org/10.1016/S0003-2670(20)30238-5).
2. **Alshammari, A.H.**, Alqahtani, Z., Suah, F.B.M., Nizar, S.A., Dunbar, A. and Grell, M., 2020. Low cost, high sensitivity detection of waterborne Al<sup>3+</sup> cations and F<sup>-</sup> anions via the fluorescence response of a morin derivative dye. *Analytica Chimica Acta*, 1105, pp.1-10.
3. Al Baroot, A., **Alshammari, A.** and Grell, M., 2019. Electrochemical gating of a hydrophobic organic semiconductor with aqueous media. *Thin Solid Films*, 669, pp.665-669.
4. **Alhulw Alshammari**, Abraham Kirwa, Alan Dunbar, Martin Grell. "Fluorescence meter for explosives detection". **Poster presentation** in the Octagon-University of Sheffield, Faculty of Science Graduate School Poster Day, United Kingdom (17th April 2018).
5. **Alhulw Alshammari**, Abraham Kirwa, Alan Dunbar, Martin Grell. "Adaptive and sensitive fibre-optic fluorimetric transducer for air- and water-borne analytes". **Poster presentation** in 7<sup>th</sup> International Symposium on Sensor Science, (09-11 May 2019 Napoli, Italy).
6. **Alhulw Alshammari**, Alan Dunbar, Martin Grell. "Sensitive fibre-optic fluorimetric transducer for airborne analyte". **Poster presentation** in 76<sup>th</sup> Gas Analysis and Sensing Group (GASG) Colloquium, (March 12<sup>th</sup> 2020 at Chicheley Hall, Buckinghamshire), **1<sup>st</sup> prize for a poster presentation**.

## **Abstract**

*This thesis describes the modifications that made to an evanescent wave fibre optic transducer with a lock-in detection for colorimetry to be a fluorimetric transducer. This includes 'side illumination' as a superior excitation mode compared with the evanescent wave excitation of fluorescence. Specifically, side illumination results in a strong fluorescent signal and very low (negligible) exciting light coupling into the optical fibre, therefore, it serves mostly as a fluorescent signal source rather than noise. The modified transducer is designed to be versatile; easily adapted for either waterborne or airborne analyte sensing. In addition, it can be also used to detect changes in fluorescence from either a sensitizer film or solution and can be applied for sensing applications even when the sensitizer degrades under the exciting light. Moreover, the transducer does not require a fluorescence spectrometer.*

*As a test of the transducer and to prove its versatility, it was applied in airborne and waterborne sensing, with minimal adaptation between these media. This was done by exposing the spray-coated stripped section of the glass optical fibres with polymer poly(phenylenevinylene) derivative poly[2-methoxy-5-(3',7'-dimethyloctyloxy)-1,4-phenylenevinylene] (MDMO-PPV) as a fluorophore, to the nitro-aromatic explosive dinitrotoluene (2,4-DNT) as an analyte, in both air and water media. Limit of detections (LoDs) of 0.48 ppb and 56 ppb were obtained for airborne and waterborne DNT respectively. These LoDs are ~ 62 times below previously reported values for DNT detection using PPV derivatives, as well as 3.3 times below LoDs for DNT sensing with different sensitizers.*

*A pyrazolyl chromene derivative known as Probe 1 was successfully used as the fluorescent sensitizer in a solid film form, thereby enabling its use for the detection of waterborne  $\text{Cu}^{2+}$  and thus avoiding the exposure to harmful solvent during sensing experiments. Specifically, a Probe 1 film was prepared via its immobilisation in a plasticised polyvinyl chloride (PVC) acting as a phase transfer membrane. It was then dip-coated onto the stripped section of an optical fibre before its exposure to a range of waterborne  $\text{Cu}^{2+}$  concentrations. The LoD of  $\text{Cu}^{2+}$  was 0.43  $\mu\text{M}$ , below the potability limit, and is also 3.7 times lower than the LoD measured by a conventional spectrofluorimeter based on the same sensitizer.*

*The good solubility and long-term stability of Morin derivative NaMSA known as an 'off  $\rightarrow$  on' fluorescent sensitizer for  $\text{Al}^{3+}$  in water, enabled it to be used in aqueous media avoiding the need for phase transfer membrane preparation. The dissolved NaMSA was used in conjunction with our fibre optic transducer to detect  $\text{Al}^{3+}$  in drinking water below the potability limit.*

*Moreover, the concentration of  $Al^{3+}$  was reliably quantified in a range of samples by using the standard addition method. It is known that morin-based  $Al^{3+}$  cation sensors can be selectively recovered by being exposed to fluoride ( $F^-$ ) anions. This method was further developed to enable complementary sensing of either fluoride anions, or aluminium cations using the same dye in both cases and achieving sub-micromolar LoDs. The transducer demonstrates a high figures-of-merit compared with previous reports on both aqueous  $Al^{3+}$  cation and  $F^-$  anion sensing.*

## List of Abbreviations

<b>AIE</b>	Aggregation induced emission
<b>AC</b>	Alternating current
<b>BODIPY</b>	Boron-dipyrromethene
<b>CHEF</b>	Chelation-enhanced fluorescence
<b>CHQE</b>	Chelating quenched transfer
<b>DNB</b>	Dinitrobenzene
<b>DNT</b>	Dinitrotoluene
<b>DI water</b>	Deionised water
<b>DC</b>	Direct current
<b>EU</b>	European Union
<b>EWS</b>	Evanescent wave sensor
<b>EDTA</b>	Ethylenediaminetetraacetic acid
<b>FWHM</b>	Full width as half maximum
<b>FAAS</b>	Flame atomic absorption spectrometry
<b>FoM</b>	Figure of Merit
<b>FQR</b>	Fluorescence quenching response
<b>GFAAS</b>	Graphite furnace atomic absorption spectrometer
<b>HOMO</b>	Higher occupied molecular orbital
<b>ICP-MS</b>	Inductive coupled plasma mass spectrometry
<b>ICP-OES</b>	Inductive coupled plasma optical emission spectroscopy
<b>ITC</b>	Intermolecular charge transfer
<b>I/V</b>	Current to voltage converter
<b>LoD</b>	Limit of detection
<b>LUMO</b>	Lower unoccupied molecular orbital
<b>LED</b>	Light emitting diode
<b>N.A</b>	Numerical aperture
<b>PET</b>	Photoinduced electron transfer
<b>PVC</b>	Polyvinyl chloride
<b>PMMA</b>	Poly(methyl methacrylate)

<b>PD</b>	Photodiode
<b>PC</b>	Personal computer
<b>ppt</b>	Parts per thousand
<b>ppm</b>	parts per million
<b>ppb</b>	Parts per billion
<b>ppt</b>	Parts per trillion
<b>PA</b>	Picric acid
<b>QCM</b>	Quartz Crystal Microbalance
<b>rms</b>	Root mean square
<b>SNR</b>	Signal to noise ratio
<b>SPR</b>	Surface plasmon resonance
<b>SV</b>	Stern Volmer
<b>TNT</b>	Trinitrotoluene
<b>THF</b>	Tetrahydrofuran
<b>US EPA</b>	United States Environmental Protection Agency
<b>UV-Vis</b>	Ultraviolet-visible
<b>WHO</b>	World Health Organization

<b>Title.....</b>	<b>I</b>
<b>Dedication.....</b>	<b>II</b>
<b>Acknowledgements.....</b>	<b>III</b>
<b>Published work and attended conferences.....</b>	<b>IV</b>
<b>Abstract.....</b>	<b>V</b>
<b>List of abbreviations.....</b>	<b>VII</b>
<b>Table of Contents.....</b>	<b>IX</b>
<b>List of Figures.....</b>	<b>XIII</b>
<b>List of Tables.....</b>	<b>XVII</b>

## Table of Contents

<b>Chapter 1: Introduction .....</b>	<b>1</b>
1.1 Background Information .....	1
1.2 Motivation for this Research.....	3
1.2.1 Motivation behind Waterborne Analyte Sensing.....	3
1.2.2 Motivation behind Airborne (Gas/Vapour) Analyte Sensing .....	4
1.3 Aim of this study.....	5
This study aims to develop a low cost, portable, and sensitive-fibre optic fluorimetric sensors for the sensing of both air- and waterborne analytes.....	5
1.4 Thesis Structure .....	7
1.4.1 Chapter 1 .....	7
1.4.2 Chapter 2.....	7
1.4.3 Chapter 3.....	7
1.4.4 Chapter 4.....	8
1.4.5 Chapter 5.....	8
1.4.6 Chapter 6.....	8
1.4.7 Chapter 7.....	8
1.4.8 Chapter 8.....	8
<b>Chapter 2: Sensors, Sensitisers and Transducers .....</b>	<b>9</b>
2.1 Introduction to Sensors .....	9
2.2 Sensor Characteristics and Performance Parameters .....	11
2.2.1 Limit of Detection.....	11
2.2.2 Sensitivity .....	12
2.2.3 Figure of Merit.....	13
2.2.4 Selectivity .....	13
2.2.5 Response Time and Reversibility .....	14

2.2.6 Sensor Calibration.....	14
2.3 Sensitisers .....	15
2.3.1 Molecular Absorption of UV–Visible Light and Light Emission (Fluorescence).....	15
2.3.1.1 Chromophore and Fluorophore.....	18
2.3.1.2 Fluorescence Turn–on (off → on) .....	19
2.3.1.3 Fluorescence Quenching (on → off).....	21
2.3.1.3.1 Static and Dynamic Quenching.....	23
2.3.2 Review of Fluorescent Sensitisers .....	24
2.3.2.1 Fluorescent Conjugated Polymers.....	24
2.3.2.2 Organic Fluorescent Dyes.....	28
2.3.2.3 Other Fluorescent Organic Compounds.....	32
2.4 Transducer Working Principle .....	34
2.4.1 Electrochemical Transducers .....	34
2.4.2 Surface Plasmon Resonance Transducers.....	36
2.4.3 Quartz Crystal Microbalance Transducers.....	37
2.4.4 Spectrophotometer Transducer .....	38
2.4.5 Fluorimeter Transducers .....	39
2.5 Physics of Fibre Optics .....	41
2.5.1 Acceptance Angle, Numerical Aperture, and Critical Angle.....	42
2.5.2 Single-Mode versus Step and Graded-Index Multi-Mode Fibre Optics .....	44
2.5.3 V-number and M-number of Modes .....	45
2.6 Evanescent Wave .....	46
2.6.1 Evanescent Wave Sensors.....	47
2.7 Fibre Optic Sensors and their Merit.....	48
2.8 Summary of the chapter .....	48
<b>Chapter 3: Fibre Optic Sensor Instrument with Lock-In Detection .....</b>	<b>49</b>
3.1 Introduction to the Optical Fibre Transducer.....	49
3.2 Electronic Noise.....	55
3.3 Digital Lock-in Amplifier as a Signal Processor .....	56
3.3.1 Lock-in Amplifier Parameters .....	59
3.3.2 Lock-in Amplifier in Conjunction with the LabVIEW Routine for data Collection .....	62
3.4 Adder Circuit (AC+DC) .....	64
3.5 The Choice of the Optical Filter and PD.....	67
3.6 The I/V Converter .....	69
3.7 Conclusions.....	70
<b>Chapter 4: Preparation of Sensitised Optical Fibres.....</b>	<b>71</b>
4.1 Introduction.....	71

4.2 Fibre Optic Preparation for Sensing Applications .....	71
4.3 Coating Stripped Section of Optical Fibres with Fluorimetric Sensitisers .....	75
4.3.1 Spray Coating Technique.....	76
4.3.1.1 Important Parameters for Spray Coating.....	78
4.3.2 Dip Coating Technique .....	80
4.3.2.1 Important Parameters for Dip Coating.....	80
4.4 Conclusions.....	83
<b>Chapter 5: An Adaptive and Sensitive Fibre-Optic Fluorimetric Transducer for Air- and Water-Borne Analytes .....</b>	<b>84</b>
5.1 Introduction.....	84
5.2 Experimental .....	85
5.2.1 Preparing Aqueous Solutions of DNT .....	87
5.3 Results and Analysis .....	88
5.3.1 Detecting Airborne DNT vapours.....	88
5.3.2 Detecting Waterborne DNT .....	92
5.4 Discussion.....	95
5.4.1 Airborne DNT Vapours .....	95
5.4.2 Waterborne DNT .....	99
5.5 Conclusions.....	102
<b>Chapter 6: Highly Sensitive and Reversible Membrane Films for Cu<sup>2+</sup> Detection.....</b>	<b>104</b>
6.1 Introduction.....	104
6.2 Experimental Procedures .....	105
6.2.1 Synthesis and Materials .....	105
6.2.2 Configuring the Measurement Setup for Waterborne Cu <sup>2+</sup> Detection .....	106
6.2.3 Preparation of Solutions for Titrations.....	107
6.3 Results and Analysis .....	107
6.3.1 Investigating the Membrane Fluorescence Stability .....	107
6.3.2 Fluorescence Quenching Response Time .....	110
6.3.3 Sensor Calibration for Cu <sup>2+</sup> Sensing .....	111
6.3.4 Quantitative Analysis.....	112
6.3.5 Reversibility and Reusability .....	115
6.4 Conclusions.....	117
<b>Chapter 7: Low Cost, High Sensitivity Detection of Waterborne Al<sup>3+</sup> Cations and F<sup>-</sup> Anions via the Fluorescence Response of a Morin Derivative Dye.....</b>	<b>118</b>
7.1 Introduction.....	118
7.2 Experimental .....	119
7.2.1 Synthesis and Materials .....	119
7.2.2 Overview of Measurement Setup.....	120

7.2.3 Preparation of Optical Fibres .....	121
7.2.4 Cuvettes.....	122
7.2.5 Preparation of Solutions.....	122
7.2.6 Titrations for Sensor Calibration.....	123
7.2.7 Data Analysis .....	125
7.3 Results and Discussion .....	127
7.3.1 Sensor Calibration for ‘off → on’ Al <sup>3+</sup> Sensors .....	127
7.3.2 Determining Al <sup>3+</sup> with Standard Addition Method.....	130
7.3.3 Sensor Calibration for ‘on → off’ F <sup>-</sup> Sensors .....	133
7.3.4 Selectivity for Fluoride over Chloride .....	136
7.3.5 The Effect of Simultaneous Presence of F <sup>-</sup> and Al <sup>3+</sup> on Activated NaMSA .....	137
7.3.6 Comparison to Prior Fluorimetric Al <sup>3+</sup> and F <sup>-</sup> Sensors .....	139
7.4 Conclusions.....	141
<b>Chapter 8: Overall Conclusions and Proposed Future Work .....</b>	<b>142</b>
8.1 Overall Conclusions.....	142
8.2 Proposed Future Work .....	143
<b>References.....</b>	<b>146</b>
<b>Appendices.....</b>	<b>166</b>
Appendix I. <i>LoDs</i> of Heavy Metals Obtained by the ICP-MS, ICP-AES, GFAAS and FASS techniques. ....	166
Appendix II. Langmuir Adsorption Isotherm Derivation. ....	166
Appendix III. Input Signal Processing via Lock-in Amplifier.....	168
Appendix IV. Block Diagram of the Lock-In (USBLockIn250) Illustrating the Function of the Basic Components. ....	170
Appendix V. Properties of the Used Optical Fibres.....	171
Appendix VI. Cooling System .....	172
Appendix VII. Repeatability of DNT Waterborne Sensing Experiments. ....	173
Appendix VIII. Fluorescence Intensity of Thin Film.....	173
Appendix IX. Repeatability of Cu <sup>2+</sup> sensing experiments.....	174
Appendix X. Copyright Permissions .....	175

## List of Figures

Figure 2. 1. Diagram showing the LoD at low concentration and above the noise floor. ....	12
Figure 2. 2. Jablonski diagram illustrating the electronic transitions (absorption) and relaxations (fluorescence and phosphorescence) as a result of UV-visible light absorption by a molecule. ....	16
Figure 2. 3. Stokes shift due to energy losses in the excited state. ....	18
Figure 2. 4. (a) Intramolecular fluorescence quenching via photoinduced electron transfer (PET). (b) Metal ion coordination with lone pair donor, which prevents PET and results in chelation-enhanced fluorescence (CHEF). ....	20
Figure 2. 5. Fluorescence quenching processes occurring in fluorophores connected as a “molecular wire” (which amplifies the sensor response) and a small molecule or isolated fluorophore. ....	24
Figure 2. 6. Pentiptycene-derived PPE structure and conceptual polymer porosity for analyte detection [48]. ....	26
Figure 2. 7. (a) MDMO-PPV and DNT chemical structure. (b) MDMO-PPV [90] and DNT energy levels [88] and exciton transitions from the LUMO of MDMO to the LUMO of DNT. ....	27
Figure 2. 8. BODIPY core chemical structure. ....	28
Figure 2. 9. Crown ether rings (a) 12-crown-4, (b) 15-crown-5, (c) and 18-crown-6 [45]. ....	29
Figure 2. 10. Fluorescence enhancement caused by preventing PET when the crown ether receptor coordinates with $K^+$ [51]. ....	30
Figure 2. 11. Chemical structure of (a) morin, (b) morin: $Al^{+3}$ complex. ....	31
Figure 2. 12. The fluorescence emission of Probe 1 (20 $\mu M$ ) in mixtures of $H_2O/THF$ with increasing water fractions [105]. ....	32
Figure 2. 13. The synthetic route for obtaining Probe 1 [104]. ....	33
Figure 2. 14. Kretschmann configuration of an SPR sensor. ....	36
Figure 2. 15. Quartz crystal microbalance sensor. ....	37
Figure 2. 16. UV-Vis spectrometer schematic diagram. ....	38
Figure 2. 17. Spectrofluorometric schematic diagram. ....	40
Figure 2. 18. Schematic diagram of a typical fibre optic cross-section. ....	42
Figure 2. 19. Illustrating that only incident light within the optical fibre acceptance cone, or the acceptance angle subject to total internal reflection. ....	43
Figure 2. 20. Schematic of the propagating modes in an optical fibre of a (a) single-mode, (b) multimode step-index, and (c) multimode graded-index type. ....	45
Figure 2. 21. Sensitised section of the multi-mode optical fibre showing the evanescent wave penetration into the sensitizer film. ....	47
Figure 3. 1. Schematic diagram of the EWS instrument and the digital lock-in amplifier built by Abraham before carrying out any modification. PD1 and PD2: Photodiodes (OSD5-5T, Farnell); $V_{in}$ : Input voltage; $V_{out}$ : Reference output voltage; BNC port 1 and BNC port 2: Connectors to reference-out terminal and input terminal of the digital lock-in amplifier. ....	49
Figure 3. 2. (a) A schematic diagram of the side illumination (upper) and evanescent wave excitation (lower); (b) Comparison of the fluorescence emitted from MDMO-PPV film	

(excitation of 450 nm) under side illumination excitation (red) with evanescent wave (black). Excitation was switched on at  $t_1 = 20$  s and was switched off at  $t_2 = 45$  s..... 52

Figure 3. 3. The MDMO-PPV fluorescence intensity recorded from a stripped and non-sensitised optical fibre under side illumination mode, that was switched on at  $t_1 = 25$  s and was switched off at  $t_2 = 55$  s without using a high pass optical filter. .... 53

Figure 3. 4. Schematic diagram of the sensor setup and test vapour generator used in the present study. .... 54

Figure 3. 5. The fluorescence intensity obtained from MDMO-PPV (450 nm excitation) when using the reflector mirror at 35-68 s exceeds that obtained without using the reflector mirror at 0-35s and 68-100s..... 55

Figure 3. 6. The main window of the digital lock-in amplifier’s GUI, including a very brief description of the parameters that can be set by the user [130]. .... 59

Figure 3. 7. Taken from digital lock-in manufacturer’s datasheet [130] showing the influence of time constant setting on the lock-in amplifier’s filter bandwidth. .... 60

Figure 3. 8. Taken from digital lock-in manufacturer’s datasheet [130] showing the impact of the roll-off (6,12, and 24 dB/oct) setting on the lock-in filter bandwidth..... 61

Figure 3. 9. (a) GUI of the LabVIEW code used when recording data from the lock-in amplifier continuously into a data file; (b) An example of real-time measurements of the interaction between a sensitizer and an analyte. .... 63

Figure 3. 10. The schematic diagram of the designed AC+DC circuit is taken from [36], where V2 and V3 are the DC voltage sources’ biasing transistors Q1 and Q2 respectively. . 65

Figure 3. 11. The emission spectrum of LED450 L (Thorlabs). .... 67

Figure 3. 12. The transmission of the optical high-pass filter (LP02–488RU-25, Semrock) measured using a spectrophotometer (UV550 Spectrophotometer, Thermo Scientific)..... 68

Figure 3. 13. The spectral response of the PD adopted in this study (OSD5-5T, Farnell)..... 69

Figure 4. 1. (a) Optical fibre reel; (b) Optical fibre after stripping 1 cm-long buffer; (c) Scalpel blade ( Swann –Morton Ltd.) used for stripping; (d) Ruby Fibre Scribe used for cleaving (image taken from the supplier’s web page)[134]. .... 72

Figure 4. 2. Microscope images of two cleaved optical fibres (FT800UMT, Thorlabs) captured by iphone-7 camera using a microscopic lens (Zenith ultra-500, UK): (a) polished and (b) non-polished optical fibre. .... 73

Figure 4. 3. Wet stripped optical fibre sections drying near the hot plate surface set to 90 °C. .... 74

Figure 4. 4. Optical fibre roughening setup: A and B indicate the direction of the sliding table, C denotes the tape used to ensure that the fibre is affixed onto the sliding table, and the red arrow indicates the rotational direction of the Dremel grinding bit..... 75

Figure 4. 5. (a) Schematic diagram of the hand-held airbrush spraying process, where sensitizer is deposited onto the stripped section of the optical fibre; (b) The airbrush utilised in the present study. .... 76

Figure 4. 6. (a) Stripped optical fibres prior to coating; (b) Stripped optical fibres which have been spray-coated with MDMO-PPV alongside the airbrush used..... 77

Figure 4. 7. Lock-in voltage output  $V_{out}$  as a measure of fluorescence intensity for five identical optical fibres sprayed with MDMO-PPV films under identical conditions while varying the nozzle to fibre distance. The films were exposed to a 450 nm exciting light

(LED450L, Thorlabs) which was turned on in the time interval between $t_1 = 8$ s and $t_2 = 64$ s. ....	79
Figure 4. 8. Schematic diagram of the dip-coating procedure. Step 1: substrate immersion into the coating solution; Step 2: the substrate is fully immersed in the coating solution; Step 3: the substrate is extracted from the coating solution.....	80
Figure 4. 9. The dip coating setup used in the present work, with red arrows indicating the movement direction of the arm and the glued optical fibre.....	81
Figure 4. 10. GUI of LabVIEW code including a brief description of the dip coating parameters that can be set by the user. ....	82
Figure 5. 1. Schematic diagram of our sensor design used for waterborne DNT sensing. ....	87
Figure 5. 2. Lock-in voltage output $V_{out}(t,p)$ as a measure of fluorescence intensity for several MDMO-PPV sensitised optical fibres under blue LED excitation shown against time after starting the exposure to DNT at $t = 0$ at different dimensionless vapour pressures, $p$ . The fibres were illuminated and the fluorescence was detected for 3 s once every minute. The non-sensitised fibre gives near-zero $V_{out}$ . ....	88
Figure 5. 3. Normalized lock-in voltage output $V_{out}(t,p)$ as a measure of fluorescence intensity for several MDMO-PPV sensitised optical fibres under blue LED excitation shown against time after starting the exposure to DNT at $t = 0$ at different dimensionless vapour pressures, $p$ . The fibres were illuminated and fluorescence was detected for 3 s once every minute.....	89
Figure 5. 4. Fluorescence quenching ratios $FQR(t,p)$ calculated from the data in Figure 5.2 with the help of Eq. 5.1. Solid lines are exponential fits to Eq. 5.2 using Origin software. ...	90
Figure 5. 5. Fluorescence quenching ratios $FQR(t,p)$ from repeating experiments under (89.7 / 8.4 / 4.8) ppb DNT calculated and fitted in the same way as in Figure 5.4. The solid line is a fit to Eq. 5.2. ....	92
Figure 5. 6. Fluorescence quenching ratios $FQR(t, c)$ under 270 ppb DNT concentration in water against time [seconds]. Solid line is a fit to Eq. 5.2.....	93
Figure 5. 7. Lock-in voltage output $V_{out}(c)$ (blue circles) as a measure of the fluorescence intensity for an MDMO-PPV sensitised optical fibre under blue LED excitation, shown against DNT concentration in water from 0 - 720 ppb. Also shown is a control experiment (red squares), vs. the number of interrogations.....	94
Figure 5. 8. $FQR[\infty,p]$ vs. airborne DNT in the concentration range (0-150) ppb, Data from table 5.1 where the solid line is a fit to Eq. 5.5.....	96
Figure 5. 11. $FQR[c]$ vs. waterborne DNT concentration, solid line is fit to Eq. 5.6.....	100
Figure 5. 12. Stern-Volmer plot for quenching of MDMO-PPV fluorescence by waterborne DNT in the concentration range (0-720 ppb). Data from table 5.2.....	101
Figure 6. 1. Chemical structure of pyrazolyl chromene derivative (Probe 1), adopted from [105]. ....	106
Figure 6. 2. The output voltage $V_{out}(c)$ vs time, as a measure of fluorescence intensity produced by the membrane film coated onto an optical fibre and under continuous blue LED excitation. The point at which the LED was switched on is indicated by the arrow. ....	108
Figure 6. 3. $V_{out}(c)$ vs time, as a measure of fluorescence intensity yielded by the membrane film coated onto an optical fibre. The membrane was excited by a blue LED light and fluorescence was detected for 20 s alternating with 10 min dark intervals. (a) Membrane before soaking; (b) Membrane after soaking in DI-water for 30 min. ....	109

Figure 6. 4. $V_{out}(c)$ vs time, as a measure of fluorescence intensity yielded by the membrane film coated onto an optical fibre when exposed to 22 $\mu\text{M}$ $\text{Cu}^{2+}$ concentration. ....	110
Figure 6. 5. $V_{out}$ as a measure of the fluorescence intensity produced by the membrane film coated onto an optical fibre, as a function of waterborne $\text{Cu}^{2+}$ solution concentration, ranging from 1 $\mu\text{M}$ to 22 $\mu\text{M}$ . ....	111
Figure 6. 6. FQR [c] vs. waterborne $\text{Cu}^{2+}$ concentration, the solid line is a fit to Eq. 6.1.....	114
Figure 6. 7. SV plot of the fluorescence quenching for the membrane film by waterborne $\text{Cu}^{2+}$ in the 0–22 $\mu\text{M}$ concentration range. ....	115
Figure 6. 8. (a) $V_{out}$ as a measure of fluorescence intensity produced by the membrane film when exposed to 22 $\mu\text{M}$ of $\text{Cu}^{2+}$ for 0–10 min followed by membrane exposure to 22 $\mu\text{M}$ of EDTA as a function of time [min]. (b) Reversible changes in membrane fluorescence intensity after subsequent exposure to 22 $\mu\text{M}$ $\text{Cu}^{2+}$ and 22 $\mu\text{M}$ EDTA.....	116
Figure 6. 9. EDTA molecule (a) in the solid form and (b) when dissolved in water, allowing it to chelate waterborne $\text{Cu}^{2+}$ (indicated by M (red) in the EDTA centre)[176]. ....	116
Figure 7. 1. a.) Chemical Structure of NaMSA when dissolved in water, this dissociates into $\text{MSA}^-$ and $\text{Na}^+$ . b.) Structure of $[\text{MSA}^-:\text{Al}^{3+}]$ complex that forms in aqueous solution when $\text{Al}^{3+}$ is added to dissolved NaMSA. ....	120
Figure 7. 2. Schematic diagram of our fibre- optic lock-in fluorimeter.....	121
Figure 7. 3. Design of bespoke cuvettes, manufactured in the University of Sheffield workshop. Cuvettes were made either of transparent material (PMMA), or a reflective material (stainless steel). The bottom compartment where the fibre is fitted has a capacity of 300 $\mu\text{L}$ while a wider upper compartment holds liquid in excess of 300 $\mu\text{L}$ . ....	122
Figure 7. 4. Example of a $V_{out}$ vs time series for NaMSA solution under stepwise additions of $\text{Al}^{3+}$ aliquots. Every arrow indicates a titration step, i.e. addition of an $\text{Al}^{3+}$ aliquot. Inset: Magnification of the short time / low $\text{Al}^{3+}$ concentration region. Note, the high increase in $V_{out}$ at ~1000 s corresponds to high $\text{Al}^{3+}$ addition compared with other additions. ....	124
Figure 7. 5. $V_{out}(c)$ as a measure of the fluorescence intensity of NaMSA in (DI-water/ HCl), pH = 5, shown against $\text{Al}^{3+}$ concentration from 1 $\mu\text{M}$ to 10 mM, the solid line is the fit to the data using Eq. 7.2 . The insets magnify the linear regime for $[\text{Al}^{3+}]$ up to 50 $\mu\text{M}$ . a.) fresh 200 $\mu\text{M}$ NaMSA solution and using the PMMA cuvette, b.) fresh 200 $\mu\text{M}$ NaMSA solution and using the stainless steel cuvette, and c.) two months old NaMSA solution and using the PMMA cuvette. ....	128
Figure 7. 6. The standard addition plots, $V_{out}$ vs $c_{add}$ , fitted with straight lines, a.) for sample A b.) for sample B and c.) for sample C. The experiment for each sample was repeated 4 times, but graph a and b show less than 4 lines or 4 experiments because of the overlaying data .....	131
Figure 7. 7. $V_{out}(c)$ as a measure of the fluorescence intensity of NaMSA dissolved in (DI water / HCl), pH = 5, and activated with 50 $\mu\text{M}$ of $\text{Al}^{3+}$ , shown against $\text{F}^-$ concentration from 10 $\mu\text{M}$ to 6 mM. The solid line is a fit to the data using Eq. 7.3. The insets show the linear regime of $1-(V_{out}(c)/V_0)$ vs $\text{F}^-$ for concentrations up to 50 $\mu\text{M}$ . The three plots are a.) fresh 200 $\mu\text{M}$ NaMSA solution as measured in the PMMA cuvette, b.) fresh 200 $\mu\text{M}$ NaMSA solution as measured in the stainless steel cuvette, and c.) two months old NaMSA measured in a PMMA cuvette.....	134
Figure 7. 8. $V_{out}(c)$ as a measure of the fluorescence of 200 $\mu\text{M}$ NaMSA solution in acidified water activated with 50 $\mu\text{M}$ of $\text{Al}^{3+}$ shown against $\text{F}^-$ and $\text{Cl}^-$ concentration, using the PMMA cuvette. The solid lines represent fits to the data according to Eq. 7.3. ....	137

Figure 7. 9.  $V_{out}(mV)$  as a measure of the fluorescence of 200  $\mu M$  NaMSA solution in acidified water. The first arrow indicates NaMSA activation with 50  $\mu M$   $Al^{3+}$ , the subsequent arrows indicate the addition of aliquots of (0.75 mM / 0.25 mM) mixed  $F^- / Al^{3+}$  solution.. 138

## List of Tables

Table 1. 1: Potability limits of waterborne analytes in drinking water according to the EU, the US EPA, and the WHO. The potability limits are reported in mg/L or $\mu g/L$ [3][4][5].....	2
Table 5. 1: Fit parameters, with errors, for FQR(t,p) shown in Figure 5.4 when fitted to Eq. 5.2 using Origin software. For some concentrations the experiment was repeated on a different fibre, repeat results are shown in brackets. ....	91
Table 5. 2: FQR(c) vs c for waterborne DNT. ....	95
Table 5. 3: Performance parameters of different fluorimetric DNT sensors. ....	102
Table 6. 1: FQR(c) vs c for waterborne $Cu^{2+}$ .....	113
Table 7. 1: Parameters obtained from fitting the data in Figure 7.5 to Eq. 7.2.....	129
Table 7. 2: The results of the standard addition experiments to determine the $Al^{3+}$ concentration of samples A, B, C, compared to the actual (calculated) value, which was revealed to the experimenter only after the measurement .....	132
Table 7. 3: Parameters such as the de-complexation constant K, slope m, and LoD obtained from fitting data in Figure 7.7(a to c) to Eq. 7.4.....	135
Table 7. 4: Performance parameters of different fluorimetric $Al^{3+}$ and $F^-$ sensors. Collated from the literature, and from tables 7.1 and 7.3 for values measured in this work. The abbreviations used for the different media refer to MeCN: Acetonitrile, DMSO: Dimethylsulfoxide, DMF: Dimethylformamide, and $CHCl_3$ : Chloroform.....	140

# Chapter 1: Introduction

## 1.1 Background Information

Sensor technology (described in Section 2.1) is a very crucial analytical tool that can tell the user about the presence of harmful chemicals in the environments. Sensing very small quantities of selective chemicals in the air or water is important for several reasons including the security in terms of explosive detection and the safety of drinking water. The explosives produced for global military conflicts that occurred over the last decades have left buried and unexploded ordnance [1]. There are approximately 120 million unexploded landmines worldwide [2]. The ongoing military conflicts in some countries are expected to leave landmines behind which stay active for a long time even when conflicts cease [1]. These unexploded landmines and the explosives controlled by terrorists threaten public safety worldwide.

Water pollutants, such as the presence of harmful or toxic ions at an abnormal level, are another environmental problem. Consequently, the World Health Organization (WHO) [3], the European Union (EU) [4], and the United States Environmental Protection Agency (US EPA) [5] have set guidelines on the maximum allowable pollutant levels (denoted as “potability limit or action level”) in drinking water that can be ingested by human beings (see Table 1.1). These guidelines are updated as new evidence emerges while motivating researchers to innovate new technologies to detect the presence of these pollutants at increasingly lower concentration. As a result of this initiative, sensitive technologies have been developed for determining minute pollutant concentrations based on atomic absorption/emission spectroscopy [6][7] and mass spectrometry [8]. The limits of detection (*LoD*) related to some of these techniques are presented in Appendix I. *LoD* is the lowest concentration of a particular pollutant that would produce a sensor reading that can be distinguished from the background noise with a specific level of confidence, as described in Section 2.2.1. Even though these technologies offer high sensitivity, resulting in low *LoD* for these pollutants (below the potability limits), they necessitate the use of expensive instrumentation and infrastructure, while often involving complex analytical processes that typically include separation and pre-concentration [9] before sample analysis. Consequently, none of these techniques can be presently applied for onsite evaluations. Therefore, samples are collected from the site and transported to the laboratory for testing, which is impractical, time-consuming and expensive. Due to these shortcomings, several portable and cheap real-time analytical techniques have been developed for onsite

pollutant detection [9][10][12]. However, these techniques are not sensitive enough to detect pollutants below the potability limit, which is particularly problematic for highly toxic pollutants e.g. mercury ( $\text{Hg}^{2+}$ ), lead ( $\text{Pb}^{2+}$ ), and cadmium ( $\text{Cd}^{2+}$ ) that need to be detected at very low concentrations. Moreover, as some of the currently available portable and cheap techniques tend to rely on colour change that is visually assessed, they are not very accurate and highly unreliable. For example, an apparatus aimed at the detection of dissolved mercury ( $\text{Hg}^{2+}$ ) in water has a high *LoD* at  $0.1 \mu\text{M}$  [13], while an even higher *LoD* of  $48 \mu\text{M}$  has been reported for the detection of dissolved lead ( $\text{Pb}^{2+}$ ) in water [14], both of which are well above the allowable levels. Thus, a new generation of portable analytical techniques is required to overcome these shortcomings, while ensuring their cost-effectiveness and ability to withstand harsh environments. It is worth noting that, in sensor technologies, the air or water pollutant chemical being analysed is referred to as the “analyte” when they are targeted for sensing.

**Table 1.1:**

<i>Analytes</i>	<i>EU [4]</i>		<i>US EPA [5]</i>		<i>WHO [3]</i>	
	<i>[<math>\mu\text{M}</math>]</i>	<i>[<math>\mu\text{g/L}</math>]</i>	<i>[<math>\mu\text{M}</math>]</i>	<i>[<math>\mu\text{g/L}</math>]</i>	<i>[<math>\mu\text{M}</math>]</i>	<i>[<math>\mu\text{g/L}</math>]</i>
Lead	0.048	10	0.0724	15	0.048	10
Cadmium	0.0445	5	0.0445	5	0.027	3
Mercury	0.005	1	0.010	2	0.030	6
Copper	31.47	2000	20.5	1300	31.47	2000
Aluminium	7.4	200	7.4	200	7.4	200
Manganese	0.91	50	0.91	50	1.82	100
Fluoride	79	1500	210.5	4000	79	1500
Nickel	0.341	20	-----	-----	1.193	70

**Table 1. 1:** Potability limits of waterborne analytes in drinking water according to the EU, the US EPA, and the WHO. The potability limits are reported in mg/L or  $\mu\text{g/L}$  [3][4][5].

## 1.2 Motivation for this Research

The main motivating factor for this research is the development of a cheap, portable, versatile and sensitive apparatus capable of detecting explosive vapour/airborne and toxic waterborne analytes in concentrations below the levels permitted by the EU, the US EPA, and the WHO. Unfortunately, currently available inexpensive and portable sensors are incapable of detecting toxic analytes at the allowable levels. Most available sensors are not versatile, therefore, each sensor can be applied to only one particular medium. Moreover, they require a sensitive element, namely “sensitiser” (discussed in detail in Section 2.3) with specific properties either water-soluble or insoluble. These shortcomings confirm the need for a new generation of cheap, portable, sensitive, and versatile sensors capable of detecting both airborne and waterborne analytes at concentrations below the potability limit. The upcoming sections discuss the specific motivations for waterborne and airborne analytes.

### 1.2.1 Motivation behind Waterborne Analyte Sensing

Some waterborne analytes are poisonous and may cause considerable harm (or even lead to death) to humans or animals when ingested at high concentrations. Long-term exposure to low concentrations of these analytes (slightly above the allowable level) has also been shown to result in serious health issues because they accumulate in the body [15]. For instance,  $\text{Pb}^{2+}$  has been considered as one of the most poisonous chemical elements for humans and animals, but is commonly found in our living environment due to its inclusion in many consumable goods, such as lead-acid batteries, wire, paint, glass, and solder [16]. Due to its high toxicity, as indicated in Table 1.1, the maximum allowable level for  $\text{Pb}^{2+}$  is regulated to be  $0.048 \mu\text{M}$  [3][4], as it is believed that exposure to greater concentrations would affect vital organs, such as the kidneys and liver, often leading to anaemia [16]. The ion  $\text{Hg}^{2+}$  is another hazardous waterborne analyte harmful to human health. It can contaminate water through inappropriate disposal of many goods contains  $\text{Hg}^{2+}$ , including batteries, paints, and most electronic devices. It is ingested through contaminated food and drink [15] and as it accumulates in the human body, it has a potential to cause permanent damage to the nervous system, brain, kidneys, and the alimentary system [13]. Available evidence indicates that exposure to air contaminated with  $\text{Hg}^{2+}$  may cause similar health issues [17].  $\text{Cd}^{2+}$  is rated among the most toxic waterborne analytes and is classified as a human carcinogen. It also has harmful effects on the kidneys and respiratory system. It is typically found in nature in low concentrations, but human activities

such as inappropriate disposal of electrical and electronic waste, jewellery and toys containing cadmium have increased its concentration to unsafe levels. Human exposure to  $\text{Cd}^{2+}$  occurs mainly through contaminated food or inhalation of smoke emitted from industries [18]. With precipitation, some of these analytes are deposited on the ground, whereby they contaminate water, often with terrible consequences. For instance, in 2012, a high level of cadmium was detected in Longjiang River located in Guangxi Zhuang Autonomous Region, China. The accident led to great damage to aquatic life, such as fish [19].

Even analytes that are beneficial at low concentrations ( $\text{Cu}^{2+}$ ,  $\text{Al}^{3+}$ ,  $\text{F}^-$ , etc.) become harmful when present in quantities above the allowable level [3][4][5]. Copper is considered as the third most abundant element in the human body; it is responsible for various biological processes. Despite, its essential biological role at low concentrations, it is deemed as a toxic environmental pollutant when present at a high level, because it can accumulate in living organisms [20] resulting in several diseases, including kidney or liver diseases, Wilson's disease [21][22], Menkes syndrome, and Alzheimer's disease [21]. Drinking water and food are of the main sources of  $\text{Cu}^{2+}$ , therefore, the US EPA has set the potability limit of  $\text{Cu}^{2+}$  to  $20.5 \mu\text{M}$  [5].

$\text{Al}^{3+}$  can contaminate water passing through water pipes made from aluminium, which is slightly soluble in aqueous media [23]. Aluminium is beneficial to human bodies but it becomes harmful when exceeding the potability limit of  $7.4 \mu\text{M}$  [5]. It has a high potential to cause serious diseases including Parkinson's, Alzheimer's diseases [24], osteoporosis and adolescent mental retardation [25]. Fluoride is another crucial analyte that is beneficial to the teeth and bones when present at small doses, but high doses can cause health problem such as Fluorosis and urolithiasis [26]. Therefore, the potability limit of fluoride in the drinking water is set to  $79 \mu\text{M}$  [4]. As having access to safe drinking water is of paramount importance, developing cheap, portable, versatile, and reliable sensors that are accessible to a high number of people is extremely important, as these can be used to regularly monitor public water quality.

### **1.2.2 Motivation behind Airborne (Gas/Vapour) Analyte Sensing**

Explosives are very dangerous analytes that have to be detected at a very low level. Explosives can be landmines or explosive residues [27]. Unexploded landmines threaten public safety, necessitating more effective land mine detection. Most landmines consist of nitro-aromatic compounds (NACs), particularly 2,4,6-trinitrotoluene (TNT) and 2,4-dinitrotoluene (2,4-DNT), which are the primary constituents of explosives [9]. DNT can be produced at the intermediate

step of TNT production. TNT is the most representative nitroaromatic explosive used in landmines [28] compared with DNT but detecting DNT as pollutants indicate the presence of the TNT in the sites [29]. Apart from posing grave risk to human life and property, explosives emit toxic gases into the environment [30]. Detecting vapour pressure from NACs is challenging and requires sensitive sensors because they have a low saturated vapour pressure, e.g., at 20 °C 2,4-DNT and 2,4,6-TNT vapour pressures are 148 ppb and 6 ppb, respectively [31]. Moreover, explosive vapours are required to be detected from distant or concealed sources. It is worth noting that, unexploded landmines or ordnance have the potential to seep into the groundwater and then contaminates the oceans [29] since some unexploded landmines consist of partial or fully water-soluble explosive compounds, such as dinitrotoluene and picric acid respectively. Contaminated groundwater or ocean with explosive compounds indicate the presence of unexploded landmines in the area. Consequently, detecting waterborne explosives are just as important as detecting airborne explosives. Several sensitive analytical techniques have been used for the detection of nitro-aromatic compounds, such as high-performance liquid chromatography (HPLC) [32], surface-enhanced Raman scattering [33], ion mobility spectroscopy (IMS) [34], gas chromatography and mass spectrometry (GC–MS) [35]. However, these techniques require very expensive instrumentation as well as complex pre-treatment steps [9]. Thus, the need for robust, cheap and portable airborne analyte sensors is evident.

### 1.3 Aim of this study

This study aims to develop a low cost, portable, and sensitive-fibre optic fluorimetric sensors for the sensing of both air- and waterborne analytes.

#### Objectives:

- I will modify the lock-in based evanescent wave fibre optic transducer sensor system developed by Abraham Kirwa [36] for colorimetric based sensing applications [37][38] such that can be used as fluorimetric sensors for the range of water and airborne analytes.
- Since fibre optic evanescent wave fluorimetric sensors usually suffer from a low fluorescence signal, an alternative excitation mode will be used.
- The targeted water- and airborne analytes include explosives nitroaromatic compounds like dinitrotoluene (DNT) in both media. Here, detecting explosives in water far below

their solubility level will be considered. On another hand, detecting airborne DNT will be at a diluted level, far below their saturated vapour pressure.

- The targeted waterborne analytes in this study also include highly toxic waterborne ions i.e. mercury  $\text{Hg}^{2+}$ , lead  $\text{Pb}^{2+}$ , cadmium  $\text{Cd}^{2+}$  even under short term exposure or harmful ions under long term exposure i.e. aluminium  $\text{Al}^{3+}$ , copper  $\text{Cu}^{2+}$ , fluoride  $\text{F}^-$ . The intended detection limit for highly toxic ions and harmful ions are below their “potability limits”.
- Detecting waterborne analytes require suitable sensitisers, which are either water-soluble or insoluble. Consequently, our transducer will be adjusted to detect the change in the fluorescence from water-soluble or insoluble sensitisers, which indicate the presence of the analytes.
- For ion sensing, water-insoluble sensitisers will be embedded into a ‘phase transfer membrane’ i.e. plasticised polyvinyl chloride (PVC) whenever needed, to allow the diffusion of ions towards the embedded sensitiser when in contact with a solution containing these ions.
- To perform ion sensing i.e. ( $\text{Hg}^{2+}$ ,  $\text{Pb}^{2+}$ ,  $\text{Cd}^{2+}$ ,  $\text{Cu}^{2+}$ ,  $\text{Al}^{3+}$ , or  $\text{F}^-$ ), a small section of the optical fibres as part of our transducer will be stripped and coated with a plasticised and sensitised PVC membrane and then subsequently tested by exposure to water containing the target ion.
- I also intend to use the water-soluble sensitiser for waterborne ion sensing also.
- Finally, the sensing of explosives will be performed by coating a stripped section of the optical fibre with a designated explosives sensitiser, such as pentaerythritol tetranitrate. This will subsequently be tested by exposure to waterborne and airborne explosives.

## **1.4 Thesis Structure**

This thesis has eight chapters. First, two chapters are divided into background information, motivations to this research, introduction to sensor technologies, and relative work that has been previously reported on the airborne and waterborne sensing. Chapter 3 and 4 describe the development process that we carried out on a colorimetric evanescent wave sensor to make it a fluorimetric fibre optic sensor. The applications of our developed sensor and findings of this work are presented in Chapters 5-7. The last chapter summarises the findings of this work and the proposed future work. A brief explanation of each of the eight chapters is presented below.

### **1.4.1 Chapter 1**

This chapter presents brief background information on the air and water pollutions. It also provides the aims and the motivations for this work.

### **1.4.2 Chapter 2**

This chapter introduces the description of the sensors including their characteristic and performance parameters. It demonstrates two crucial models that can describe the sensor response characteristic such as Langmuir adsorption and Stern Volmer Models. Then it provides a brief description of known sensitizers and transducers (including colorimetric and fluorimetric optical transducers). Finally, the physics of optical fibre and its applications as part of the optical transducers are discussed.

### **1.4.3 Chapter 3**

This chapter explains the modifications undertaken to render the colorimetric EW fibre optic sensor suitable for fluorimetric sensing of airborne and waterborne analytes. It also shows the advantages of the side illuminations as excitation mode over the evanescent wave. In addition, it clarifies the functionality of the electrical and the optical components that are involved in the transducer.

#### **1.4.4 Chapter 4**

In this chapter, the preparation of the multimode optical fibre to be sensitised such as cutting, stripping, cleaning and drying is described. In addition, this chapter has a description of two coating techniques i.e. spray coating and dip coating that were used in this work to coat the sensitisers on the stripped section of the optical fibre.

#### **1.4.5 Chapter 5**

In this chapter, the fluorimetric fibre optic transducer is successfully tested for the sensing of either airborne- or waterborne analytes. The airborne sensing was performed by exposing the coated section of the optical fibres with the generic fluorescent polymer namely poly(phenylene-vinylene) derivative MDMO-PPV to a variety of vapour pressures of 2,4 dinitrotoluene (DNT). The DNT waterborne sensing was performed by exposing the coated section of the optical fibre with MDMO-PPV to a range of DNT concentrations in water.

#### **1.4.6 Chapter 6**

This chapter discusses the successful use of pyrazolyl chromene derivative (probe 1) in a solid film rather than an aggregated state when it was immobilised in a plasticised PVC membrane and then coated onto the stripped section of the optical fibre for the sensing of  $\text{Cu}^{2+}$  waterborne.

#### **1.4.7 Chapter 7**

This chapter describes the use of morin derivative, NaMSA, dissolved in water for either  $\text{Al}^{3+}$  (fluorescence off  $\rightarrow$  on sensor) or  $\text{F}^-$  (fluorescence on  $\rightarrow$  off sensor) sensing. The possibility of quantifying the concentration of  $\text{Al}^{3+}$  using the standard addition method was also demonstrated.

#### **1.4.8 Chapter 8**

The main findings of this research are summarised in this chapter alongside the proposed future work.

## Chapter 2: Sensors, Sensitisers and Transducers

### 2.1 Introduction to Sensors

In Chapter 1, the presence of harmful or toxic ions as waterborne analytes at an abnormal level that may lead to horrible human health consequences were discussed, to highlight the necessity of a robust sensor technology. In addition, the negative impact of the air or waterborne explosives to the human security was also discussed. Yet, despite the growing awareness of the detrimental effects of harmful airborne and waterborne analytes to human health, human security and the environment, limited work has been done to develop a versatile, cheap, portable, sensitive fluorimetric sensor that can detect both air and waterborne analytes below their potability limit, which was the primary motivation behind this present study. This chapter commences with the definition of a sensor, followed by the classification based on composition, key characteristics and performance parameters. Then, different types of fluorescent fluorophores (sensitisers), such as fluorescent conjugated polymers and fluorescent dyes with receptors, are introduced, followed by their applications as optical sensors. Some commonly used transducers, including colorimetric and fluorimetric optical transducers, are described before outlining the physics of optical fibres, which are an essential component of the sensors used in this work.

In general, sensors are classified as ‘physical’ or ‘chemical’ sensors, depending on their applications. Physical sensors are devices that measure physical quantities, such as temperature, moisture, force, speed, pressure, density, etc., whereas chemical sensors provide a reading related to a particular quantity (e.g., voltage, absorbance, fluorescence intensity, current, or frequency) that can be precisely correlated to the presence of a certain chemical (at a particular concentration) in a sample. Such sensors are also commonly referred to as detectors, and the chemical to be detected is called the analyte. In some situations similar or lower readings may be produced by different chemicals, those that are not the measurement target, are known as interferants. Sensors usually comprise a sensitiser (or receptor) and transducer. The sensitiser interacts with the analyte (e.g. by binding to it) thus inducing changes in its physical properties. The transducer then translates these changes into the sensor reading. Some sensors are “stoichiometric” rather than “indicating”, whereby their reading will increase with time even under constant analyte concentration, rather than respond linearly to an increase in concentration, as is the case with indicating sensors. Nonetheless, the rate of increase will depend on the analyte concentration [38]. The sensor developed as part of the present study

exhibits indicating behaviour, as shown in Chapter 5–7. In such cases, the reaction between the sorbate (analyte) and the sorption site (sensitiser) is usually reversible (as discussed in Section 2.2.5). Therefore, the chemical reaction can be expressed as follows:



where  $S$  is sorption site or sensitiser,  $A$  is sorbate or analyte,  $SA$  denotes the sensitiser/ analyte complex, and  $k$  quantifies the interaction strength between the sensitiser and analyte, which can be expressed as follows:

$$k = \frac{[SA]}{[S]*[A]}$$

In the expression above, the brackets refer to concentrations, whereby  $[SA]$  is proportional to the occupied sensitiser sites, and  $[S]$  and  $[A]$  are proportional to the sensitiser available sites and the analyte concentration, respectively. When a surface with adsorption sites (i.e. a sensitiser) is immersed in a liquid (gas or liquid) containing the analyte at a certain concentration / partial pressure, the following Langmuir adsorption isotherm,  $\theta(c)$  can be applied to describe the fraction of sensitiser sites occupied by the analyte:

$$\theta(c) = \frac{ap}{(ap+1)} = \frac{kc}{(kc+1)} \quad (2.2)$$

where  $\theta(c)$  describes the fraction of the occupied sensitiser sites with a bound analyte;  $a$  and  $k$  are the stability or binding constants which quantify the interaction strength between the sensitiser and the analyte in vapour and liquid media, respectively; and  $p$  and  $c$  denote the analyte partial pressure and concentration respectively. The derivation of the Langmuir adsorption isotherm relation is given in Eq. (2.2) and presented in Appendix II. Denoting the analyte concentration when half of the sensitiser sites are bound to the analyte as  $c_{1/2}$ , it is evident that  $\theta(c) = kc$  for  $c \ll c_{1/2}$ , while  $\theta(c) = 1$  for  $c \gg c_{1/2}$ , and  $\theta(c) = 1/2$  for  $c_{1/2} = 1/k$

[39]. The same assumptions would apply to the analyte in vapour form. It is worth noting that, Eq. (2.2) describes the quantitative response of many sensors, apart from electrochemical sensors, which follow a different law.

## 2.2 Sensor Characteristics and Performance Parameters

Sensor performance is quantified by several parameters, most of which can be obtained through calibration, which involves exposing the sensor to known analyte concentrations and recording its readings (response). For the sensor used in the present study, at lower analyte concentrations, the response was proportional to  $c$ . However, this linear relationship changed at intermediate concentrations, resulting in a curve that typically plateaued at a certain analyte concentration, indicating saturation. Irrespective of the response function, the calibration chart can be used to obtain a limit of detection ( $LoD$ ), the sensitivity, and a figure of merit, as described in the sections that follow. Other parameters or properties, such as selectivity and reversibility, require additional measurements, as outlined also in later sections.

### 2.2.1 Limit of Detection

$LoD$  is the lowest analyte concentration that can be confidently distinguished from the transducer noise floor [40][41]. It depends on the strength of the sensitiser/analyte interaction (discussed quantitatively in Section 2.3.1.3) and the transducer's signal-to-noise ratio (SNR). The latter can be improved by a lock-in amplifier, as described in Chapter 3. The  $LoD$  can be determined from the linear regime of the calibration chart, to which a straight line should be fitted to obtain the slope  $m$  and intercept  $b$ , with the estimated standard error  $\Delta b$  [41] as shown in Figure 2.1. The intercept  $b$  should be close to zero, which should be contained in the  $b \pm \Delta b$  range, whereby  $\Delta b$  is largely controlled by the transducer's resolution and noise floor, rather than the analyte/sensitiser interaction.  $LoD$  is defined as follows [42]:

$$LoD = \frac{3\Delta b}{m} \quad (2.3)$$

where the factor 3 is a convention that determines a specific confidence level [43].  $LoD$  is obviously dimensionless, given that  $m$  and  $\Delta b$  are represented by the same units.

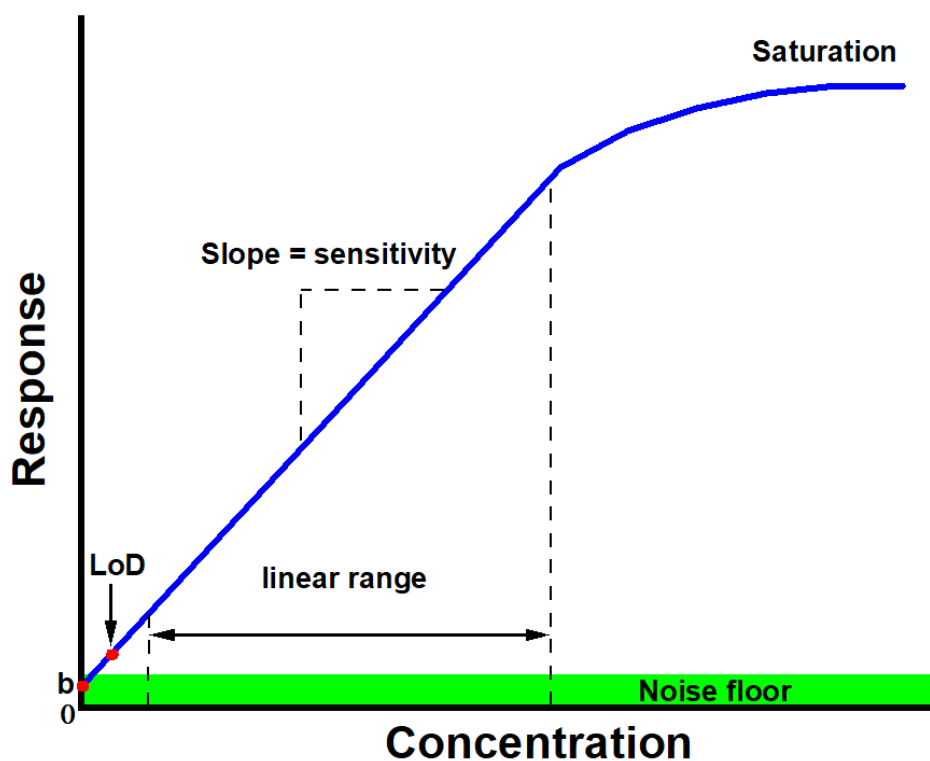


*Figure 2. 1. Diagram showing the LoD at low concentration and above the noise floor.*

### 2.2.2 Sensitivity

Sensitivity pertains to the smallest signal change that can be detected by the sensor. For sensors exhibiting a linear response to an analyte concentration, sensitivity can be easily obtained from the calibration chart [43]. However, for many common sensors (e.g. those of Hildebrand-Benesi or Nernstian type), the relationship between response and analyte concentration is non-linear. In the linear case, the slope  $m$  of a straight line fitted to the calibration chart represents sensitivity. On the other hand, in the non-linear case, the sensitivity evaluation is limited to the slope of the linear portion of the response [43], making it less accurate. Highly sensitive sensors will be able to detect the analyte with LoD.

It is important to note that even linear calibration charts yield somewhat ambiguous sensitivity quantities, as different sensors may transduce a response into different physical quantities (frequency, capacitance, voltage, fluorescence intensity, etc.). Consequently, sensitivity will be expressed in different units, making comparisons among different sensors challenging. Moreover, many transducers rely on electronic amplification, which can be set arbitrarily, making sensitivity a rather arbitrary quantity. This is particularly problematic when simple electronic amplification is applied, as both signal and noise would be amplified. This issue can

be avoided by use of a lock-in amplifier, as it can suppress noise and thus improve the *LoD*. Nevertheless, the strength of analyte/sensitiser interaction is a key factor affecting sensitivity.

### 2.2.3 Figure of Merit

Transducer quality is quantified by defining a figure of merit (*FoM*). While the binding constant  $k$  and  $c_{1/2} = 1/k$  is a measure of the strength of the interaction between sensitiser and analyte only, *LoD* depends on both the strength of interaction and the SNR in the transducer. Hence, *FoM* is defined as follows:

$$FoM = \frac{c_{1/2}}{c_{LoD}} = \frac{1}{k * c_{LoD}} \quad (2.4)$$

*FoM* is a dimensionless measure of the quality of a transducer, as it normalises  $1/LoD$  to unit  $k$ , i.e. it separates the contribution to lowering *LoD* of the transducer from the contribution due to the binding constant  $k$  [44].

### 2.2.4 Selectivity

Selectivity reflects a sensor's ability to discriminate between a target analyte and an interferant, and is quantified as follows [45][46]:

$$S = \log\left[\frac{k_{sa}}{k_{si}}\right] \quad (2.5)$$

where  $k_{sa}$  and  $k_{si}$  are the binding constants between sensitiser and analyte, and the sensitiser and interferant, respectively. Note that, as amplification in the transducer applies equally to both analyte and interferant, neither high amplification nor better SNR can improve selectivity. Consequently, selectivity is largely controlled by the sensitiser, and is independent of the transducer.

### **2.2.5 Response Time and Reversibility**

Response time ( $t_{95}$ ) is defined as the time required for the sensor's response signal to achieve 95% of its saturation response signal. Thus, when calibrating a sensor, the response data should be read after the response has had enough time to equilibrate (i.e. the sensor should be allowed sufficient time to respond fully to a new concentration). The response time is governed by analyte diffusion rate into the sensitiser film or solution, complex formation rate, and complex dissociation rate between the sensitiser and the analyte. Moreover, it has been established that the response time is dependent upon the sensitiser film thickness and analyte concentration [47]. Clearly, a fast response time is desirable in real-life applications, especially for explosives sensing and medical diagnostics.

Sensor reversibility or recovery refers to the time required for the sensor reading to return to the background level prior to analyte exposure, which occurs once the sensitiser binding site becomes free of the analyte. Good sensors should recover when exposed to clean air or water, but some sensors require exposure to EDTA, which stands for ethylenediaminetetraacetic acid or another compound that competes favourably with the sensitiser for the analyte. Certain sensors recover when exposed to analyte ions that can also form a strong complex with the target ion already bound to the sensitiser. The advantage of this approach stems from the ability to use the same sensitiser to sense two different ions.

### **2.2.6 Sensor Calibration**

Some sensors should be calibrated frequently to ensure that reliable readings are obtained when performing actual measurements. As a pH sensor is used in the present work, the calibration process is described using this example. A pH sensor is calibrated by immersing the electrode into a solution of known pH (usually 7), and setting the reading to that value. The process is repeated with a different solution of known pH (e.g. with a pH = 2). It is worth noting that even modern sensors need calibration because internal electronic components may produce a signal (voltage) drift over time due to changes in temperature or pressure. For example, optical sensors are calibrated by performing a control experiment e.g. sensor readings vs time under zero analyte concentration. If signal reduction due to drift in the transducer signal or change in the optical properties of the sensitiser cannot be corrected, this shift must be accounted for when interpreting the analyte sensing data, as described in Chapter 5. Some optical sensors

require calibration due to the non-zero reference signal, whereby their readings need to be subtracted from the baseline or background, as described in Chapter 7.

As discussed previously in section 2.1, the optical sensor depends on a sensitiser and a transducer, therefore, the function of several sensitiser types is described next.

## 2.3 Sensitisers

As the type of sensitiser employed depends on its application, it is important to determine how it responds to the analyte needing to be detected. Chemiresistors, for example, change conductivity, while humidity sensors are based on variations in sensitiser capacitance, and sensitisers that increase the membrane potential are needed for electrochemical sensors. In this section, only sensitisers that have been implemented in optical sensors for analyte detection [37][48][49][50][51][52][53] are described, as others are beyond the scope of the present study. Some optical sensitisers are classified into colorimetric and fluorimetric sensitisers, whereby the former change their optical properties (absorbance) when interacting with the analyte by binding to it, while the latter change their optical properties (fluorescence). The transducer translates the change in the optical properties (absorbance or fluorescence) into a sensor reading, as discussed in Section 2.1. Choosing a suitable sensitiser for optical sensing applications requires a fundamental knowledge of their optical properties, which are discussed next, followed by optical fluorescent sensitisers serving as fluorophores.

### 2.3.1 Molecular Absorption of UV–Visible Light and Light Emission (Fluorescence)

The lowest energy state of a molecule is defined as its ground state, and subsequently its higher energy states are denoted as excited states. In this context, the terms HOMO and LUMO are defined, as highest occupied molecular orbital and lowest unoccupied molecular orbital, respectively. The energy difference between the HOMO and the LUMO is called the band gap energy. Similarly,  $S_0$  denotes the first ground state, while  $S_1$  and  $S_2$  are the first and second singlet excited state, respectively, with  $T_1$  denoting the first triplet excited state. The ground and excited states are split into a series of vibrational levels  $v = 0, 1, 2, 3$ . The energy difference between vibration levels is much lower than the energy difference between the ground ( $S_0$ ) and excited states ( $S_1$ ) or between excited states ( $S_1$  and  $S_2$ ). At room temperature, most molecules remain in the ground state. However, when exposed to light (photons) with energy equivalent

to or greater than the energy difference between HOMO and LUMO levels, the HOMO electrons can absorb that energy and undergo a transition, depending on the amount of absorbed energy. If the energy absorbed from the photon by the electron is equal to or greater than the energy difference between  $S_0$  and  $S_1$  or  $S_2$ , the electron will transition almost instantaneously (within  $\sim 10^{-15}$  s) to  $S_1$  or  $S_2$ , as shown in Figure 2.2 [54].

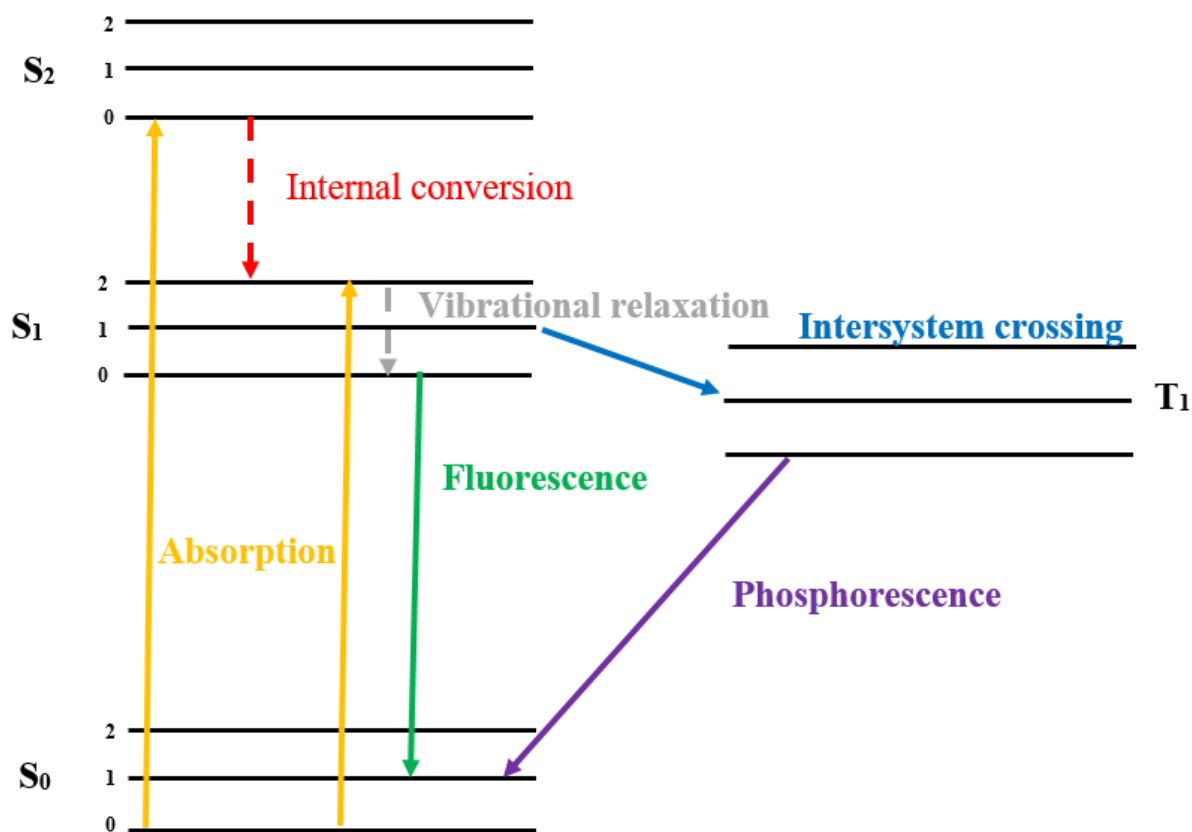


*Figure 2. 2. Jablonski diagram illustrating the electronic transitions (absorption) and relaxations (fluorescence and phosphorescence) as a result of UV-visible light absorption by a molecule.*

If the energy absorbed from the photon by the ground state electron matches the energy difference between the vibrational level  $v = 0$  in  $S_0$  state and the vibrational level  $v = 2$  in  $S_1$  state, electronic transition from  $v = 0$  in  $S_0$  to  $v = 2$  in  $S_1$  will take place. The electron in the high vibrational level of the excited state undergoes internal conversion or vibrational relaxation to the lowest energy level  $v=0$  of that excited state within  $10^{-12}$  s, as indicated by the dotted grey arrow in Figure 2.2 [55] by dissipating its excess energy in the form of heat to the surrounding molecules. As the electrons at the lowest energy level of the excited state relax to

the ground state, they undergo radiative or non-radiative decay. Radiative decay results in luminescence (fluorescence or phosphorescence), as shown in Figure 2.2. Fluorescence emission typically occurs within nanoseconds [56] when the electron in  $S_1$  relaxes to the ground state. Note that not all electrons relaxing to  $S_0$  will emit fluorescent light, as some will dissipate their energy as heat, or will expend it in collisions with other molecules - a phenomenon known as quenching. Some molecules never emit fluorescence because their excited electrons relax to the ground state via non-radiative decay. Electron transition from the singlet excited state  $S_1$  to triplet excited state  $T_1$ , namely intersystem crossing, is rare and usually occurs when the vibrational levels of  $S_1$  and  $T_1$  overlap, because little or no energy is then needed for this transition. Electrons can also transition to  $S_1$  from  $T_1$  and then to  $S_0$  accompanied by delayed fluorescence or delayed non-radioactive decay. During intersystem crossing, some electrons relaxing to  $S_0$  from the lowest energy level in  $T_1$  emit light, a process denoted as phosphorescence that can last several seconds [56], as shown in Figure 2.2. Thus, the main physical factor in discriminating between fluorescence and phosphorescence is the time spent by a fluorophore in the excited state (luminescence lifetime).

The energy difference between  $S_0$  and  $S_1$  or  $S_0$  and  $S_2$  of a molecule indicates the portion of the UV-Visible electromagnetic spectrum that should be absorbed. Thus, wavelengths at which the absorption and emission peak of a molecule appear within the spectrum correspond to the probable allowed electronic transitions from  $S_0$  to  $S_1$  or  $S_2$  and from  $S_1$  or  $T_1$  to  $S_0$ , respectively, whereby the energy difference  $\Delta E$  between electronic levels is related to the wavelength of the absorbed light  $\lambda$  as follows:

$$\lambda = \frac{hc}{\Delta E} \quad (2.6)$$

where  $c$  is the speed of light ( $3 \times 10^8$  m/s), and  $h$  denotes Planck's constant ( $6.626 \times 10^{-34}$  J·s).

The emission peak produced by fluorescent molecules typically does not coincide with the absorption peak, as shown in Figure 2.3. This phenomenon, known as Stokes shift, results from the energy dissipation of excited electrons occupying the vibrational levels when interacting with its surroundings, for example the solvent when in solution, due to which only a part of the absorbed energy is emitted as fluorescence or phosphorescence.

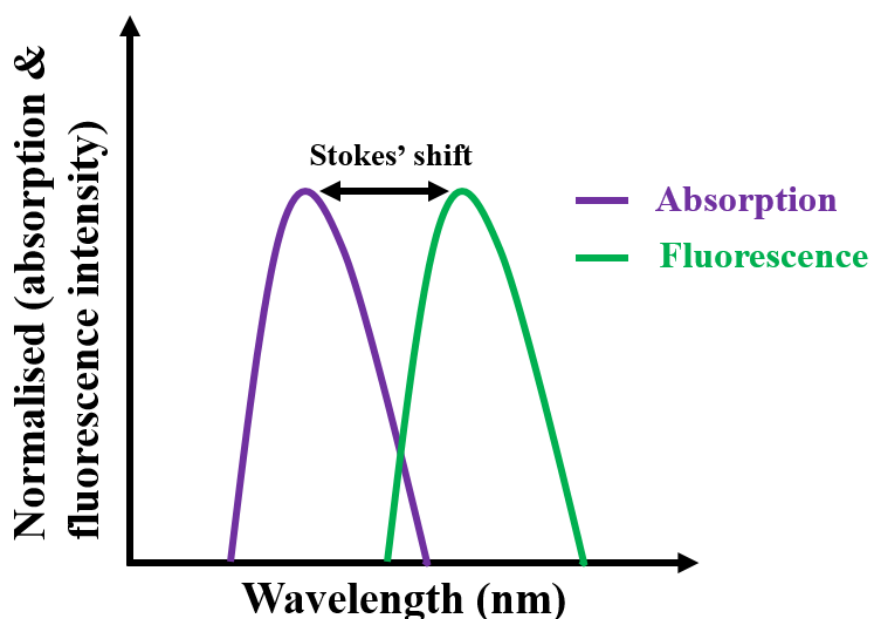


*Figure 2. 3. Stokes shift due to energy losses in the excited state.*

The molecules absorbing incident light can be classified according to their optical properties, as described in the next section.

### 2.3.1.1 Chromophore and Fluorophore

A chromophore is a specific part of the molecule that undergoes electronic transition when exposed to electromagnetic radiation at a wavelength that matches the energy difference between its orbitals [58][59]. As the incident photons interact with the chromophore, their energy is absorbed, causing electronic transition from the ground to the excited state. Some molecules containing chromophores can be used as colorimetric sensitiser in optical sensors because their absorption bands shift when they interact with analytes. Chromophores that bind to ions as analytes are called chromoionophoric chromophores. The analyte binds to the chromophore and in doing so changes its energy levels and therefore the wavelengths of light that it can absorb. For example, 1-(2-pyridylazo)-2-naphthol (PAN) has been used as a chromoionophoric sensitiser in an optical sensor aimed at detecting waterborne  $Zn^{2+}$  [37]. Sensitisers that are an essential part of optical sensors can also be of the fluorimetric type (a fluorophore). The fluorophore is often an organic molecule [58] capable of absorbing

wavelengths in the UV–Vis spectral region, while emitting light (fluorescence) in the visible to near-infrared region, as described in Section 2.3.1. The fluorescence intensity of the fluorophore sensitizer changes upon binding to analytes. The amount of change depends on the chemical interaction between fluorophore's units (a donor and an acceptor) or the fluorophore and the analyte. Upon binding with analytes, fluorescence of some fluorophores is enhanced (off  $\rightarrow$  on)[60], as explained in the next section, while others are quenched (on  $\rightarrow$  off) [51][61][62], as described in Section 2.3.1.3.

### 2.3.1.2 Fluorescence Turn-on (off $\rightarrow$ on)

Fluorescence turn-on (off  $\rightarrow$  on) refers to the fluorescence enhancement when the fluorescent molecule or dye (sensitizer) binds to an analyte. The off  $\rightarrow$  on fluorescence usually occurs when intramolecular photoinduced electron transfer (PET) is prevented. Intramolecular PET can take place when the HOMO orbital of donor atoms (lone pair electrons, such as oxygen, nitrogen, or sulphur atoms) is at a higher energy level than that in the fluorophore. Therefore, when the electron in the HOMO of the fluorophore is excited to the LUMO state, the electrons in the HOMO comprising these lone pairs transition downward to fill the partially unoccupied HOMO of the fluorophore. In this case, excited electrons cannot return to the HOMO of the fluorophore, leading to fluorescence quenching, as shown in Figure 2.4a. PET blocking is one of the most common methods for transforming a non-fluorescent molecule to a fluorescent molecule [63]. In such cases, presence of an appropriate analyte (typically metal ions) reduces or prevents the PET [51][61], leading to fluorescence enhancement (off  $\rightarrow$  on). This mechanism can be utilised in the detection of metal ions as analytes. When a metal ion is coordinated with the lone pair, it brings the HOMO energy of the lone pair atom below that of the fluorophore due to the charge transfer from the ligand to the metal ion. As this process suppresses PET or fluorescence quenching, it gives rise to chelation-enhanced fluorescence (CHEF or off  $\rightarrow$  on), as shown in Figure 2.4b [63][64].

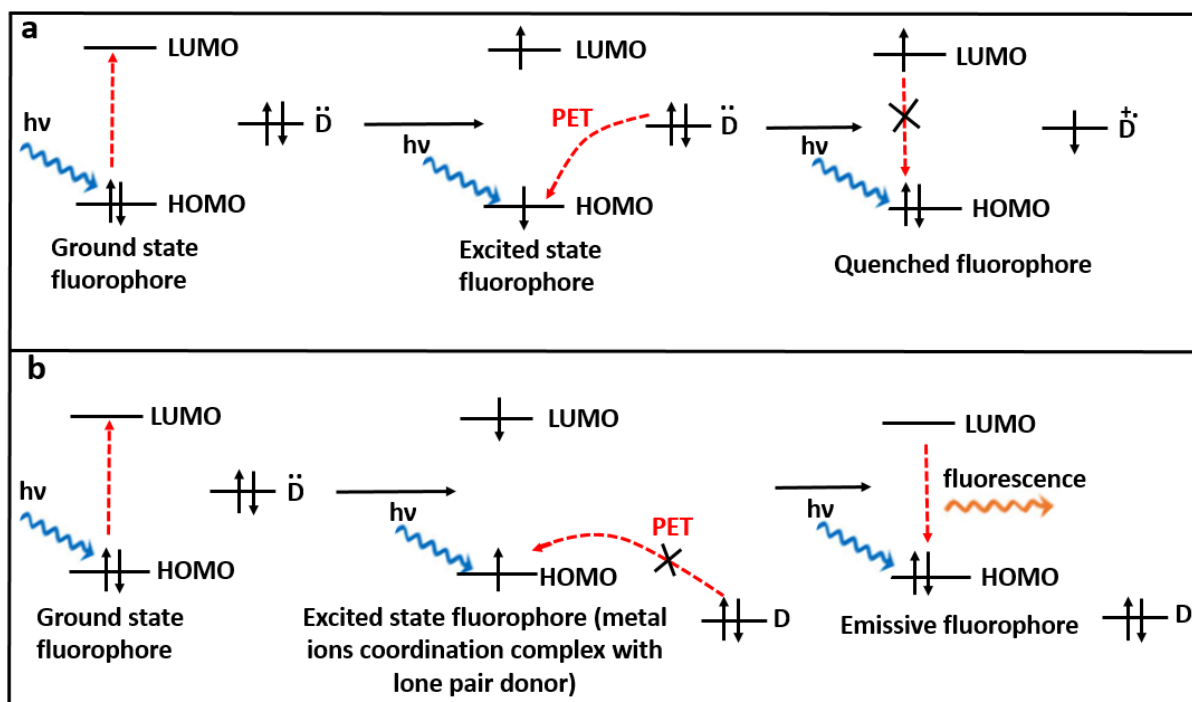


**Figure 2. 4.** (a) Intramolecular fluorescence quenching via photoinduced electron transfer (PET). (b) Metal ion coordination with lone pair donor, which prevents PET and results in chelation-enhanced fluorescence (CHEF).

The off  $\rightarrow$  on behaviour is more desirable in optical sensors compared with fluorescence quenching, as it produces a completely dark background that minimises potential false-positive signals [65][66][67][68]. The response characteristic of off  $\rightarrow$  on fluorimetric sensors  $I(c)$  can be described by the differential equation of adsorption, as indicated below:

$$I(c) = I(\infty)[1 - \exp\left(-\frac{t}{\tau}\right)] \quad (2.7)$$

where  $I(c)$  and  $I(\infty)$  denote the fluorescence intensity of the sensitizer in the presence of analyte at a particular concentration, and in the presence of an excessive amount of the analyte, respectively,  $1/\tau = k_a c + k_d$ ;  $k_a$  and  $k_d$  are rates of adsorption and desorption, respectively, and  $c$  is the analyte concentration. The ratio of  $k_a/k_d = K_A$  [ $M^{-1}$ ] is an important characteristic called as association constant, which is equivalent to  $k$  in the thesis. The reciprocal value  $K_D$  [ $M$ ] =  $1/K_A$  is known as the dissociation constant.

Once  $k$  is determined,  $c_{1/2}$  is known as it is equal to  $1/k$ . The obtained  $c_{1/2}$  value (and thus  $k$ ) enables the estimation of the binding strength between the sensitiser and the analyte, which is related to the standard Gibbs energy of adsorption  $\Delta G^0$  by the Boltzmann factor, as shown below:

$$k = \exp\left(-\frac{\Delta G^0}{RT}\right) \quad (2.8)$$

where  $R$  is the gas constant (8.314 J/mol\*K) and  $T$  is the absolute temperature (in K). It is obvious from Eq. (2.8) that  $k$  (representing the same property as that described by Eq. 2.2) is given by  $\Delta G^0$ . The above expression can be rewritten as follows:

$$\Delta G^0 = -RT \ln(k) \quad (2.9)$$

It is worth noting that Eq. (2.9) cannot be applied to calculate  $\Delta G^0$  because  $k$  is inversely proportional to  $c_{1/2}$  (and is therefore expressed in  $M^{-1}$ ) and logarithms can only be applied to dimensionless quantities. To avoid this issue, Xueyong and Xin [69] converted  $k$  into a dimensionless quantity  $k^0$  giving rise to the expression below:

$$\Delta G^0 = -RT \ln(k^0) \quad (2.10)$$

This transformation was achieved by multiplying  $k$  with the molar concentration of the solvent (in this case water, expressed as M) since  $k = 1/c_{1/2}$ . As the density of water is  $\frac{1\text{kg}}{\text{L}} = \frac{1000\text{g}}{\text{L}}$ , and its molar mass is  $\frac{18\text{g}}{\text{mole}}$ , the corresponding concentration is  $\frac{1000\text{g}}{\text{L}} * \frac{\text{mole}}{18\text{g}} = 55.56 \text{ M}$ . Consequently,  $c_{\text{water}}$  (M) cancels the unit of  $c_{1/2}$  (M), leading to a dimensionless quantity, as shown below:

$$k^0 = kc_{\text{water}} = \frac{c_{\text{water}}}{c_{1/2}} \quad (2.11)$$

### 2.3.1.3 Fluorescence Quenching (on → off)

Fluorescence quenching (on → off) refers to fluorescence intensity quenching of a fluorophore (sensitiser) when its excitation energy is transferred to surrounding chemicals, namely ‘analytes’ or ‘quenchers’ [70] instead of by emission of photons. Fluorescence quenching as a result of the energy transfer from the fluorophore to the analyte usually occurs through PET,

which usually takes place between electron-rich and electron-deficient molecules. PET occurs when an electron-rich fluorophore acts as an electron donor, and an electron-deficient analyte serves as the electron acceptor. Therefore, an electron in the LUMO of the excited fluorophore is donated to a low-lying LUMO of the analyte, resulting in fluorescence quenching [66]. However, it is important to note that quenching due to energy transfer occurs through a variety of mechanisms, giving rise to static and dynamic quenching (collisional quenching) [27], as discussed in the following section. Fluorescence quenching has wide applications in chemical and biological sensing. For example, it can be used to detect the presence of toxic ions in water at low concentrations [71][72][73], as well as at high concentrations [42][74]. It has also been applied for determining the presence of explosive compounds in both water and gas media [1][9][28][48][75][76][77][78], and glucose in blood [79]. The characteristic response of an on → off fluorimetric sensor is controlled by  $1 - \Theta(c)$  which represents the fraction of sensitiser sites that are unoccupied by analyte, as shown below:

$$I(c) = I(0) * (1 - \Theta(c)) \quad (2.12)$$

where  $I(c)$  and  $I(0)$  denote the fluorescence intensity of the sensitiser in the presence of analyte at a particular concentration, and in the presence of zero analyte, respectively.

Substituting the expression for  $\Theta(c)$  given by the Eq. (2.2) yields:

$$I(c) = I(0) * \left(1 - \frac{kc}{kc+1}\right) \quad (2.13)$$

Further simplifications results in:

$$\frac{I(c)}{I(0)} = \left(\frac{1}{kc+1}\right) \quad (2.14)$$

This expression can be further transformed, giving rise to Stern-Vollmer (SV) equation:

$$\frac{I(0)}{I(c)} - 1 = kc \quad (2.15)$$

where  $k$  can be quantified by plotting  $\frac{I(0)}{I(c)} - 1$  as a function of  $c$ , whereby the slope is equal to  $k$  and  $c_{1/2}$  is equal to  $1/k$  [80]. As already noted in Section 2.2.2, sensitivity depends on the binding constant, which plays a significant role in the interaction between the sensitiser and the analyte [81].

#### 2.3.1.3.1 Static and Dynamic Quenching

Both static and dynamic quenching occurs when fluorophore molecules are in contact with the analyte, whereby static quenching results from the complex formation in the ground state between the fluorophore and the analyte, independent of excitation. The complexed fluorophores are non-fluorescent while un-complexed fluorophores continue to produce fluorescence emission according to their native natural lifetime. On the other hand, dynamic quenching occurs via collisions between excited fluorophores and the analyte. These collisions cause the excited electrons to relax to the ground state without fluorescence [66]. The energy that the electrons possessed in the excited state dissipates in the form of heat energy to the surrounding fluorophores or molecules (analytes). Compared with static quenching, dynamic quenching is faster and also a more reversible process, which results in low sensitivity and selectivity due to the low binding constant [27]. Fluorophores characterised by a long lifetime have a higher probability of interacting with the analyte, which tends to result in more dynamic quenching, given that the analyte can travel a longer distance to encounter the electron of the excited fluorophore. For either static or dynamic quenching, the response characteristic (fluorescence intensity vs. analyte concentration) follows the SV law described in Eq. 2.15 [80].

There are many types of fluorescence sensitisers, some of which are briefly described in the sections that follow

## 2.3.2 Review of Fluorescent Sensitisers

### 2.3.2.1 Fluorescent Conjugated Polymers

Fluorescent conjugated polymers (CPs) comprise of many repeating fluorophore units. CPs consist of an organic molecule with alternating single and double bonds, forming a backbone chain, which allows for electron delocalisation along its backbone. The polymer backbone acts as a molecular wire [82], therefore excitons (electron and electron hole bound state which are electrostatically attracted to each other by the Coulomb force) can travel long distances along the backbone, which increases the likelihood of the exciton interacting with a bound analyte which could be attached to any of the many fluorophore units before relaxing to its ground state. The exciton travel distance is controlled by the exciton migration rate and the lifetime of the excited state [82]. Thus, using fluorescent CPs enhances the sensitivity of fluorescence based sensing via signal amplification because a single analyte interaction can quench a significant number of fluorophores. Consequently, fluorescent CPs are highly desirable in optical sensor applications. On the other hand, fluorescence based on small (non-conjugated) molecules is less sensitive because the exciton is confined within a single molecule and can only interact with analyte at its binding site, restricting the quenching potential [48][65]. A schematic diagram depicting the mechanism of action of a fluorescent CP sensor and a small molecule sensor is shown in Figure 2.5. For example, Swager and colleagues have synthesised a very sensitive fluorescent PC “Penttiptcene” for the detection of nitroaromatic explosives [48], as described in Section 2.3.2.1.1.

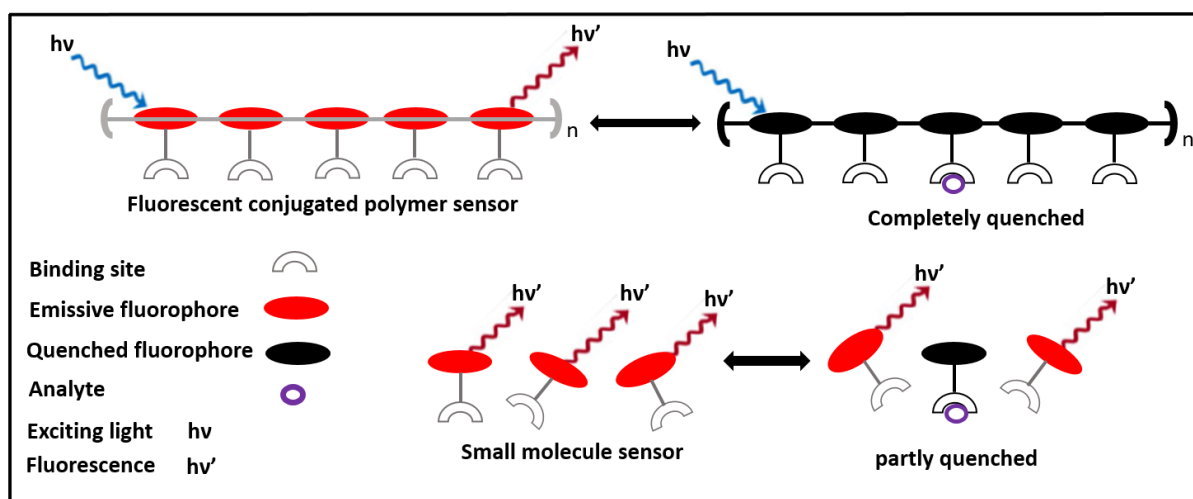


**Figure 2. 5.** Fluorescence quenching processes occurring in fluorophores connected as a “molecular wire” (which amplifies the sensor response) and a small molecule or isolated fluorophore.

### 2.3.2.1.1 Pentipitycene Polymer

The pentipitycene polymer with its backbone chains is shown in Figure 2.6. [48][49]. This polymer has been used in the solid form as a sensitizer film for nitroaromatic compound vapour detection. The polymer consists of a three-dimensional rigid, bulky pentipitycene structure, which reduces self-quenching from backbones of conjugated polymer chains, commonly known as  $\pi$ -stacking. Moreover, it creates cavities or porous structures within the polymer film, thus enabling small molecules to diffuse and exclude larger molecules. The polymer interacts with molecules via several possible mechanisms. For example, as molecule size must be small in comparison to the size of the cavities, smaller molecules (such as TNT) would fit in, but larger ones would not. In some cases, an electrostatic interaction can occur between the polymer and the analyte. Consequently, when exposed to different analytes at the same vapour pressure, an electron-rich polymer would preferentially bind to a more electron-deficient analyte. As an example, a pentipitycene- polymer binds to TNT more than to DNT, even though TNT has a lower saturated vapour pressure (10 ppb at 25 °C) compared with 2,4-DNT (193 ppb at 22 °C), because TNT is more electron deficient. The presence of TNT quenches the fluorescence of the pentipitycene film 4 times more than DNT when they present at same quantities (100 picogram) [82]. This conjugated polymer was engineered by linking individual fluorescent monomers. The backbone of a conjugated polymer acts as a wire through which excitons can propagate. Therefore, as excitons travel across many receptors before transitioning to the ground state, the probability of sampling one of the explosive analyte molecules is high, as shown in Figure 2.5. This process plays a major role in sensitivity enhancement by amplifying the signal. This polymer was applied successfully in a commercially available device “Fido” for real detection of buried explosives, using the exciting and emission wavelengths of 370 nm and 460 nm, respectively. The detection limit towards TNT based on fluorescence quenching was 6 parts per trillion (ppt) [82] indicating very high sensitivity. The schematic diagram of the pentipitycene-derived PPE structure and thin-film porosity is shown in Figure 2.6.

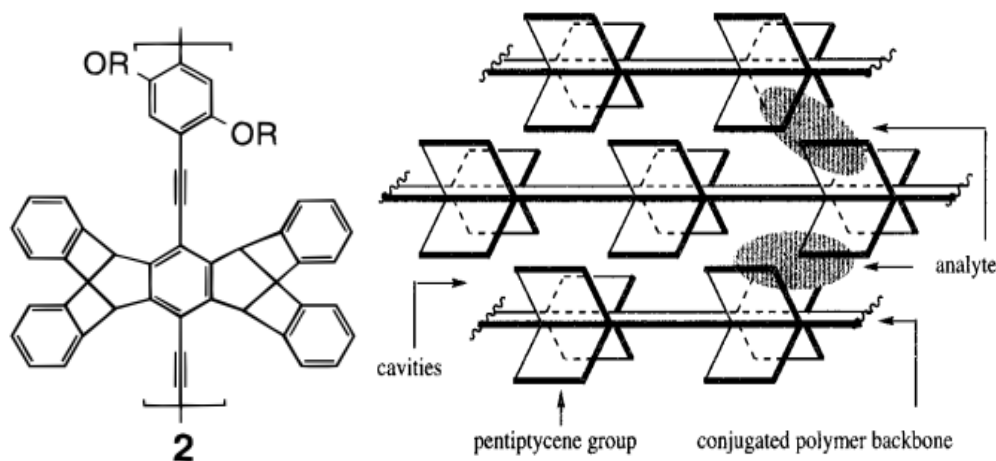


**Figure 2. 6.** Pentiptycene-derived PPE structure and conceptual polymer porosity for analyte detection [48].

### 2.3.2.1.2 MDMO-PPV

PPVs are a family of conjugated polymers with good photoluminescence. They are water-insoluble but dissolve readily in many organic solvents, including toluene, 1,2-dichlorobenzene, and chloroform [83]. PPVs have been used in solar cells [84] and organic light-emitting diodes [85]. In addition, PPV derivatives have been successfully used in fluorescent sensor applications [1][77][86][87]. Their main drawback stems from the aggregation in the condensed state, resulting in fluorescence quenching due to  $\pi$ - $\pi$  stacking even in the absence of analyte. To overcome this issue, bulky substituted moieties were incorporated into PPV backbones for explosive sensing applications [27]. Poly(phenylene-vinylene) derivatives MEH-PPV and DP10-PPV have been used as fluorescent sensitizers to detect DNT and TNT vapour [88]. In another study, MEH-PPV films at three different concentrations were deposited on the exposed tip of an optical fibre (obtained by removing the cladding from one end of the optical fibre). These films on fibres were used to detect 1,4-dinitrobenzene (DNB) in acetone and to study the effect of these concentrations on the quenching response [86]. MEH-PPV has also been used to detect DNB in acetone, and a detection limit of 37.5  $\mu$ M was reported [77]. A super yellow polymer, a derivative of PPV family, has been coated on the glass substrate to detect DNT in the gas state, yielding a *LoD* of 30 ppb [1]. Moreover, poly[2-methoxy-5-(3',7'-dimethyloctyloxy)-1,4-phenylenevinylene] (MDMO-PPV) has been used to detect TNT in chloroform [89]. In the present study, fluorescent poly(phenylene-vinylene) derivative MDMO-PPV was adopted to detect DNT in water and air at low concentrations. Fluorescence

of this derivative is known to quench as a result of exposure to many nitroaromatic explosives [87]. Its fluorescence quenching is static in type because complex formation occurs in the ground state. Moreover, as it takes a few minutes to reach equilibrium, this excludes dynamic (collisional) quenching which is diffusion-limited, as discussed in Section 2.3.1.3.1. When DNT binds to MDMO-PPV, the excitons in the LOMO of MDMO transit to the low-lying LUMO of DNT, quenching its fluorescence. The chemical structure of MDMO-PPV and DNT is shown in Figure 2.7a, while their energy levels and exciton transitions are shown in Figure 2.7b.

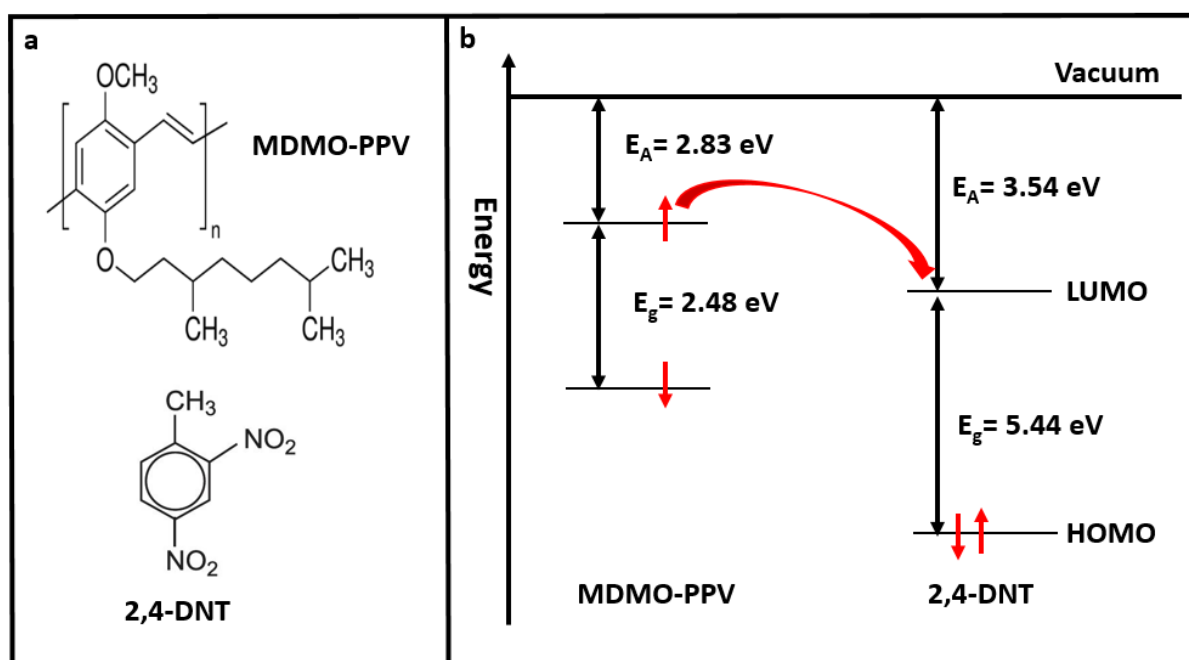


**Figure 2. 7.** (a) MDMO-PPV and DNT chemical structure. (b) MDMO-PPV [90] and DNT energy levels [88] and exciton transitions from the LUMO of MDMO to the LUMO of DNT.

In addition to fluorescent polymers, in practice, fluorescent dyes have also been extensively used for ion sensing. For example, chemically tuned boron-dipyrromethene (BODIPY) dye when linked to ion receptors have been used for ion sensing, and these are described in the next section.

### 2.3.2.2 Organic Fluorescent Dyes

#### 2.3.2.2.1 BODIPY Fluoroionophore

Boron-dipyrromethene (BODIPY) is a fluorescent dye comprising of dipyrromethene coordinated with a boron centre, typically BF<sub>2</sub>. The majority of BODIPY dyes are characterised by a small Stokes shift and a high fluorescence quantum yield, even in water. Moreover, their absorption and emission bands remain approximately at the same wavelengths even if exposed to different solvents. Owing to these beneficial features, BODIPY can be adopted as a sensitiser for fluorimetric sensing applications [91]. The BODIPY core structure is depicted in Figure 2.8.

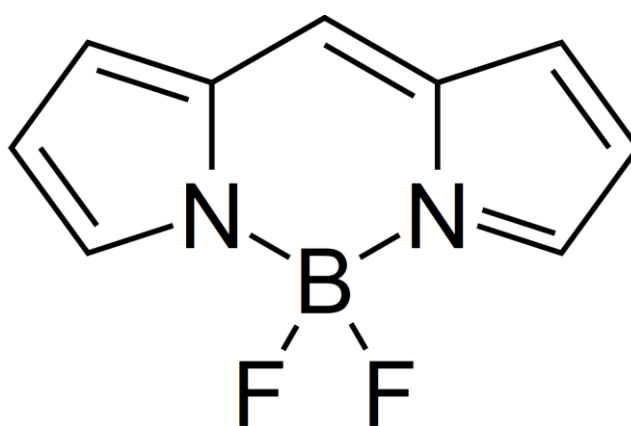


*Figure 2. 8. BODIPY core chemical structure.*

BODIPYs can be tuned for fluorescent sensing applications by chemically linking them to metal ion receptors (i.e. ionophore or crown ethers), which results in fluoroionophores. An ionophore is a chemical compound functioning as a reversible ion carrier across a hydrophobic membrane. It captures a target ion from the water sample and transfers it across the hydrophobic membrane to the binding sites of the sensitiser. Once in contact with the sensitiser, the ionophore releases the ions, which can subsequently induce changes in the sensitiser's physical properties, such as fluorescence, absorption, etc. For example, valinomycin is considered to be a good ionophore [92][93] as it selectively binds to K<sup>+</sup> in the water sample and transports these ions across a plasticised hydrophobic membrane, typically polyvinyl chloride (PVC), to the sensitiser binding sites. Other ionophores are designed to form hydrophilic channels within the hydrophobic membrane, allowing selective ions to be transported to the binding sites of the sensitiser without being in direct contact with a hydrophobic membrane.

Crown ethers that were invented by Pedersen (Nobel prize) [94] are heterocyclic organic compounds comprising of multiple ether groups [45]. The ring has a central cavity that is specific to each particular crown ether, as shown in Figure 2.9. The crown ether rings mainly consist of oxygen atoms that possess a high binding affinity to alkali and alkaline earth metallic cations. Thus, a crown ether forms a strong metallic coordination complex at its centre, whereas its exterior is hydrophobic.

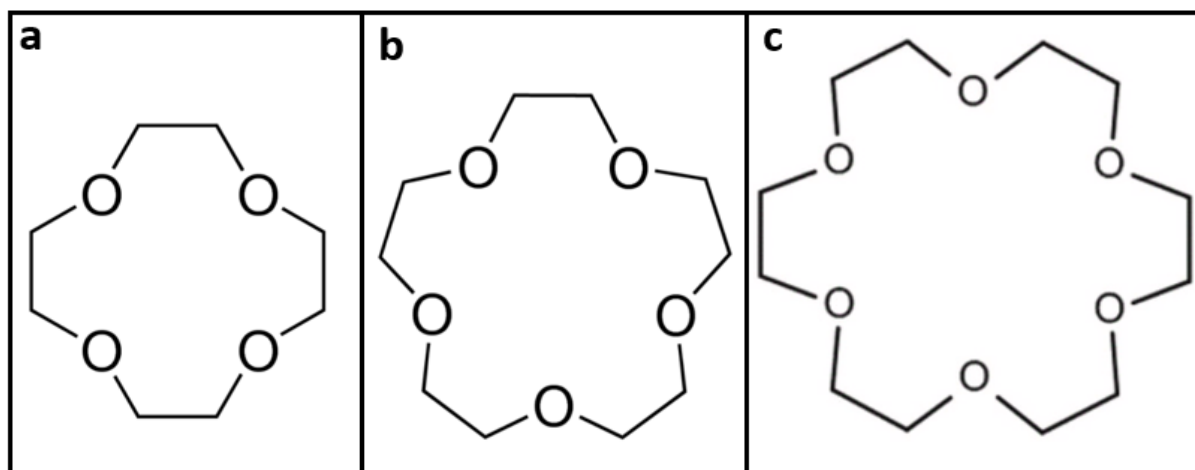


**Figure 2. 9.** Crown ether rings (a) 12-crown-4, (b) 15-crown-5, (c) and 18-crown-6 [45].

Certain crown rings can be modified by replacing some of the oxygen atoms with other donor atoms, such as nitrogen [51] and sulphur [95]. These atoms also contribute to the cation complex formation at the centre of the ring. Owing to these beneficial properties, the crown ether rings have been used for cation detection in optical sensor applications [51][95][96][97]. Each of the crowns shown in Figure 2.9 is capable of selectively coordinating with a specific cation, whereby the 12-crown-4, 15-crown-5, and 18-crown-6 strongly coordinate with lithium, sodium and potassium cations, respectively [45]. The crown ethers and the ionophores are not fluorescent molecules; however, when they are linked to a suitable fluorophore, optical transduction can take place. Consequently, the target ions will be detected by changes in optical transduction.

As fluoroionophores consisting of BODIPYs and crown ethers have been shown to exhibit weak fluorescence emission in the absence of analytes due to the intramolecular PET effect, they have been used as off  $\rightarrow$  on sensitizers [51][95][96]. For example, Klimant and co-workers [51] have synthesised a selective fluoroionophore for the detection of waterborne  $K^+$ , as shown in

Figure 2.10. It consists of diaza-18-crown-6 ether as a receptor and BODIPY as a fluorophore. These authors have shown that, even though PET takes place between nitrogen lone pair within the diaza-18-crown-6 and the BODIPY, presence of  $K^+$  reduces the PET, leading to fluorescence enhancement. Surprisingly, this sensitiser is water insoluble, therefore a polymeric matrix or phase transfer material (hydrogel matrix or plasticised PVC membrane) is required to act as a mediator between the waterborne ions such as  $K^+$  in this case and the sensitiser in its solid form. Thus, Klimant has successfully immobilised the sensitiser in a hydrogel matrix with sufficient permeability for waterborne  $K^+$ . When the sensitiser is immobilised in a polymeric matrix, this usually results in sensitiser leaching, low hydrophilicity due to insufficient hydrogel, and aggregation due to incompatibility between sensitiser and the hydrogel. However, these obstacles were overcome when they immobilised the sensitiser in a hydrogel matrix. Interestingly, the sensitiser is pH independent, and exhibits selective fluorescence enhancement in response to a range of  $K^+$  concentrations, including the regular intracellular ( $150 \times 10^3$ ) and extracellular ( $5 \times 10^3$ ) concentrations. Finally, it was successfully applied to foetal bovine serum (FBS) to prove its application on a real sample [51]. In the next section, a well known dye that has a verity of applications in different sensors is discussed.

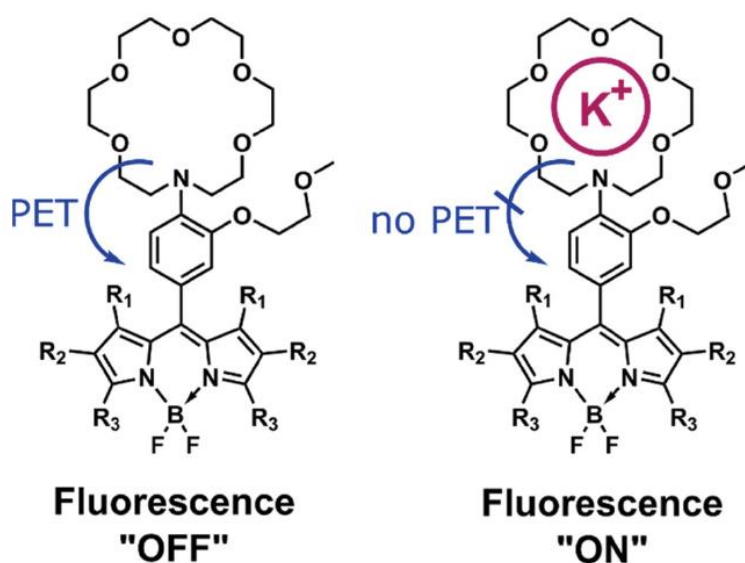


**Figure 2. 10.** Fluorescence enhancement caused by preventing PET when the crown ether receptor coordinates with  $K^+$  [51].

### 2.3.2.2.2 Morin Dye

2',3,4',5,7-Pentahydroxyflavone or Morin is a well-known aluminium (III) selective fluoroionophore [98] but its application has been extended, allowing it to act as a potentiometric sensor [99]. Morin is a weakly fluorescent molecule when excited by light of a wavelength that matches its absorption band (417 nm) [98]. Its weak fluorescence emission ~ 500 nm [100] is attributed to intramolecular PET that occurs when the electrons in the free ligand are induced by exciting light to transfer from the lone pairs of the donor atoms (i.e. oxygen) to the fluorophore (Figure 2.11a). However, its fluorescence intensity increases drastically when those lone pairs bind to  $\text{Al}^{3+}$  [101], as shown in Figure 2.11b. The morin: $\text{Al}^{3+}$  complex formation is accompanied by the release of a proton from the hydroxyl group into the surrounding solution. The sensing medium must be acidified to prevent aluminium from forming hydroxide complexes. However, it should not be strongly acidic to avoid displacing the  $\text{Al}^{3+}$  ion with protons. Aluminium sensing studies based on fluorescence enhancement using the same molecule were carried out at pH~5. The binding constant  $k$  at that pH was  $3.3 \times 10^4 \text{ M}^{-1}$  [98]. Although morin is only slightly soluble in water, Kopazc [102] has rendered it highly water-soluble by modifying it into a water-soluble sodium salt of morin sulfonic acid (NaMSA). Consequently, in the present study, a water-soluble NaMSA is used as the sensitiser for  $\text{Al}^{3+}$  and  $\text{F}^-$  sensing, as discussed in Chapter 7.

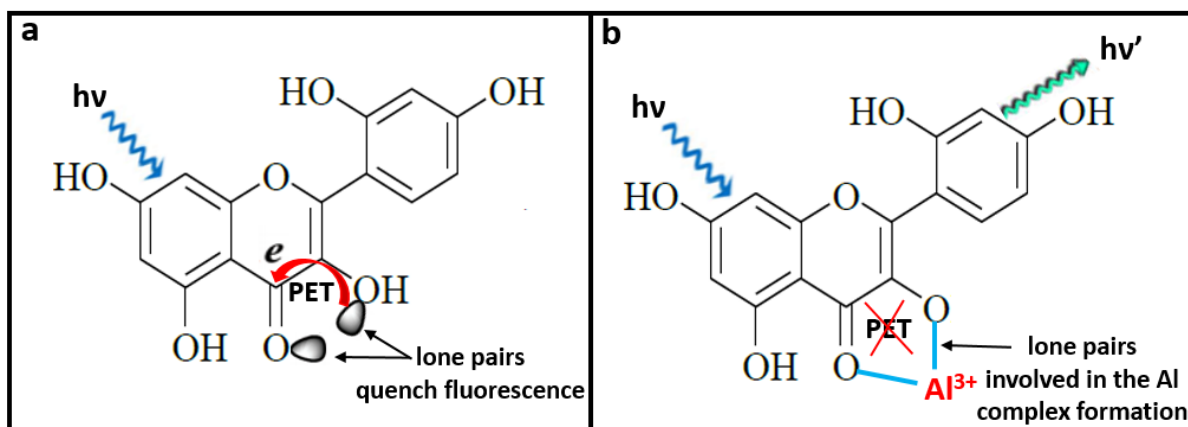


**Figure 2. 11.** Chemical structure of (a) morin, (b) morin: $\text{Al}^{3+}$  complex.

### 2.3.2.3 Other Fluorescent Organic Compounds

#### 2.3.2.3.1 Pyrazolyl Chromene Derivative (Probe 1)

Many fluorescent organic molecules are not highly emissive in solid form (due to aggregation) but become emissive when dissolved in a good solvent. However, the opposite may be true for some molecules that have rotational groups with a certain degree of freedom, as they do not release the absorbed energy as fluorescence when excited, but rather relax back through non-radiative rotations. Dissolving these molecules in poor solvents reduces these rotations and increases the fluorescence. This is a well-known phenomenon and is known as aggregation-induced emission (AIE), and was discovered by Tang and co-workers in 2001 [103]. These authors also noted that the ratio of solvents in a mixture plays a major role in the strength of the fluorescence.

A fluorescent sensitizer referred to as Probe 1 has been synthesised by Kumaravel and Vasuki [104] it is an organic molecule that exhibits AIE. It is highly emissive in a poor solvent (a mixture comprising of a solvent and non-solvent) reaching maximum brightness in a 8.5:1.5 (v/v) H<sub>2</sub>O-THF mixture, despite its weak emission in a good solvent such as Tetrahydrofuran (THF) (Figure 2.12). Probe 1 aggregation into large particles in higher water content solutions is attributed to the molecule's hydrophobicity. Dissolving Probe 1 in a good solvent allows C–C single bond rotations that lead to non-radiative decay. Upon increasing the water (non-solvent) fraction in the solvent mixture, C–C rotations are restricted by the intramolecular hydrogen bonds between donors and acceptors in the aggregated receptor, which enhances fluorescence [105].



**Figure 2. 12.** The fluorescence emission of Probe 1 (20  $\mu$ M) in mixtures of H<sub>2</sub>O/THF with increasing water fractions [105].

Pannipara and co-workers [105] has used Probe 1 as fluorimetric sensitiser for selective metal ion detection of waterborne  $\text{Cu}^{2+}$  and  $\text{Ni}^{2+}$  against other cations, i.e.  $\text{Ag}^{1+}$ ,  $\text{Cd}^{2+}$ ,  $\text{Co}^{2+}$ ,  $\text{Zn}^{2+}$ ,  $\text{Hg}^{2+}$ ,  $\text{Pb}^{2+}$  and  $\text{Mn}^{2+}$ . The aggregated sensitiser shows a fluorescence quenching upon exposure to waterborne  $\text{Cu}^{2+}$  and  $\text{Ni}^{2+}$  while exhibiting ratiometric behaviour in the presence of waterborne  $\text{Hg}^{2+}$ . Fluorescence quenching of Probe 1 results from ligand to metal charge transfer (LMCT) between  $\text{Cu}^{2+}$  or  $\text{Ni}^{2+}$  and Probe 1 that is attributed to the paramagnetic nature of  $\text{Cu}^{2+}$  and  $\text{Ni}^{2+}$ . The absorption and emission of Probe 1 occurs at  $\lambda = 400$  and  $532$  nm, respectively. The response characteristic of these metal ions follows the SV law, which was described in Section 2.3.1.3, while the *LoDs* for  $\text{Cu}^{2+}$  and  $\text{Ni}^{2+}$  are  $1.61 \mu\text{M}$  and  $1.91 \mu\text{M}$ , respectively. Moreover, based on the slope of the linear plots depicting the response as a function of cation concentrations, the SV constants *k<sub>sv</sub>* of  $7.2 \times 10^5 \text{ M}^{-1}$  and  $1.9 \times 10^6 \text{ M}^{-1}$  were obtained for  $\text{Cu}^{2+}$  and  $\text{Ni}^{2+}$ , respectively. The synthesis procedure is reported in [104] and is depicted in Figure 2.13.

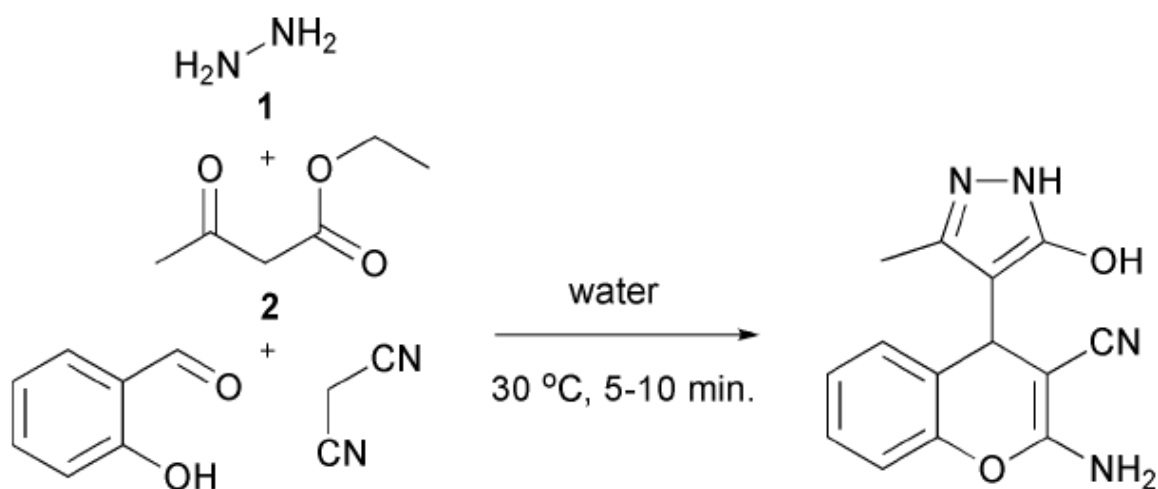


**Figure 2. 13.** The synthetic route for obtaining Probe 1 [104].

In the present study, we immobilised Probe 1 in a plasticised PVC membrane (thin film) rather than using it in the aggregated state to sense waterborne  $\text{Cu}^{2+}$  as discussed in Chapter 6.

In the next section, different transducer types, including colorimetric and fluorimetric transducers, are described.

## 2.4 Transducer Working Principle

As previously noted, most sensors comprise a sensitiser and a transducer, whereby the latter detects the changes in physical properties resulting from the interaction between the former and the analyte and then translates these changes into a quantitative signal. A good transducer can display reliable data by isolating the signal stemming from the sensitiser/analyte interaction over the noise background. The structure and working principle of some commonly used transducers, i.e. electrochemical, Surface Plasmon Resonance, Quartz Microbalance, colorimetric (spectrophotometer) and fluorimetric (fluorimeter) transducers, are presented in the forthcoming sections.

### 2.4.1 Electrochemical Transducers

An electrochemical transducer converts the electrochemical interaction between the sensitiser (ionophore) and the analyte into electrical signal (quantitative data). It has several configurations in terms of the type of electrical signal being measured (i.e. voltage, current, or conductivity) as a means of quantifying sensitiser-waterborne analyte interaction. As an example of this transducer type, the potentiometric transducer is described next.

Potentiometric ion sensors are devices to determine the concentration of a 'target' ion (the 'analyte') in aqueous solution via measurement of an electric voltage, i.e. the sensor transduces analyte ion concentration into a voltage without optical measurements. As with all sensors, a key challenge is to determine analyte concentration unaffected by 'interferants' that may simultaneously be present in the investigated sample. Potentiometric ion sensors are based on 'ionophores', i.e. molecules that selectively bind to a 'target' analyte ion (usually a cation) even when presented with an excess of non-targeted 'interferant' ions. Typical examples are ring shaped organic molecules ('macrocycles') with a central cavity of clearly defined size. The macrocycle selects analyte over interferant for complexation in its central cavity via size selection, even when interferant is chemically similar to analyte (e.g.  $K^+$  vs  $Na^+$ ). Synthetic examples are e.g. calixarenes [106] and crown ethers [94] (previously shown in Figure 2.9), a natural example is valinomycin [92]. Organic macrocycles typically are in-soluble in water, while analyte ions are dissolved in water. For complexation of ions in the ionophore's cavity we therefore require 'phase transfer' of the analyte ion, i.e. transfer from the aqueous to a solid phase as previously discussed in Section 2.3.2.2.1. This is facilitated by embedding the ionophore into a matrix of a polymer that is polar but insoluble in water. The polymer also is

softened by a suitable 'plasticiser'. Typically, polyvinylchloride (PVC) or polyvinylidene fluoride (PVDF) are used. Polymer, plasticiser, ionophore are dissolved in a common solvent, solution is then cast into a flat dish to allow solvent to evaporate [107]. The resulting soft film is then used as 'phase transfer membrane' (often just called 'membrane') for potentiometry. When the surface of such a membrane comes into contact with an aqueous solution of analyte ion, the plasticised polar polymer matrix allows the diffusion of ions towards the embedded ionophore, where it can be complexed. The membrane thus extracts charge (usually positive charge when cations are complexed) from the aqueous medium, building up a charged membrane/water interface, known as an electric double layer (EDL). The EDL is associated with an interface potential, known as membrane potential. As the magnitude of the potential depends on the concentration of analyte ion in the sample solution, the measurement of such interface potentials in principle allows determination of ion concentration in the sample solution. This is the basic concept of ion potentiometer. For ion potentiometry, the *LoD* has a typical range of (100nM -1 $\mu$ M) [108]. Therefore, *LoD* for potentiometry is sufficient for common ions ( $\text{Na}^+$ ,  $\text{K}^+$ ,  $\text{Ca}^{2+}$ ,  $\text{Mg}^{2+}$ ) but not for poisons like  $\text{Pb}^{2+}$ ,  $\text{Cd}^{2+}$ , or  $\text{Hg}^{2+}$  and *LoD* is an innate property of the ionophore so better apparatus cannot help. When sub-100nM detection is needed, there is a case for fluorimetry, as the SV law has no lower cutoff in principle; *LoD* is only limited by signal/noise of the transducer. In classic electrochemical potentiometry, membrane potentials are measured as potential differences (i.e., Voltages) between two membrane surfaces. Therefore, the membrane is mounted to separate two reservoirs, the 'sample' and the 'reference' reservoirs. The reference reservoir is filled with a solution of analyte ion at known concentration  $c_{ref} \gg c_{LoD}$ . This leads to a clearly defined interface potential at the membrane/reference reservoir interface. The sample reservoir is then filled with sample solution of unknown analyte ion concentration, giving a defined potential at the sample reservoir /membrane interface. The potentials of both reservoirs are probed by electrochemical reference electrodes, and the potential difference between the reference electrodes is measured as a voltage with a voltmeter. The measured potential difference depends on a number of potentials built into the apparatus (e.g., for practical reasons the electrode on the reference side makes contact to the reference solution via auxiliary electrolytes while the electrode on the sample side does not), but these are constant and can be calibrated. Further, the measured voltage does depend on the interface potential at the membrane/sample solution interface which is related to the unknown analyte ion concentration.

### 2.4.2 Surface Plasmon Resonance Transducers

A Surface Plasmon Resonance (SPR) transducer is an instrument used to detect changes in thickness and refractive index at the surface of a metal possessing ‘free electrons’ (typically gold) by detecting the resonator angle which is related to the binding of the target analyte [109]. Most SPR transducers comprise of a light source, a polariser, a prism, a photodetector, and a dielectric material (e.g. glass substrate) coated with a particular conductive metal film. If the momentum of the polarised light incident on the metal-coated glass substrate matches that of the free electrons, surface plasmons (SPs) will be emitted as an evanescent wave field that will propagate along the metal–glass substrate interface. Thus, part of the incident light beam is absorbed by the free electrons, which leads to a dark line in the reflected beam at a certain angle, as shown in Figure 2.14. The angle at the minimum reflected light intensity is called the resonance angle ( $\theta_R$ ). Therefore, the refractive index and thickness can be obtained from the  $\theta_R$  shift. For sensing purposes, the metal surface must be coated with a sensitiser to detect the target analyte. When the analyte binds to the sensitiser, the refractive index at the metal surface changes, resulting in resonant angle shifts, whereby a change in the angular shift  $\Delta\theta_R$  is proportional to the analyte concentration  $c$  bound to the sensitiser [109].

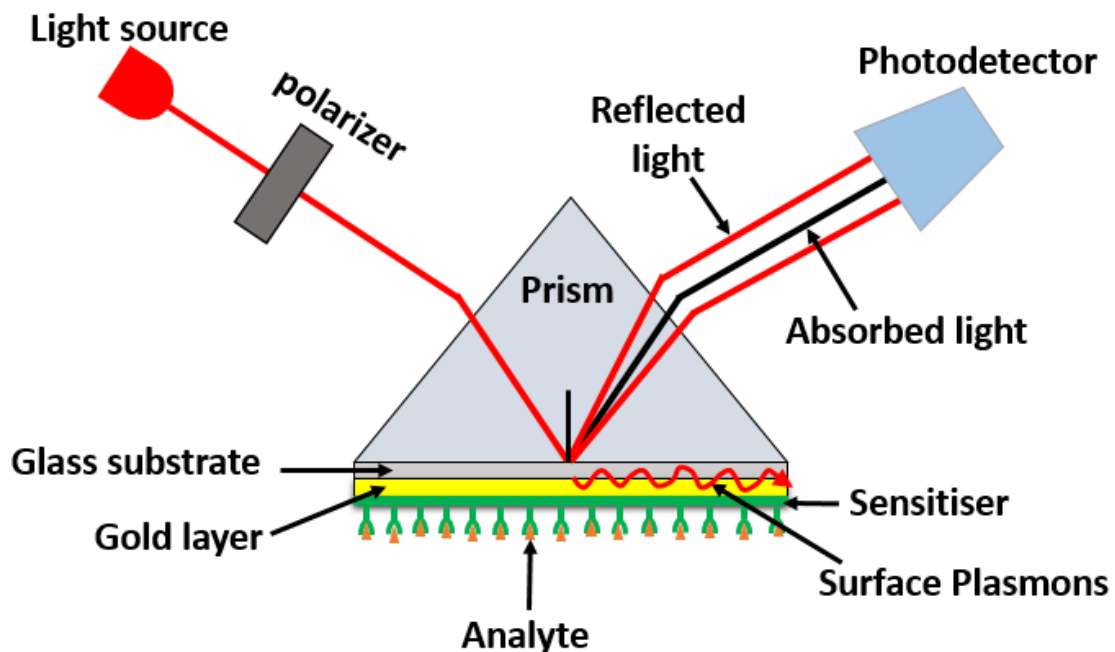


*Figure 2. 14. Kretschmann configuration of an SPR sensor.*

### 2.4.3 Quartz Crystal Microbalance Transducers

Quartz crystal microbalance (QCM) transducers measure the frequency of a quartz crystal to reveal minute changes in mass (on the order of  $10^{-9}$  kg per unit area). The main component of this transducer is a quartz (piezoelectric material) crystal coated with metal electrodes, such as gold. Oscillations in the crystal structure are sustained by an electric drive circuit that locks at the crystal's resonant frequency, as shown in Figure 2.15. The quartz crystal can oscillate at a given frequency when an appropriate voltage is applied to the metal electrodes on its surface. Since this instrument is mass-dependent, the oscillation frequency can be modified by adding or removing mass to/from the surface of metal electrodes or sensor surface. QCM is a versatile technique that can be applied under vacuum, as well as in a gas or liquid environment to monitor the deposition rate (under vacuum), or to determine mass densities and to sense an analyte. For sensing purposes, the gold-coated electrodes on the quartz surface must be coated with an appropriate sensitizer film and exposed to airborne or waterborne analyte. Binding of the analyte to the film modifies the film mass which in turn changes the crystal oscillation frequency, based on the linear relationship described by Sauerbrey [110]:

$$\Delta m = -C \Delta f \quad (2.16)$$

where  $\Delta m$  is the changes in mass,  $C$  is a proportionality constant (quartz crystal property), and  $\Delta f$  denotes change in frequency. Thus, the concentration of the detected analyte can be determined from the frequency change. The QCM has been used for analyte sensing such as acetic acid vapour [111].

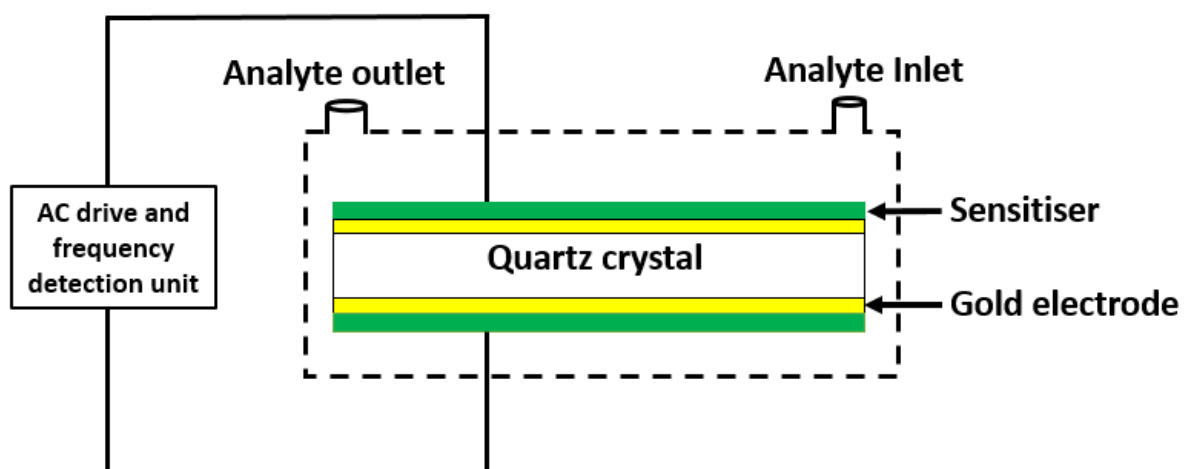
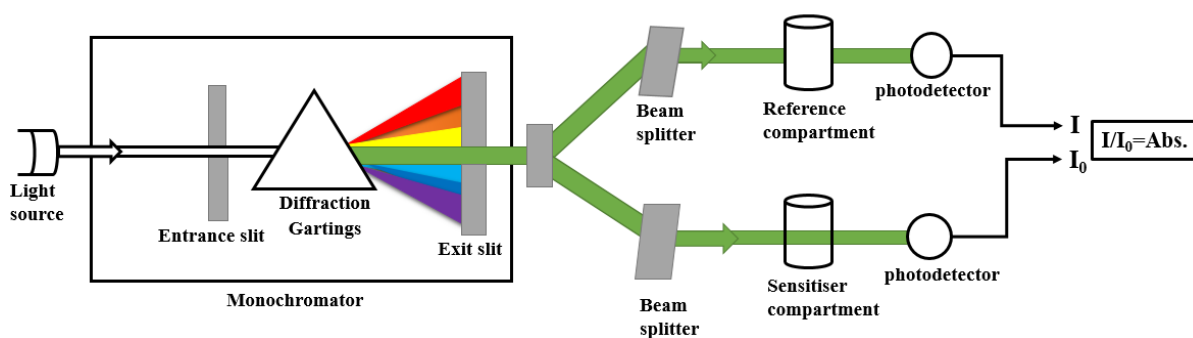


Figure 2. 15. Quartz crystal microbalance sensor.

#### 2.4.4 Spectrophotometer Transducer

Ultraviolet-visible (UV-Vis,  $\lambda = 200\text{--}800\text{ nm}$ ) spectrophotometers are commonly used as transducers for measuring light absorption by a colorimetric sensitiser or sensitiser-analyte complex by converting UV-Vis light intensity to readable electrical signals after passing through the sensitiser and the reference sample. A colorimetric sensitiser changes its absorption spectrum when it binds to an analyte, thus allowing its quantification. The UV-Vis spectroscopy apparatus typically consists of a light source, monochromator, beam splitter, two compartments to hold the transparent quartz cuvettes, and two photodetectors (PDs), as shown in Figure 2.16.



*Figure 2. 16. UV-Vis spectrometer schematic diagram.*

When utilising the arrangement shown in Figure 2.16, light from a white (broadband) light source passes through a scanning monochromator (passing chosen wavelengths), after which the beam splitter separates the light beam into two components (at a 50/50 ratio), one of which passes through the reference compartment and the other passes through the sensitiser compartment before being detected by the PDs. If the beams have equal intensities, 100% transmittance is attained. However, if the sensitiser absorbs wavelengths in the UV-Vis range due to its interaction with an analyte or interferants, light transmittance decreases, as described in below equation:

$$\text{Transmittance } (T) = \frac{I}{I_0} \quad (2.17)$$

where  $I$  and  $I_0$  denote light intensities after passing through the sample and the reference compartment, respectively. The absorbance can be obtained from the transmittance via the expression 2.18 which is the working principle of spectrophotometer.

$$Abs = -\text{Log}_{10}(T) = \text{Log}_{10} \left( \frac{1}{T} \right) \quad (2.18)$$

where  $T$  denotes transmittance and Abs represents absorbance. Absorbance is related to the sample concentration by the Beer-Lambert law:

$$Abs = \epsilon cL \quad (2.19)$$

where  $\epsilon$  is the absorption coefficient of the sample,  $c$  is the sample concentration, and  $L$  denotes the optical path length of the cuvette.

It is worth noting that not all spectrophotometers have a beam splitter, as some operate using a single beam, whereby the intensities of light before ( $I_0$ ) and after ( $I$ ) passing through the sample compartment are measured.

In sensing applications, spectrophotometers have been utilised to measure a change in absorption in response to analyte-sensitiser binding [112][113]. The observed change in absorption versus analyte concentrations usually follows the Langmuir adsorption isotherm model, (described earlier in Section 2.1) which can be applied to find the  $c_{1/2}$  and the binding constant  $k$ . The Langmuir law also permits the intensity of one particular wavelength (or overall intensity) to be used for quantitative analysis.

#### 2.4.5 Fluorimeter Transducers

Fluorimeters can serve as transducers when the aim is measuring fluorescence enhancement or quenching of a fluorophore in either solution or solid form. Fluorimeters can also be incorporated into sensors for measuring changes in the sensitiser emission when it binds to the analyte, allowing its quantification. As can be seen from the schematic diagram of the fluorimeter shown in Figure 2.17, its design is similar to UV-Vis spectrophotometer. It consists of an excitation light source, an excitation monochromator, a sample compartment, an optical filter to block the excitation light, a fluorescence monochromator and a photodetector. The excitation light from the light source passes through the monochromator, which transmits a chosen wavelength toward the sensitiser compartment. The photodetector is positioned perpendicular to the excitation light direction to reduce the likelihood of its detection. In

addition, an optical filter is placed between the sensitiser and the fluorescence monochromator to block the excitation light. The fluorescent signal is scanned by the fluorescence monochromator before it reaches the photodetector, thus producing the required fluorescence spectrum.

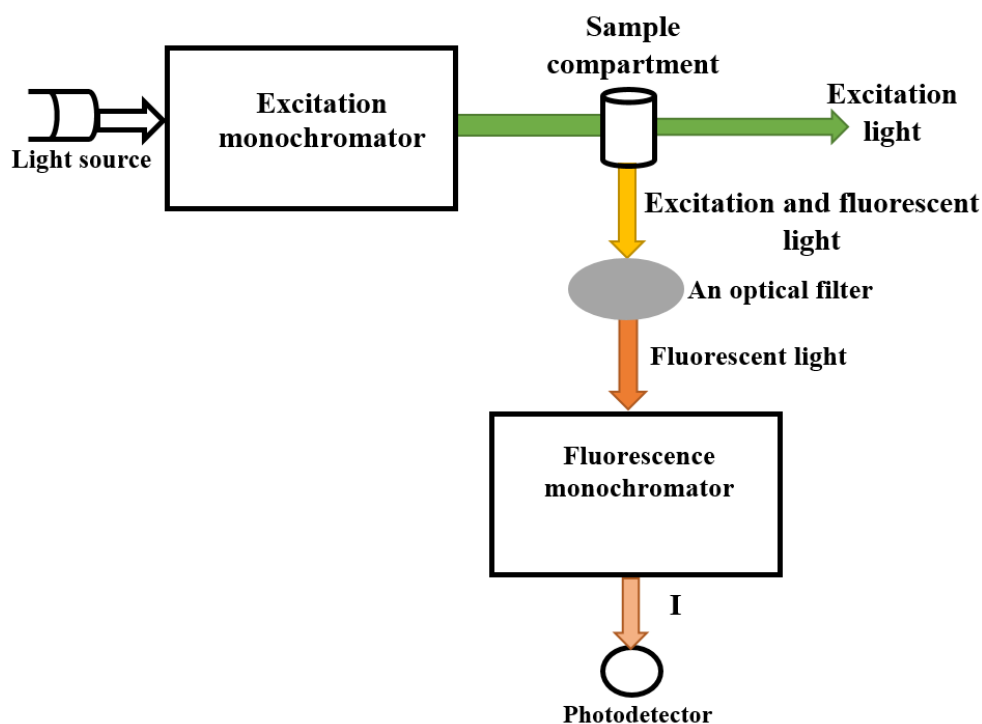


*Figure 2. 17. Spectrofluorometric schematic diagram.*

Spectrofluorometers are commonly used as transducers for chemical, biological and medical sensing. For example, they have been used to measure either fluorescence enhancement or quenching of sensitiser exposed to explosive compounds in water [114] and air [115], and have been proven effective in detecting toxic ions at low concentrations [61][71]. The operating principle of fluorescent sensitiser is discussed in Section 2.3.2. The strength of the interaction (as indicated by the binding constant  $k$ ) between the sensitiser and the analyte can be quantified by the Stern-Vollmer law, as described in Section 2.3.1.3. For its application in quantitative analysis, the intensity of one particular wavelength or overall intensity is sufficient.

Fibre optics have been used as a part of fluorimetric transducers to guide the exciting light to the sensitiser, or to guide the fluorescent light from the sensitiser coated on their exposed core to the photodetector [9][52][61][77][86].

In this work fibre optics are used to couple the fluorescence emitted from various sensitizers to a photodiode, with lock-in amplification of the photodiode signal. Therefore the general functionality of fibre optics and their function as a part of a fluorimetric transducer are discussed in the forthcoming section.

## 2.5 Physics of Fibre Optics

Optical fibres were developed for communications purposes due to their immunity to electromagnetic interference, high bandwidths [116], versatility [117], and low attenuation [118]. Optical fibres were designed to guide light via total internal reflection [119] from a source to the target. Due to their flexibility and resistance to harsh environments, these fibres can pass through curvatures to guide the light to a target location. Fibre optics can be used to connect a light source to samples, as well as transmit sample transmission or fluorescence signal to spectrometers. Thus far, fibre optics have been integrated with sensitizer films as part of fluorimetric sensor for analyte sensing applications [9][51][61]. In this research, fluorimetric intensity measurements were transmitted via optical fibre for sensing purposes, thus avoiding the need for spectroscopy. This is highly beneficial, as fibre optics can be directly integrated with a lock-in amplifier.

Optical fibres consist of a core and cladding with very low optical absorbance, and a protective buffer layer. The core is fabricated from glass (silica) or plastics (PMMA) and has a slightly larger refractive index than the surrounding cladding to ensure total internal reflection at the core-cladding interface, thus confining the light signal within the fibre core. As expected, a fibre with a large core transmits more light than that composed of a small core. Optical fibre cladding is covered with a buffer coating to protect it from accidental impacts that might cause damage to the functional parts of the fibre (core and cladding). Fibre optics can be designed as single- or multi-mode fibres, whereby the latter has a larger diameter, as explained in Section 2.5.3. The typical structure of a multi-mode optical fibre is shown in Figure 2.18, where  $r_1$  and  $r_2$  are the radius of the fibre core and cladding, respectively.

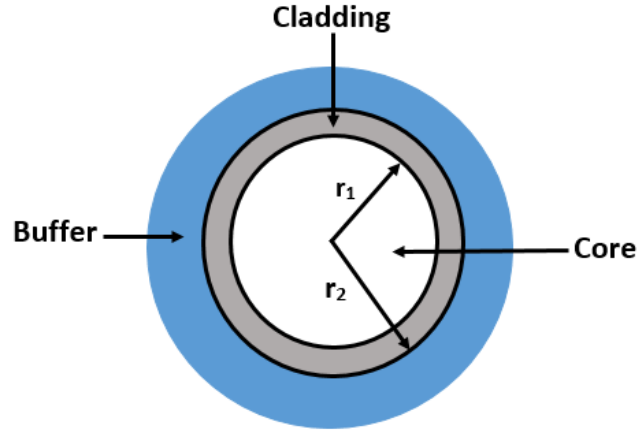


**Figure 2. 18.** Schematic diagram of a typical fibre optic cross-section.

The light incident on the fibre end-face within a certain cone, denoted as the “fibre acceptance cone,” can enter and propagate along the optical fibre. Consequently, the angle formed by the half-cone is called the acceptance angle ( $\theta_a$ ), as depicted in Figure 2.19. For total internal reflection to occur, two conditions must be met, (1) the optical density of the fibre core must be greater than that of the cladding, and (2) the angle of the light ray incident on the core–cladding boundary must be greater than the critical angle  $\theta_c$ , which is related to the acceptance angle  $\theta_a$  as explained in the next section [119].

### 2.5.1 Acceptance Angle, Numerical Aperture, and Critical Angle

The acceptance angle is the maximum angle of the incident light that would result in total internal reflectance at the core-cladding boundary and is quantitatively defined as:

$$\theta_a = \sin^{-1}\left(\frac{1}{n}\sqrt{n_{core}^2 - n_{clad}^2}\right) \quad (2.20)$$

where  $n$  is the refractive index of the region between the light source and the fibre core,  $\theta_a$  is the maximum acceptance angle of the incident light that would ensure total internal reflection, and  $n_{core}$  and  $n_{clad}$  are the refractive indices of the fibre core and cladding, respectively. The  $\theta_a$  is  $18^\circ$  (in water) and  $24.5^\circ$  (in air) for the multimode optical fibre used in this work (FT800UMT, Thorlabs). The value of  $\theta_a$  is controlled by the numerical aperture ( $NA$ ) of the fibre, which

denotes its light-gathering ability. The  $NA$  depends on the refractive indices of the core and cladding, as shown below:

$$NA = \sin\theta_a = \frac{1}{n} \sqrt{n_{core}^2 - n_{clad}^2} \quad (2.21)$$

For multi-mode optical fibres, as explained in Section 2.5.2, the light that enters the core within the  $NA$  of the fibre optics will propagate down the core. Even though some of the light enters the core at angles exceeding the  $NA$ , those rays do not reflect off the core-cladding interface, as shown in Figure 2.19.

The critical angle  $\theta_c$  is defined as the angle of incidence that results in a  $90^\circ$  refracted angle, and is calculated using the following expression:

$$\theta_c = \sin^{-1} \left( \frac{n_{clad}}{n_{core}} \right) \quad n_{clad} < n_{core} \quad (2.22)$$

Only the incident light on the fibre end face with the  $\theta_a$  will be incident on the core-cladding interface at an angle  $> \theta_c$  and be subject to total internal reflection [120] as shown in Figure 2.19.

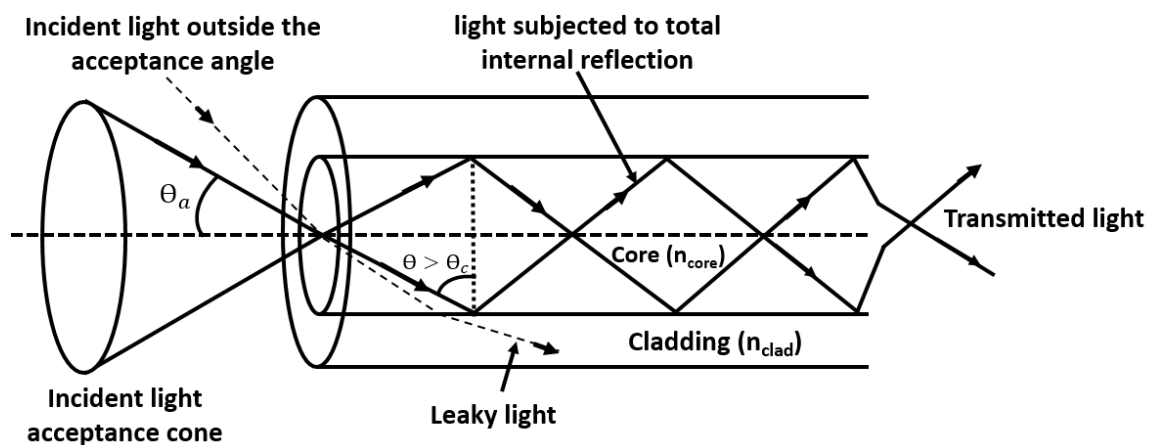


**Figure 2. 19.** Illustrating that only incident light within the optical fibre acceptance cone, or the acceptance angle subject to total internal reflection.

### 2.5.2 Single-Mode versus Step and Graded-Index Multi-Mode Fibre Optics

Fibre optics are classified according to the modes or pathways into single- and multi-mode fibres. Single-mode optical fibres have a small core diameter (typically  $\sim 5\text{-}10\ \mu\text{m}$ ) that allows only one mode to be transmitted. The light transmitted through a single-mode fibre propagates in a straight line, rather than via a zigzag path, as shown in Figure 2.20a. It is not desirable for sensing applications because it is limited to a small core (hard to handle), low  $NA$ , and long wavelengths [120].

Multi-mode optical fibres have a larger core and can be of either step-index or graded-index type. The multi-mode step-index fibre has a core characterised by a uniform refractive index that differs from that of the cladding. This difference results in light being reflected at the core-cladding interface, confining the beam and allowing it to travel within the core following a zigzag path, as shown in Figure 2.20b. This fibre design supports light propagation in more than one mode. As present, this fibre type is commercially available with a core diameter in the  $50\text{--}1500\ \mu\text{m}$  range, as discussed in Section 2.5.1. The graded-index multi-mode optical fibre, on the other hand, has a core comprising of many layers of glass, whereby the refractive index of consecutive layers decreases gradually as the distance from the core centre increases. Consequently, the light travels through the core following a sinusoidal (parabolic) path [120], as shown in Figure 2.20c. The light rays that travel in high parabolic paths (those characterised by low refractive index) are faster than the rays that travel along a less parabolic path (corresponding to high refractive index). The bandwidth of the multi-mode graded-index fibre is higher than that of multi-mode step-index fibre, but is lower than that of the single-mode fibre optic.

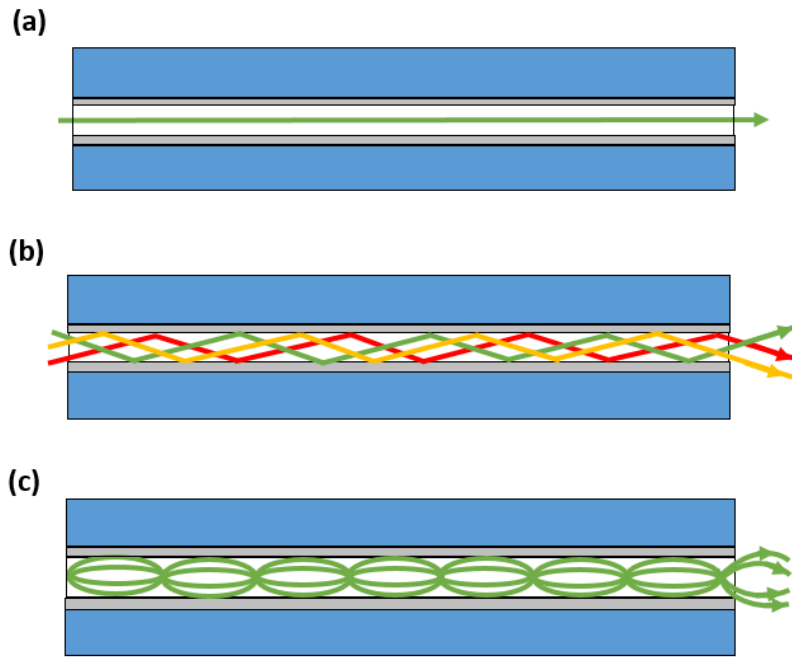


**Figure 2. 20.** Schematic of the propagating modes in an optical fibre of a (a) single-mode, (b) multimode step-index, and (c) multimode graded-index type.

### 2.5.3 V-number and M-number of Modes

The V-number is a parameter used to identify the number of modes that can be supported by an optical fibre [121]. It depends on the core radius, the wavelength of the propagated light and  $NA$ , as shown below:

$$V = 2\pi \frac{r}{\lambda} * N.A \quad (2.23)$$

where  $r$  is the optical fibre core radius,  $\lambda$  is the wavelength of the operating light, and  $NA$  denotes the numerical aperture. For a given wavelength, when  $V \leq V_{CUTOFF} = 2.405$ , the step-index fibre becomes a single-mode; therefore, the maximum wavelength of propagating light in the single-mode fibre is given by  $\lambda = 2.6 * r * NA$ . On the other hand, step-index fibre becomes multi-mode when  $V > 2.405$  [120].

In a multi-mode fibre, light can propagate via many pathways, denoted as modes. The number of propagating modes ( $M$ ) for a step-index multi-mode fibre optic is nearly double the number of the propagating modes in a graded-index multi-mode fibre, as described below [121]:

$$M \approx V^2/2 \quad (2.24)$$

$$M \approx V^2/4 \quad (2.25)$$

This is only approximately true for  $M \gg 1$ . The number of modes depends on the  $V$  number, which is governed by the core radius, the wavelength of propagating light, and numerical aperture.

## 2.6 Evanescent Wave

When light propagates along the optical fibre under the total internal reflection condition, a decaying field known as an “evanescent wave or evanescent field” occurs at the core–cladding interface. An evanescent wave is a near-field wave, whereby its intensity decays exponentially as a function of the distance from the core–cladding interface. The penetration of the evanescent wave into the cladding is defined by penetration depth ( $dp$ ) that can be calculated using the expression below [122]:

$$dp = \frac{\lambda}{2\pi[(n_{core}^2)\sin^2\theta - (n_{clad}^2)]^{\frac{1}{2}}} \quad (2.26)$$

where  $\lambda$  is the light wavelength, and  $\theta$  is the incidence angle at the fibre core-cladding interface. These evanescent waves are a crucial phenomenon in optical sensor technology that has extensive applications in optical sensors [37][122][123], it is discussed in detail in the next section.

### 2.6.1 Evanescent Wave Sensors

Evanescent wave sensor (EWS) is a fibre optic sensor that uses an evanescent wave to excite the sensitiser. When optical fibre is used as a part of the optical sensor, its cladding is stripped and is replaced with an alternative coating, such as optical sensitiser film. If exciting light with a wavelength matching the absorption band of the sensitiser-analyte complex is coupled into one of the fibre ends and propagates along the fibre, the resulting evanescent wave excites the sensitiser film. Figure 2.21 illustrates a section of the optical fibre modified by stripping the buffer and cladding and coating it with a sensitiser, while also depicting the penetration of the evanescent wave into the sensitiser film. Moreover, fibre optic transducers can have many configurations, based on user requirements. As an example, a sensitiser can be coated on the fibre tip section, allowing the same fibre to guide both the excitation light (used excite the sensitiser immersed in analyte solution by the evanescent wave) and the fluorescent light to the detector [61]. In another study, a specific length of the core was exposed in two fibres, and the exposed core of the first fibre was wrapped around the exposed core of the second fibre, which was coated with a fluorimetric sensitiser. This design allowed the evanescent wave produced in the first fibre to be absorbed by the sensitiser in the second fibre, which would in turn allow the resulting fluorescence to be guided to the photodetector [124]. The evanescent wave sensor can be used as a colorimetric or fluorimetric base, depending on the properties of the coated sensitiser. However the fibre optic evanescent wave fluorescence sensors usually suffer from a low florescence signal, due to which an alternative excitation mode has been proposed [117] as explained in sext section.

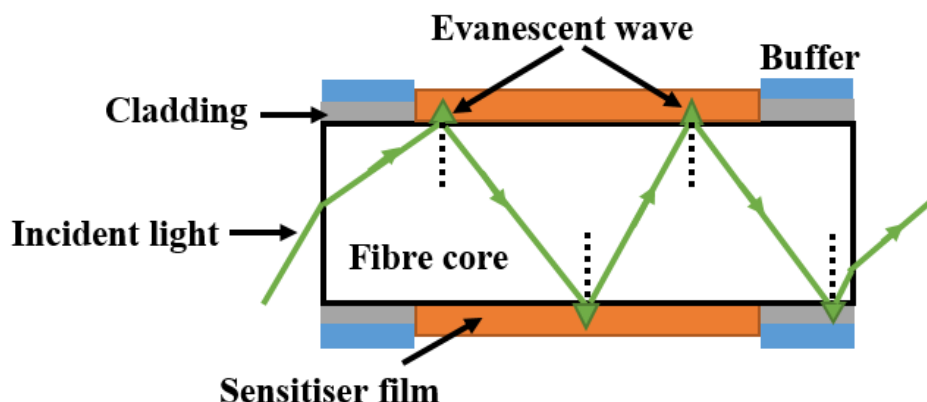


*Figure 2. 21. Sensitised section of the multi-mode optical fibre showing the evanescent wave penetration into the sensitiser film.*

## **2.7 Fibre Optic Sensors and their Merit**

Since the evanescent wave is a weak excitation mode for fluorimetric sensitiser [117], a different excitation mode was considered in this work which results in stronger excitation when the exciting light source is projected onto the coated sensitiser at right angles to the fibre direction –a geometry referred to as “side illumination” [117][125]. Under this setup, the excitation waves travel through water or air before being absorbed by the sensitiser. By using side illumination, the sensitiser will be exposed to light of high intensity, resulting in brighter fluorescence compared to that produced by from evanescent wave excitation as explained in Section 3.1.

## **2.8 Summary of the chapter**

In this chapter, sensor classification, definition, composition, characteristics and performance parameters were introduced. This was followed by descriptions of several fluorescent fluorophores that can serve as sensitiser (such as fluorescent conjugated polymers and fluorescent dyes) with their receptors. Conventional transducers, including colorimetric and fluorimetric transducers, were presented next, along with the physics of optical fibres, since they have been widely used as a part of colorimetric and fluorimetric transducer and will be used as an essential part of our developed optical fibre fluorimetric sensor (described in next chapter).

## Chapter 3: Fibre Optic Sensor Instrument with Lock-In Detection

### 3.1 Introduction to the Optical Fibre Transducer

The definition, classification, characteristics and performance parameters of sensors were discussed in Chapter 2, and a description of the commonly used sensitiser and transducers, including the colorimetric and fluorometric transducers, was provided. This was followed by an explanation of the physics of the fibre optic and evanescent wave sensor (EWS). Thus, this chapter commences with a brief description of the fibre optic EW transducer that was designed by Dr Abraham Kirwa along with its uses in colorimetric sensing applications. The modifications undertaken as part of this work to render this transducer with fluorescent sensitiser suitable for fluorimetric sensing of airborne and waterborne analytes are described next. For this purpose, the colorimetric EW fibre optic sensor set up shown in Figure 3.1 was employed. It is worth noting that, the sensor consists of a transducer and a sensitiser as described previously in Section 2.1. The fibre optic EW transducer comprises electrical and optical components, in addition to a digital lock-in amplifier (USBLockIn250, Anfattec Instruments AG). Certain components (i.e. adder circuit (AC+DC), PD, I/V converter, and the digital lock-in amplifier) were not changed and were used as they are in the colorimetric EW fibre optic transducer. Consequently, they are briefly described in Sections 3.3–3.6 to demonstrate their performance as they contributed to our results in thesis chapters 5, 6 and 7.

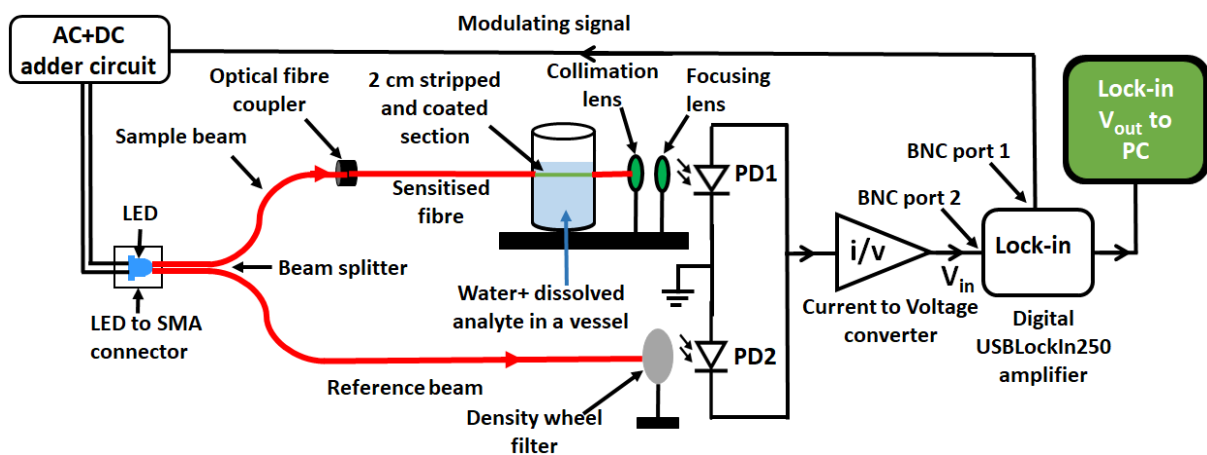


**Figure 3. 1.** Schematic diagram of the EWS instrument and the digital lock-in amplifier built by Abraham before carrying out any modification. PD1 and PD2: Photodiodes (OSD5-5T, Farnell);  $V_{in}$ : Input voltage;  $V_{out}$ : Reference output voltage; BNC port 1 and BNC port 2: Connectors to reference-out terminal and input terminal of the digital lock-in amplifier.

The following briefly describes the basic function of the colorimetric EW fibre optic sensor, as previously published in [36] and its previous applications. In this sensor, the LED as an exciting light source is fixed on the circuit board, and the light is coupled into the beam splitter to be split into 50/50% as sample and reference beam. The reference beam is focused onto a circular neutral density filter (54079, Edmund optics) that is fixed in front of photodiode PD2. The sample beam is coupled into one end of the sensitised multimode fibre optic with a 400  $\mu\text{m}$  silica core (FT400UMT, Thorlabs), the outgoing light is focused on PD1 using lenses that are fixed in front of PD1. The PDs (PD1 and PD2) are connected in such a way as to subtract the current from one another. The net current is fed into the I/V converter, then the voltage of the converter is fed into the lock-in  $V_{in}$  port. The net current can be adjusted to zero by trimming the circular neutral density filter to cause the light reaching the PD2 to be equal to the light reaching PD1. When an analyte binds to a coated sensitizer on the fibre, the sensitizer absorbs some of light travelling through the fibre, which reduces the light reaching the PD1. Therefore, a difference between the amount of light reaching PD1 and PD2 will be observed. The difference between the light received by PD1 and PD2 represents the absorption of light by the sensitizer-analyte complex, and this is displayed as a lock-in voltage output to the user. The above configuration was successfully implemented by Kirwa *et al.* for the low limit of detection ( $LoD$ ), 54 nM of a waterborne analyte (i.e.  $\text{Zn}^{2+}$ ), whereby a 2 cm stripped section of fibre optic coated with PAN 1-(2-pyridylazo)-2-naphthol served as a colorimetric sensitive element, and was exposed to various  $\text{Zn}^{2+}$  concentrations [37]. In addition, it was again implemented by Kirwa *et al* for low  $LoD$  below 1  $\mu\text{M}$  of waterborne amines when zinc 5-(4-carboxyphenyl),10,15,20-triphenyl porphyrin (ZnTPP) was used as a colorimetric sensitive element rather than PAN [38].

Since the present study focuses on fluorimetry, the fibre optic EW sensor was modified in several respects. Specifically, the beam splitter shown in Figure 3.1 and the reference signal path were omitted, as these are not necessary for fluorescence measurements. The reference signal was not required because the reference is zero or nearly zero for the off  $\rightarrow$  on sensitizer. In contrast, for the on  $\rightarrow$  off sensitizer, the reference is the fluorescence intensity measured in the absence of the analyte during the same time intervals of the actual sensing experiment. However, in this present work, the LED, rather than being placed on the circuit board, was focused on the stripped fibre optic coated by a sensitizer (under  $90^\circ$  excitation). In addition, a

rocker switch was connected to the LED to control the excitation time. A Fibre optic (FT800UMT, Thorlabs) of 800  $\mu\text{m}$  silica core diameter (rather than 400  $\mu\text{m}$  that was used in the colorimetric EW fibre optic transducer) was used to provide sufficient surface area to be sensitised within a particular distance  $\sim 1$  cm. In the original colorimetric EW fibre optic sensor there were issues with inconsistent light scattering between the fibre end and the PD. Therefore, in this work, to reduce the gap and minimise the scattering, the PD, optical filter and fibre optic end face were placed into a holder constructed at the University of Sheffield. The holder has a compartment that is designated for the PD and the optical filter. The compartment has a lid that can push the optical filter until being in contact with the active area of the PD. The lid has a hole with a size matching the diameter of the used optical fibre therefore the fibre can be pushed until being in contact with the optical filter. Finally, to enhance the fluorescent emission from the sensitised fibre, a new excitation mode was adopted namely “side illumination”, rather than an evanescent wave, as defined in Section 2.7 and shown in Figure 3.2a.

To test the effectiveness of this approach, the detected fluorescence intensities under evanescent wave and side illumination were compared. For this purpose, two identical sensitised optical fibres were stripped (as described in Section 4.2) and sprayed with the same sensitiser poly(phenylene-vinylene) derivative MDMO-PPV (as described in Section 4.3.1) under the same conditions. They were then left in the dark to dry for an hour. A 450 nm LED (LED450 L, Thorlabs) modulated at the lock-in amplifier reference frequency (5.641 kHz) served as the excitation source for the sensitiser, as described in Section 3.4. In order to compare the outputs produced, evanescent wave and side illumination mode were respectively applied to the sensitised fibres. For side illumination, the sensitised section of the fibre was excited by LED light (450 nm) from  $\sim 5$  mm distance under  $\sim 90^\circ$  angle. The resulting fluorescence partly coupled into the fibre and was detected at the end face. For evanescent wave excitation, the LED light (450 nm) was coupled into the fibre from one end face and propagated within the fibre. In the sensitised section of the fibre, the propagating 450 nm evanescent wave light excited fluorescence in the sensitiser that partly coupled back into the fibre. One face of the fibre projected fluorescence onto a Centronic OSD5-5T photodiode (PD) via a high-pass optical wavelength filter (LP02-488RU-25, Semrock) with a cut-on wavelength of 488 nm that blocks exciting light from the 450 nm LED but allows light from the MDMO-PPV fluorescence band (with an onset around 500 nm in the solid state) to reach the PD [126].

The findings indicate that the detected fluorescent intensity under side illumination substantially exceeds that obtained in the evanescent wave mode, as shown in Figure 3.2b. This was expected, because in order to generate fluorescence, the exciting light must first be absorbed, and this process is weaker for evanescent excitation when compared to absorption under side illumination [77][126]. Consequently, for the sensing experiments described in Chapters 5, 6, and 7, side illumination was utilised to enhance the fluorescence signal. The coupling of fluorescence from side illumination into optic fibres is strong, whereas coupling of the exciting light from the side illumination into the stripped but non-sensitised optical fibre is three orders of magnitude weaker than the fluorescence intensity, as shown in the Figure 3.3. Side excitation under  $90^\circ$  is far outside the  $18^\circ$  ‘acceptance angle’ given by the fibre’s numerical aperture ( $NA$ ) [126] (described previously in Section 2.5.1). Moreover, when using evanescent wave excitation, a high-pass optical filter is required to block the exciting light reaching the photodiode (as discussed in Section 3.5). Good optical filters are usually very expensive; therefore, by using the side illumination we eliminated the additional cost of an optical filter.

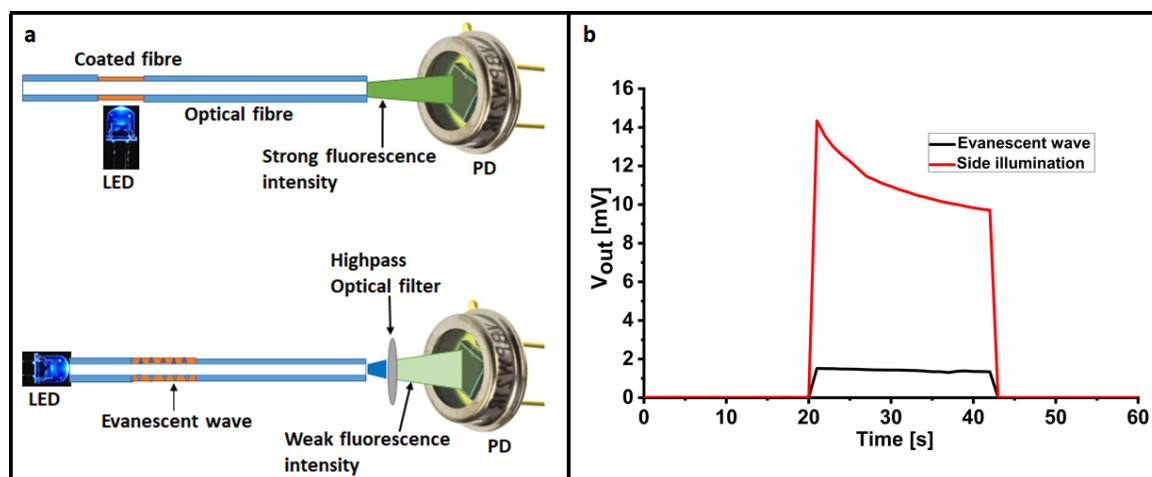


**Figure 3. 2.** (a) A schematic diagram of the side illumination (upper) and evanescent wave excitation (lower); (b) Comparison of the fluorescence emitted from MDMO-PPV film (excitation of 450 nm) under side illumination excitation (red) with evanescent wave (black).

Excitation was switched on at  $t_1 = 20$  s and was switched off at  $t_2 = 45$  s.

Figure 3.2b illustrates that MDMO-PPV fluorescence intensity rapidly degrades under side illumination far more than under EW excitation. The fluorescence intensity degradation is attributed to the ether moieties in each repeat unit of the MDMO-PPV, which are known to become degraded under excitation [127]. However, for the sensing experiment, the excitation

duration was short to allow for a brief ‘interrogation’, with extended dark periods between interrogations or read-out to minimise fluorescence degradation unrelated to the analyte [126]. The photophysical degradation was accounted for using a control experiment, as described in Chapter 5.

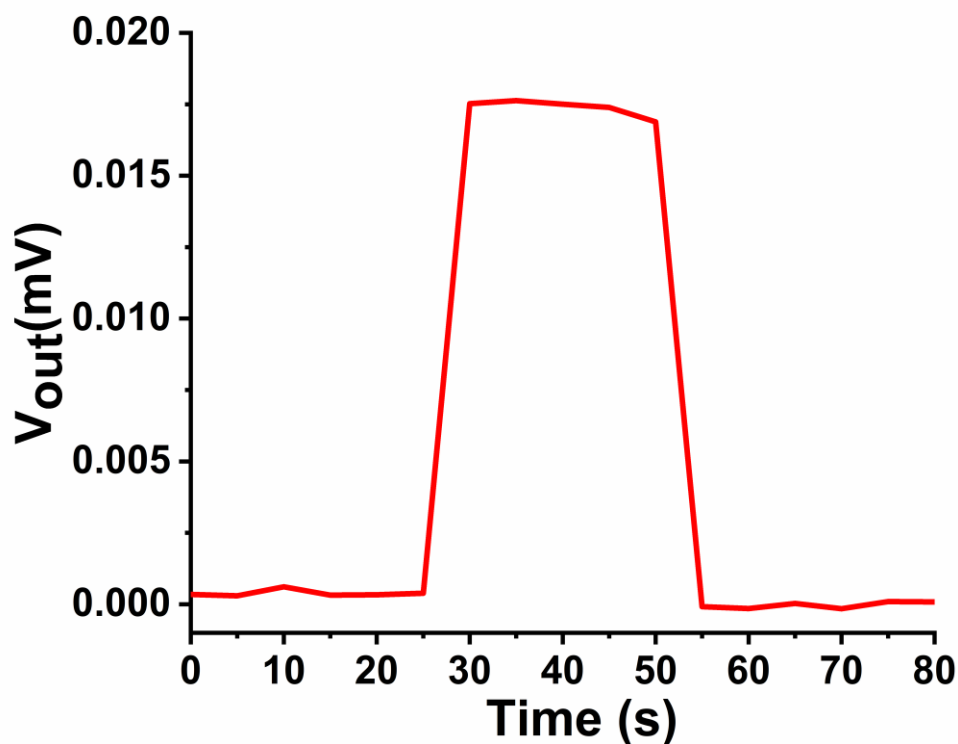


*Figure 3. 3. The MDMO-PPV fluorescence intensity recorded from a stripped and non-sensitised optical fibre under side illumination mode, that was switched on at  $t_1 = 25$  s and was switched off at  $t_2 = 55$  s without using a high pass optical filter.*

In the present study, the modified sensor shown in Figure 3.4 was successfully utilised for airborne 2,4 dinitrotoluene (DNT) sensing. A temperature-controlled water bath was used to control the temperature, and therefore vapour pressure of the DNT to be tested. The DNT vapour was carried on a stream of dry air into the gas testing chamber, as described in Section 5.2. The gas chamber also had a reflective mirror added to the configuration to mirror back the LED light from the opposite side for improved excitation. To test the effectiveness of the mirror, the detected fluorescence intensities with and without a mirror were compared. The detected

fluorescence intensity when using a mirror exceeds that obtained without using a mirror by 24% as shown in Figure 3.5. Consequently, the mirror was implemented in the gas chamber.

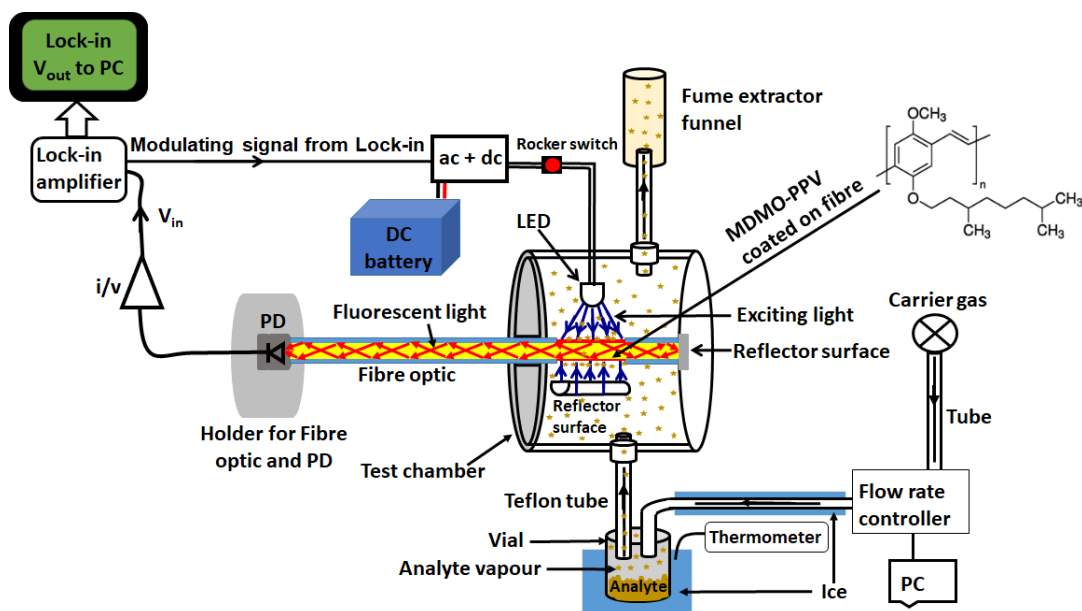


**Figure 3. 4.** Schematic diagram of the sensor setup and test vapour generator used in the present study.

The modified fibre optic sensor is versatile and can easily be adapted for waterborne DNT sensing by replacing the gas chamber shown in Figure 3.4. with a water vessel while using the same sensitiser (MDMO-PPV) and analyte, as explained in Chapter 5 and shown in Figure 5.1. For the sensing of both airborne and waterborne DNT, the sensitiser film was coated onto the stripped optical fibre as describe in Section 4.3.1. The same fibre optic transducer used to detect fluorescence quenching of MDMO-PPV, due to the presence of the waterborne DNT, was used to detect fluorescence quenching of probe 1 due to the presence of waterborne  $\text{Cu}^{2+}$ . The Probe 1 was immobilised in a plasticised PVC membrane and coated on the stripped fibre optic as described in Section 4.3.2.1. The results of waterborne  $\text{Cu}^{2+}$  sensing are described in Chapter 6. Moreover, the fibre optic transducer was also adapted for waterborne analyte sensing with additional modifications (as described in Chapter 7 and shown in Figure 7.2) whereby both sensitiser (NaMSA) and analytes ( $\text{Al}^{3+}$  and  $\text{F}^-$ ) were in solution form.

The fibre optic sensor developed as a part of this study includes a digital lock-in amplifier (USBLockIn250, Anfatec Instruments AG), which was used to extract the low-level AC voltage signal from the noise, in order to improve the signal-to-noise ratio (SNR) of the transducer. This resulted in low *LoD*-the most challenging aspect of sensor technologies. As signal or electrical noise is unavoidable, it is discussed in the following section.

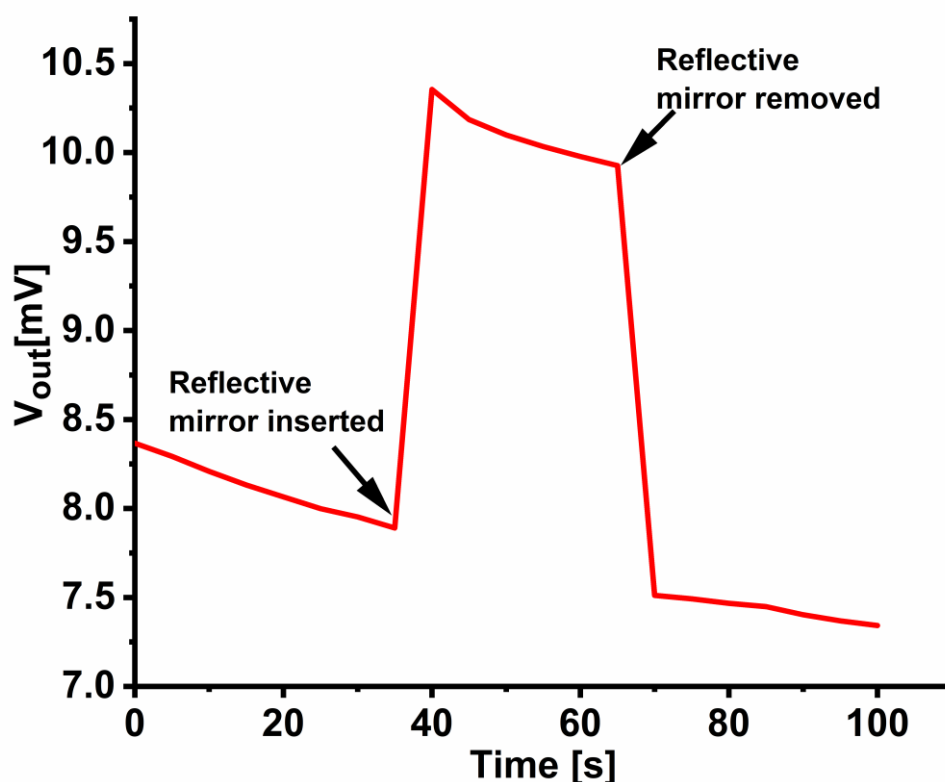


*Figure 3. 5. The fluorescence intensity obtained from MDMO-PPV (450 nm excitation) when using the reflector mirror at 35-68 s exceeds that obtained without using the reflector mirror at 0-35s and 68-100s.*

### 3.2 Electronic Noise

Some components of the electrical circuits introduce noise into the measured signal and thus increase the transducer *LoD* level. This is highly undesirable particularly when detecting toxic or explosive analyte, where a very low *LoD* is necessary. Therefore, two example of a most common electrical noise are discussed next-Johnson noise, and flicker noise-along with the strategies that can be adopted to suppress this issue in the measured signal.

“**Johnson noise**” arises as voltage noise or voltage fluctuations across the resistor terminals due to the thermal agitation. It arises from random motions of electrons across the resistor terminals [128], which generate output voltage fluctuations. Johnson voltage noise is described by the expression below:

$$V_{jn} = \sqrt{(4k_B TR\Delta f)} \quad (3.1)$$

where  $V_{jn}$  is the root mean square of the Johnson voltage noise,  $k_B$  is the Boltzmann constant ( $k_B = 1.38 \times 10^{-23}$  J/K),  $T$  and  $R$  are the resistor temperature (K) and resistance ( $\Omega$ ), respectively, and  $\Delta f$  is the noise bandwidth (Hz).

“**Flicker noise or 1/f noise**” is also known as pink noise and is not well understood. It refers to the noise signal whose frequency spectrum component is inversely proportional to the frequency of the measured signal [129]. Consequently, measurements at low frequencies are more affected by flicker noise. Therefore, by operating the instrument at higher frequencies (kHz), the flicker noise can be minimised. Since toxic and explosive analyte detection requires very low *LoD*, minimising signal noise from the measured signal is necessary. Therefore, in this work, the sensor was equipped with a lock-in amplifier, as described in the following sections.

### 3.3 Digital Lock-in Amplifier as a Signal Processor

A lock-in amplifier is an instrument designed to minimise the noise in the measured voltage. The noise minimisation is achieved by blocking all signals whose frequencies deviate from the reference voltage frequency. Electronic noise, such as flicker noise can be avoided when modulating a signal at 5 kHz frequency and blocking all other frequencies. In older models of lock-in amplifiers, the reference voltage signal ( $V_{ref}$ ) is generated with a fixed frequency by an external oscillator to modulate the instrument, whereby its response or voltage signal ( $V_{sig}$ ) is detected at that frequency by the lock-in amplifier. However, more recent versions of the lock-in amplifier, such as USBLockIn250 (Anfatec Instruments AG) used in this work, generate the internal reference signal directly by relying on the internal digital oscillator [130]. Thus, the reference signal is obtained from the lock-in Ref-out terminal.

The lock-in amplifier processes the voltage signals ( $V_{sig}$ ) in several steps. The input signal can be described by Eq. 3.2 below, where  $f_{sig}$  is the modulation frequency applied to the signal amplitude  $V_{AC}$ ,  $DC$  is a DC voltage component and  $\varphi$  is the phase angle describing the phase lag between the reference frequency and the modulated signal, and the unwanted noise are fed into its input terminal as follows:

$$V_{sig} = V_{DC} + V_{AC} \sin((2\pi f_{sig})t + \varphi) + Noise \quad (3.2)$$

Once the input voltage signal is amplified [131], it is digitised and split into two separate channels. One of the digitised signal components is multiplied by the Ref-out voltage signal using a digital signal processing (DSP) chip [131], whereby the Ref-out voltage signal is characterised by a frequency ( $f_L$ ) and amplitude ( $V_L$ ) as described below:

$$V = V_L \sin((2\pi f_L)t) \quad (3.3)$$

As  $\omega = 2\pi f$ , henceforth,  $2\pi f$  will be replaced by  $\omega$ .

$V_L$  and  $\omega_L$  are usually selected by the user when the USBLockIn250 digital lock-in amplifier is initially set up [130], as described in Section 3.3.1. For the noise to be removed,  $\omega_L$  should be equal to  $\omega_{sig}$ . The DSP chip performs the multiplication followed by filtration mathematically, based on the expression below:

$$V_{sig} \times V = [V_{DC} + V_{AC} \sin(\omega_{sig}t + \varphi) + Noise] \times [V_L \sin(\omega_L t)] \quad (3.4)$$

Using the known trigonometrical identities shown in Appendix III, Eq. (3.4) can be reduced to:

$$V_{sig} \times V = \frac{1}{2} V_{AC} V_L \cos(\varphi) \{ [\cos(\omega_{sig} - \omega_L) t] - [\cos(\omega_{sig} + \omega_L) t] \} + [Noise(V_L \sin \omega_L t)] + [V_{DC}(V_L \sin \omega_L t)] \quad (3.5)$$

As shown in the brackets in Eq. (3.5), the output of the processed signal comprises four AC voltage signals, all of which depend upon the reference frequency  $\omega_L$ . However, the first has a frequency difference ( $\omega_{sig} - \omega_L$ ), the second has a sum frequency ( $\omega_{sig} + \omega_L$ ), and the remaining two pertain to noise and DC voltage, respectively. All AC voltage signals are removed by the lock-in amplifier's lowpass filter. However, if  $\omega_{sig} = \omega_L$ ,  $\cos(\omega_{sig} - \omega_L) = 1$ , it results in a voltage without the frequency component that is proportional to the measured signal  $V_{out}$  [130][131], as shown below:

$$V_1 \propto \frac{1}{2} V_{AC} V_L \cos(\varphi) \quad (3.6)$$

It is evident from the discussion above that, for the noise to be filtered from the measured signal via a lock-in amplifier, the  $\omega_{sig}$  must be equal to  $\omega_L$ . The  $\varphi$  term is a phase or signal delay arising from a particular electrical component of the measuring instrument, in this case the LED that serves as the light source (described in Section 3.4). It can also be due to the photocurrent conversion to a voltage by an unbiased photodiode (as discussed in Section 3.5).

On other hand, the digital chip in the lock-in amplifier multiplies the second component with the reference voltage shifted by  $90^\circ$  phase (for more information see appendix IV). In this case, the reference voltage is expressed as  $V = V_L \sin \omega_L t + 90^\circ$ ; hence, the output voltage of the lowpass filter is given by:

$$V_2 \propto \frac{1}{2} V_{AC} V_L \sin(\varphi) \quad (3.7)$$

In summary, the lock-in amplifier produces two output voltage signals, proportional to  $\cos(\varphi)$  and  $\sin(\varphi)$ , respectively. Assuming  $V = \frac{1}{2} V_{AC} V_L$ , and labelling the first output signal  $Y$  and the second output signal  $X$ , these signals can be expressed as  $Y = V \sin(\varphi)$  and  $X = V \cos(\varphi)$ . The lock-in amplifier output voltage has a real and an imaginary part (complex number) given by  $V_{out} = X + iY$ . Thus, the magnitude of its output ( $R$ ) is independent on the phase between the voltage signal and reference frequency [131], as shown below:

$$|V_{out}| = (x^2 + y^2)^{\frac{1}{2}} \quad (3.8)$$

The lock-in amplifier is also able to measure the phase ( $\varphi$ ) between the signal frequency and the lock-in reference frequency, which is given by  $\theta = \tan^{-1} (Y/X)$ . It has several parameters affecting its noise filtration capacity, as described in the next section.

### 3.3.1 Lock-in Amplifier Parameters

The manufacturer of the USBLockIn250 digital lock-in amplifier (Anfatec Instruments AG) adopted in this work supplies a LabVIEW-based graphical user interface (GUI) that allows all pertinent parameters to be set by the user. These parameters can be classified according to their functions into the following: (1) those that enhance the filtering quality of the internal lowpass filter within the lock-in amplifier (such as time constant, roll-off, dynamic mode, etc.); and (2) those that affect the modulating signal of the LED acting as the light source, such as its frequency (Hz) and amplitude ( $V_{rms}$ ) [130]. The function of each parameter is briefly described in the sections that follow.

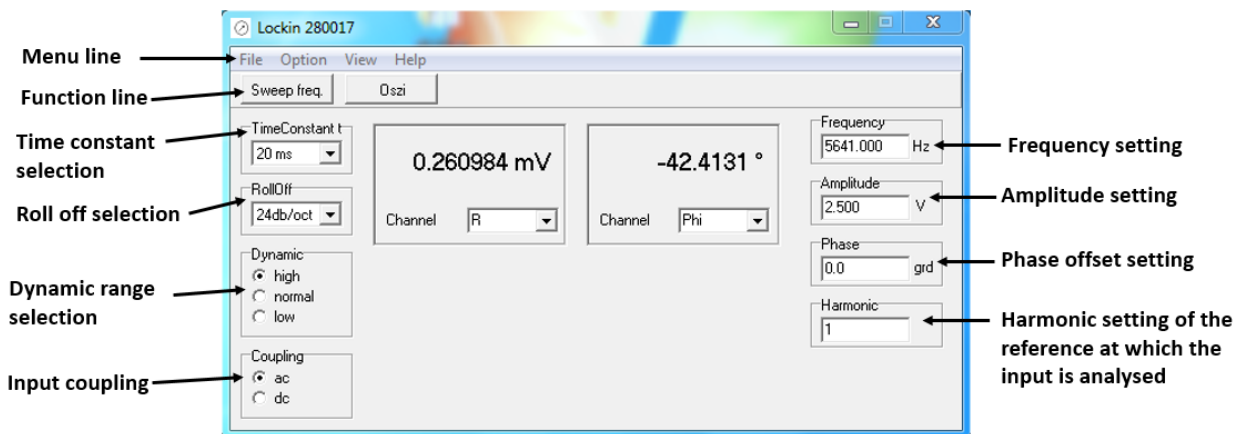


**Figure 3. 6.** The main window of the digital lock-in amplifier’s GUI, including a very brief description of the parameters that can be set by the user [130].

#### Time Constant

The time constant is the time taken by the lock-in amplifier to average the data prior to displaying it to the user. It can be set directly in the GUI. Electronically, it is the RC time of

the lock-in amplifier's internal filter, which has an inverse relationship with its bandwidth, as shown below:

$$f = \frac{1}{RC} \quad (3.9)$$

where  $f$  and  $RC$  are bandwidth and the time constant respectively. For the lock-in amplifier (USBLockIn250, Anfattec Instruments AG) used in this work, the time constant is within the [0.2 ms, 5 s] range [130]. Therefore, selecting the highest time constant value (5 s) results in the lowest noise bandwidth of 0.2 Hz, while the lowest time constant (0.2 ms) corresponds to the highest noise bandwidth of 5 kHz. In the present study, the time constant used in Chapter 5 was 1 s. On the other hand, for the work reported in Chapter 6 and 7, a time constant of 5 s was chosen due to its low filter noise bandwidth. Figure 3.7 shows the influence of different time constants on the bandwidth of the internal filter of the lock-in amplifier while keeping the frequency and the reference signal amplitude constant (at 100 kHz and 20 mV<sub>rms</sub> respectively).

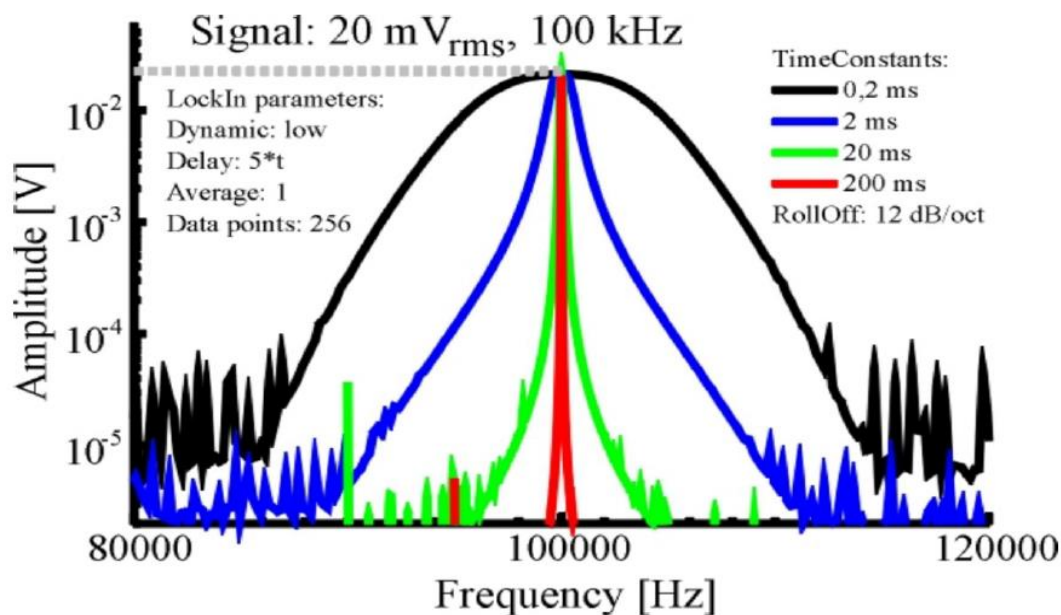


**Figure 3. 7.** Taken from digital lock-in manufacturer's datasheet [130] showing the influence of time constant setting on the lock-in amplifier's filter bandwidth.

As can be seen from the graph shown in Figure 3.7, the narrowest noise bandwidth relates to the highest time constant of 200 ms (red line) and the lowest 0.2 ms (black line).

### Roll-Off

This parameter can be set by the user through the GUI to control the noise bandwidth of the lock-in filter. The filter within the USBLockIn250 digital lock-in amplifier has three attenuation characteristics of 6, 12 and 24 dB/oct [130]. Figure 3.8 illustrates the impact of different roll-off attenuation characteristics at 100 kHz and 20 mV<sub>rms</sub> on the noise bandwidth of the lock-in filter. It is evident that 24 dB/oct roll-off produces the narrowest noise bandwidth (red line), and was thus chosen in all fibre optic sensor applications discussed in this work.

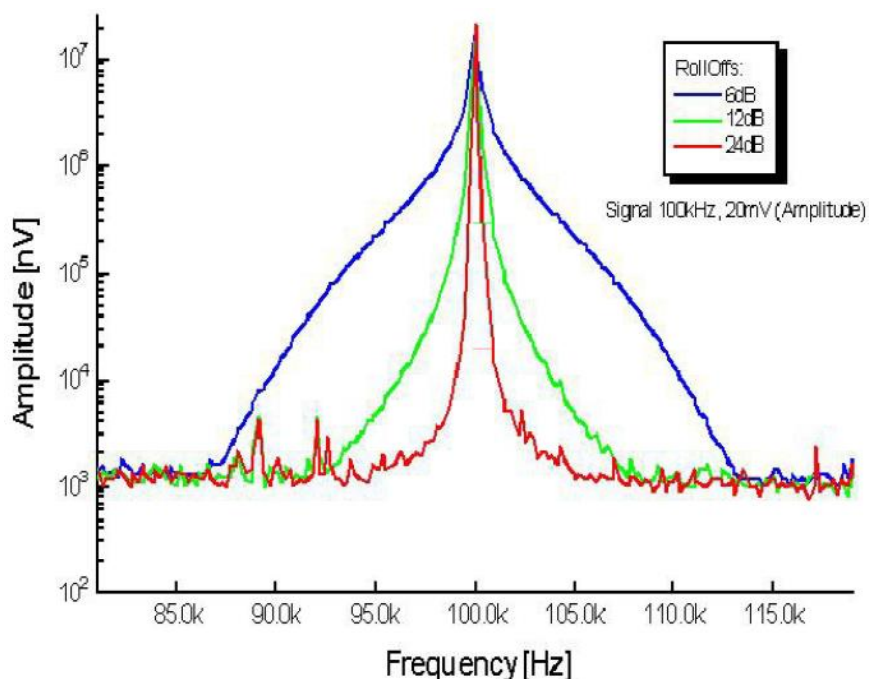


**Figure 3. 8.** Taken from digital lock-in manufacturer’s datasheet [130] showing the impact of the roll-off (6,12, and 24 dB/oct) setting on the lock-in filter bandwidth.

### Dynamic Mode

The lock-in amplifier utilised in the present study has three dynamic modes (i.e. high, normal and low) [130]. These dynamic parameters are used to amplify the analogue input voltage

signal of the lock-in amplifier (by a factor of 1, 10, or 100 respectively) prior to digitising it. As the low dynamic mode yields the highest resolution, the lock-in amplifier should be set to this mode when the amplitude of the input voltage is  $\leq 100$  mV to achieve a high-resolution output voltage. This is because amplifying the input voltage by a factor of 100 (low dynamic) does not exceed the sensitivity range which, is limited to 10 V [130]. However, if the input signal amplitude is in the 100 mV–1 V range, the “normal” dynamic setting is suitable because, after the amplification, the output voltage amplitude cannot exceed the sensitivity limit. Finally, if the amplitude of the input voltage is greater than 1 V, the lock-in amplifier should be set to the “high” dynamic mode, to prevent amplification from being within the sensitivity range. The output voltage amplitude of the fibre optic sensor utilised in the present study does not typically exceed 100 mV. Therefore, the lock-in amplifier was set to the low dynamic setting during measurements to achieve the highest resolution.

### **Other Parameters**

The user of the digital lock-in amplifier employed in the present study (USBLockIn250, Anfatec Instruments AG) is able to set the frequency and the amplitude ( $V_{rms}$ ) of the reference signal to modulate the LED, as described in Section 3.4. Input coupling is a coupling parameter that enables switching from the AC to the DC -coupled mode or vice versa. Prior to digitisation, the lock-in amplifier was set to the AC-coupled mode to discard all DC components obtained from the AC+DC circuit, as described in Section 3.4. On the other hand, the phase setting was ignored, as it is less than  $5^\circ$  at 5.641 kHz, which is within the limits beyond which errors would be introduced in output voltage data  $V_{out}$  (measurements). In the sections that follow, methods adopted for accessing, retrieving, and saving the data into an electronic file are described.

### **3.3.2 Lock-in Amplifier in Conjunction with the LabVIEW Routine for data Collection**

In the present study, the input signal was completely processed by the digital lock-in amplifier (USBLockIn250, Anfatec Instruments AG) and I/V converter (discussed in Section 3.6). The user can access the processed (filtered) signal from the digital lock-in amplifier using the LabVIEW code. The USBLockIn250 manufacturer granted the permission for the use of proprietary LabVIEW code for the present investigation, allowing seamless communication with the hardware. In addition, permission was obtained for writing additional LabVIEW code (to meet the user requirements) to interact with the proprietary code. Consequently, additional

LabVIEW software code was written by Abraham Kirwa to continuously record the lock-in amplifier's output voltage ( $V_{out}$ ) and phase data into a dedicated data file stored in the memory of a desktop PC. Figure 3.9a depicts the GUI of the newly developed LabVIEW routine. Communication between the lock-in amplifier's software and the new LabVIEW software requires that all parameters shown in Figure 3.9a match those set previously by the user (Figure 3.6). When performing measurements, the original code should be run first to start the communication between the lock-in amplifier's LabVIEW code and the hardware. This should be followed by executing the newer code to communicate with the proprietary code in order to extract the data from the lock-in amplifier, this communication is through the USB port and the data is saved as a data file on the desktop PC. The blue square button at the top of the panel is an error indicator that changes to red in case of any problems with the data.

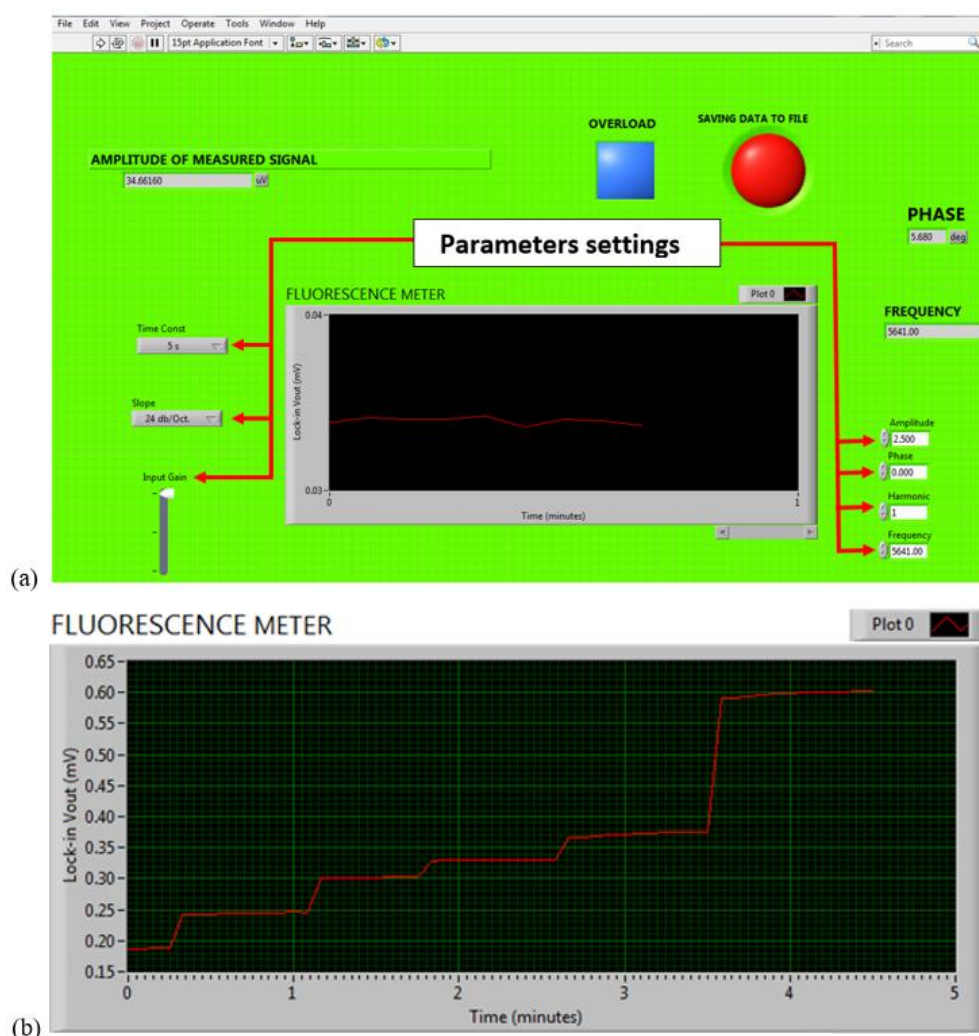


**Figure 3. 9.** (a) GUI of the LabVIEW code used when recording data from the lock-in amplifier continuously into a data file; (b) An example of real-time measurements of the interaction between a sensitizer and an analyte.

An example of real-time analyte sensing measurements is shown in Figure 3.9b (taken from Chapter 7), where the lock-in  $V_{out}$  is a measure of the fluorescence intensity. This example was obtained from a sensor (shown in Figure 7.2) that is similar to the sensor shown in Figure 5.1, but in this instance the sensitiser was in solution rather than having been coated on a stripped fibre. The step-wise increments in  $V_{out}$  (the red curve) represent interactions between the sensitiser (NaMSA) and the analyte ( $Al^{3+}$ ). For the off  $\rightarrow$  on sensor, as addition of analyte to the sensitiser increases, the fluorescence intensity increases; thus, step-wise increments can be observed in Figure 3.9b. The measurement data was saved immediately as decimal numbers in an excel file format with three data columns (i.e. time,  $V_{out}$ , and phase data) when the red button shown in Figure 3.9a was pressed. This could then be used for further analysis. As can be seen from Figure 3.9b, as no analyte was introduced for the first 20 s, the lock-in  $V_{out} \sim 0.18$  mV was a result of the exciting light still passing through the highpass optical filter and the weak fluorescence from the sensitiser in the absence of analyte. After 20 s, the analyte was added to interact with the sensitiser and it took approximately 40 s to reach the equilibrium. As the first four analyte additions were equal in concentration, the increments in the  $V_{out}$  were similar. The last addition was higher in concentration, and the  $V_{out}$  increment was correspondingly higher. It is evident from the graph that the  $V_{out}$  increment is proportional to the analyte concentration; a finding that will be further discussed in Chapter 7. It should be noted that the graph shown above represents the off  $\rightarrow$  on fluorescence. For the on  $\rightarrow$  off fluorescence, the  $V_{out}$  as a measure of fluorescence intensity, it is expected to be high and should decline when the sensitiser interacts with the analyte. In this case, a downward rather than upward trend is expected. In the sections that follow, the remaining components adopted in this work are described.

### 3.4 Adder Circuit (AC+DC)

The adder circuit employed in this study was designed and built by Dr Abraham Kirwa. The adder circuit can be used in conjunction with the lock-in amplifier to modulate the excitation LED. It adds a DC voltage to the AC reference voltage from the lock-in and subsequently used to drive the LED. Adding an appropriate level of DC voltage to the AC modulating signal guarantees that the LED never switches off completely, but rather its brightness varies with the

modulating signal cycles. The DC voltage is supplied by 9 V batteries and the AC voltage (a sinusoidal signal) is obtained from the lock-in amplifier's Ref-out terminal. As noted previously, the lock-in's modulation frequency and amplitude can be set using a LabVIEW routine. The AC+DC voltage is applied to the LED that is protected by a resistor, R3, connected in series, as shown in Figure 3.10. This allows the LED output to be modulated in order to improve the signal-to-noise ratio of the lock-in detection, thus reducing the  $LoD$  (discussed in Section 2.2.1). As R3 is removable, a protective resistor appropriate for each LED can be incorporated into the circuit, because different sensitiser require different LEDs.

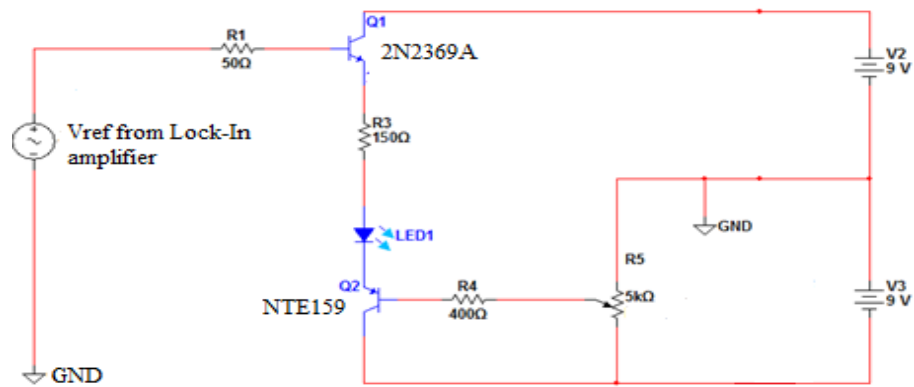


**Figure 3. 10.** The schematic diagram of the designed AC+DC circuit is taken from [36], where V2 and V3 are the DC voltage sources' biasing transistors Q1 and Q2 respectively.

Choosing an appropriate value of the LED protective resistor is necessary. Fortunately, this value can be accurately calculated. All parameters for the calculation are usually given in the LED and transistor manufacturers' datasheets such as maximum forward voltage for the LED ( $V_{bias}$ ) and steady current ( $I_{DC}$ ). The following calculation is required for each different LED used as a light source:

$$V_{DC} = V_{bias} + V_{RLED} \tag{3.10}$$

where  $V_{DC}$  denotes the DC voltage from the adder circuit (AC+DC) applied to the R3–LED serial combination, and  $V_{bias}$  and  $V_{RLED}$  represent voltage decline across the LED and its protective resistor respectively.

As previously noted, a 450 nm LED (LED450 L, Thorlabs) was used in the present study, and was thus used in the calculation below, this is required to protect the LED from the overload current. According to the manufacturer's datasheet, the maximum LED forward voltage ( $V_{bias}$ ) is 4 V and the maximum DC forward current is 30 mA. Similarly, the datasheet of the used transistor (2N2369, Farnell) provides a base-emitter voltage ( $V_{BE}$ ) of 0.85 V and, as it is biased by a 9 V battery (Eveready Zinc Carbon 9V battery, RS Components), the following applies:

$$V_{DC} = 9 V - 0.85 V = 8.15 V$$

The resistance needed to protect the LED from the high current is given by the Ohm's law:

$$R = \frac{V_{DC}}{I_{DC}} = \frac{(8.15 - 4)}{0.03} = 138\Omega$$

This value was rounded to 150  $\Omega$  due to the availability of such a resistor in our lab.

The choice of LED used as the excitation source for the sensor depends on the wavelength of the absorption peak of the sensitiser, as described in Section 2.3.1. The LED peak emission wavelength should thus be chosen to overlap with the absorption peak of the sensitiser, at least within the LED emission band's full width at half maximum (FWHM). For example, LED450 L (Thorlabs) has a maximum emission at 450 nm and an FWHM of 20 nm, which aligns well with the absorption band of used sensitiser in this work (discussed in Chapter 5). The emission spectrum of this particular LED is shown in Figure 3.11.

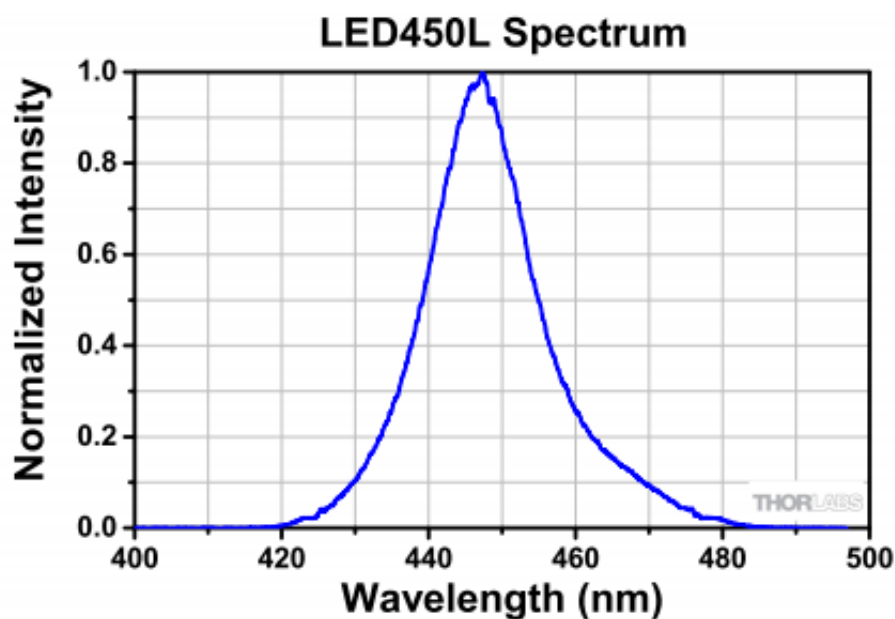


*Figure 3. 11. The emission spectrum of LED450 L (Thorlabs).*

In the sensor examined in the present study, the LED light excites the sensitiser coated on the fibre optic (as described in Section 4.3). This produces fluorescence in the absence of the analyte for on  $\rightarrow$  off sensitiser or in the presence of analyte for off  $\rightarrow$  on sensitiser. The fluorescence is guided via the optical fibres to strike the active area of the photodiode (PD), as shown in Figure 3.4 and described in the next section. Consequently, the light detected by the PD is converted to an oscillating current (as described in Section 3.5). Finally, the oscillating current is converted to a voltage via an I/V converter (Section 3.5), which is described quantitatively by Eq. (3.2).

### **3.5 The Choice of the Optical Filter and PD**

In Chapters 5 and 6, no filter was used because the amount of light at the excitation wavelength coupled into the fibre was minimal. However, when the fibre was roughened, as in Chapter 7, some of the excitation wavelength could couple into the fibre. In this case, a filter was used. In this section, important factors that should be considered when choosing the optical filter and the PD are introduced. Optical filters are used to pass preferential wavelengths and reject others. There are many types of optical filters, such as low-pass, high-pass, and bandpass, amongst others. A low-pass optical filter passes the short wavelengths and blocks the high wavelengths,

while a high-pass optical filter does the opposite. A bandpass optical filter as opposed to the other two passes only the wavelengths in a particular range. If the required cut-off wavelength is in close proximity to the desired wavelength, a sharp cut-off optical filter is required. For the experimental set up used in Chapter 7, some of the exciting light was coupled into the roughened fibre. The amount of the exciting light that coupled into the roughened fibre was more than which coupled into the smooth fibre (as used in Chapters 5 and 6). Therefore, a high-pass optical filter (LP02-488RU-25, Semrock) with a 488 nm cut-on wavelength was necessary to block the excitation light and permit the transmission of the fluorescent signal only, as shown in Figure 3.12. In the case considered here, these two signals partly coupled into the fibre optic, but the excitation light was blocked via the optical filter at the end-face of the fibre, allowing only the fluorescence to be detected by the PD.

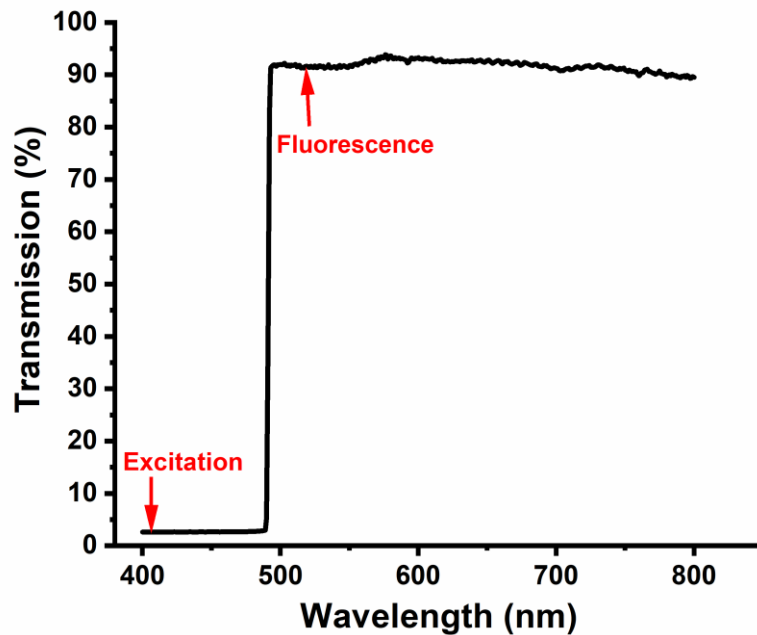


**Figure 3. 12.** The transmission of the optical high-pass filter (LP02-488RU-25, Semrock) measured using a spectrophotometer (UV550 Spectrophotometer, Thermo Scientific).

The photodiode (PD) converts the detected light to a photocurrent. Consequently, PD specifications must meet the user requirements. For example, it is relatively straightforward to focus the light beam on the large active area PD  $\approx 5 \text{ mm}^2$  (OSD5-5T, Farnell) as opposed to a small active area PD  $\approx 0.12 \text{ mm}^2$  (S5973, Hamamatsu). On the other hand, a PD with a larger active area (OSD5-5T) is characterised by a slower response, generating phase delay when the

frequency of the incident light exceeds 50 kHz because it has a much larger junction capacitance (130 pF at 0 V bias) compared to S5973 (1.6 pF). For the present study, we continued using OSD5-5T which was chosen for the original colorimetric EW fibre optic sensor despite its larger capacitance, because the sensor operates at 5.641 kHz (rather than > 50 kHz, as explained in Section 3.6). It is worth noting that the response characteristics to different wavelengths (in the UV to near infrared spectral range) differ for different PDs. Thus, the response characteristic of OSD5-5T (Farnell) is shown in Figure 3.13, where it can be seen that its maximum response is at  $\lambda = 850$  nm, while it still performs well in the visible region.

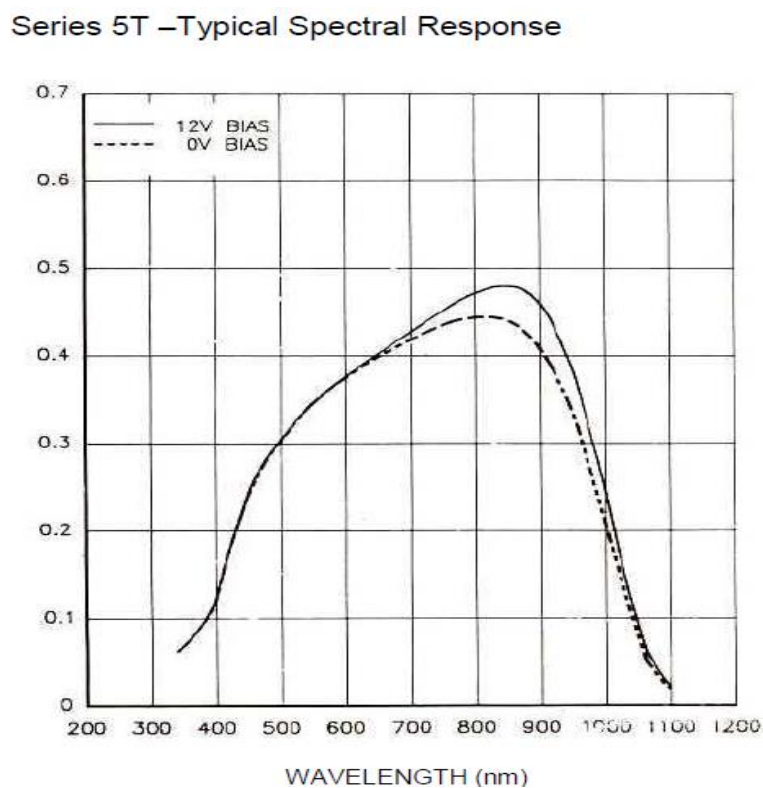


*Figure 3. 13. The spectral response of the PD adopted in this study (OSD5-5T, Farnell).*

### 3.6 The I/V Converter

As discussed in Section 3.3, the lock-in amplifier used in the optical fibre sensor developed in this work requires voltage rather than current as its input. Hence, the I/V converter as described by [36] was used to convert the current from the PD into a voltage ( $V_o$ ). Finally,  $V_o$  is fed into the input of the lock-in amplifier to be processed. Abraham Kirwa has built the I/V circuit by referring to I/V converter manufacturer’s datasheet [132] and he found that, through

experimentation the gain of the I/V converter is stable up to 70 kHz using an 18 pF bypass capacitor and a 100 k $\Omega$  feedback resistor, but becomes unstable for a bypass capacitor in the 1.3-16 pF range [36]. In addition, he proved that an appropriate frequency (5.641 kHz) works well for the sensor with high sensitivity [36][37][38].

### 3.7 Conclusions

In the present work, we have described how the colorimetric EW fibre optic transducer (built by Abraham and shown in Figure 3.1) was modified to be a fluorimetric transducer. We have established 'side illumination' as superior excitation mode compared with evanescent wave excitation of fluorescence. The modified transducer was applied successfully to detect the fluorescence quenching of MDMO-PPV as a sensitiser coated on an optical fibre when exposed to airborne DNT, as shown in Figure 3.4. It was then modified slightly as shown in Figure 5.1 to detect the fluorescence quenching of MDMO-PPV when exposing to waterborne DNT. The results of the airborne and waterborne DNT sensing and the easy adaptation between those media are presented in Chapter 5. The same waterborne transducer was applied to detect the fluorescence quenching of the immobilised probe 1 in a plasticised PVC membrane and coated on an optical fibre when exposed to waterborne Cu<sup>2+</sup>, as presented in Chapter 6. In addition, the fibre optic transducer was again modified to detect the change in the fluorescence of a sensitiser (NaMSA) that was dissolved in water rather than coated on the fibre when exposed to waterborne Al<sup>3+</sup> and F<sup>-</sup>, as shown in Figure 7.2. The electronics of the fluorimetric fibre optic transducer (i.e. voltage adder circuit (AC+DC), photodiode, and I/V converter and the digital lock-in amplifier were briefly described.

## Chapter 4: Preparation of Sensitised Optical Fibres

### 4.1 Introduction

As the optical fibres are an integral part of the fluorimetric sensor developed as a part of the present study (described in Chapter 3), this chapter focuses on their preparation; optical fibres aimed at sensing applications have to be coated with “a fluorimetric sensitiser” as the sensitive element. The preparation starts with stripping a 1 cm segment of the fibre optic cladding that confines the light in the fibre core. Next, the stripped section is coated with a fluorimetric sensitiser, which changes its optical properties whereby exposure to the target analytes results in either a fluorescence on  $\rightarrow$  off or off  $\rightarrow$  on switch (as described in Section 2.3.1.1 and 2.3.1.2). The sensor is capable of quantifying the changes in the fluorescence and its output can be used for further analysis and calibration to determine the analyte concentration in the sample. Thus, this chapter commences with the description of the optical fibre preparation process (comprising of the cutting, stripping, cleaving, polishing, cleaning, and drying steps). This is followed with a brief outline of the coating techniques used to apply the sensitiser adopted in the present work.

### 4.2 Fibre Optic Preparation for Sensing Applications

Two types of multimode optical fibres were used, the first of which (FT800UMT, Thorlabs) was used to guide the fluorescence from the sensitiser film coated on its stripped section to the photodiode, while the second optical fibre (FT1500UMT, Thorlabs) was used to guide the fluorescence from the sensitiser solution surrounding its stripped and roughened section to the photodiode. These fibres have a silica glass core and a transparent polymer cladding with refractive indices of 1.4668 and 1.406 nm at 436 nm, respectively. The cladding has a lower refractive index compared with the core to ensure that the light is confined in the fibre core. FT800UMT has  $800 \pm 10 \mu\text{m}$  core diameter,  $30 \pm 10 \mu\text{m}$  cladding, and a  $210 \pm 30 \mu\text{m}$  thick protective coating of fluoropolymer “Tefzel,” whereas FT1500UMT has a  $1500 \pm 30 \mu\text{m}$  core diameter,  $50 \pm 31 \mu\text{m}$  of cladding, and a  $500 \pm 100 \mu\text{m}$  thick protective coating. These fibres have the same numerical aperture ( $NA = 0.39$ ) [133] (for more information see appendix V) and acceptance angle ( $\theta_a = 18^\circ$  in water and  $24.7^\circ$  in air), as determined by applying Eq. 2.21. The V numbers, as described in Section 2.5.3 and calculated using Eq. 2.24, are 2402 and 4517 for FT800UMT and FT1500UMT, respectively, which corresponds to 2884802 and 10201644.5

supporting modes ( $M = V^2/2$ ). It is worth noting that the light entering the fibre within its  $NA$  and acceptance angle is confined in the fibre as long as the penetration depth (as described in Section 2.6) of the evanescent light wave at the core-cladding interface is shorter than the cladding thickness. The protective coatings of the aforementioned fibres are mechanically strippable and the cladding polymer can be dissolved in acetone [133]. In the present study, the optical fibre with 800  $\mu\text{m}$  core diameter (FT800UMT, Thorlabs) was prepared for sensing application by cutting approximately a 30 cm length of a multimode optic fibre from a fibre reel, shown in Figure 4.1a, using micro cutting pliers (PA-101, Pro'sKit). The 1 cm-long buffer (Tefzel), shown in Figure 4.1b, was stripped off from the section near the fibre end using a scalpel blade (Figure 4.1c) to expose the cladding. Next, the transparent polymer cladding was wiped off by Kimwipes wet with acetone solvent, taking advantage of the core's insolubility in acetone. The remaining end faces ( $\sim 1$  cm in length) of the fibre core were stripped and cleaved at  $90^\circ$  using a Ruby Fibre Scribe (S 90R, Thorlabs) shown in Figure 4.1d.

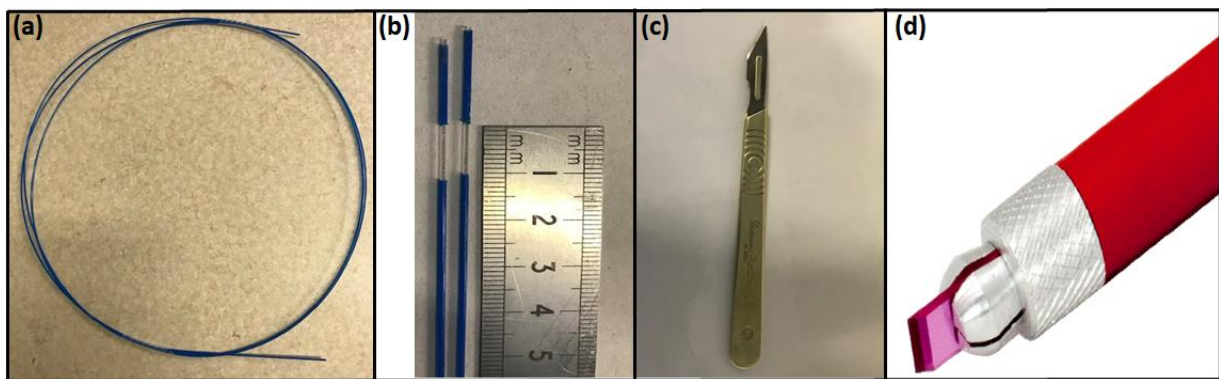


**Figure 4. 1.** (a) Optical fibre reel; (b) Optical fibre after stripping 1 cm-long buffer; (c) Scalpel blade ( Swann –Morton Ltd.) used for stripping; (d) Ruby Fibre Scribe used for cleaving (image taken from the supplier's web page)[134].

To minimise the fluorescence scattering when leaving the fibre end face, the end faces of the fibres were subsequently polished using lapping sheets (Thorlabs) by gently moving the end faces (with the fibre at  $90^\circ$  to the sheet) over LFG5P (5  $\mu\text{m}$  grit size), followed by LFG1P (1  $\mu\text{m}$  grit size), and finally LFG1P (0.3  $\mu\text{m}$  grit size) [135]. In Figure 4, an image of cleaved and polished optical fibre is shown alongside a cleaved and non-polished optical fibre for comparison.

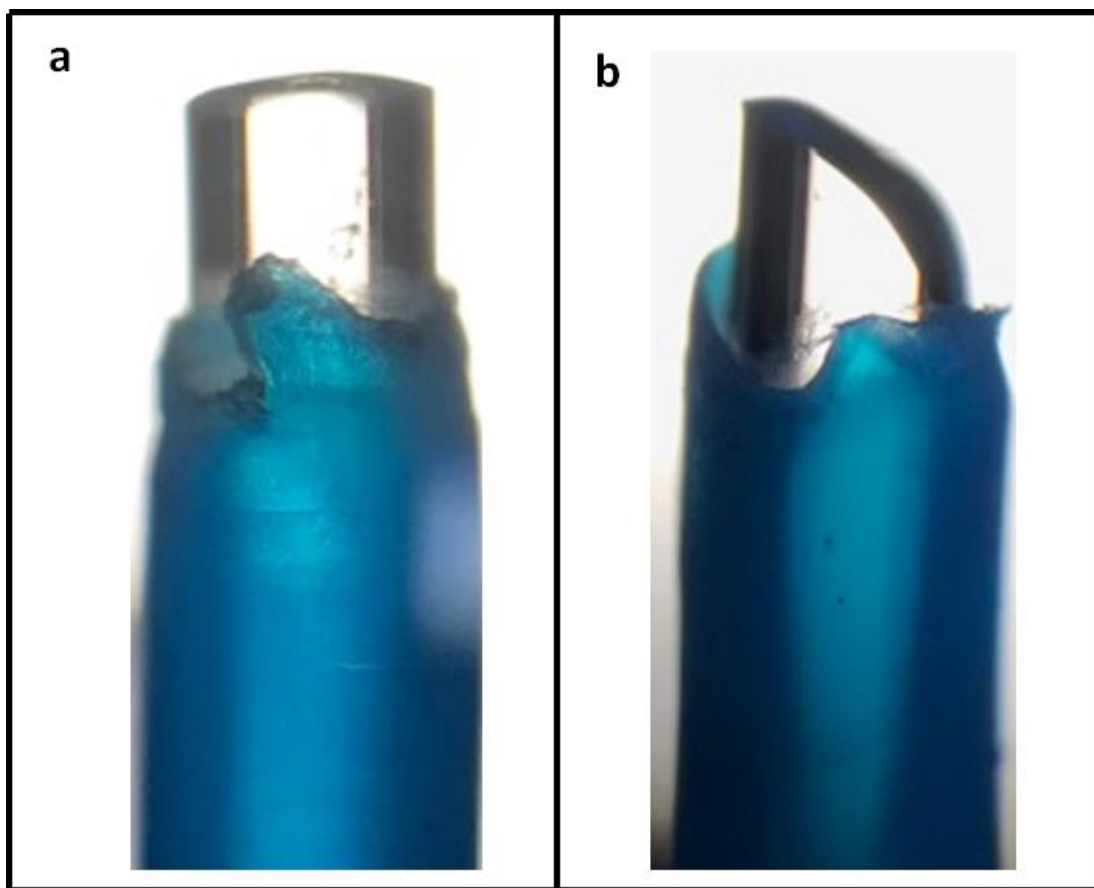


*Figure 4. 2. Microscope images of two cleaved optical fibres (FT800UMT, Thorlabs) captured by iphone-7 camera using a microscopic lens (Zenith ultra-500, UK): (a) polished and (b) non-polished optical fibre.*

Usually, during the stripping process, some impurities will be deposited on the fibre core. Consequently, to remove these impurities, the stripped fibre sections were washed with acetone and then rinsed with DI-water, followed by an isopropanol wash and a further DI-water rinse. To dry the wet sections, they were placed under a nitrogen flow and then held over a hot plate at  $\sim 90$  °C (as shown in Figure 4.3) for an hour, following a previously described procedure [37]. After one hour had elapsed, the hot plate was switched off for 10 min to enable the stripped fibre sections to cool down to room temperature. Once this process had been completed, the stripped sections were ready for coating with a fluorimetric sensitizer, as described in the forthcoming sections.



*Figure 4. 3. Wet stripped optical fibre sections drying near the hot plate surface set to 90 °C.*

The optical fibre with 1500  $\mu\text{m}$  core diameter (FT1500UMT, Thorlabs) preparation process was similar to that outlined above for the FT800UMT. An approximately 10 cm-long segment was cut from a fibre reel and a 1 cm length of the fibre core was exposed at one end by stripping away both the cladding and the buffer. The fibre was cleaned and dried using the same process as described previously for the fibre with an 800  $\mu\text{m}$  core diameter. Since a smooth exposed fibre core picks up only very little fluorescence from the sensitizer solution (as discussed in Chapter 7), the entire surface of the stripped section was roughened using a Dremel ‘Corded Multi-Tool 3000’ rotary tool as described previously [38]. For this purpose, the optical fibre was strapped onto a slide table that was fixed on a telescopic platform moving sideways in directions denoted as A and B in Figure 4.4. The Dremel was clamped into a fixed position and its diamond grinding bit was positioned directly above the stripped section. A telescopic platform was used to adjust the vertical position of the sliding table in order to bring the stripped section of the fibre in contact with the rotating grinding bit. Then, the sliding table was carefully moved back and forth until the side of the stripped section was completely roughened. Next,

the telescopic platform was moved downward, and the fibre was unstrapped and rotated by approximately 90°. The procedures described above were repeated until the entire stripped section was roughened.

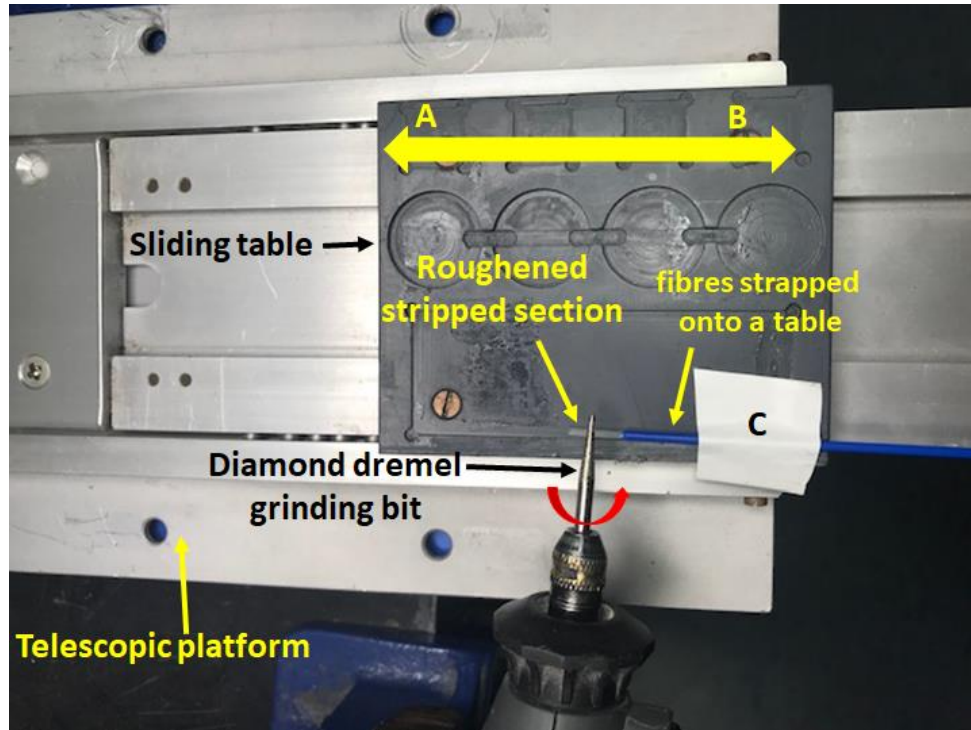


*Figure 4. 4. Optical fibre roughening setup: A and B indicate the direction of the sliding table, C denotes the tape used to ensure that the fibre is affixed onto the sliding table, and the red arrow indicates the rotational direction of the Dremel grinding bit.*

### **4.3 Coating Stripped Section of Optical Fibres with Fluorimetric Sensitisers**

The success of coating the silica fibre core or glass substrate with a thin film of fluorimetric or fluorophore sensitizer (described in Section 2.3) is highly sensitive to environmental conditions, which is why all coating procedures must be carried out under cleanroom conditions. In addition, the glass surfaces (i.e., stripped silica optical fibres, as described in Section 4.2) must be clean. As cylindrical silica glass fibres were adopted in the present study, certain coating techniques (i.e., spin coating) could not be applied, and spray coating and dip coating techniques (described in Section 4.3.1 and 4.4.1) were used as the best alternatives. The properties of the film processed using these techniques depend on several parameters, as described later in this chapter.

### 4.3.1 Spray Coating Technique

Spray coating is a process whereby a fine coating of solution droplets are deposited and coalesce on the surface of the object. This can be achieved either through ultrasonic spray coating or by applying a conventional airbrush technique, both of which have been used as low-cost techniques for coating perovskite solar cells [136], organic thin film transistors [137], and organic light-emitting diodes (OLED) [138]. When the area to be coated is large or cylindrical, spray coating is highly preferable, and also yields superior results when there is a need to deposit multiple layers. For the present study, a hand-held airbrush was chosen rather than the ultrasonic spray coating technique, due to lower cost and fewer equipment requirements (only compressed gas was needed), as well as ease of operation. A schematic diagram of the hand-held airbrush coating technique is depicted in Figure 4.5a and the actual airbrush utilised in this work is shown in Figure 4.5b.

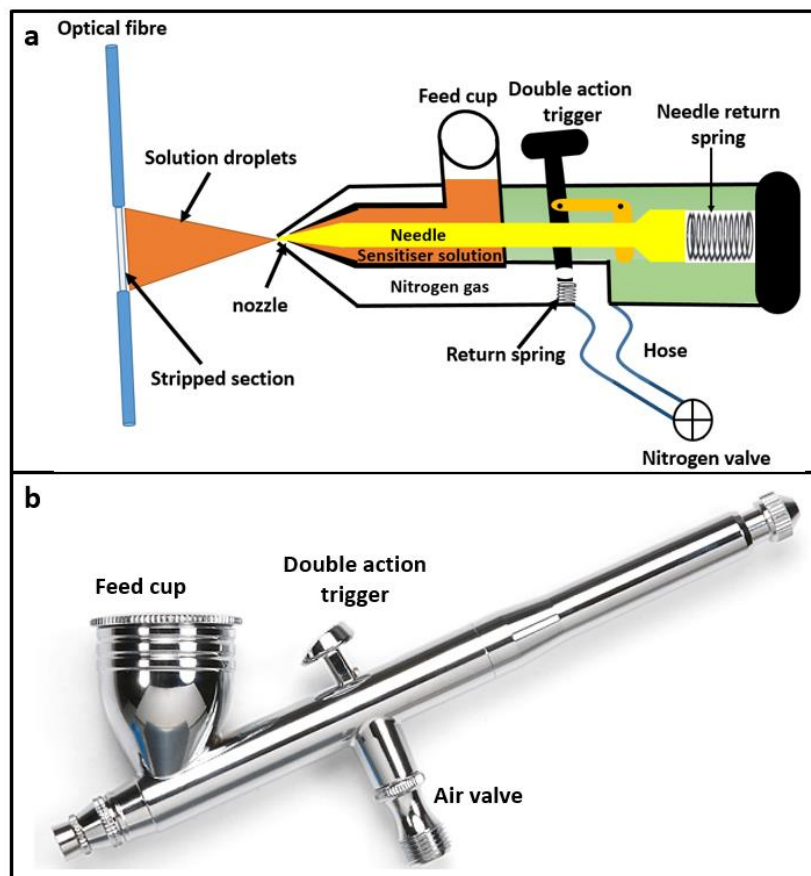


**Figure 4. 5.** (a) Schematic diagram of the hand-held airbrush spraying process, where sensitizer is deposited onto the stripped section of the optical fibre; (b) The airbrush utilised in the present study.

The spray coating procedure started with plugging the compressed nitrogen gas into the airbrush valve, followed by loading the coating solution into the feed cup of the airbrush. The nitrogen gas is used to break down the solution passing through the narrow slot (the nozzle) into tiny droplets. The airbrush utilised in the present study has a needle with a diameter that gradually decreases towards one of its ends that closes the nozzle. In addition, it has a trigger that simultaneously controls the airflow and the amount of the spray solution leaving the nozzle. Pushing the trigger down allows the compressed gas to enter the airbrush and leave through its nozzle, while pulling it back retracts the needle allowing the spray solution to escape through the open slot. Therefore, as soon as the trigger is pushed down and pulled back, the coating solution passes through the nozzle and is exposed to the compressed gas flow, generating tiny droplets. These droplets will be deposited on the substrate and will coalesce as a uniform film if the substrate is held within the optimal distance from the airbrush nozzle. In the present work, a WilTec airbrush (WilTec, Konigsbenden 28, DE-52249 Eschweiler, sourced *via* ManoMano; nozzle diameter 0.3 mm) shown in Figure 4.5b was used to spray the stripped fibre with coating solution, whereby the fibre was held perpendicular to the airbrush nozzle at a distance of 4 cm. The fibre was repeatedly rotated by 90° during the spraying to ensure a uniform film deposition. The spraying cycles were repeated until a film was clearly observed to have been deposited on the stripped section of each fibre. Fibres spray coated with MDMO-PPV are shown alongside non-sprayed fibres in Figure 4.6.

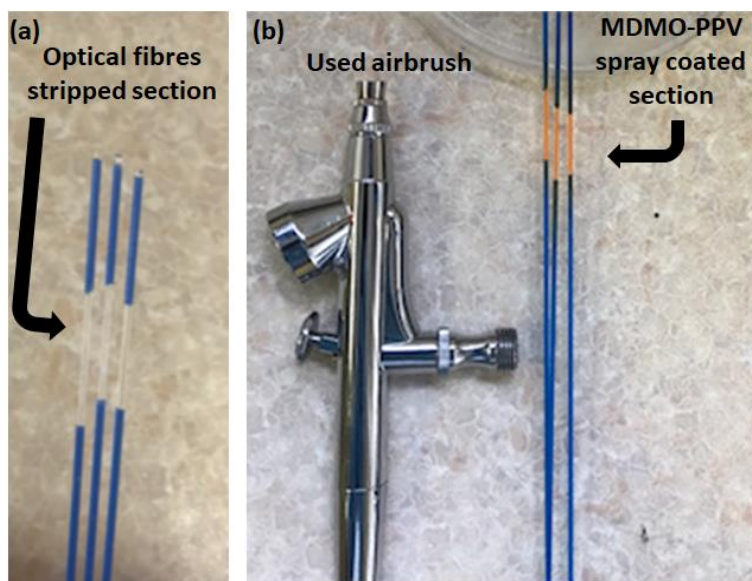


**Figure 4. 6.** (a) Stripped optical fibres prior to coating; (b) Stripped optical fibres which have been spray-coated with MDMO-PPV alongside the airbrush used.

#### 4.3.1.1 Important Parameters for Spray Coating

To deposit a uniform film by spray coating, it is essential to consider several parameters that affect the film quality and thickness, namely airbrush nozzle to substrate distance, compressed gas pressure, the spraying solution concentration, spraying duration, and the number of spraying cycles (puffs) [139]. These parameters can be controlled manually or can be programmed into the apparatus. The distance between the airbrush nozzle and the substrate or stripped optical fibre should be within a certain range depending on the boiling point of the solvent used in the spraying solution [140]. As solvent solutions with a lower boiling point have shorter evaporation time [141], the optimal distance between the nozzle and the substrate will be shorter. This distance controls the formation of the fine solution droplets landing on the substrate. Changing the nozzle to the substrate distance can result in three types of regions, i.e., wet, intermediate, and dry. Wet regions are created when the nozzle to substrate distance is short. In this case, wet droplets land on the substrate surface resulting in inhomogeneous film due to the formation of wet layers or re-dissolution of the previously deposited layers. In contrast, dry regions can emerge when the distance between the nozzle and the substrate is large, as the solution will dry before reaching the substrate and will be deposited in powder form. Hence, in order to obtain a homogenous film, the distance between the nozzle and the substrate must be optimised (intermediate regions). This is typically done by experimenting with different distances, striving to achieve uniform film thickness, which should be proportional to the spraying duration [140][142] and the number of puffs [143]. In the present work, the optimal distance for spraying the 1 mg/mL solution of MDMO-PPV in dichloromethane (prepared by stirring for an hour at 50 °C) was investigated experimentally whereby the process described above was performed on five identical fibres, adopting different distance (2, 3, 4, 5 and 7 cm) in each case while keeping other parameters constant. The nozzle to substrate distance of 4 cm was found to be optimal, because the film deposited from this distance had the highest fluorescence intensity. This was a crucial parameter for the present investigation, as highly fluorescent film has a greater number of active units, leading to high sensitivity when used as an on → off sensitiser.

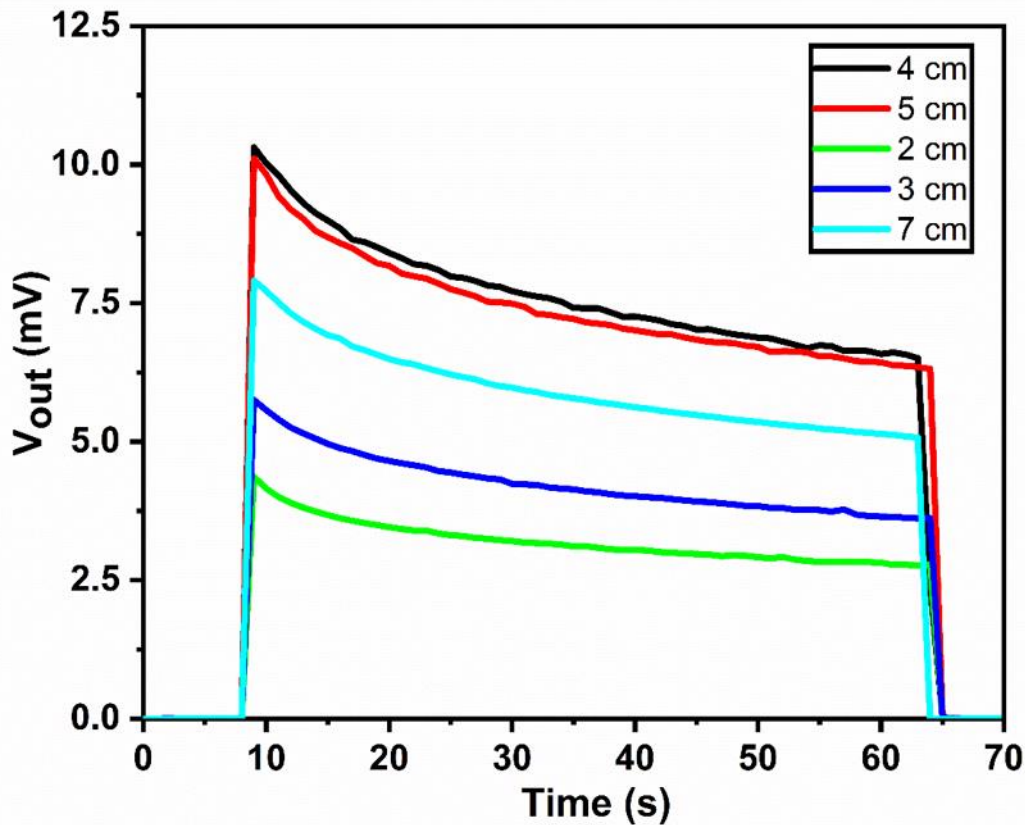


**Figure 4. 7.** Lock-in voltage output  $V_{out}$  as a measure of fluorescence intensity for five identical optical fibres sprayed with MDMO-PPV films under identical conditions while varying the nozzle to fibre distance. The films were exposed to a 450 nm exciting light (LED450L, Thorlabs) which was turned on in the time interval between  $t_1 = 8$  s and  $t_2 = 64$  s.

Carrier gas ( $N_2$  in our case) pressure is also an important parameter influencing film formation, as it atomises the coating solution and propels it as fine droplets toward the substrate [144]. To ensure that it was within a suitable range and thus ensure fine atomisation, in the present work, nitrogen gas pressure was set to 1.5 bar, in line with the previously adopted methodology [145]. In practice, increasing the coating solution concentration, the spraying duration, or the number of spraying cycles (puffs) should result in a greater film thickness when other parameters are kept constant. However, in the present work, the coating solution concentration was set to  $8.4 \mu\text{M}$  (1mg/1ml), as reported previously [87], and either the spraying duration or the number of spraying cycles was modified until a uniform film was achieved. The goal of the spray coating process was to deposit the MDMO-PPV solution on the stripped section of optical fibre, allowing detection of airborne and waterborne DNT, as described in Chapter 5.

### 4.3.2 Dip Coating Technique

Dip coating is widely used to produce thin films of viscous solution, as it is a facile and reliable coating technique. It is carried out by immersing a substrate at a constant speed into a coating solution and subsequently withdrawing it at a constant speed to form a homogenous and wet film on its surface. The wet film must be left at room temperature or on a hot surface for some time to dry by evaporation of the incorporated solvent [146]. A schematic diagram of the dip-coating procedure described above is shown in Figure 4.8.

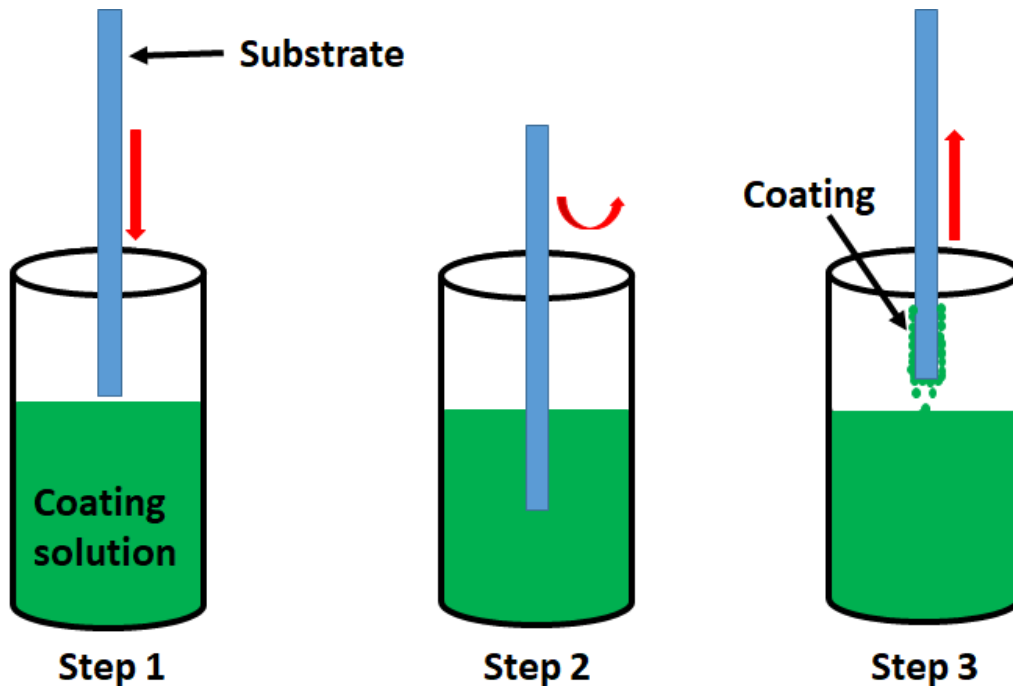


*Figure 4. 8. Schematic diagram of the dip-coating procedure. Step 1: substrate immersion into the coating solution; Step 2: the substrate is fully immersed in the coating solution; Step 3: the substrate is extracted from the coating solution.*

#### 4.3.2.1 Important Parameters for Dip Coating

When applying the dip-coating technique, film thickness is controlled by a number of parameters, such as the coating solution concentration, withdrawal speed, number of dipping cycles [147], and the viscosity and surface tension of the coating solution. Dip coating is an appropriate technique for sol-gel or plasticised polyvinyl chloride (PVC) membrane coating. It has been applied to coat a thin film of sol-gel doped with europium trivalent ( $\text{Eu}^{3+}$ )-doped yttrium aluminium garnet (YAG) as a fluorescent material onto a flat quartz substrate. The film thickness and fluorescence intensity of  $\text{Eu}^{3+}$ : YAG have been shown to increase with the

number of dipping cycles, with film thicknesses after the 1<sup>st</sup>, 6<sup>th</sup> and 12<sup>th</sup> cycle of 74 nm, 386 nm, and 803 nm film thickness respectively [143]. Other authors adopted dip coating to coat sol-gel onto a cylindrical plastic optical fibre [148] and to coat the immobilised Rhod-5N (sensitiser) in sol-gel onto the tip of an optical fibre for mercury ( $\text{Hg}^{2+}$ ) detection [61]. In the present study, specifically during the work described in Chapter 6, dip coating was applied to coat plasticised PVC membrane incorporating the organic sensitiser (a pyrazolyl chromene derivative (probe 1)) onto the 1 cm-long stripped section of the optical fibre to sense  $\text{Cu}^{2+}$ . This coating technique was chosen due to the use of plasticised PVC membrane as a part of the coating solution. The coating solution or membrane cocktail (including probe 1 as sensitiser) was prepared by dissolving 1 mg of probe 1, 33 mg of PVC, and 66 mg of plasticiser (2-Nitrophenyl octyl ether) in 1 mL of tetrahydrofuran (THF). The membrane cocktail was stirred for an hour at room temperature. The dip coating setup (NIMA, Coventry England) adopted in this work is shown in Figure 4.9.

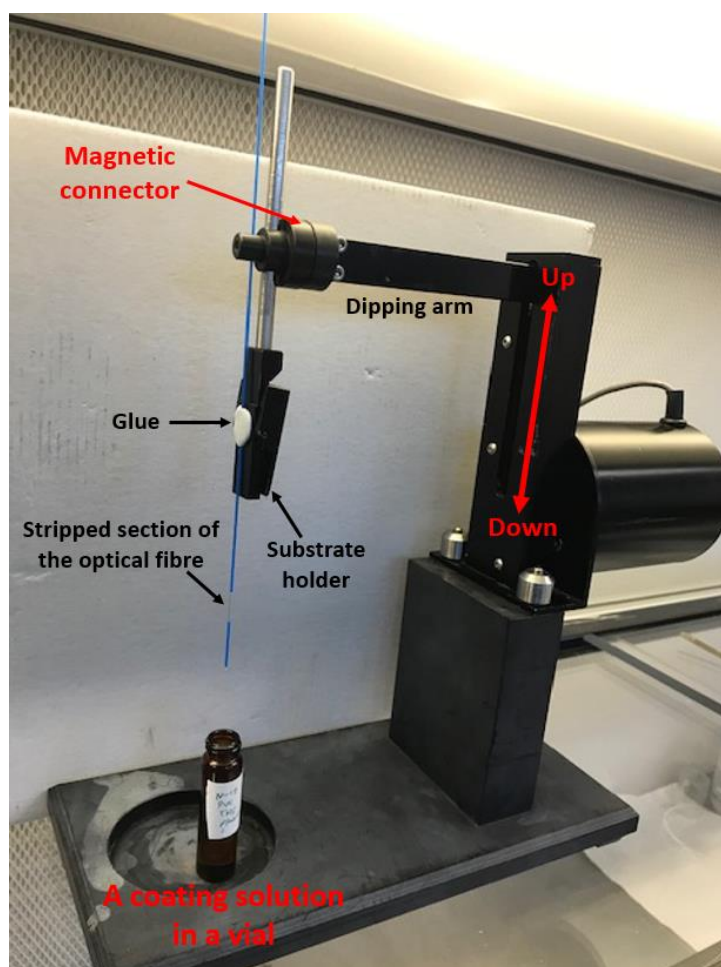


**Figure 4. 9.** The dip coating setup used in the present work, with red arrows indicating the movement direction of the arm and the glued optical fibre.

The arm of the dip coating setup moves in a straight line up and down with a speed controlled by the user through a GUI. This arm has a magnetic tip to attract the magnetic side of the substrate holder. In the present work, the stripped optical fibre was glued to the substrate holder and its position was adjusted to ensure that it was situated directly above the membrane cocktail in a glass vial. Therefore, when the arm moves downward, the stripped section of the optical fibre is dipped into the membrane cocktail. In addition to the dipping and withdrawal speed, the number of dipping cycles can be set through the GUI, as shown in Figure 4.10.

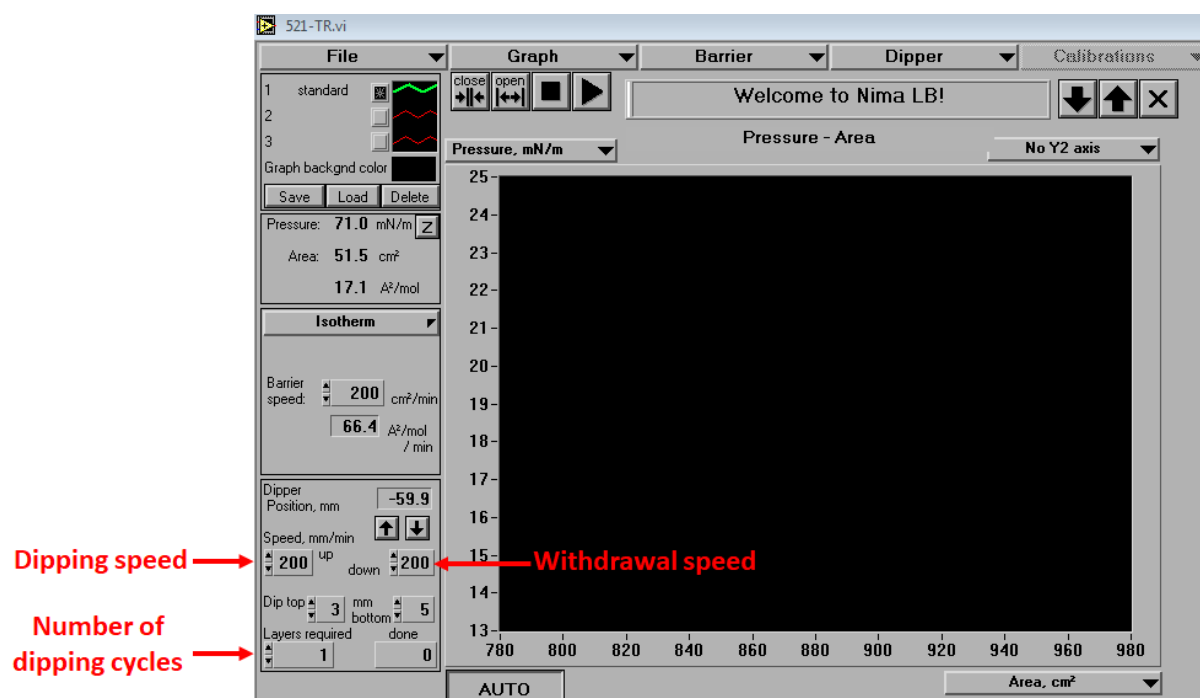


*Figure 4. 10. GUI of LabVIEW code including a brief description of the dip coating parameters that can be set by the user.*

In the present study, both the dipping and the withdrawal speed were set to 200 mm/min, and one dipping cycle was chosen, resulting in a membrane film nominally 1112 nm thick. The dip-coated membrane film was left over night at room temperature to dry. The thickness was determined by measuring a similar film dip coated onto a flat glass substrate. To perform a thickness measurement using a profilometry instrument (Veeco Dektak XT), the membrane film was deposited onto the flat glass substrate because the instrument requires a scratched film-coated flat surface rather than cylindrical fibre. Consequently, a glass substrate was dip coated by applying the dip coating procedures identical to those adopted for the stripped optical fibre. As profilometry reveals the membrane film thickness by comparing the thickness of a

scratched and an unscratched region of the film-coated substrate thus, the membrane film deposited onto the glass substrate was scratched by scalpel blade before performing the measurements. The thickness measurements was performed by a collaboration with Dr. Thomas Routledge, and Dr. Faleh Aljashaam, Sheffield University. The membrane films with nominally 1112 nm thickness were chosen for the sensing experiments as it emits high fluorescence compared with the membrane film of 725 nm thickness (as described later in Section 6.3.2) that was obtained when both the dipping and the withdrawal speed were set to 100 mm/min with one dipping cycle. The 1112 nm membrane film thickness exhibited detectable fluorescence and reasonable  $\text{Cu}^{2+}$  sensing response time ( $\sim 7$  min), as described in Chapter 6. It is worth noting that, in the present work, most of the parameters affecting the spray and dip coating films were not investigated in depth. Rather, their values were determined in line with published data or by few experimental attempts. That is because we have not fully concentrated on finding the most sensitive film thickness for our sensing experiment but we focussed instead on obtaining a film that emits detectable fluorescence intensity, sensitive to the presence of the target analyte and yielding a reasonable response time. As very thick films tend to produce a slow response time (as described in Section 2.2.5), and very thin films yield a very weak fluorescent signal, the goal was to achieve an intermediate thickness.

#### **4.4 Conclusions**

The preparation methods adopted in the present study for the two multimode silica optical fibres (cutting, stripping, cleaving, polishing, and roughening) as required for the sensing applications were described in this chapter. In addition, the spray and dip coating techniques used were introduced, and their advantages outlined, along with the key parameters influencing the coating film. In this work, we do not fully focus on finding the most sensitive film thickness. The preparation was considered acceptable as long as the coated film emits an easily detectable fluorescence intensity and demonstrates a sensitive response to the presence of the target analyte within a reasonable response time.

## Chapter 5: An Adaptive and Sensitive Fibre-Optic Fluorimetric Transducer for Air- and Water-Borne Analytes

### 5.1 Introduction

In recent years, fibre optics have been used for a variety of applications beyond their original purpose in data communication. One such application is in the optical sensing of air or water-borne target chemicals ('analytes'), where an analyte causes a change of optical absorption, or fluorescence, in a sensitizer, namely a 'chromophore' (absorption) or 'fluorophore' (fluorescence). In some cases, optical fibres are used to guide light to the sensitizer and/or collect the transmitted or fluorescent light to guide it to a spectrometer for detection [61][75][77]. However, it has become increasingly common to use fibres directly as the substrate for the sensitizer, by stripping the fibre cladding from the core within a short section and then coating sensitizer directly onto the fibre core in that section. This more direct use of the fibre optics as the substrate is favourable because of easy handling and fabrication (including cutting, stripping, cleaving, and polishing), low cost and attenuation, flexibility, and can lead to high sensitivity [117][149]. Fibres may detect the absorption of propagating fibre modes via their evanescent waves in the sensitized section [37][150], or collect fluorescence of the sensitizer that has been excited by absorption of evanescent waves [9][75][151][152][153]. However, evanescent wave excited fluorimetric sensors often suffer from low intensity despite efforts to increase their sensitivity by fibre tapering and longer sensitized sections [9][117][121][152]. Alternatively, fluorescence may be excited by an external source and then couple into a propagating fibre mode [117].

In this study, we adapt a lock-in based light detector that was originally developed as an evanescent wave absorption sensor [37] such that the transducer (shown in Figure 3.1) is now a fluorimetric sensor. As an example analyte, we used the nitroaromatic explosive dinitrotoluene (DNT) both in vapour- and aqueous phase, we used the fluorescent polymer poly(phenylene-vinylene) derivative poly[2-methoxy-5-(3',7'-dimethyloctyloxy)-1,4-phenylenevinylene] (MDMO-PPV) as the fluorophore. MDMO-PPV is known to be quenched by trace amounts of nitroaromatic explosives dissolved in either water or organic solvents [87][89], however, it has not previously been used for nitroaromatic vapour sensing. We here show that fibre-based MDMO-PPV sensors can be deployed for nitroaromatic sensing in both aqueous (waterborne) and vapour (airborne) phase with minimal adaptation required between the different phases. We study the required response times and the photophysical degradation

of the fluorophore. Photophysical degradation is found to be rapid so an optimised operational procedure and ‘baseline’ experiments to account for this degradation are developed. The sensors require several minutes to equilibrate under airborne DNT, but respond much faster to waterborne DNT. The response characteristic for airborne DNT follows a Langmuir-Freundlich isotherm while the response characteristic follows a Langmuir adsorption isotherm (described previously in Section 2.1) for waterborne DNT. The Langmuir-Freundlich isotherm plot indicates inhomogeneity between the sensitizer sites, which may result from the air pollutants in traces amounts. The binding constants for air and waterborne DNT obtained from both Langmuir plots and SV plots are approximately equal. We find a dimensionless Stern Volmer constant (discussed earlier in Section 2.3.1.3) that quantifies the strength of the DNT / MDMO-PPV interaction relative to analyte / carrier medium interaction of  $k_{SV} = 1.14 \times 10^7$  for airborne DNT and  $k_{SV} = 5.8 \times 10^6$  for waterborne DNT. The Limit- of- detection (*LoD*) for airborne DNT is 0.48 ppb and 55.7 ppb for waterborne DNT. Our transducer compares favourably to alternative systems using PPV fluorophores for the detection of nitroaromatic vapours [1] and solutions [77][78], and we propose to adopt it more widely for fluorimetric sensing.

## 5.2 Experimental

To prepare sensitised fibres, first a 30 cm length of multimode optical fibre (FT800UMT, Thorlabs), was cut from a fibre reel, and prepared (stripped, cleaved, polished, cleaned, dried) as previously described in Section 4.2. Then the stripped section of the fibres were spray coated with the MDMO-PPV solution in dichloromethane as described in 4.3.1. To determine the fluorescence intensity, the sensitizer film of MDMO-PPV was excited with a blue (450 nm) LED (LED 450L, Thorlabs), this wavelength matches the absorption band of MDMO-PPV [154]. The excitation duration was controlled via an external manual switch (a rocker switch) which enabled the excitation time to be minimised. Details of how the LED was modulated to excite the MDMO-PPV film, and detection of the resulting fluorescence were explained extensively in Sections 3.3-3.6. In brief, the LED was driven in series with a 150  $\Omega$  resistor from an AC + DC voltage adder circuit, adding an 8.15 V DC bias to a 5.641 kHz AC signal of  $\pm 2.5$  V taken from the reference output of a digital lock-in amplifier (USB LockIn250, Anfatec). The sensitised fibre was excited under side illumination whereby one face of the sensitised fibre projected fluorescence onto a Centronic OSD5-5T photodiode (PD) as previously shown in Figure 3.2. The resulting PD photocurrent is fed into the input of a

current/voltage (i/v) converter with a transimpedance gain of 100 k $\Omega$ . The voltage delivered by the i/v converter was linked into the measurement input of the lock-in, set to AC coupling with a 100-fold pre-amplification and a 1 s output filter. The filter within the lock-in amplifier was set to 1 s despite a 5 s output filter being better for low noise bandwidth, as previously described in Section 3.3.1. Setting the output filter to 1 s is the required time to average the data before displaying to the user, and so keeps the excitation time short (starting from 1 s) therefore minimising the photophysical degradation of MDMO-PPV. The output of the filter within the lock-in is a DC ' $V_{out}$ ' reading in the mV range, this signal is proportional to MDMO-PPV fluorescence intensity. The  $V_{out}$  value was recorded vs. time on a PC running a bespoke LabVIEW routine. The MDMO-PPV was excited briefly for 3 s with longer 'dark' intervals (1 and 2 minutes for airborne and waterborne DNT detection respectively) between measurements to minimise photophysical degradation of the fluorophore.

An open bottle containing 250 mg of high explosive 2,4 dinitro toluene (DNT) was placed in a thermalised container to generate the required test vapours. The thermalised DNT container was purged with pressurised dry nitrogen carrier gas that was pre-cooled by running several coils of pipe through same cooling medium (cooling medium is shown in appendix VI) after passing through the Tylan FC-260 mass flow controller. The container was thermalised at different temperatures (air at two different temperatures (20.1 and 16.3  $^{\circ}\text{C}$ ), ice bath (0  $^{\circ}\text{C}$ ), two salt/ice mixtures (-5 / -15)  $^{\circ}\text{C}$ ). The temperature was measured using a testo 925 digital thermometer. The different temperatures at and below ambient temperature establish different saturated vapour pressures  $p_{sat}$ . A flow rate of carrier gas passing through the flow controller was set to 500 mL/min by the LabVIEW routine. Reducing the temperature of the source allowed generation of DNT concentrations down to very low levels. The resulting DNT concentration is expressed as a normalised partial pressure  $p$ , given as the ratio of the DNT saturated vapour pressure to standard atmospheric air pressure,  $p = p_{sat}(T) / p_{atm}$ . Where  $T$  is the temperature of the DNT source,  $p_{sat}(T)$  is the saturated vapour pressure of DNT at  $T$ , and  $p_{atm} = 101.325$  kPa. The resulting  $p$  is dimensionless and we express it in parts per billion (ppb). The temperature dependency of the DNT saturated vapour pressure  $p_{sat}(T)$  was given by Pella [155]. Thus, DNT vapour concentrations of  $p = (150 / 89.7 / 8.4 / 4.8 / 0.73)$  ppb were obtained, respectively, *i.e.* covering the range from ambient saturation (150 ppb at 20.1  $^{\circ}\text{C}$ ) down to approximately a 200-fold dilution. To realise an extremely low vapour pressure, we used picric acid (PA) instead of DNT. Picric acid (PA) is another nitroaromatic explosive but it has much lower vapour pressure than DNT, 0.028 parts per trillion (ppt) at ambient temperature [156].

Also, as a control experiment, we generated a saturated vapour of a non-nitrated aromatic, toluene, at ambient temperature, equal to 29.6 parts per thousand (ppt) [157]. The resulting vapours were delivered into a closed fibre optic test chamber (31 mL volume) held at ambient temperature via short tubes  $\approx 7$  cm (to minimise parasitic condensation) with a similar exhaust tube leading into a fume extractor funnel. The test chamber is hence purged within 4 seconds. Our system for detection of airborne DNT is illustrated in Figure 3.4.

### 5.2.1 Preparing Aqueous Solutions of DNT

A stock solution of DNT was prepared by stirring 1 mg of DNT crystals in 1 ml of deionized water for a week using a teflon magnetic stirrer bar at 22 °C, resulting in a saturated solution of 1.03 mM concentration [158]. To allow direct comparison with partial pressures of airborne DNT, we here express solution concentrations in the same dimensionless format as partial pressures. Given that 1L of water equals 55.6 mole, we can equate 1.03 mM to 18.5 parts-per-million (ppm). The stock solution was filtered through PTFE syringe mounted filters (0.2  $\mu$ M pore size) and transferred into a clean vial. 53.7, 54, 54.3, 54.6, 54.9, 55.2, 55.5, and 55.8  $\mu$ L aliquots of 18.5 ppm DNT stock solution were then pipetted respectively into a vessel holding 11 mL of DI water, leading to DNT concentrations of (90, 180, 270, 360, 450, 540, 630, 720) ppb. For waterborne DNT detection, we modified the set-up as shown in Figure 5.1. Instead of a test chamber, we used a vessel to hold DI water or DNT solution. Fluorescence excitation and detection remained the same.

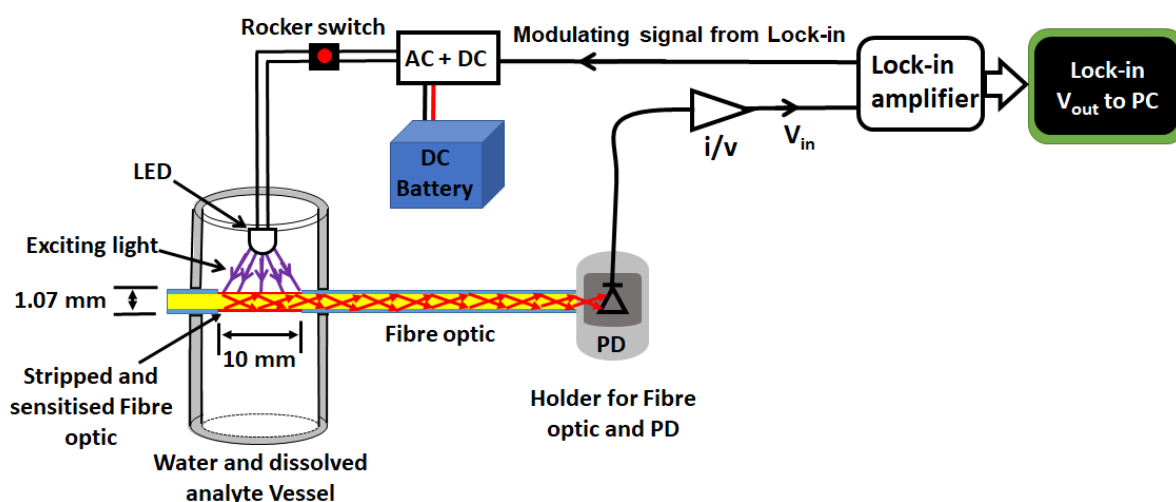


*Figure 5. 1. Schematic diagram of our sensor design used for waterborne DNT sensing.*

## 5.3 Results and Analysis

### 5.3.1 Detecting Airborne DNT vapours

Figure 5.2 shows the recorded values of the lock-in output voltage  $v_s$  time at different DNT vapour concentrations,  $p$ ,  $V_{out}(t, p)$ , including a control experiment in a DNT- free atmosphere. For comparison, results for a fibre non- sensitised with MDMO-PPV are also shown.

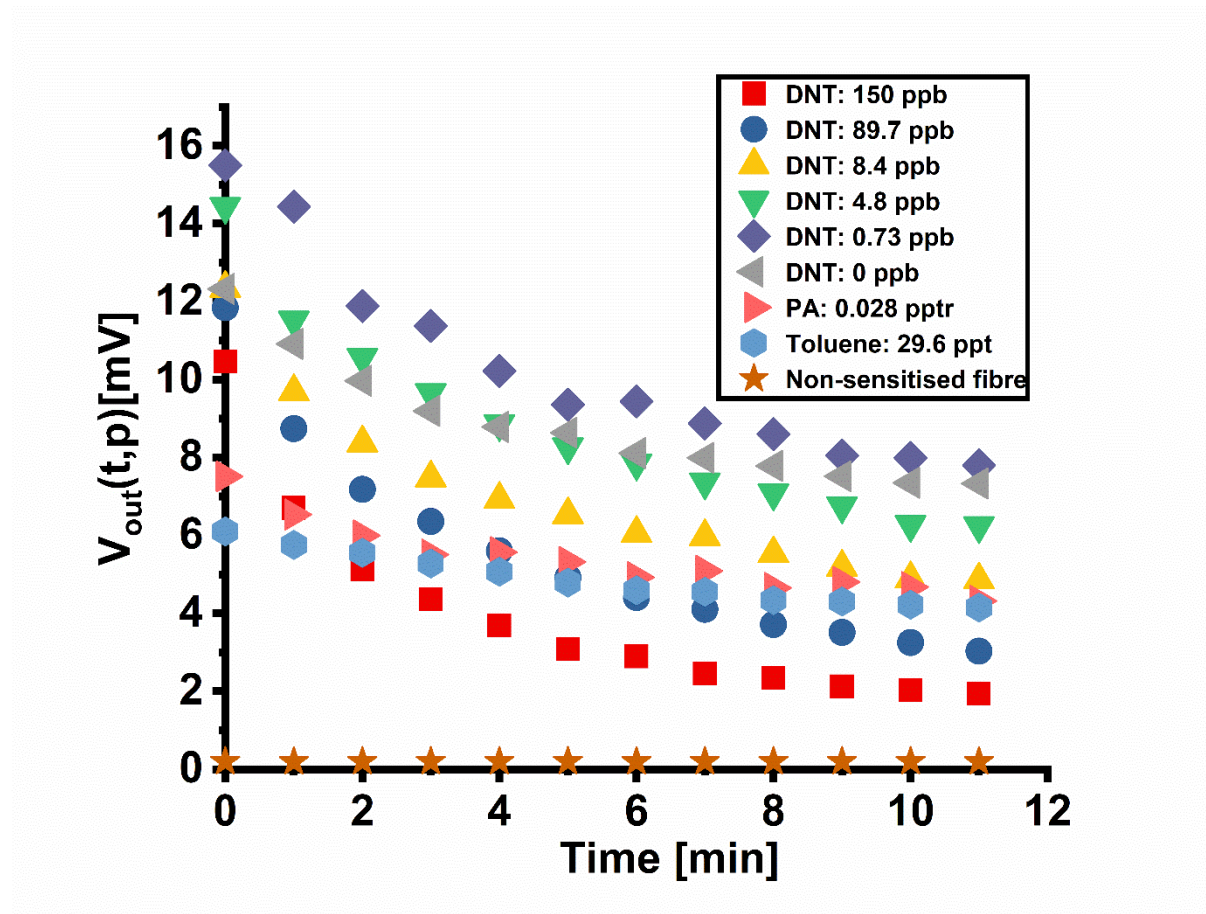


*Figure 5. 2. Lock-in voltage output  $V_{out}(t,p)$  as a measure of fluorescence intensity for several MDMO-PPV sensitised optical fibres under blue LED excitation shown against time after starting the exposure to DNT at  $t = 0$  at different dimensionless vapour pressures,  $p$ . The fibres were illuminated and the fluorescence was detected for 3 s once every minute. The non-sensitised fibre gives near-zero  $V_{out}$ .*

The non-sensitized fibre shows near-zero  $V_{out}(t,0)$ , confirming that the exciting light does not significantly couple into the fibre under side illumination. For all sensitised fibres during the first 3 s of ‘interrogation’, the recorded  $V_{out}$  for all non-zero DNT partial pressures  $p$ ,  $V_{out}(0,p)$ , was in the range (10.5 ... 15.5) mV, with some variation between fibres. Also, even at zero DNT pressure, recorded  $V_{out}(t,0)$  decays slightly with every interrogation, even though there

can be no DNT-induced quenching. This indicates some photophysical degradation of MDMO-PPV (as described previously in Section 3.1) even under brief excitation, which underscores the need to keep the excitation time as short as possible.

Further, the measured value for  $V_{out}(t,p)$  is proportional to the number of fluorescence-active MDMO-PPV units, while our interest is focussed on the fluorescence-inactive units, as it is the quenched (inactive) rather than active units that indicate presence of DNT ('on  $\rightarrow$  off').

Hence, for further analysis, all recorded values for  $V_{out}(t,p)$  were normalised and processed into a 'fluorescence quenching response'  $FQR(t,p)$  [28] to account for these factors: First, all  $V_{out}(t,p)$  data were normalised to their initial values  $V_{out}(0,p)$  as shown in Figure 5.3. Then they were multiplied by  $V_{out}(0,0) / V_{out}(t,0)$  to account for photodegradation unrelated to DNT, and finally subtracted from 1 to convert from a measure of active fluorophores into a measure of quenched fluorophores.

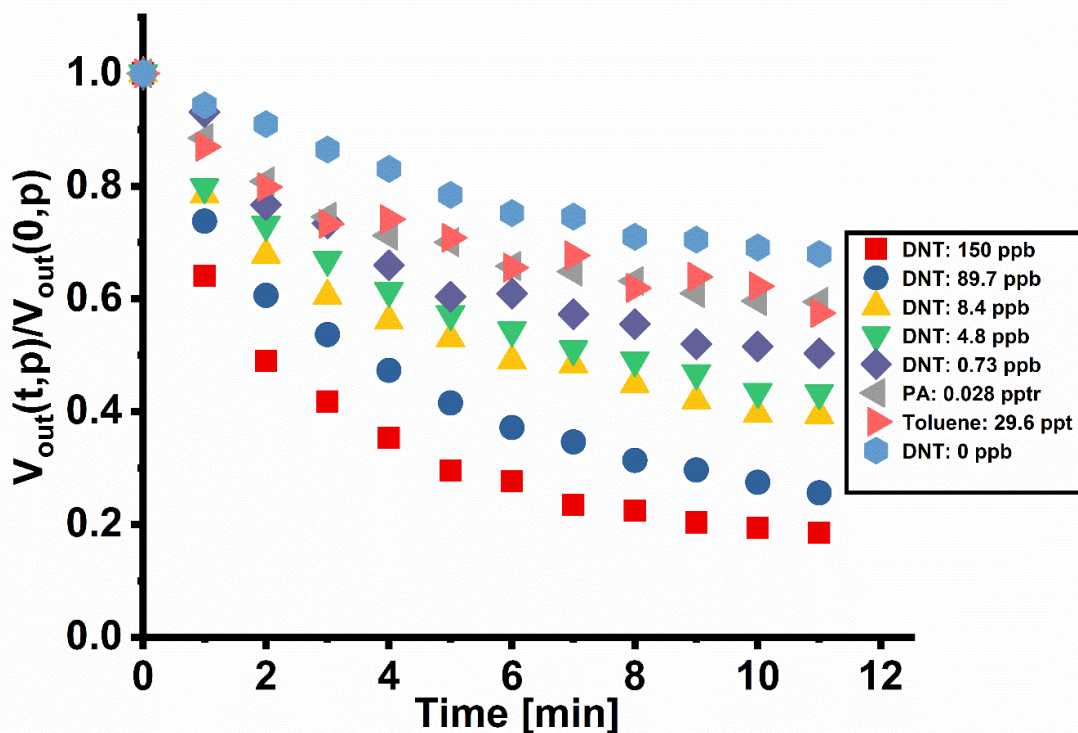


**Figure 5. 3.** Normalized lock-in voltage output  $V_{out}(t,p)$  as a measure of fluorescence intensity for several MDMO-PPV sensitised optical fibres under blue LED excitation shown against time after starting the exposure to DNT at  $t = 0$  at different dimensionless vapour pressures,  $p$ . The fibres were illuminated and fluorescence was detected for 3 s once every minute.

In summary,  $FQR(t,p)$  represents the ratio of DNT-complexed vs. total MDMO-PPV fluorescent units and is calculated from  $V_{out}(t,p)$  by:

$$FQR(t,p) = 1 - \left[ \frac{V_{out}(t,p)}{V_{out}(0,p)} \times \frac{V_{out}(0,0)}{V_{out}(t,0)} \right] \quad (5.1)$$

$FQR(t,p)$  ranges from zero (no quenching) to 1 (complete quenching). For ‘off  $\rightarrow$  on’ fluorescence sensors, data would have to be analysed without the subtraction from 1. The resulting  $FQR(t,p)$  calculated from the  $V_{out}$  data shown in Figure 5.2 via eq. 5.1 are shown in Figure 5.4. Other researchers found curves of similar shape and timescale, e.g. [9][28][115].

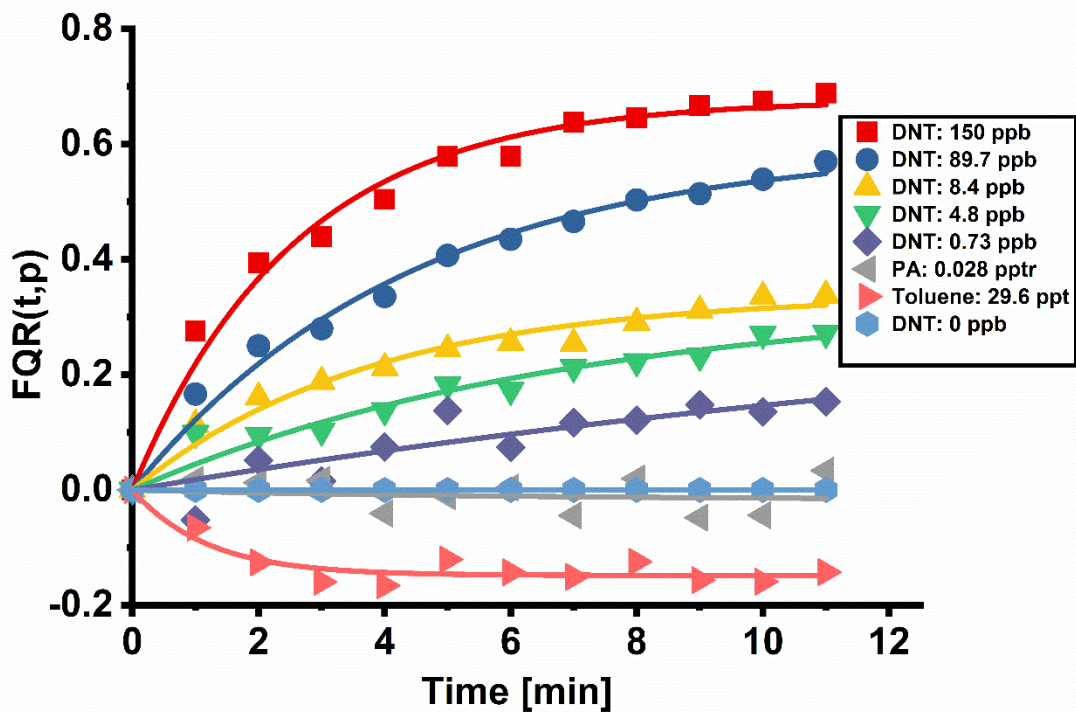


**Figure 5. 4.** Fluorescence quenching ratios  $FQR(t,p)$  calculated from the data in Figure 5.2 with the help of Eq. 5.1. Solid lines are exponential fits to Eq. 5.2 using Origin software.

By construction,  $FQR(t,0)$  remains zero at all times, reflecting the absence of DNT- induced quenching in the absence of DNT. All  $FQR(t,p)$  data under DNT show an initial increase over time, steeper for higher  $p$ , which after a few minutes approaches a final equilibrium value,  $FQR(\infty,p)$ , that increases with increasing  $p$ . This approach to equilibrium was fitted with an exponential model, Eq. 5.2:

$$FQR(t, p) = FQR(\infty, p)[1 - \exp(-\frac{t}{\tau(p)})] \quad (5.2)$$

With two fit parameters, an equilibrium value  $FQR(\infty, p)$  is approached with a time constant,  $\tau(p)$ . The model provides good fits, shown as solid lines in Figure 5.4. The fit parameters that obtained from the fitted data to the Eq. 5.2 are summarised in table 5.1.

**Table 5.1:**

$p$ [ppb]	$FQR(\infty, p)$	$\tau(p)$ [min]
0.73	$0.10 \pm 0.01$	$9.7 \pm 1.2$
4.8	$0.25 \pm 0.05$ [ $0.30 \pm 0.01$ ]	$6.9 \pm 1.9$ [ $8.2 \pm 3.9$ ]
8.4	$0.34 \pm 0.02$ [ $0.31 \pm 0.01$ ]	$4.75 \pm 0.54$ [ $1.7 \pm 0.4$ ]
89.7	$0.60 \pm 0.02$ [ $0.57 \pm 0.02$ ]	$4.4 \pm 0.4$ [ $3.3 \pm 0.3$ ]
150	$0.68 \pm 0.01$	$2.6 \pm 0.2$

**Table 5. 1:** Fit parameters, with errors, for  $FQR(t, p)$  shown in Figure 5.4 when fitted to Eq. 5.2 using Origin software. For some concentrations the experiment was repeated on a different fibre, repeat results are shown in brackets.

Table 5.1 includes some fit parameters shown in brackets which were extracted from repeating experiments under (89.7 / 8.4 / 4.8) ppb DNT with another fresh fibre as shown in Figure 5.5.

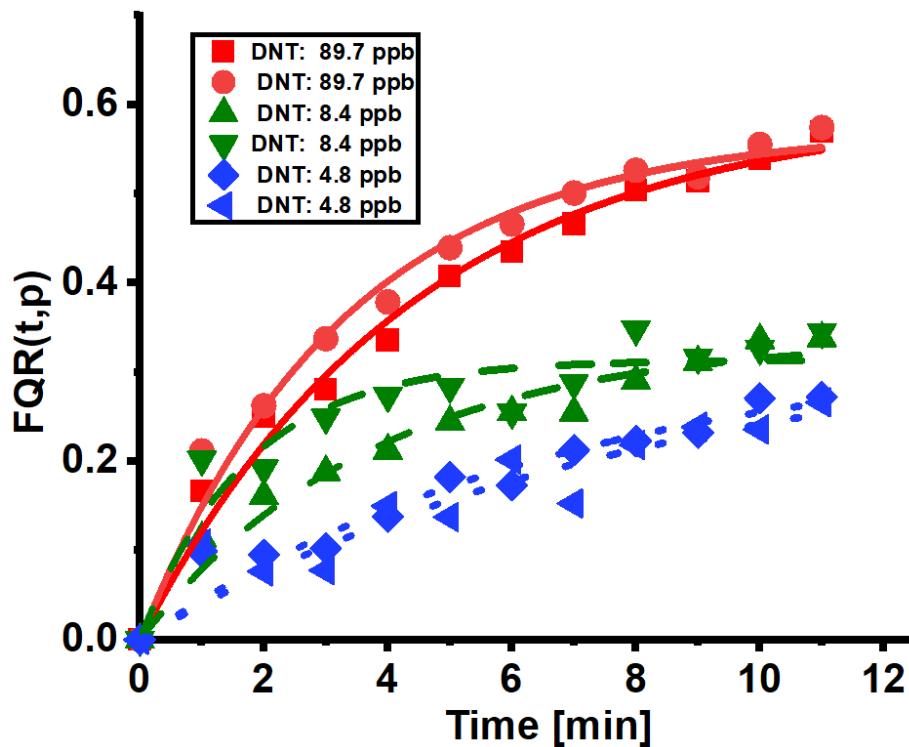


**Figure 5. 5.** Fluorescence quenching ratios  $FQR(t,p)$  from repeating experiments under (89.7 / 8.4 / 4.8) ppb DNT calculated and fitted in the same way as in Figure 5.4. The solid line is a fit to Eq. 5.2.

Fibres that had been used in an exposure experiment did recover 85% of their initial fluorescence intensity after 40 hrs storage under dynamic vacuum at 50 °C, as was observed for other fluorescent nitroaromatic explosive sensors previously [115]. This suggests that the fluorophore/nitroaromatic complex is slowly reversible, but not the photodegradation that is independent of complexation. Therefore, we conducted all experiments with freshly prepared fibres only, so that every curve in Figure 5.2 was taken on a different fibre.

### 5.3.2 Detecting Waterborne DNT

The same optical fibres and transducer can also be used for the detection of waterborne DNT with minimal adaptation, *cf.* experimental section. We now find that when we add DNT stock solution to water, the fluorescence response (discussed in Section 2.2.5) to increased DNT concentration is very fast and is complete within 120 seconds, as shown in Figure 5.6. This allows for a simpler calibration procedure where a single fibre is measured repeatedly while it is titrated with DNT in concentration ( $c$ ) increments of 90 ppb added in 2 minute intervals. Due to the fast equilibration, measured  $V_{out}(t = 2 \text{ minutes}, c)$  can be taken as  $V_{out}(t \rightarrow \infty, c)$  and is

simply reported as  $V_{out}(c)$ . The equilibration for DNT detection in air lasts longer ~11 minutes therefore, the experimental protocol is different from DNT detection in water.

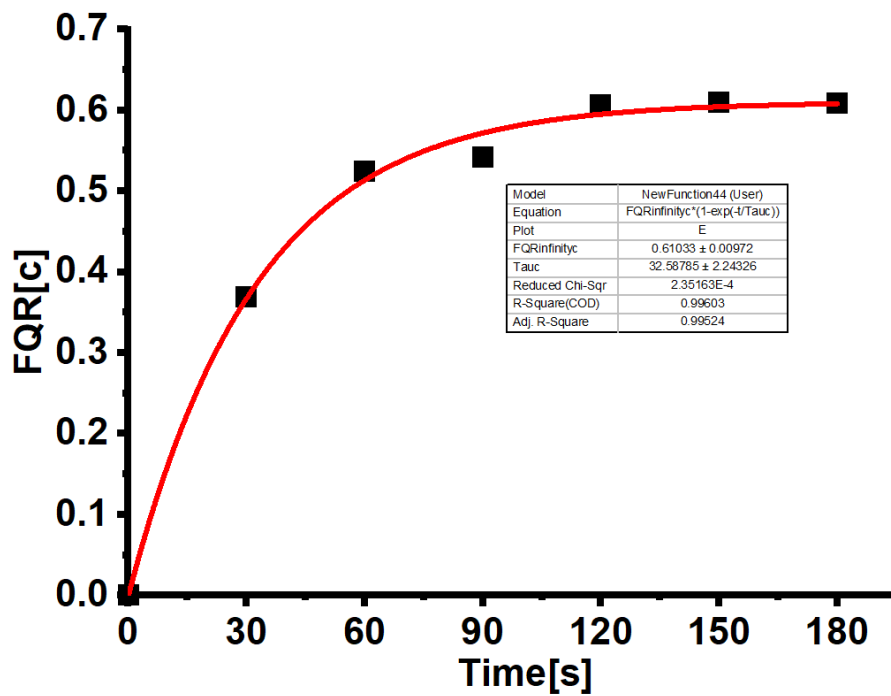


**Figure 5. 6.** Fluorescence quenching ratios  $FQR(t, c)$  under 270 ppb DNT concentration in water against time [seconds]. Solid line is a fit to Eq. 5.2.

Note we annotate waterborne concentrations as ‘c’ to distinguish them from partial pressures,  $p$ , of the airborne analyte, but report both as dimensionless fractions, ppm or ppb, relative to the respective carrier medium. However, there is again a decay of fluorescence intensity due to photodegradation with every 3 second fibre ‘interrogation’. This is again accounted for by a control experiment where a (different) fibre was repeatedly interrogated at the same 2 minute intervals in DI water, without DNT titration and the results are shown in Figure 5.7.

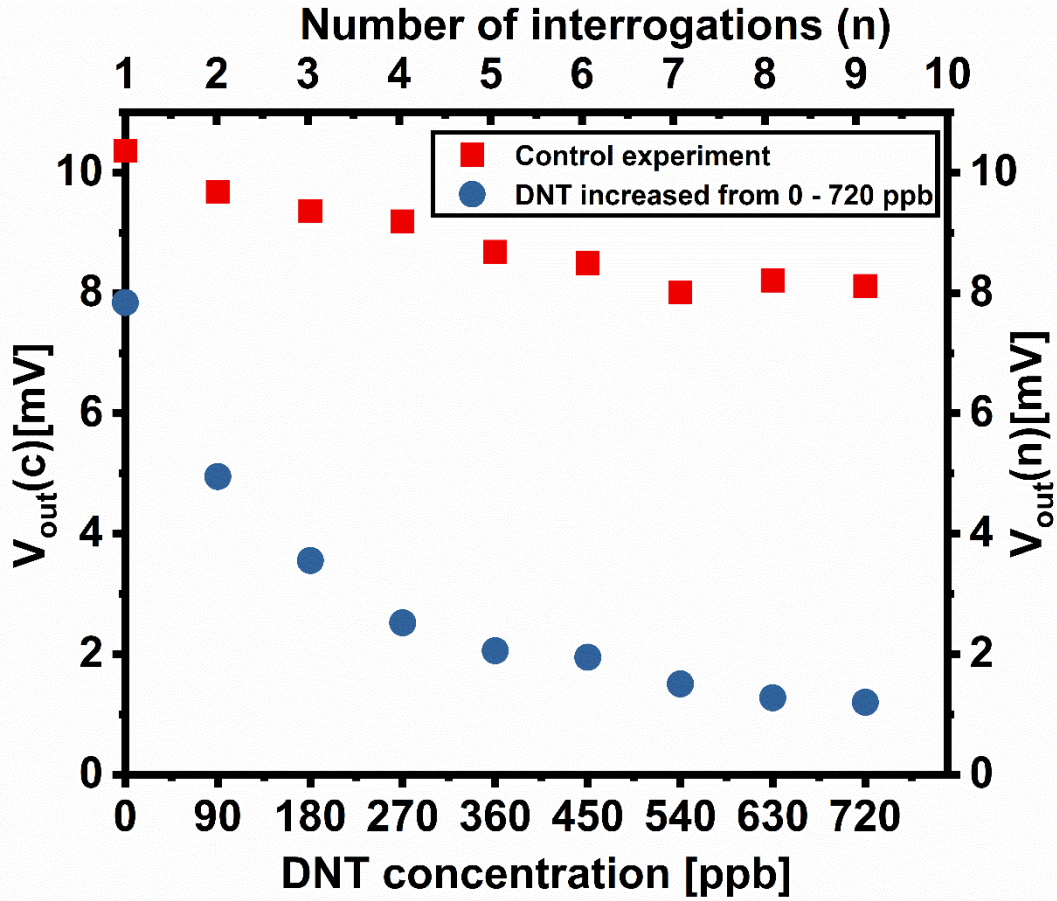


**Figure 5. 7.** Lock-in voltage output  $V_{out}(c)$  (blue circles) as a measure of the fluorescence intensity for an MDMO-PPV sensitised optical fibre under blue LED excitation, shown against DNT concentration in water from 0 - 720 ppb. Also shown is a control experiment (red squares), vs. the number of interrogations.

The resulting fluorescence quenching ratio  $FQR(c)$  for waterborne DNT, which corresponds to  $FQR(\infty,p)$  for airborne DNT, is calculated from the data in Figure 5.7 using Eq. 5.3:

$$FQR(c) = 1 - \left[ \frac{V_{out}(c)}{V_{out}(c=0)} \times \frac{V_{out}(n=1)}{V_{out}(n)} \right] \quad (5.3)$$

Note how the second factor on the right- hand side compensates for the photodegradation that is independent of DNT concentration, similar as in Eq. 5.1. The resulting  $FQR(c)$  is tabulated in table 5.2:

**Table 5.2:**

$c$ [ppb]	90	180	270	360	450	540	630	720
$FQR(c)$	0.32	0.50	0.64	0.69	0.70	0.75	0.79	0.80

**Table 5. 2:  $FQR(c)$  vs  $c$  for waterborne DNT.**

The DNT sensing experiments were replicated on a different fibre and their data (FQR) were fitted to Langmuir model as shown in Appendix VII.

## 5.4 Discussion

### 5.4.1 Airborne DNT Vapours

The time constants  $\tau$  required to reach equilibrium  $FQR(\infty, p)$ , are in the order of a few minutes with systematic variation with  $p$ , and significantly longer than the 4 seconds required to purge the sample chamber volume (31 mL) by a flow of 500 mL/minute test vapour. This observation is consistent with a ‘static’ quenching process [e.g. 24] where DNT vapour first binds to the MDMO-PPV fibre coating to form fluorophore/DNT complexes that then quench excitons when excited by LED illumination. A ‘dynamic’ quenching process would instead rely on the collision of a DNT molecule with a previously uncomplexed fluorophore whilst this is in the excited state; this would not need minutes to build- up as we previously described in Section (2.3.1.3.1). In addition, the fibre takes 40 hrs to recover as explained in Section 5.3.1, the dynamic quenching is expected to have fast recovery [27][81].

We therefore, believe  $\tau$  represents the required time for analyte to fly from its source and binds to the MDMO-PPV film layer coated onto the fibre, which does depend on  $p$ . The time  $\tau$  is long because the density of the analyte in the airborne phase is low.

On the other hand, the equilibrium value of fluorescence quenching response  $FQR(\infty, p)$  does systematically depend on DNT concentration, *i.e.* the dimensionless partial pressure  $p$ . Here,  $FQR(\infty, p)$  are considered for further quantitative analysis. Qualitatively, Figure 5.4 shows that at the lowest DNT concentration used here of  $p = 0.73$  ppb we still find  $FQR$  above the noise

level. This is at  $\approx 200$ - fold dilution of the saturated vapour pressure at ambient temperature, using only a generic fluorescent polymer. Under the extremely low (saturated) vapour pressure of picric acid (0.028 ppt), no clear response can be found though. For quantitative analysis, since the response characteristic  $FQR(\infty, p)$  follows a Langmuir-Freundlich isotherm rather than Langmuir adsorption isotherm model, we fit the  $FQR(\infty, p)$  data (table 5.1) to the Langmuir-Freundlich isotherm Eq. 5.4, as shown in Figure 5.8, using the non-linear fit routine in Origin 2018 software.

$$FQR(\infty, p) = \frac{(kc^m)}{(kc^m+1)} \quad (5.4)$$

The Langmuir-Freundlich isotherm generalises the known Langmuir adsorption isotherm (described previously in Section 2.1) that has the special case of  $m=1$ . The term  $k$  is the binding constant, this quantifies analyte/sensitiser binding strength,  $m \leq 1$  describes inhomogeneity between sensitiser sites [46][159].

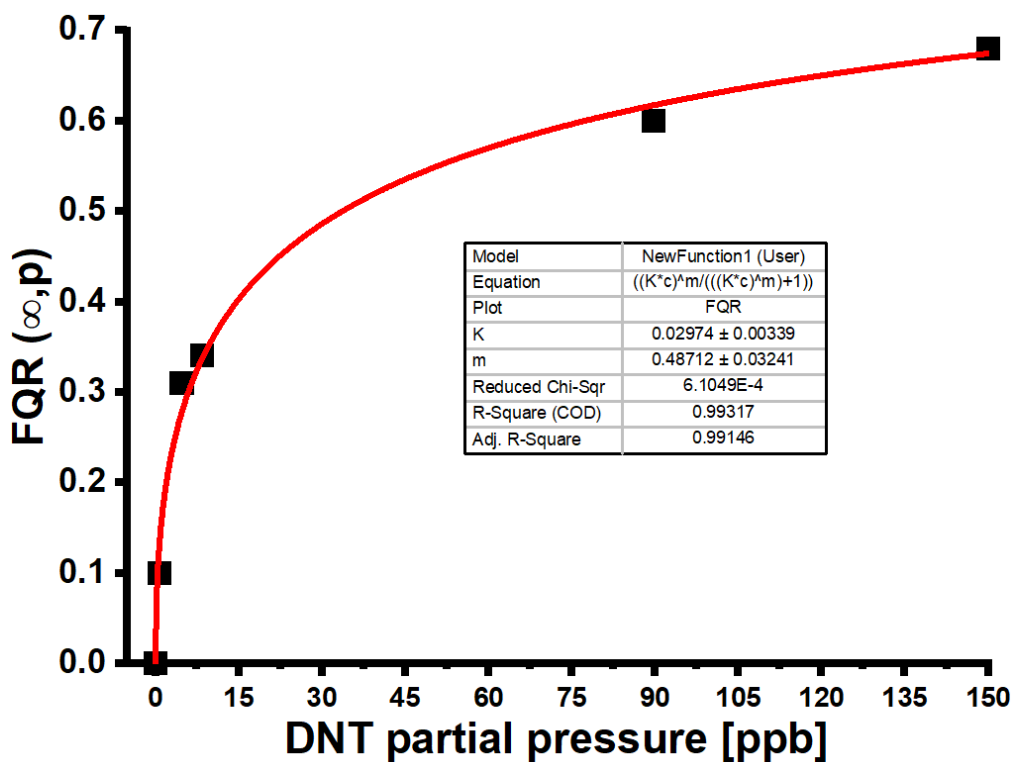


Figure 5. 8.  $FQR[\infty, p]$  vs. airborne DNT in the concentration range (0-150) ppb, Data from table 5.1 where the solid line is a fit to Eq. 5.5.

The binding constant obtained from a non-linear plot (Figure 5.8) of the Langmuir-Freundlich isotherm is  $k = (2.97 \pm 0.00339) \times 10^7$ . Note,  $k$  is dimensionless as it is evaluated from the dimensionless partial pressure. The parameter  $m$  is equal to 0.49, which indicates the inhomogeneity between the binding sites of the sensitiser. This may be due to the occupation of the traces of airborne pollutants such as carbon dioxide (CO) or nitrogen dioxide (NO) to sensitiser binding sites. These air pollutants are probably presented in the compressed air used in the gas sensing experiment as carrier gas.

To obtain the  $LoD$ , we plotted  $FQR(\infty, p)$  vs. low range of DNT partial pressure [ppb] which shows linear fit in Figure 5.9.

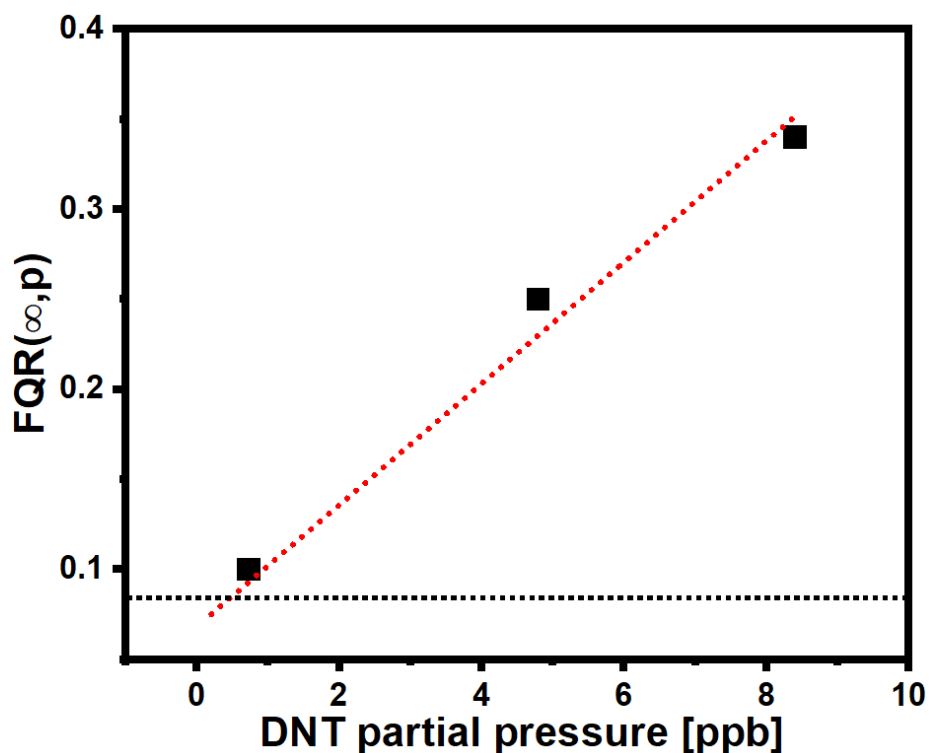
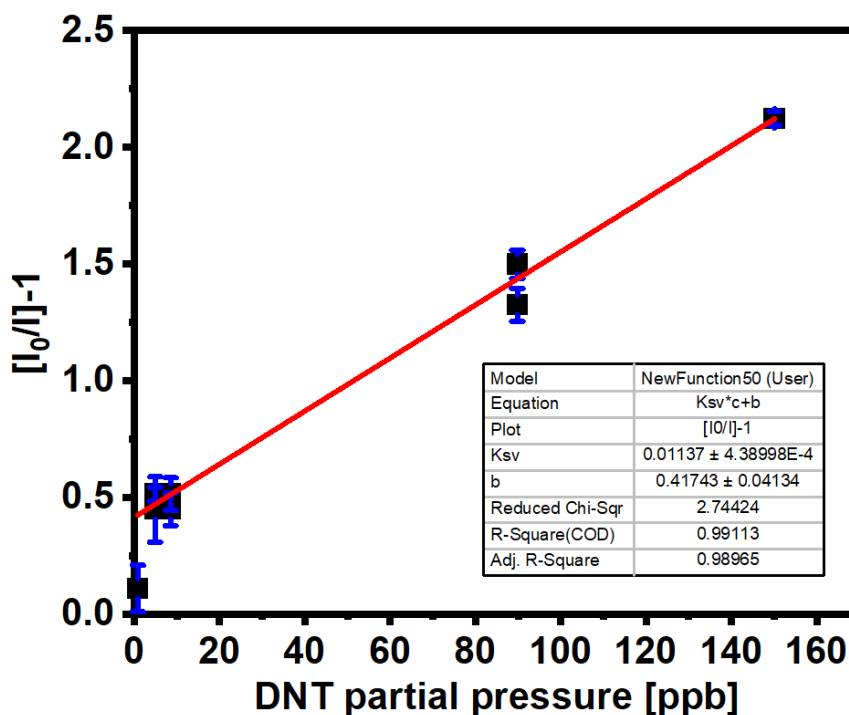


Figure 5.9.  $FQR [\infty, p]$  vs. airborne DNT in the concentration range (0-8.4) ppb, Data from table 5.1.

In Figure 5.9, we extrapolate the calibration line until it crosses the triple value of estimated noise as 0.09 to find the  $LoD$ . The value of the  $LoD$  was found to 0.48 ppb.

For further quantitative, we present the response as a Stern-Volmer (SV) plot, Figure 5.10. The SV is known for an on  $\rightarrow$  off fluorescent sensor as previously described in Section 2.3.1.3. In

the SV plot, fluorescence quenching is expressed as  $\left[\frac{I_0}{I} - 1\right] = \left[\frac{I_0}{I} - 1\right]$  this is related to  $FQR(\infty, p)$  by  $\left[\frac{I_0}{I} - 1\right] = \frac{FQR(\infty, p)}{1 - FQR(\infty, p)}$ .



**Figure 5. 10.** A Stern-Volmer plot for the quenching of MDMO-PPV fluorescence by airborne DNT in the concentration range (0-150) ppb. Data from table 5.1.

A straight line is fitted having an intercept and we find the value  $b \pm \Delta b$  which gives the DNT / MDMO-PPV Stern Volmer constant,  $k_{SV}$ , as its slope.  $k_{SV}$  quantifies the strength of analyte / sensitiser interaction relative to analyte / carrier medium interaction. Fitting the straight line slope in Figure 5.10 gives  $k_{SV} = (1.14 \pm 0.00044) \times 10^7$ . Note  $k_{SV}$  is dimensionless as it is evaluated from dimensionless partial pressure, however, since  $p$  is expressed as ppb ( $10^{-9}$ ),  $k_{SV}$  is  $10^9$  times the value of the slope in a plot vs.  $1/p$  (in ppb). The value  $1/k_{SV}$  defines a characteristic vapour pressure  $p_{1/2} = 1/k_{SV} = 88$  ppb where  $FQR(\infty, p) = 1/2$ .  $P_{1/2}$  is nearly half of the saturated vapour pressure of DNT at room temperature. The fit in Figure 5.10 also gives an intercept ( $b$ ) with error  $\Delta b$ , and we calculate a limit- of- detection ( $LoD$ ) by the common ‘3 errors’ criterion,

$$LoD = \frac{3\Delta b}{K_{SV}} \quad (5.5)$$

Which here leads to a  $LoD = 10.9$  ppb for the detection of airborne DNT. Note however that the plot does not give zero intercept ( $b$ ) as expected, so the SV relation is not a good fit at very low  $p$ . This accounts for the formally evaluated  $LoD$  of 10.9 ppb being rather larger than the clearly visible response to 0.73 ppb in Figure 5.4. Therefore, we followed the conventional approach that was presented in Figure 5.9 to evaluate the  $LoD$  for airborne DNT. Nevertheless, both obtained  $LoDs$  from either the conventional approach or from the SV plot compare favourably to the  $LoD$  value of 30 ppb reported in [1] (shown in table 5.3) for detection of DNT with similar PPV polymer and a fluorimetric developed sensor. The binding constant  $k$  obtained from the non-linear (Langmuir Freundlich isotherm) plot is approximately equal to  $k_{sv}$ .

PPV based polymers are generally sensitive to several nitroaromatic explosive vapours. However, selectivity between different nitroaromatics is not practically desirable, as all of them should be detected. We have therefore not investigated it here, instead we made sure MDMO-PPV is selective between nitroaromatics and their non-nitrated analogue, toluene. Despite toluene's much higher vapour pressure (saturated vapour pressure 29.6 parts-per-thousand (ppt) at ambient temperature [157]), it elicits no fluorescence quenching in MDMO-PPV, cf Figure 5.4. Fluorescence intensity is in fact enhanced (formally expressed as negative  $FQR$ ) under toluene vapour, which agrees with the known property of PPV polymers that they are highly fluorescent in organic solvents [154], even brighter than in solid films, due to separation of fluorophores from mutual interactions. Sensing is hence not compromised by a response to interferants.

#### 5.4.2 Waterborne DNT

As we show in Figure 5.6, the fibres respond to waterborne DNT much faster than for airborne DNT. We assign this to the higher density of the carrier medium. Note, concentrations are given as molar fractions (or partial pressures for airborne DNT, which is equivalent to molar fraction). For any given molar fraction, the density of analyte measured per unit volume is far larger in the denser liquid carrier medium than in the vapour phase, leading to a faster supply of DNT to the fluorophore. Thus, the exponential fit of Figure 5.6 has a time constant of 33 s, significantly shorter than those for airborne DNT as shown in table 5.1.

Figure 5.7 shows a clear quenching response even under 90 ppb waterborne DNT, going far beyond the photophysical degradation under interrogation in the absence of DNT. This indicates a *LoD* significantly below 90 ppb. The photodegradation- compensated  $FQR(c)$  data presented in table 5.2 are fitted to the Langmuir adsorption isotherm Eq. 5.6, as shown in Figure 5.11 using the non-linear fit routine in Origin 2018 software.

$$FQR(c) = \frac{kc}{kc+1} \quad (5.6)$$

where  $k$  is the binding constant that quantifies the analyte/sensitiser binding strength.

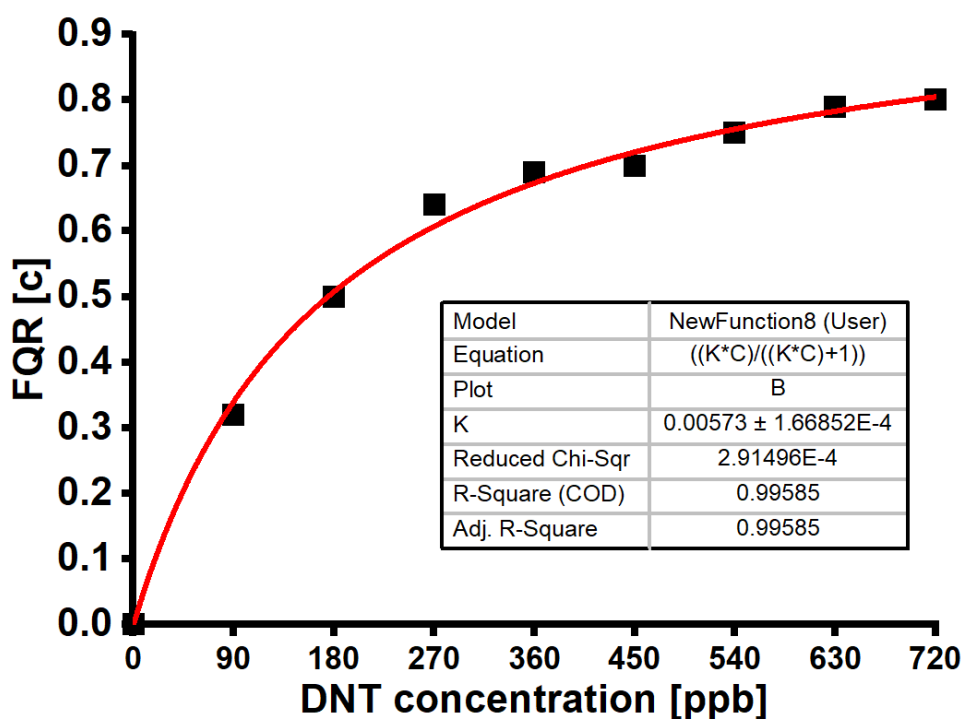


**Figure 5. 9.**  $FQR [c]$  vs. waterborne DNT concentration, solid line is fit to Eq. 5.6.

The non-linear fit gives the binding constant  $k = (5.73 \pm 0.00017) \times 10^6$  which in turn provides the characteristic concentration  $c_{1/2} = 1/k = 174$  ppb.

For further analysis, the  $FQR(c)$  data (table 5.2) are again presented in the Stern- Volmer plot, Figure 5.12.

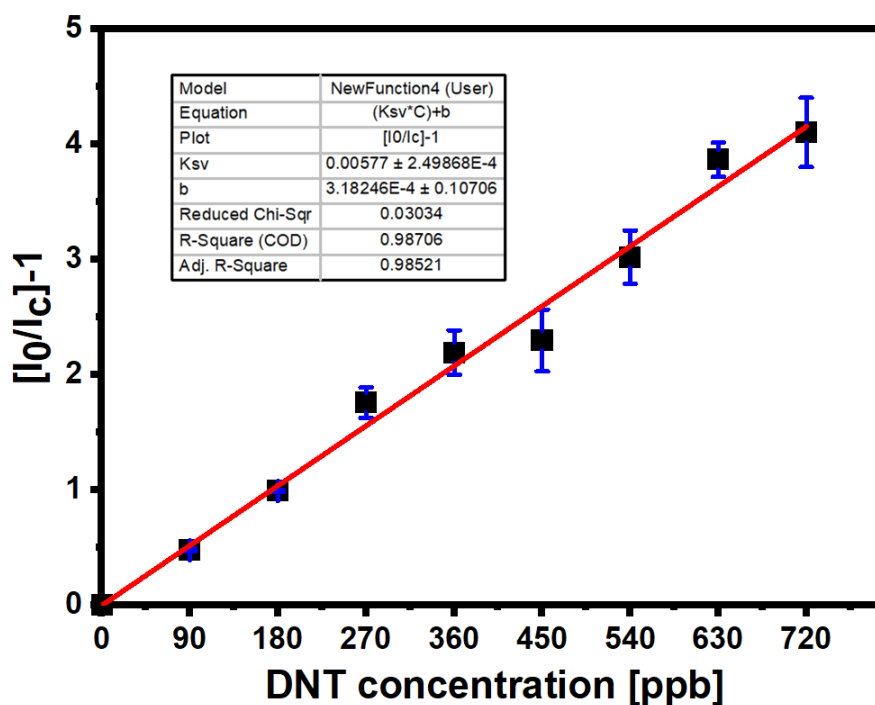


**Figure 5. 10.** Stern-Volmer plot for quenching of MDMO-PPV fluorescence by waterborne DNT in the concentration range (0-720 ppb). Data from table 5.2.

We now find a straight-line fit with near-zero intercept ( $b$ ), indicating full agreement with the Stern Volmer law, albeit we have not explored extremely low concentrations ( $c \ll 1/k_{SV}$ ) as we did for the gas sensing. The Stern Volmer constant  $k_{SV}$  is now  $k_{SV} = (5.8 \pm 0.00025) \times 10^6$ , again in dimensionless format, less than half that in the vapour phase. As  $k_{SV}$  quantifies analyte / sensitiser interaction relative to analyte / carrier medium interaction, the smaller  $k_{SV}$  value shows that it is harder for the sensitiser to extract DNT from water than from air, as the aqueous carrier medium provides better solvation. The  $LoD$  is evaluated in the same way as for airborne DNT,  $LoD = 56$  ppb for the detection of waterborne DNT, less than half as reported in [78] and shown in table 5.3.  $1/k_{SV}$  defines a characteristic concentration  $c_{1/2} = 1/k_{SV} = 172$  ppb which is 107.5 times lower than the solubility level of DNT in water  $\sim 18.5$  ppm at 22 °C [158]. The binding constants from the non-linear fit (Langmuir adsorption isotherm) and the linear fit (SV)  $k_{SV}$  are approximately equal.

Table 5.3 summarises the  $LoDs$  and the  $k_{SV}$  values for a number of DNT fluorimetric sensors using different sensitisers and transducers working in different media. Despite the majority of DNT sensors were tested under saturation vapour pressure at room temperature, our transducer compares favourably to the few sensors that have shown  $LoDs$  for DNT in the air and aqueous media.

**Table 5.3:**

<i>No.</i>	<i>Sensitiser</i>	<i>LoD [ppb]</i>	<i>k<sub>SV</sub></i>	<i>Medium</i>	<i>Ref.</i>
1	PPV derivative (Super Yellow)	30	-----	Air	[1]
2	MDMO-PPV	0.48	1.14x10 <sup>7</sup>	Air	This work
3	Pyrene derivatives	182	5.3 x10 <sup>6</sup>	Water	[160]
4	Dansyl tagged copolymer P(MMA-co-Dansyl-Ala-HEMA) (DCP),	181.8	-----	THF	[161]
6	Conjugated polymer Super Yellow	148	-----	Water	[78]
7	MDMO-PPV	55.7	5.8x10 <sup>6</sup>	Water	This work

*Table 5. 3: Performance parameters of different fluorimetric DNT sensors.*

## 5.5 Conclusions

We have developed a fibre optic transducer with lock-in detection for fluorimetry that can be easily adapted for sensing either airborne or waterborne analytes. Our transducer requires no optical spectrometer. The easy adaptation between sensing in air or water allows us to compare the sensing performance of sensitiser/analyte systems between different carrier media. We investigate this on the example of the nitroaromatic explosive DNT detected by the fluorescent polymer MDMO-PPV, which had previously only been reported in water [87]. In both media, MDMO-PPV fluorescence rapidly decays over time even in the absence of analyte. We minimise this by limiting read-out to short excitation intervals, separated by extended ‘dark’

periods. We also show how to account for the remaining degradation. The sensor response is significantly faster for waterborne than for airborne analyte, which we attribute to the higher density of the liquid *vs.* the gaseous medium. Many previous reports on fluorescence-based detection of explosive vapours only tested under saturation pressure at ambient temperature [9][88][151][162], which does not allow the determination of a Stern Volmer constant ( $k_{sv}$ ) or limit-of-detection ( $LoD$ ), and is unrealistic in practical situations where sources may be distant or concealed. Here, we explored a range of analyte concentrations, expressed in dimensionless (parts-per-billion) format. Despite using the same sensitiser and analyte for both media, the calibration curve for airborne DNT sensing was shown to follow the non-linear Langmuir-Freundlich model, which is typically applied when assuming heterogeneity in the analyte/sensitiser binding sites. On the other hand, calibration curves for waterborne DNT sensing followed the non-linear Langmuir adsorption isotherm, typically applied when considering homogeneous analyte/sensitiser binding sites. Inhomogeneity of the sensitiser binding sites is attributed to sites occupied by airborne traces, such as carbon dioxide, nitrogen dioxide, etc., that may be generated by the air compressor used in the gas sensing setup. The binding constants obtained from non-linear plot (Langmuir adsorption isotherm and Langmuir Freundlich) and SV plots are approximately equal for both air and waterborne DNT. The Stern Volmer constant for fluorescence quenching is larger for airborne rather than waterborne analyte,  $k_{sv}(air) \sim 1.14 \times 10^7$  *vs.*  $k_{sv}(water) \sim 5.8 \times 10^6$ . This indicates better solvation of analyte in water *vs.* air. We found  $LoD$  of 0.48 ppb in air and 56 ppb in water which are  $\sim 62$  times below previously reported  $LoDs$  for DNT sensing with PPV derivatives [1][78] and 3.3 times below  $LoDs$  for DNT sensing with different sensitisers [160][161]. We consider our study of the MDMO-PPV / DNT system as a successful test of our transducer design. The included results in this chapter have been published as “Alshammari, A.H. et. al, Talanta, 2019, 199”

## Chapter 6: Highly Sensitive and Reversible Membrane Films for Cu<sup>2+</sup> Detection

### 6.1 Introduction

Certain metals such as zinc (Zn) [163], manganese (Mn) [164], iron (Fe) [165], copper (Cu) [166], and molybdenum (Mo) [167] are essential for the proper functioning of the human body, as they are involved in various metabolic activities, such as gene transcription and neural signal transmission. In particular, copper ions (Cu<sup>2+</sup>) are deemed one of the essential ions, owing to their vital role in the wide range of biological processes in diverse plant and animal species [53]. Moreover, it is the third most abundant metal ion in the human body after iron (Fe<sup>2+</sup>) and zinc (Zn<sup>2+</sup>) [166]. Consequently, it is vitally important for optimal human health, but its intake must not exceed the allowable level [168]. According to the U.S. Environmental protection Agency (EPA), the ‘potability limit’ of Cu<sup>2+</sup> in the drinking water is 20.5 μM [169]. Cu<sup>2+</sup> intake that exceeds cell requirements is toxic and can cause serious diseases, including kidney or liver diseases, Wilson’s disease [21][22], Menkes syndrome, and Alzheimer’s disease [21]. Hence, detecting Cu<sup>2+</sup> at low concentrations before it reaches the toxicity level is essential, but this requires a highly sensitive sensor, comprising of a sensitiser and a transducer. To date, a number of analytical techniques (transducers) have been developed to quantify the Cu<sup>2+</sup>, such as an electrochemical sensor [170], atom absorption spectroscopy [171], surface plasmon resonance [22], colorimetry [21], and fluorimetry [53][105][166]. Kumaravel and Vasuki [104] have synthesised a pyrazolyl chromene derivative (Probe 1) and a few years later, Pannipara et al. [105] discovered that Probe 1 can be used as a novel fluorimetric sensitiser and also exhibits aggregation induced emission (AIE) activity (the AIE phenomenon was described in Section 2.3.2.3.1). In general, AIE active compounds have contributed widely to the widespread use of organic luminescent materials in different applications, such as optical devices [172], and fluorescent sensors [173]. In their work, Pannipara and colleagues [105] have used AIE active Probe 1 dissolved in a H<sub>2</sub>O-THF mixture (at 8.5:1.5 ratio, v/v) as a sensitiser for the detection of waterborne Cu<sup>2+</sup> and Ni<sup>2+</sup> via fluorescence quenching. However, sensors based on ion detection in a mixture of THF and H<sub>2</sub>O have limited practical applications, and cannot be used for testing drinking water. Moreover, exposure to such solvents is harmful to human health, as they accumulate in the body [174]. In this work, the fluorescence emission of Probe 1 in the aggregated state is extended for the use in a solid film, which can be adopted for detecting waterborne Cu<sup>2+</sup>. Hence, Probe 1 in a film form is used as a sensitiser. It is prepared by

immobilising it in a plasticised PVC phase transfer membrane (described previously in Section 2.3.2.2.1). We used the same lock-in fibre optic transducer described in Chapter 5, Section 5.2.1 (Figure 5.1) to detect the fluorescence quenching of Probe 1 due to the presence of  $\text{Cu}^{2+}$ . The photophysical degradation of Probe 1 when immobilised in PVC is investigated under continuous 405 nm LED light exposure, and also under short pulses of ~20 s duration separated by extended (~ 7 min) dark periods. The required soaking time for the membrane film in the DI-water, the response time and reversibility of the membrane are also examined. The response curve has a good fit to both Langmuir and the Stern-Volmer (SV) models. The SV constant for  $\text{Cu}^{2+}$ /Probe 1 complex is  $k_{sv} = 1.96 \times 10^5 \text{ M}^{-1}$  and the limit of detection (*LoD*) is 0.43  $\mu\text{M}$ , which is well below the potability limit of  $\text{Cu}^{2+}$ . The lock-in fibre optic transducer developed and presented here demonstrates a lower *LoD* compared with a conventional spectrofluorimeter [166] based on the same sensitiser.

## 6.2 Experimental Procedures

### 6.2.1 Synthesis and Materials

A pyrazolyl chromene derivative (Probe 1) shown in Figure 6.1 was obtained from our research partner Mehboobali Pannipara (Department of Chemistry, King Khalid University, Saudi Arabia) who synthesised it according to the synthesis route previously reported by Kumaravel and Vasuki [104]. Tetrahydrofuran, 2-Nitrophenyl octyl ether (NPOE), and polyvinyl chloride (PVC) were obtained from Sigma Aldrich. Copper nitrate hydrate [ $\text{Cu}(\text{NO}_3)_2 \cdot x\text{H}_2\text{O}$ ], nickel chloride hexahydrate [ $\text{Cl}_2\text{Ni} \cdot 6\text{H}_2\text{O}$ ], nickel bromide [ $\text{NiBr}_2$ ], nickel acetate tetrahydrate [ $\text{Ni}(\text{OCOCH}_3)_2 \cdot 4\text{H}_2\text{O}$ ], and ethylenediaminetetraacetic acid (EDTA) were also purchased from Sigma Aldrich.

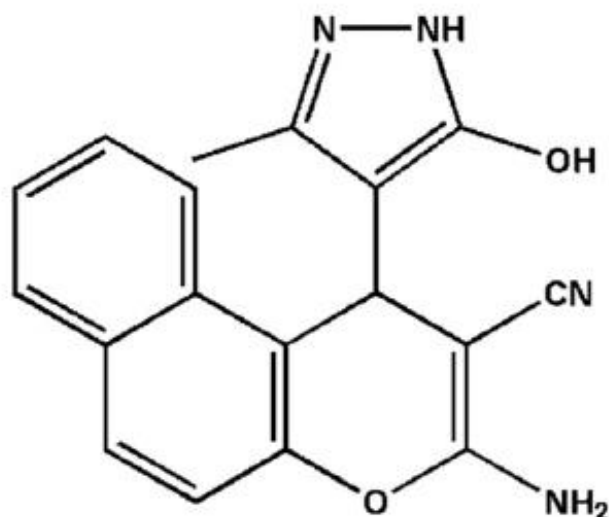


*Figure 6. 1. Chemical structure of pyrazolyl chromene derivative (Probe 1), adopted from [105].*

### 6.2.2 Configuring the Measurement Setup for Waterborne Cu<sup>2+</sup> Detection

The fibre optic fluorimetric sensor setup adopted for waterborne Cu<sup>2+</sup> detection was described in Section 5.2.1. and is shown in Figure 5.1. Similarly, the multimode optical fibre (FT800UMT, Thorlabs) preparation was described in Section 4.2. The preparation of the membrane cocktail (including Probe 1 as a sensitiser) and the dip-coating procedure were described in Section 4.3.2.1. To determine the fluorescence intensity, the optical fibre was coated with the membrane film and was excited under side illumination by a blue (405 nm) LED (LED 405L, Thorlabs), matching the absorption band of Probe 1 [105]. The LED was operated via a rocker switch to control the excitation time. The LED modulation utilised to excite the membrane film and the subsequent detection of the resulting fluorescence aligned with those described in Section 5.2, with the exception of the excitation period, dark intervals between interrogations, and the time constant of low-pass filter within the lock-in amplifier. Specifically, the membrane film was excited for 20 s (instead of a 3 s period for each exciting pulse as used for MDMO-PPV) with longer ‘dark’ intervals (7 min) between interrogations. Since the fluorescence of the membrane film was almost stable under 20 s excitation (duration of a single pulse), the lock-in amplifier filter was set to the maximum available time constant (5 s) rather than the previously adopted 1 s. Setting the filter to 5 s is preferable due to its low noise bandwidth, as described in Section 3.3.1.

For waterborne  $\text{Cu}^{2+}$  and  $\text{Ni}^{2+}$  sensing, the stripped section of optical fibre coated with the sensitised membrane film was passed through DI-water held in a vessel, as shown in Figure 5.1. Next, the DI-water was titrated with aliquots of  $\text{Cu}^{2+}$  or  $\text{Ni}^{2+}$  as described in the following section.

### **6.2.3 Preparation of Solutions for Titrations**

All solutions were prepared in DI-water. Stock solutions needed for titration aliquots, namely copper nitrate hydrate [ $\text{Cu}(\text{NO}_3)_2$ ], nickel chloride hexahydrate [ $\text{Cl}_2\text{Ni}$ ], nickel bromide [ $\text{NiBr}_2$ ], and nickel acetate [ $\text{Ni}(\text{OCOCH}_3)_2$ ] solution, were prepared at 1 mM concentration by dissolving the required amount of their respective salts in DI-water. Aliquots of 1 mM  $\text{Cu}^{2+}$  stock solution were then pipetted respectively into a vessel holding 11 mL of DI-water, resulting in 1, 2, 3, 4, 6, 8, 10, 12, 14, 16, 18, 20, and 22  $\mu\text{M}$   $\text{Cu}^{2+}$  concentrations.

## **6.3 Results and Analysis**

### **6.3.1 Investigating the Membrane Fluorescence Stability**

The experimental findings revealed that the fluorescence of the membrane film coated onto the stripped section of an optical fibre degraded under continuous exposure to light excitation, even in the absence of the analyte. Figure 6.2 shows the fluorescence degradation when the membrane coated on the optical fibre was passed through DI-water and was exposed to continuous LED illumination for 70 min.

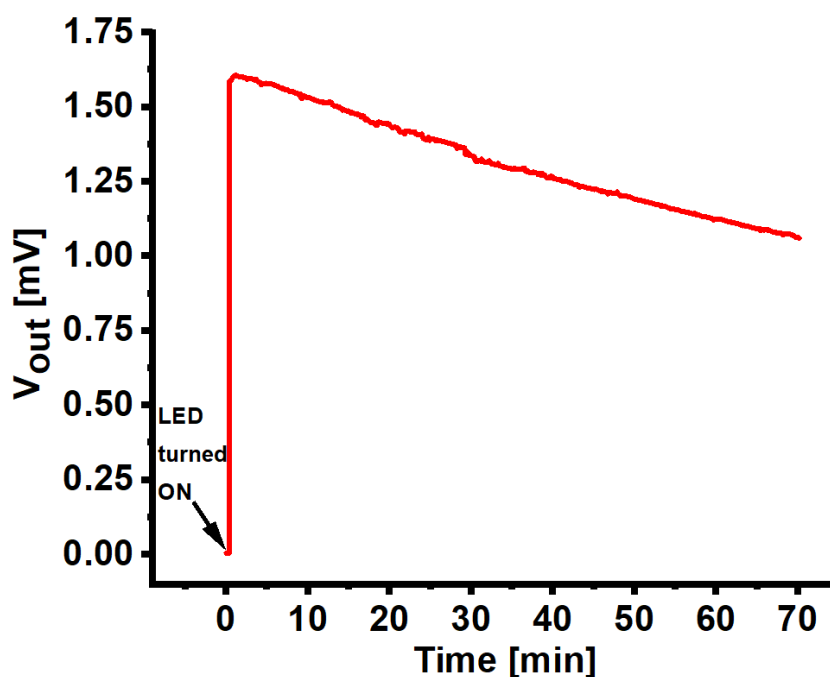
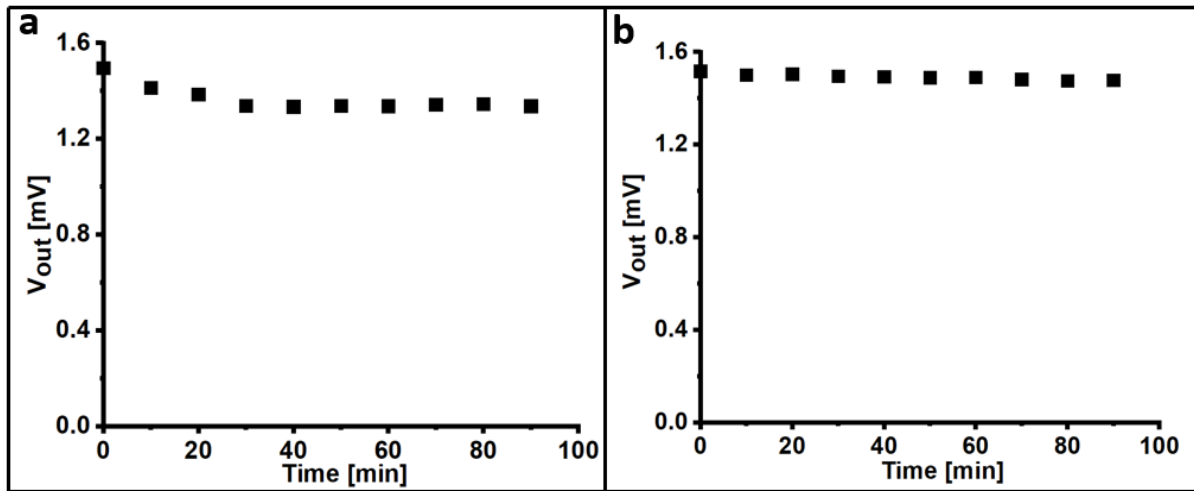


*Figure 6. 2. The output voltage  $V_{out}(c)$  vs time, as a measure of fluorescence intensity produced by the membrane film coated onto an optical fibre and under continuous blue LED excitation. The point at which the LED was switched on is indicated by the arrow.*

The observed fluorescence degradation is attributed to fluorophore exposure to the high intensity of the exciting light under side illumination. In fact, the majority of fluorophores suffer from fluorescence degradation even under low intensity of the exciting light [175].

As significant fluorescence degradation occurs under continuous illumination, the reduction in fluorescence intensity produced by membrane film was minimised by employing short pulses of exciting light ( $\sim 20$  s) separated by much longer dark intervals (approximately 10 min), as shown in Figure 6.3a. The initial fluorescence intensities vary between membrane-coated fibres due to the number of parameters (including length of the fibre coated with the membrane film, thickness of the membrane, intensity and alignment of the excitation source), which will differ across experimental runs. Quantitatively, the observed reduction in fluorescence intensity of the membrane film exposed to short pulses of exciting light (20 s) separated by 10 min dark intervals (overall 90 minutes period) is 10.4% of its initial value (Figure 6.3a), while a 33.3% reduction is measured under continuous illumination for 70 min (Figure 6.2). As shown in Figure 6.3a, the fluorescence intensity declines during the exposure to the first three pulses, after which it remains almost stable. This fluorescence intensity reduction is attributed to the membrane swelling in the water whereby soaking the membrane in the water for sufficient time,

which is 30 minutes in our case, prevents reduction in the fluorescence intensity as shown in Figure 6.3b.



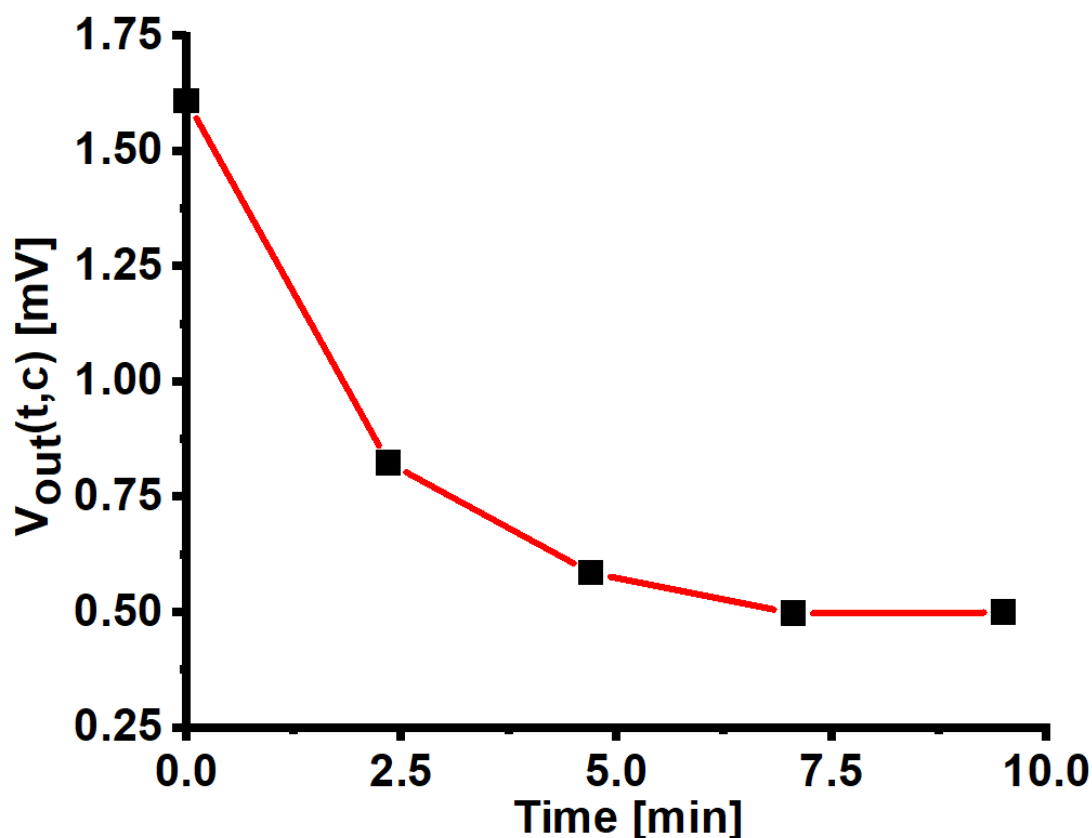
**Figure 6. 3.**  $V_{out}(c)$  vs time, as a measure of fluorescence intensity yielded by the membrane film coated onto an optical fibre. The membrane was excited by a blue LED light and fluorescence was detected for 20 s alternating with 10 min dark intervals. (a) Membrane before soaking; (b) Membrane after soaking in DI-water for 30 min.

Figure 6.3b shows the stability of the fluorescence intensity measurements of a membrane soaked in DI-water for 30 min. Soaking the plasticised PVC membrane containing a fluorophore is well known [96], whereby the optimal soaking time depends on the membrane composition. For our membrane film composition, 30 min soaking time was found to be sufficient because after this soaking time there is no observed fluorescence intensity reduction as shown in Figure 6.3b. Consequently, the stripped section of the optical fibres coated with the membrane films were all soaked for 30 min before carrying out the sensing measurements. During the soaking, the membrane swells due to water absorption. Consequently, some of the active fluorescent units immobilised in the membrane and coated onto the fibre core move further away from the core. This reduces the fluorescence coupling in the fibre, which results in the fluorescence reduction within the first 30 min, or during the first three interrogations, as shown in Figure 6.3a.

Once the soaking time of the membrane in the water becomes known, the fluorescence quenching response time towards  $\text{Cu}^{2+}$  must be obtained before carrying out waterborne  $\text{Cu}^{2+}$  sensing experiment as explained in the next section.

### 6.3.2 Fluorescence Quenching Response Time

The fluorescence quenching response (discussed in Section 2.2.5) of the membrane film to the presence of 22  $\mu\text{M}$  waterborne  $\text{Cu}^{2+}$  lasts for 7 min, after which it is stabilised, as shown in Figure 6.4. This may be the required time for the waterborne  $\text{Cu}^{2+}$  to diffuse into the membrane.



*Figure 6. 4.  $V_{out}(c)$  vs time, as a measure of fluorescence intensity yielded by the membrane film coated onto an optical fibre when exposed to 22  $\mu\text{M}$   $\text{Cu}^{2+}$  concentration.*

The obtained response time is acceptable, and is limited by the membrane thickness, which was measured at  $\sim 1112$  nm by Dektak, as discussed in Section 4.3.2.1. Although reducing the membrane thickness may shorten the response time, it would reduce the fluorescence intensity [143]. For example, a 725 nm thick membrane film has approximately 50% less fluorescence intensity compared to a 1112 nm thick membrane (see Appendix VIII). The required response time for the membrane was applied between waterborne  $\text{Cu}^{2+}$  titrations as presented in the next section.

### 6.3.3 Sensor Calibration for Cu<sup>2+</sup> Sensing

For waterborne Cu<sup>2+</sup> sensing, as previously described, an optical fibre coated with a membrane film was passed through DI-water contained within a vessel. Next, the DI-water was titrated with waterborne Cu<sup>2+</sup> solution aliquots, allowing 7 min between titrations. Fluorescence measurements of the membrane were performed 7 min after each titration by applying 20 s excitation pulses. Aliquots of Cu<sup>2+</sup> were added to cover the full range of concentrations required for the experiment (spanning from 1 μM to 22 μM), as shown in Figure 6.5.

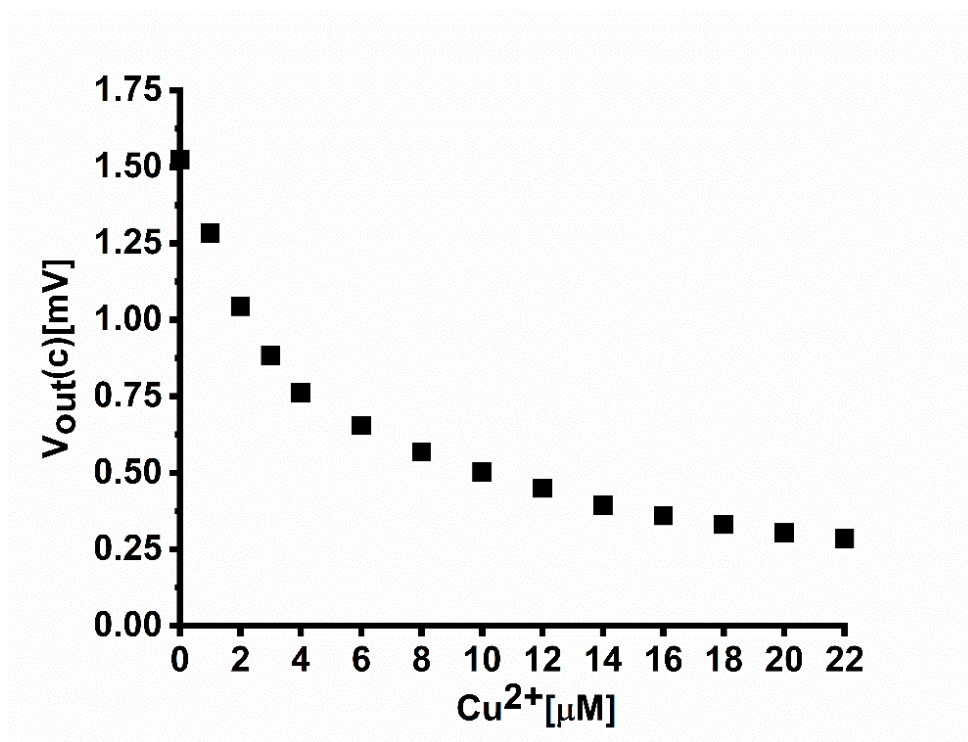


*Figure 6. 5. V<sub>out</sub> as a measure of the fluorescence intensity produced by the membrane film coated onto an optical fibre, as a function of waterborne Cu<sup>2+</sup> solution concentration, ranging from 1 μM to 22 μM.*

The graph in Figure 6.5 confirms that the previously shown fluorescence quenching of Probe 1 [105] in response to waterborne Cu<sup>2+</sup> is still retained when Probe 1 is immobilised in a plasticised PVC membrane and prepared in a film form, rather than dissolving it in a H<sub>2</sub>O-THF mixture (8.5:1.5, v/v). The sensitivity of the membrane film to the presence of waterborne Cu<sup>2+</sup> indicates that the binding sites of Probe 1 within the membrane are as available and active for waterborne Cu<sup>2+</sup> as when Probe 1 is in the aggregated state in solution. Surprisingly, this membrane does not exhibit fluorescence quenching when exposed to very high concentrations of waterborne Ni<sup>2+</sup>, even though, in its aggregated state, Probe 1 has shown a fluorescence

quenching response to both  $\text{Cu}^{2+}$  and  $\text{Ni}^{2+}$ . This finding may be attributed to the binding energy of  $\text{Cu}^{2+}$ /Probe 1 (77.22 kcal/mol) which is greater than that of  $\text{Ni}^{2+}$ /Probe 1 (54.12 kcal/mol) [105]. Consequently, waterborne  $\text{Cu}^{2+}$  can diffuse into the membrane and bind to Probe 1. For this particular sensitiser (Probe 1 shown in Figure 6.1), the metal ion has two bonding possibilities, as it can bind to nitrogen and oxygen of the cyano group and hydroxyl group, respectively, or it can bind to the nitrogen of the cyano group and pyrazole moiety. If the latter is the case, i.e. in solution  $\text{Ni}^{2+}$  is binding to the nitrogen of the cyano group, and pyrazole moiety this may be prevented by preferential binding of  $\text{Ni}^{2+}$  to the plasticiser which also contains nitrogen. Therefore, rather than adopting 2-Nitrophenyl octyl ether as the plasticiser, bis(2-ethylhexyl) sebacate was utilised, as it does not contain nitrogen in its chemical structure. This was essential, as nitrogen in the plasticiser may act as a binding site for  $\text{Ni}^{2+}$ , which would prevent it from reaching Probe 1 binding sites. However, a membrane containing bis(2-ethylhexyl) sebacate plasticiser does not exhibit fluorescence quenching response to different  $\text{Ni}^{2+}$  solutions that were prepared from different  $\text{Ni}^{2+}$  salts (nickel chloride hexahydrate, nickel bromide, and nickel acetate tetrahydrate). In summary, the reason behind the absence of the fluorescence quenching response of Probe 1 towards  $\text{Ni}^{2+}$  solutions remains unexplained.

#### 6.3.4 Quantitative Analysis

The measured  $V_{out}(c)$  value is proportional to the number of fluorescence-active Probe 1 units, while our interest is concentrated on the fluorescence-inactive units (as described in Section 5.3.1), as it is inactive or quenched instead of active units that indicate presence of  $\text{Cu}^{2+}$  (on  $\rightarrow$  off) [126].

Hence, for further analysis, all recorded  $V_{out}(c)$  values as shown in Figure 6.5 were normalised to their initial value  $V_{out}(0)$  and then processed into a  $FQR(c)$ . This was achieved by subtracting the normalised values ( $V_{out}(c)/V_{out}(0)$ ) from 1 to convert from a measure of active fluorophores into a measure of quenched fluorophores [126]. The resulting  $FQR(c)$  is tabulated in table 6.1:

**Table 6.1:**

$Cu^{2+}[\mu M]$	$FQR(c)$
1	0.158
2	0.315
3	0.420
4	0.499
6	0.571
8	0.627
10	0.670
12	0.705
14	0.741
16	0.764
18	0.783
20	0.801
22	0.813

**Table 6. 1:**  $FQR(c)$  vs  $c$  for waterborne  $Cu^{2+}$ .

Since the Langmuir adsorption isotherm (described previously in Section 2.1) and  $FQR(c)$  are both expressed as the fraction of occupied binding sites of the sensitizer by the analyte, we fit the  $FQR(c)$  shown in table 6.1 to the Langmuir adsorption isotherm Eq. 5.6 as shown in Figure 6.6, using the non-linear fit routine in Origin 2018 software.

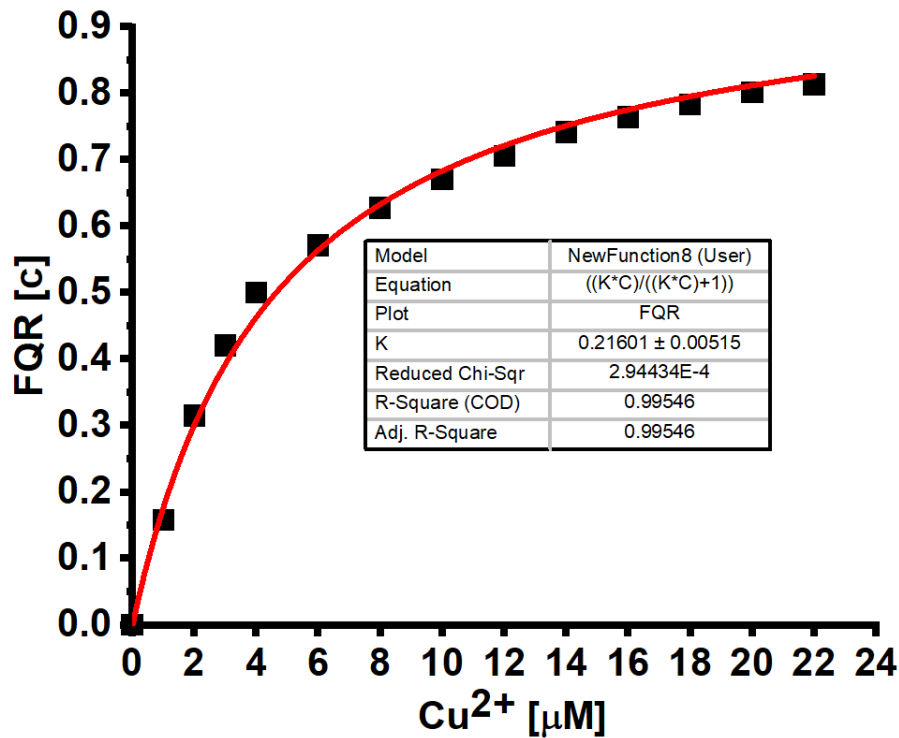


**Figure 6. 6.** *FQR [c] vs. waterborne  $Cu^{2+}$  concentration, the solid line is a fit to Eq. 6.1.*

The non-linear fit gives the binding constant  $k = 2.16 \times 10^5 \text{ M}^{-1}$  which in turn provides a characteristic concentration  $c_{1/2} = 1/k = 4.6 \text{ } \mu\text{M}$  (below the potable limit) [169]. For further quantitative analysis, the response is also presented as an SV plot (as described in Section 2.3.1.3) as shown in Figure 6.7. In the SV plot, fluorescence quenching is expressed as  $\left[ \frac{I_0}{I} - 1 \right]$  this is related to  $FQR(\infty, p)$  by  $\left[ \frac{I_0}{I} - 1 \right] = \frac{FQR(c)}{1 - FQR(c)}$  as discussed in Section 5.4.1. Thus,  $\frac{I_0}{I} - 1$  is plotted against  $Cu^{2+}$  concentration in Figure 6.7, after which a straight line is fitted to the data points to determine the intercept and  $b \pm \Delta b$ . The slope of the straight line is equal to the SV constant  $k_{SV}$ , which quantifies the  $Cu^{2+}$ /Probe 1 binding strength. The slope of the fitted straight line yields  $k_{SV} = 1.96 \times 10^5 \text{ M}^{-1}$ , which in turn provides a characteristic concentration  $c_{1/2} = 1/k_{SV} = 5.1 \text{ } \mu\text{M}$ . From the extensively used equation provided in Section 2.2.1 as Eq. (2.3),  $LoD = 0.43 \text{ } \mu\text{M}$  was obtained, which is considerably below the potability limit. When the same sensitizer was used in its aggregated state to detect waterborne  $Cu^{2+}$  using a conventional spectrofluorimeter, a 3.7 times higher ( $1.61 \text{ } \mu\text{M}$ )  $LoD$  was achieved [105].

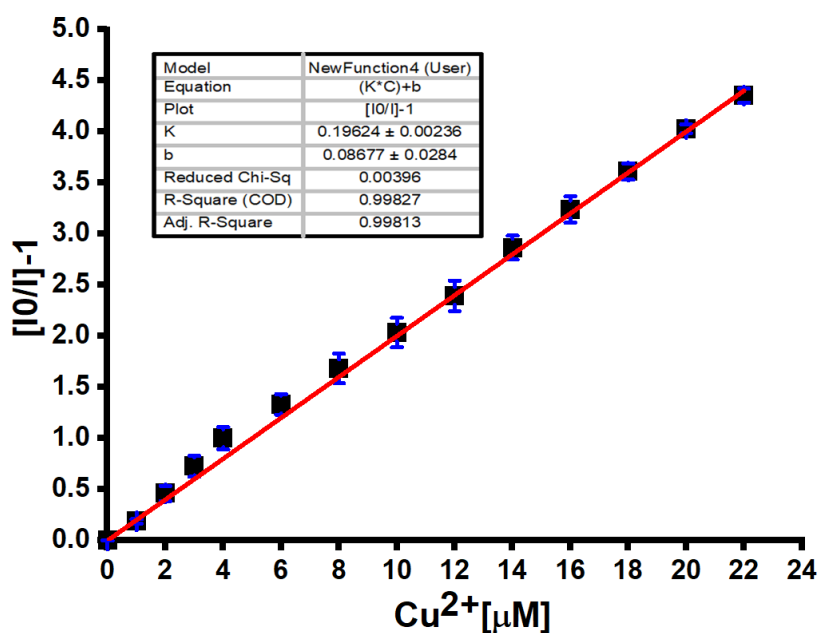


**Figure 6. 7.** SV plot of the fluorescence quenching for the membrane film by waterborne  $\text{Cu}^{2+}$  in the 0–22  $\mu\text{M}$  concentration range.

The Binding constants from non-linear fit (Langmuir adsorption isotherm) and the linear fit (SV) are approximately equal. The  $\text{Cu}^{2+}$  sensing experiments were replicated on a different fibre and their data (*FQR*) were fitted to Langmuir model as shown in Appendix IX.

As long as this sensor is robust and able to detect the waterborne  $\text{Cu}^{2+}$  below its potability limit, it is worth to investigate the reversibility of the sensor as described in the next section.

### 6.3.5 Reversibility and Reusability

Reversibility is a crucial aspect in the application of optical sensors, as a reversible sensor can be reused, significantly reducing costs. To test the reversibility of the membrane developed as a part of the present study, a known metal cation recovery agent (EDTA) was used. Since EDTA dissolves in water with  $\text{pH} = 8$ , NaOH was added to DI-water to increase the  $\text{pH}$  to the required level, as measured by a CyberScan  $\text{pH}$  meter 300. For this purpose, a 1 mM solution of EDTA was prepared by dissolving 292.2 mg of EDTA in 1 L of DI-water (with  $\text{pH} = 8$ ) under vigorous stirring (the preparation of EDTA solution was done by a collaboration with Dr. Ali Alkorbi, University of Sheffield). The graph depicted in Figure 6.8a shows that, when the sensitised and plasticised PVC membrane is exposed to 22  $\mu\text{M}$  of waterborne  $\text{Cu}^{2+}$ , this initially results in fluorescence quenching during the first 7 minutes, but after 10 minutes, a fluorescence enhancement occurs due to the addition of waterborne EDTA, resulting in 22  $\mu\text{M}$ ,

which plateaus after 22 minutes. Figure 6.8b depicts three reversible cycles, commencing with the membrane exposure to 22  $\mu\text{M}$  of waterborne  $\text{Cu}^{2+}$  followed by the membrane exposure to 22  $\mu\text{M}$  EDTA. After completion of each reversible cycle, the membrane is removed from the surrounding water (containing  $\text{Cu}^{2+}$ -EDTA) and rinsed with DI-water. Then, it is bathed again in  $\text{Cu}^{2+}$  and EDTA-free water, after which the previously described processes are repeated.

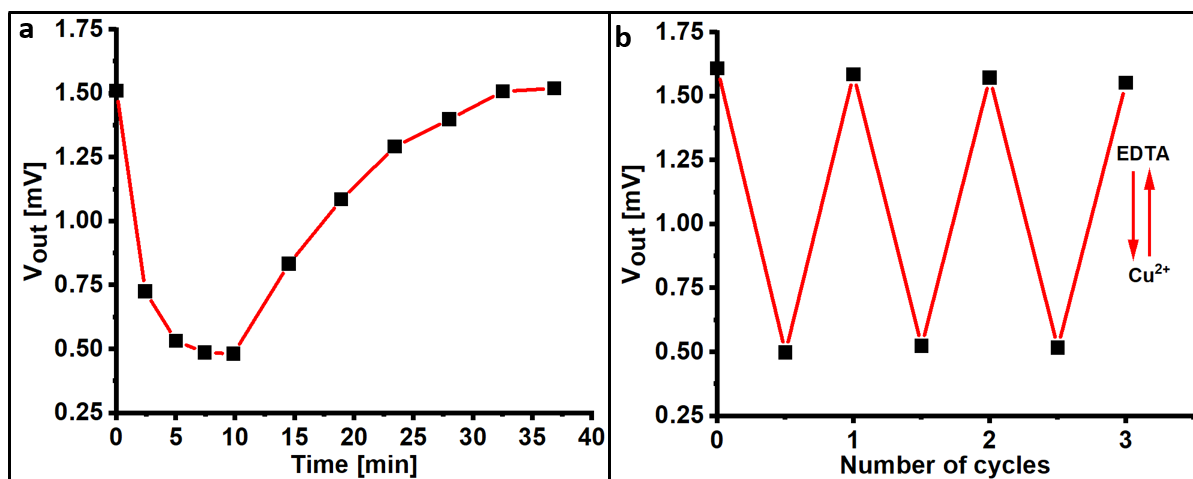


**Figure 6. 8.** (a)  $V_{out}$  as a measure of fluorescence intensity produced by the membrane film when exposed to 22  $\mu\text{M}$  of  $\text{Cu}^{2+}$  for 0–10 min followed by membrane exposure to 22  $\mu\text{M}$  of EDTA as a function of time [min]. (b) Reversible changes in membrane fluorescence intensity after subsequent exposure to 22  $\mu\text{M}$   $\text{Cu}^{2+}$  and 22  $\mu\text{M}$  EDTA.

Membrane reversibility can be attributed to the fact that EDTA chelates waterborne  $\text{Cu}^{2+}$  cations and removes them from the membrane, as the binding affinity of EDTA towards  $\text{Cu}^{2+}$  is greater than that of Probe 1 immobilised in the membrane.

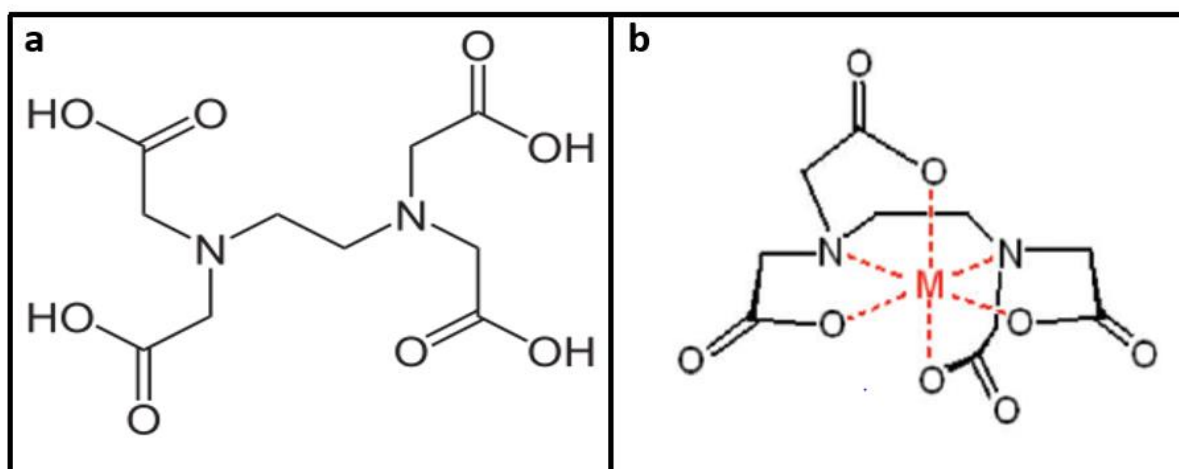


**Figure 6. 9.** EDTA molecule (a) in the solid form and (b) when dissolved in water, allowing it to chelate waterborne  $\text{Cu}^{2+}$  (indicated by M (red) in the EDTA centre)[176].

EDTA has six potential binding sites for metal cations, i.e., two amino and four carboxyl groups, as shown in Figure 6.9a. These binding sites within the ligand form a strong chelating complex with all waterborne cations at a 1:1 ratio. The resulting complex is stable due to multiple EDTA binding sites that surround waterborne  $\text{Cu}^{2+}$ , acting as a cage to isolate cations from the solvent [177], as shown in Figure 6.9b (Note that, M represents  $\text{Cu}^{2+}$ ).

## 6.4 Conclusions

In this chapter, a successful process for transferring the sensitizer Probe 1 from the aggregated state to a solid film sensitizer was described, thereby enabling its use in a solid film to detect waterborne  $\text{Cu}^{2+}$ . Specifically, Probe 1 was prepared in a film formed by immobilising it in a plasticised PVC phase transfer membrane to overcome its hydrophobicity. Under continuous LED light exposure, the photophysical degradation of the membrane is relatively high compared with the negligible degradation obtained when Probe 1 is subjected to short light pulses. The soaking time, response time and the reversibility of the membrane film were also investigated. The response curves result in good fits to both the Langmuir and the Stern-Volmer (SV) theory and the binding constants obtained from these fits are approximately equal. The SV constant  $k_{sv}=1.96 \times 10^5 \text{ M}^{-1}$  was obtained for the  $\text{Cu}^{2+}$ /Probe 1 and the limit of detection (*LoD*) was  $0.43 \mu\text{M}$ , which is considerably below the potability limit. This novel lock-in fibre optic transducer is characterised by a 3.7 times lower *LoD* compared to that of a conventional spectrofluorimeter [105] using the same sensitizer. Finally, we recommend this lock-in approach for application with similar sensitizers that exhibit the AIE to be converted into solid plasticised PVC membrane films, avoiding the exposure to the harmful organic solvent during the analyte sensing experiment.

# Chapter 7: Low Cost, High Sensitivity Detection of Waterborne Al<sup>3+</sup> Cations and F<sup>-</sup> Anions via the Fluorescence Response of a Morin Derivative Dye.

## 7.1 Introduction

Aluminium is commonly used in food packing, clinical tools, food processing equipment, kettles and water pipes. Metallic aluminium is slightly soluble in aqueous media in the form of its Al<sup>3+</sup> cation [23]. Intake of Al<sup>3+</sup> into the human body may cause serious diseases, including Alzheimer's [24][178] and Parkinson's [24] diseases. The concentration of Al<sup>3+</sup> in drinking water is therefore regulated, with a 'potability limit' of 7.4 μM [3]. Consequently, a number of analytical techniques have been developed to quantify Al<sup>3+</sup> in water, including spectrophotometric [179], fluorimetric [50][52], and electrochemical [99] sensors. An important Al<sup>3+</sup> selective ionophore is 2',3,4',5,7-Pentahydroxyflavone, known as 'morin', its structure was shown earlier in Figure 2.11. Section 2.3.2.2.2. Morin is known to selectively complex with waterborne Al<sup>3+</sup>, forming a [morin:Al<sup>3+</sup>] complex. Morin has therefore been used both as an ionophore in electrochemical Al<sup>3+</sup> sensors [99] and in 'off → on' fluorescent sensors [98] because the [morin:Al<sup>3+</sup>] complex shows green- coloured fluorescence, while uncomplexed morin shows weak fluorescence. The [morin:Al<sup>3+</sup>] complex has poor solubility in buffered aqueous solution [52] and absorbs light between 390 nm to 440 nm [98] and emits a broad band between 450 nm and 550 nm [100] as discussed earlier in Section 2.3.2.2.2. Embedding morin in a permeable membrane which allows the transfer of Al<sup>3+</sup> enables it to be used as an Al<sup>3+</sup> sensor [98]. Alternatively, Kopacz [102] has described a chemical modification of morin into a sodium salt of morin sulfonic acid, NaMSA, Figure 7.1a, this dissolves well in water (dissociating into Na<sup>+</sup> / MSA<sup>-</sup>), without the need to promote solubility by adding organic solvents, as is required for some other ion- selective fluorophores, *e.g.* [15][53][180][181]. NaMSA can still be immobilised in a permeable membrane [52], but preparation of such membranes is difficult and time- consuming. Plasticised PVC membranes often show slow response [53] and may suffer from dye leaching [182] as described earlier in Section 2.3.2.2.1. In this work , we take advantage of the good solubility of NaMSA in water to extend the use of NaMSA as an Al<sup>3+</sup>- selective 'off → on' fluorescent sensitiser [183] when immobilised in a phase transfer membrane to a morin derivative, instead using the NaMSA dissolved in water, avoiding the need for membrane preparation. We find that dissolved NaMSA retains its ability to complex with Al<sup>3+</sup> into a fluorescent [MSA<sup>-</sup>:Al<sup>3+</sup>] complex, Figure 7.1b. We quantify Al<sup>3+</sup>

in water samples by fluorimetry using dissolved NaMSA. Instead of a conventional spectrofluorimeter, we adopted a fibre-optic fluorimeter with LED excitation and lock-in amplification which has been described previously [126] for solution-based fluorimetry. We establish a limit-of-detection (*LoD*) for  $\text{Al}^{3+}$  below its potability limit, a high figure-of-merit for the fibre-optic instrument, and quantify  $\text{Al}^{3+}$  in a few example samples using the standard addition method [184]. Further, we take advantage of the possibility to recover NaMSA-based  $\text{Al}^{3+}$  sensors after use by treatment with concentrated fluoride ( $\text{F}^-$ ) solutions [183]. We develop this into a complementary ‘on  $\rightarrow$  off’ fluorescent sensor for fluoride by prior ‘activation’ of the dissolved NaMSA with  $\text{Al}^{3+}$  to form the fluorescent  $[\text{MSA}^-:\text{Al}^{3+}]$  complex that we then titrate with aliquots of fluoride to gradually turn its fluorescence off. Fluoride is another interesting analyte because small doses of fluoride are beneficial to bones and teeth [26], but higher doses can be detrimental causing fluorosis and urolithiasis [185]. Fluoride in drinking water is therefore subject to a potability limit of  $79 \mu\text{M}$  [3]. Again we demonstrate a *LoD* well below the legal potability limit. In summary, we show the ‘complementary’ fluorimetric detection of two relevant ions ( $\text{Al}^{3+}$  and  $\text{F}^-$ ) in water below their respective potability limits, using the same dye for both, together with a low-footprint instrument. The results in this chapter were published recently as “Alshammari, A.H. et al, *Analytica Chimica Acta*, 2020, 1105”.

## 7.2 Experimental

### 7.2.1 Synthesis and Materials

Morin was purchased from Sigma Aldrich and chemically modified into the water-soluble sodium salt of morin sulfonic acid (NaMSA) by Faiz et al. [52] following the route reported by Kopacz [102]. From an initial 10g of morin approximately 7g of NaMSA was obtained. Figure 7.1 shows the chemical structure NaMSA, and the complex that NaMSA forms with  $\text{Al}^{3+}$ . Acetone, Hydrochloric acid 37% (HCL), aluminum nitrate nonahydrate ( $\text{Al}(\text{NO}_3)_3 \cdot 9\text{H}_2\text{O}$ ), sodium fluoride (NaF) and sodium chloride (NaCl) were obtained from Sigma aldrich.

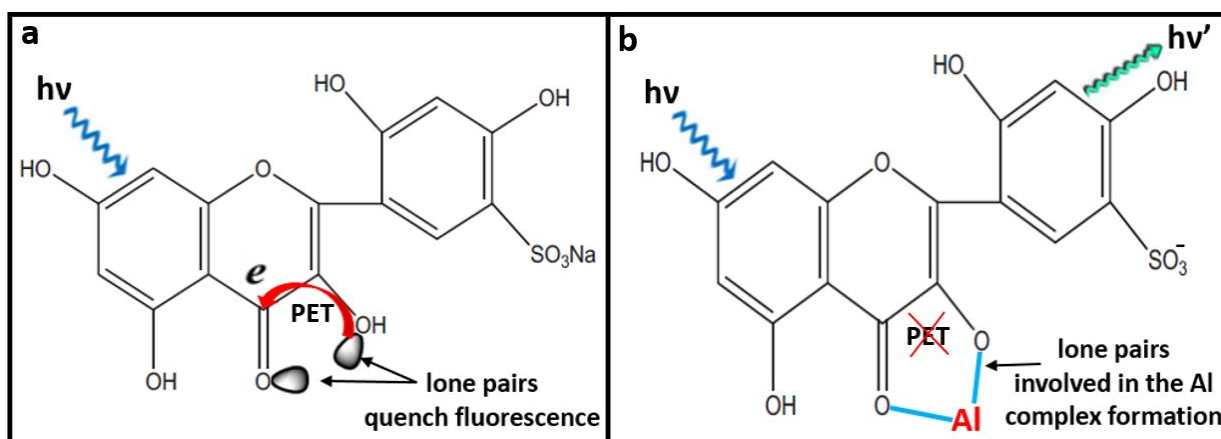


**Figure 7. 1.** a.) Chemical Structure of NaMSA when dissolved in water, this dissociates into  $\text{MSA}^-$  and  $\text{Na}^+$ . b.) Structure of  $[\text{MSA}^-:\text{Al}^{3+}]$  complex that forms in aqueous solution when  $\text{Al}^{3+}$  is added to dissolved NaMSA.

### 7.2.2 Overview of Measurement Setup

Figure 7.2 gives an overview over our fibre optic lock-in fluorimeter. The instrument is adapted from earlier work as shown in chapter 5 [126] Figure 5.1. Here, instead of exciting the sensitiser film coated on the stripped section of the fibre by the LED light, we excite the sensitiser (NaMSA) solution. A mixture of the analyte sample and the fluorophore solution is held in a bespoke cuvette (Figure 7.3) fitted with an optical fibre that has been treated to pick up fluorescence and guide it to a photodiode (PD) circuit for measurement. Fluorescence is excited using a 405 nm LED (LED 405 L, Thorlabs) at a distance of  $\sim 1.2$  cm from the surface of the liquid in the cuvette at approximately  $90^\circ$ . The LED is driven in the same way as detailed in Section 5.2. The optical power from the LED was measured using an optical power meter (PM100D, Thorlabs) at a distance of 1.2 cm and measured to be 5.9 mW. This power when divided by the exposed surface area of the power meter sensor to give a power density of  $83.1 \text{ W/m}^2$ .

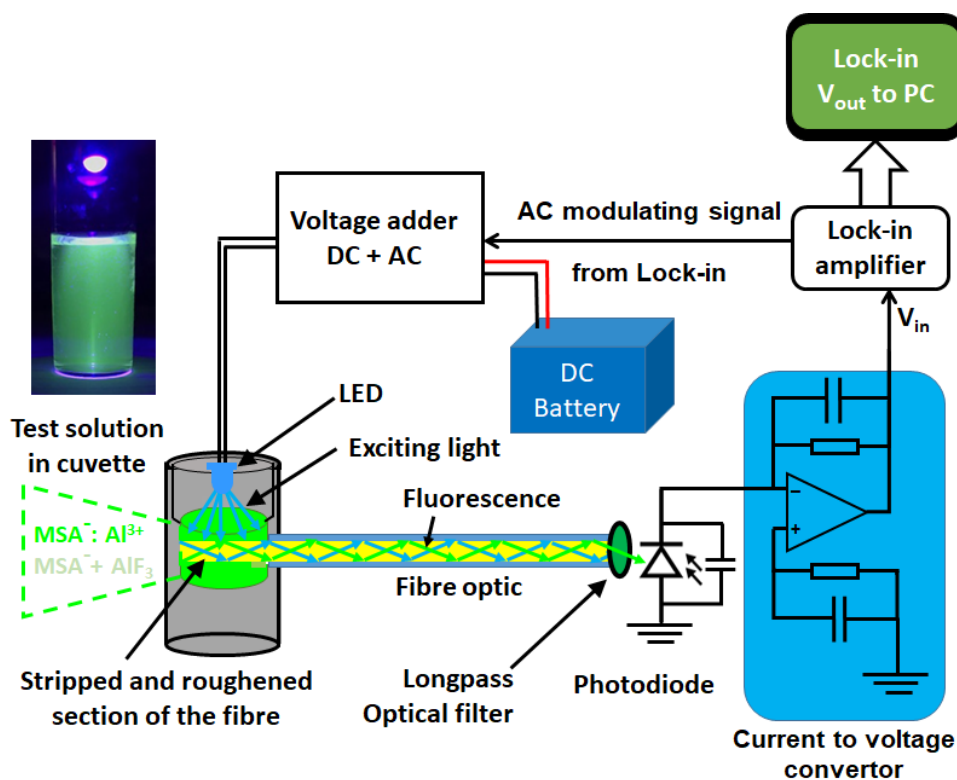


*Figure 7. 2. Schematic diagram of our fibre- optic lock-in fluorimeter.*

A longpass optical filter with an edge at 488 nm (as shown in Figure 3.12) was inserted before the PD (Figure 3.13) to block the 405 nm excitation while allowing most of the morin fluorescence to pass. The PD output current was converted into a voltage, amplified and then coupled into the Anfatec digital lock-in as explained in Section 5.2. The lock-in provides a DC output voltage,  $V_{out}$ , that is proportional to the AC component of the light intensity,  $I$ , picked up by the fibre.  $V_{out}(t)$  is recorded over time by a bespoke LabVIEW routine, an example is shown in Figure 7.4.

### 7.2.3 Preparation of Optical Fibres

We used multimode optical fibres (FT1500UMT, Thorlabs) with a 1.5 mm silica core diameter and a 50  $\mu\text{m}$  transparent polymer cladding, coated in a non-transparent outer 'buffer'. 10 cm of fibre was cleaved from a reel and a 1 cm length of the fibre core was exposed at one end, cleaned and dried as previously described in Section 4.2. Since a smooth exposed fibre core picks up only very little fluorescence, the stripped section of the fibre was roughened all around

its surface using a Dremel ‘Corded Multi- Tool 3000’ rotary tool as described previously in Section 4.2.

### 7.2.4 Cuvettes

Bespoke cuvettes were manufactured by the University of Sheffield workshop, as shown in Figure 7.3. Two cuvettes were made and while identical in shape, one was made of transparent PMMA as commonly used for conventional fluorimetric cuvettes, and the other was made of stainless steel. The stainless cuvette was polished on the inside so that its walls act as a mirror to increase the amount of fluorescence picked up by the fibre.

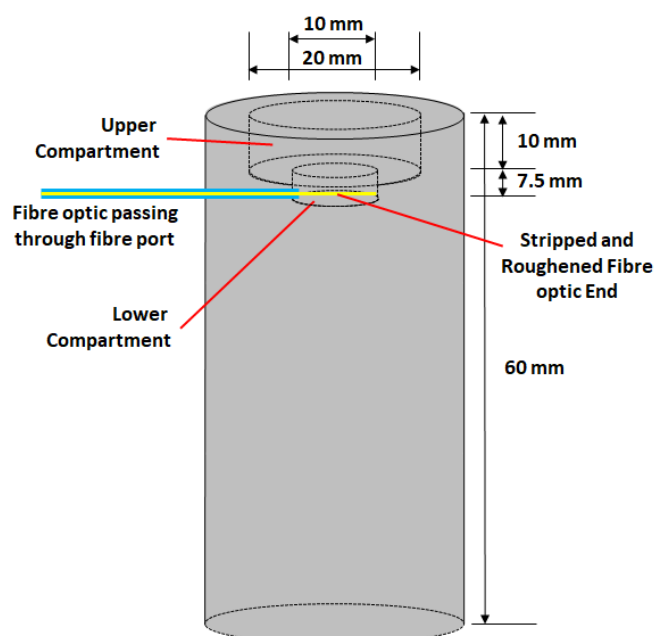


*Figure 7. 3. Design of bespoke cuvettes, manufactured in the University of Sheffield workshop. Cuvettes were made either of transparent material (PMMA), or a reflective material (stainless steel). The bottom compartment where the fibre is fitted has a capacity of 300  $\mu$ L while a wider upper compartment holds liquid in excess of 300  $\mu$ L.*

### 7.2.5 Preparation of Solutions

All solutions were prepared in deionised water of resistivity 15 M $\Omega$ .cm at 20 °C as measured by our DI Water system that first had been acidified by adding hydrochloric acid (HCl) to adjust the pH to 5, as measured by a CyberScan pH meter 300. An acidic medium is required to prevent the formation of Al<sup>3+</sup> hydroxide complexes [98] that would compete with MSA<sup>-</sup>/Al<sup>3+</sup>

complexation. Solutions of  $\text{Al}^{3+}$  (from aluminium nitrate nonahydrate),  $\text{F}^-$  (from NaF), and  $\text{Cl}^-$  (from NaCl) for titration aliquots were prepared at a few concentrations (100  $\mu\text{M}$ , 1 mM, 10 mM, 100 mM) by dissolving the required amount of their salts in 200 solution of the NaMSA fluorophore that were prepared in acidified water. For standard addition tests, three  $\text{Al}^{3+}$  solutions with concentrations in the order of the potability limit were prepared by a co-worker who was not otherwise involved with the work reported here. Concentrations were noted but not reported to the worker undertaking the standard addition test, but only labelled as ‘A, B, C’. To prepare the  $\text{Al}^{3+}$  sensitive solution, 200  $\mu\text{M}$  solution of the NaMSA fluorophore was prepared in acidified water. A sample of the 200  $\mu\text{M}$  fluorophore solution in acidified water was kept in the lab for two months to check the lifetime of the fluorophore. To ‘activate’ the NaMSA solution for fluoride sensing, a solution of  $[\text{Al}^{3+}:\text{MSA}^-]$  complex was prepared by adding 15.8  $\mu\text{L}$  of 1 mM  $\text{Al}^{3+}$  solution to 300  $\mu\text{L}$  of 200  $\mu\text{M}$  NaMSA solution, resulting in a  $\sim 50$   $\mu\text{M}$  solution of  $[\text{Al}^{3+}:\text{MSA}^-]$  complex. We used an excess of dissolved NaMSA over  $\text{Al}^{3+}$  to make sure all the  $\text{Al}^{3+}$  ions complex with  $\text{MSA}^-$ , with no remaining free  $\text{Al}^{3+}$ . Again, some of the activated solution was kept in the lab for two months to check the lifetime of the solution. To test the effect of the simultaneous presence of fluoride and aluminium, a 1 mM solution of  $\text{F}^-$  (from NaF) and a 1 mM of  $\text{Al}^{3+}$  (from  $\text{Al}(\text{NO}_3)_3$ ) were prepared in acidified NaMSA solution (pH = 5). Then these solutions were mixed in a 3:1 ratio of fluoride solution: aluminium solution by volume, resulting in a (0.75 mM  $\text{F}^-$  / 0.25 mM  $\text{Al}^{3+}$ ) solution.

### 7.2.6 Titrations for Sensor Calibration

The  $\text{Al}^{3+}$  sensor was calibrated using 300  $\mu\text{L}$  of NaMSA solution, which was transferred into the PMMA or stainless steel cuvettes, fitted with a roughened optical fibre, as described above. For titration, small amounts of  $\text{Al}^{3+}$  solutions that were dissolved in NaMSA solution were pipetted into the filled cuvettes and mixed by gentle stirring. Then the same volume as that just added was removed from the cuvette via pipette, in order to keep the solution volume at exactly 300  $\mu\text{L}$ , which is  $\sim 3$  cm above the roughened fibre. This was done in order to ensure that the excitation geometry remained the same throughout the titration series. The new analyte concentration,  $c$ , was calculated from known volumes and concentrations of stock solutions. Pipetting was repeated to cover a range of concentrations from below  $\mu\text{M}$  to 10 mM. Fluorescence was excited continuously by the LED and the intensity was monitored over time via the lock-in amplifier output,  $V_{out}$ , and recorded by bespoke LabView software. The  $\text{F}^-$  sensor was calibrated in a similar manner to the  $\text{Al}^{3+}$  sensor calibration, only now we filled the cuvettes

with  $[\text{Al}^{3+}:\text{MSA}^-]$  complex solution instead of NaMSA solution. Then we added  $\text{F}^-$  aliquots to cover a range of concentrations from 10  $\mu\text{M}$  to 6 mM. The fluorescence was excited and monitored exactly as in the  $\text{Al}^{3+}$  sensor calibration.

An example of the  $V_{out}(t)$  trace resulting from a typical titration as described above is shown in Figure 7.4.

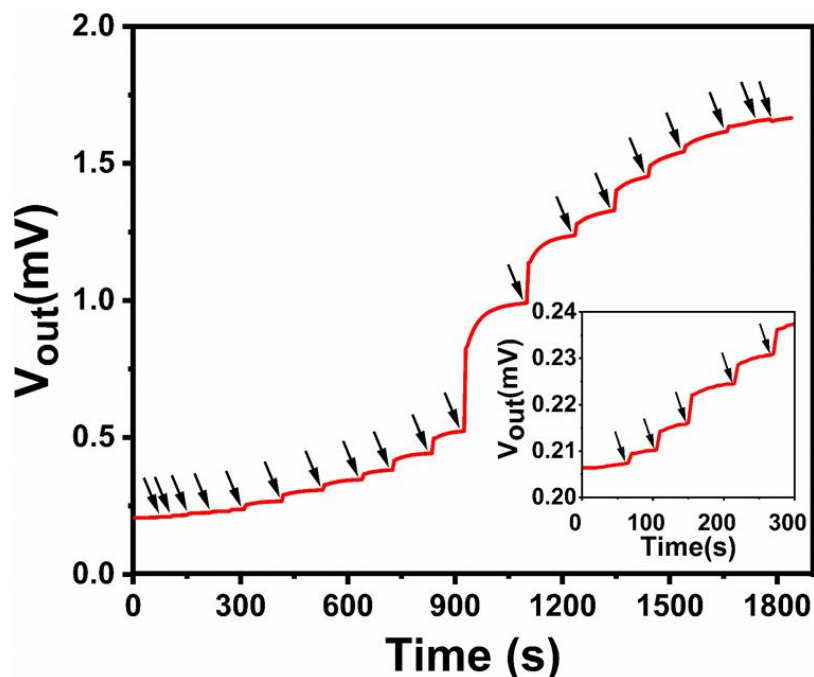


**Figure 7. 4.** Example of a  $V_{out}$  vs time series for NaMSA solution under stepwise additions of  $\text{Al}^{3+}$  aliquots. Every arrow indicates a titration step, i.e. addition of an  $\text{Al}^{3+}$  aliquot. Inset: Magnification of the short time / low  $\text{Al}^{3+}$  concentration region. Note, the high increase in  $V_{out}$  at  $\sim 1000$  s corresponds to high  $\text{Al}^{3+}$  addition compared with other additions.

Although morin is an ‘off  $\rightarrow$  on’ dye, we note that even at  $t = 0$ , i.e. when the concentration  $c = [\text{Al}^{3+}] = 0$ ,  $V_{out}(0) > 0$ . The initial  $V_{out}(0)$  results from two contributions: namely, some of the exciting light still passes through the longpass optical filter between the fibre and the PD (no fluorescence involved), and uncomplexed  $\text{MSA}^-$  in solution is very weakly fluorescent (i.e. there is some fluorescence in the absence of analyte). We call the former ‘background’, and the latter ‘zero analyte fluorescence’. Taken together they give the initial  $V_{out}(0)$ . Note, ambient light does not contribute to  $V_{out}(0)$  as the lock-in discards all signals at frequencies other than its reference frequency, making it ‘blind’ to ambient light.

For  $\text{Al}^{3+}$  standard addition titrations, the roughened fibre section was fitted into the PMMA cuvette, then 300  $\mu\text{L}$  of 200  $\mu\text{M}$  NaMSA was pipetted into the cuvette. The background  $V_{out}(c = 0)$  was recorded, then the cuvette was washed three times with DI water, refilled with NaMSA solution and the background  $V_{out}(c = 0)$  was recorded again; and this was repeated number of times. Results were very similar on each occasion with  $V_{out} \sim 0.185 \text{ mV} \pm 0.02$ , and were averaged to give an average background for subsequent correction. The cuvette was again washed three times with DI water, then 300  $\mu\text{L}$  of unknown solution concentration  $c_{sample}$  was pipetted into the cleaned cuvette, and  $V_{out}(c = c_{sample})$  was recorded. Finally, the solution of  $c_{sample}$  was titrated with aliquots of  $\text{Al}^{3+}$  solution of known concentration to increase  $c_{sample}$  by  $c_{added}$  in steps of 10  $\mu\text{M}$ , and  $V_{out}(c = c_{sample} + c_{added})$  was recorded after each titration.

### 7.2.7 Data Analysis

The  $V_{out}(t)$  data recorded during titrations shown in Figure 7.4 were converted into  $V_{out}(c)$  by relating the time to ion concentration,  $c$ . As a first step in the data analysis for ‘off  $\rightarrow$  on’ fluorescence, we calibrated by adding increasing concentration,  $c$ , of  $\text{Al}^{3+}$  to a non- fluorescent NaMSA solution, we adjust all  $V_{out}(c)$  data by subtracting the initial  $V_{out}(0)$  prior to further analysis, hence  $V_{out}(0) = 0$  by definition. On the other hand, for ‘on  $\rightarrow$  off’ fluorescence when we add aliquots of  $\text{F}^-$  to fluorescent  $[\text{MSA}^-:\text{Al}^{3+}]$  complex, we adjust by subtracting the final  $V_{out}(c \rightarrow \infty)$  from all data. Practically,  $V_{out}(c \rightarrow \infty)$  was taken at a concentration much larger than  $c_{1/2} = 1/k$ , see below. Hence,  $V_{out}(c \rightarrow \infty)$  becomes 0 by definition. For further analysis of  $V_{out}(c)$  which is proportional to  $I(c)$ , where  $I(c)$  is the fluorescence intensity, we assume the fraction  $\theta(c)$  of the dye complexed by the analyte at an analyte concentration  $c$  is given by a Langmuir-like relationship (described previously in Section 2.1):

$$\theta(c) = \frac{kc}{(kc+1)} \quad (7.1)$$

With  $0 \leq \theta(c) < 1$ , and  $k$  is a stability constant which quantifies the ‘strength’ of the analyte / sensitiser interaction.

Properties of  $\theta(c)$  are  $\theta(0) = 0$ ,  $\theta(c) \approx kc$  for  $c \ll 1/k$ ,  $\theta(c_{1/2}) = 1/2$  for  $c_{1/2} = 1/k$ , and  $\theta(c \rightarrow \infty) \rightarrow 1$  as discussed in Section 2.1.  $V_{out}(c)$  will depend both on  $\theta(c)$ , and a number of parameters specific to a particular experimental setup (length and roughness of the fibre, geometry and

type of cuvette, intensity and alignment of excitation source, gain in the transimpedance amplifier, etc...) which will differ between different experimental runs. However, with the help of Eq. 7.1 we can account for these parameters and determine the stability constant,  $k$ , and a limit-of-detection ( $LoD$ ).

For ‘off  $\rightarrow$  on’ fluorescence, the dye in the absence of analyte is non-emissive (or weakly emissive but this is accounted for by the aforementioned prior subtraction of  $V_{out}(0)$ ), but becomes emissive in the presence of analyte. Here this was the case for sensing  $Al^{3+}$  with dissolved NaMSA.  $V_{out}(c)$  is given by the relative fraction of complexed dye,  $\theta(c)$ :

$$V_{out}(c) = V_{\infty} \theta(c) = V_{\infty} \frac{kc}{kc+1} \quad (7.2)$$

Wherein  $V_{\infty} = V_{out}(c \rightarrow \infty)$ . To determine  $k$ , we therefore fitted the experimental  $V_{out}(c)$  data to Eq. 7.2 using the non-linear fit routine in Origin 2018 software. To evaluate the limit-of-detection ( $LoD$ ) for an ‘off  $\rightarrow$  on’ dye, we considered only the data for ‘small’ concentrations *i.e.*  $c \ll 1/k$ , where we expect a linear relationship, as  $\theta(c) \approx kc$  for  $c \ll 1/k$ . For  $c \ll 1/k$  we fitted with  $V_{out}(c) = mc + b$  with slope  $m$  and intercept  $b \pm \Delta b$ , with  $b$  expected to overlap zero within at most  $1.96 \Delta b$  (on a 5% significance level). The analyte concentration at the  $LoD$ ,  $c_{LoD}$ , is then given by Eq. 2.3 in Section 2.2.1.

To determine unknown  $Al^{3+}$  concentrations we used the standard addition method [184]. We first subtract the previously established average background from all  $V_{out}$  data (*cf.* 7.2.6), then plot background corrected  $V_{out}(c_{add})$  vs  $c_{add}$ , fit a straight line and identify the previously unknown  $c_{sample}$  as the negative of the intercept of the fitted straight line with the (negative)  $c_{add}$  - axis.

For ‘on  $\rightarrow$  off’ fluorescence the dye in an analyte-free medium emits and adding analyte makes the dye becoming non-emissive. Here this was the case for the sensing of  $F^{-}$  with  $[Al^{3+}:MSA^{-}]$  complex. Now,  $V_{out}(c)$  is given by the fraction of remaining  $[Al^{3+}:MSA^{-}]$  complex,  $1 - \theta(c)$ :

$$V_{out}(c) = V_0 [1 - \theta(c)] = \frac{V_0}{(kc+1)} \quad (7.3)$$

Wherein  $V_0 = V_{out}(c = 0)$ . To determine  $k$ , we therefore fitted the experimental  $V_{out}(c)$  data to Eq. 7.3 using the non-linear fit routine in Origin 2018 software. To evaluate the  $LoD$  for an ‘off  $\rightarrow$  on’ dye we again consider only data at ‘small’ concentrations,  $c \ll 1/k$ , where Eq. 7.3 can be approximated by Eq. 7.4:

$$V_{out}(c) \approx V_0(1 - kc) \Rightarrow 1 - V_{out}(c)/V_0 \approx kc \quad \text{for } c \ll 1/k \quad (7.4)$$

We therefore plotted  $1 - V_{out}(c)/V_0$  vs.  $c$  for  $c \ll 1/k$  and again fitted a straight line  $mc + b$  with slope  $m$  (here expected to equal  $k$ ) and intercept  $b \pm \Delta b$ , and using Eq. 2.3 again to find  $c_{LoD}$ . Note the different units of  $m$  and  $b$  between ‘off  $\rightarrow$  on’ and ‘on  $\rightarrow$  off’ evaluation.

Finally, we quantify the quality of a transducer by defining a figure-of-merit ( $FoM$ ) as explained earlier in Section (2.2.3). The  $FoM$  tells the contribution of the transducer to lowering  $LoD$  independent of the contribution of  $k$ .

## 7.3 Results and Discussion

### 7.3.1 Sensor Calibration for ‘off $\rightarrow$ on’ $Al^{3+}$ Sensors

Figure 7.5 (a and b) show the measured  $V_{out}(c)$  for the titration of fresh NaMSA solutions in acidified water as function of  $c = [Al^{3+}]$  using different cuvettes. The data in Figure 7.5c. is using the same stock solution as in Figure 7.5 (a and b) but with a two month old NaMSA solution, as described in 7.2.5 and also using a PMMA cuvette.

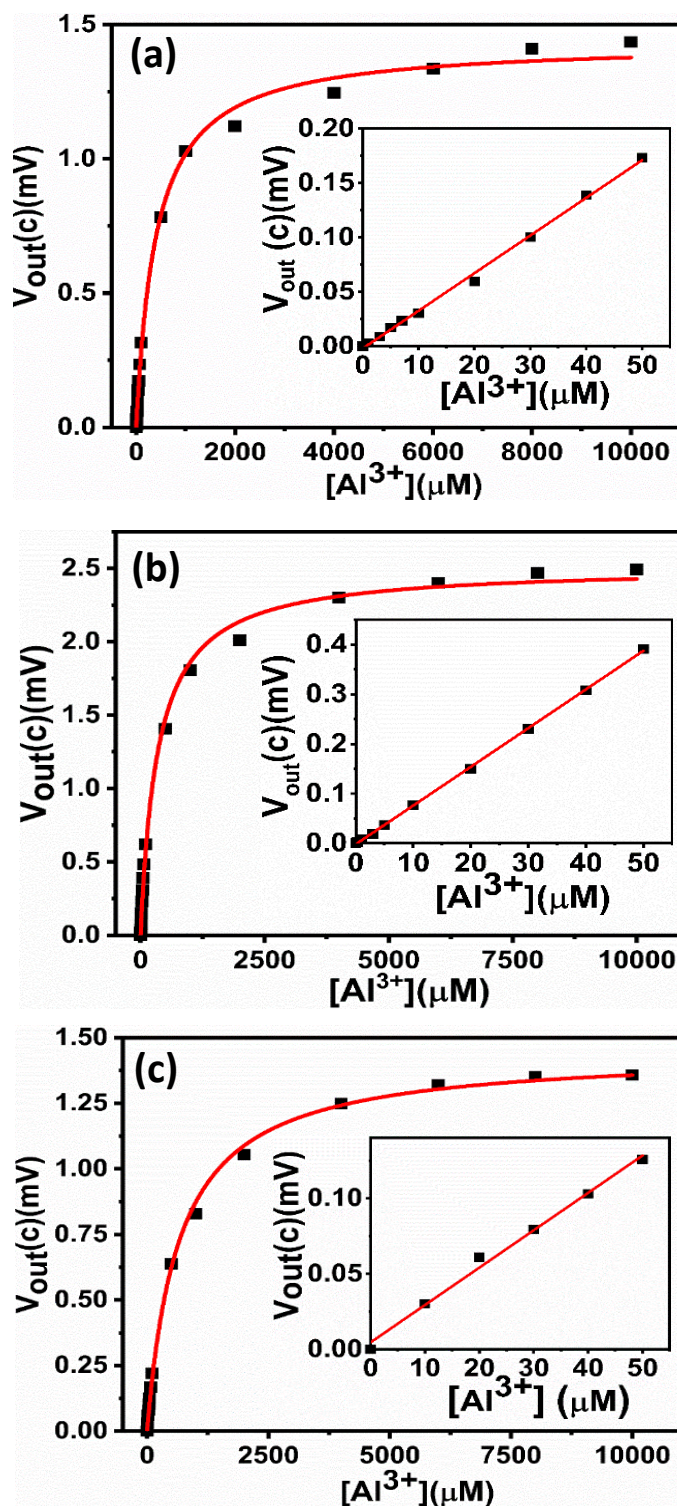


**Figure 7. 5.**  $V_{out}(c)$  as a measure of the fluorescence intensity of NaMSA in (DI-water/ HCl),  $pH = 5$ , shown against  $Al^{3+}$  concentration from  $1 \mu M$  to  $10 \text{ mM}$ , the solid line is the fit to the data using Eq. 7.2 . The insets magnify the linear regime for  $[Al^{3+}]$  up to  $50 \mu M$ . a.) fresh  $200 \mu M$  NaMSA solution and using the PMMA cuvette, b.) fresh  $200 \mu M$  NaMSA solution and using the stainless steel cuvette, and c.) two months old NaMSA solution and using the PMMA cuvette.

Figure 7.5 clearly confirms that the previously known response of morin (or its derivative, NaMSA) to waterborne  $Al^{3+}$  is retained when NaMSA is dissolved in water rather than immobilised in a membrane. In the absence of  $Al^{3+}$ , the NaMSA undergoes an intermolecular PET, therefore it has a weak fluorescence. The PET occurs when the exciting light induces the lone pair electrons on the donor oxygen (hydroxyl group) in the free ligand to transfer to the fluorophore, reducing the fluorescence emission (Figure 7.1a) as described previously in Section 2.3.1.2. Upon the presence of the waterborne  $Al^{3+}$ , those lone pairs will be involved in complex formation with the  $Al^{3+}$ , which suppresses PET and enhances the fluorescence (Figure 7.1b). The response characteristics are fitted well by the theoretical model, Eq. 7.2, with the best match in the linear regime  $c \ll 1/k$ , which is the most significant for analysis. The resulting sensor parameters are evaluated as described in the ‘Data Analysis’ section 7.2.7, and are summarised in table 7.1.

**Table 7.1:**

	$V_{\infty} [mV]$	$k [M^{-1}]$	$m [M^{-1} mV]$	$b [mV]$	$\Delta b [mV]$	$LoD [\mu M]$
PMMA cuvette 200 $\mu M$ NaMSA	1.43 $\pm 0.02$	2460 $\pm 160$	3460 $\pm 60$	-0.0021	0.001	0.9
Steel cuvette 200 $\mu M$ NaMSA	2.51 $\pm 0.03$	2800 $\pm 180$	7790 $\pm 50$	-0.0018	0.0011	0.4
PMMA cuvette old 200 $\mu M$ NaMSA	1.45 $\pm$ 0.02	1520 $\pm 80$	2470 $\pm 100$	0.0025	0.0032	3.84

**Table 7. 1:** Parameters obtained from fitting the data in Figure 7.5 to Eq. 7.2.

As expected, the association constants,  $k$ , are similar to each other between the different experimental protocols for fresh NaMSA solution while  $k$  for the two months old solution is relatively lower.  $k$  is a property of the interaction of the dye and the analyte in a given medium and should therefore not depend on the details and parameters of experiments undertaken to establish it. We find  $k \approx 2.5 \times 10^3 \text{ M}^{-1}$  for the  $[\text{MSA}^-:\text{Al}^{3+}]$  complex when both complex partners are dissolved in water. This is about 5 times smaller than  $k$  for the  $[\text{morin}:\text{Al}^{3+}]$  complex for (unmodified) morin in a cellulose membrane at a pH in the range 4 to 5 [98]. Further, we find that unlike  $k$ , the  $LoD$  does depend on experimental protocol. Using a reflective stainless steel cuvette leads to a higher  $V_{\infty}$ , as defined in Eq. 7.2, and therefore an improvement in  $LoD$ . To the best to our knowledge, reflective cuvettes have not been used in any fluorimetric system. We therefore recommend the use of reflective cuvettes as a measure to improve  $LoD$  with fibre optic instruments, an opportunity inaccessible to conventional fluorimetry. However, even a conventional PMMA cuvette allows the detection of waterborne  $\text{Al}^{3+}$  with a  $LoD$  of  $0.9 \mu\text{M}$ , below the potability limit of  $7.4 \mu\text{M Al}^{3+}$ , despite the relatively small  $k$ . When using aged solution and a PMMA cuvette we detected waterborne  $\text{Al}^{3+}$  with a  $LoD$  of  $3.8 \mu\text{M}$ , still below the potability limit of  $7.4 \mu\text{M Al}^{3+}$ , despite the relatively small  $k$ . The  $LoD$  reported here is similar to previous work on morin and NaMSA immobilised in a membrane [52][98][183]. Here we find value for the  $FoM$ , as defined previously by Eq. 2.4 in section 2.2.3, of  $FoM \approx 300$  for our fibre optic Lock In transducer, which compares very favourably to  $FoM \approx 30$  reported for conventional fluorimetry of  $\text{Al}^{3+}$  with morin in [98].

### 7.3.2 Determining $\text{Al}^{3+}$ with Standard Addition Method

Three samples, known as ‘A, B, C’, were analysed in our fluorimeter using the standard addition method. Each sample was tested 4 times. The actual concentrations (calculated from the NaMSA mass and water volume) were not known to the experimenter beforehand, as solutions A, B, C had been prepared independently by a different worker, who willfully but secretly chose concentrations overlapping the potability limit of  $\text{Al}^{3+}$  of  $7.4 \mu\text{M}$ . The resulting standard addition plots are shown below in Figure 7.6.

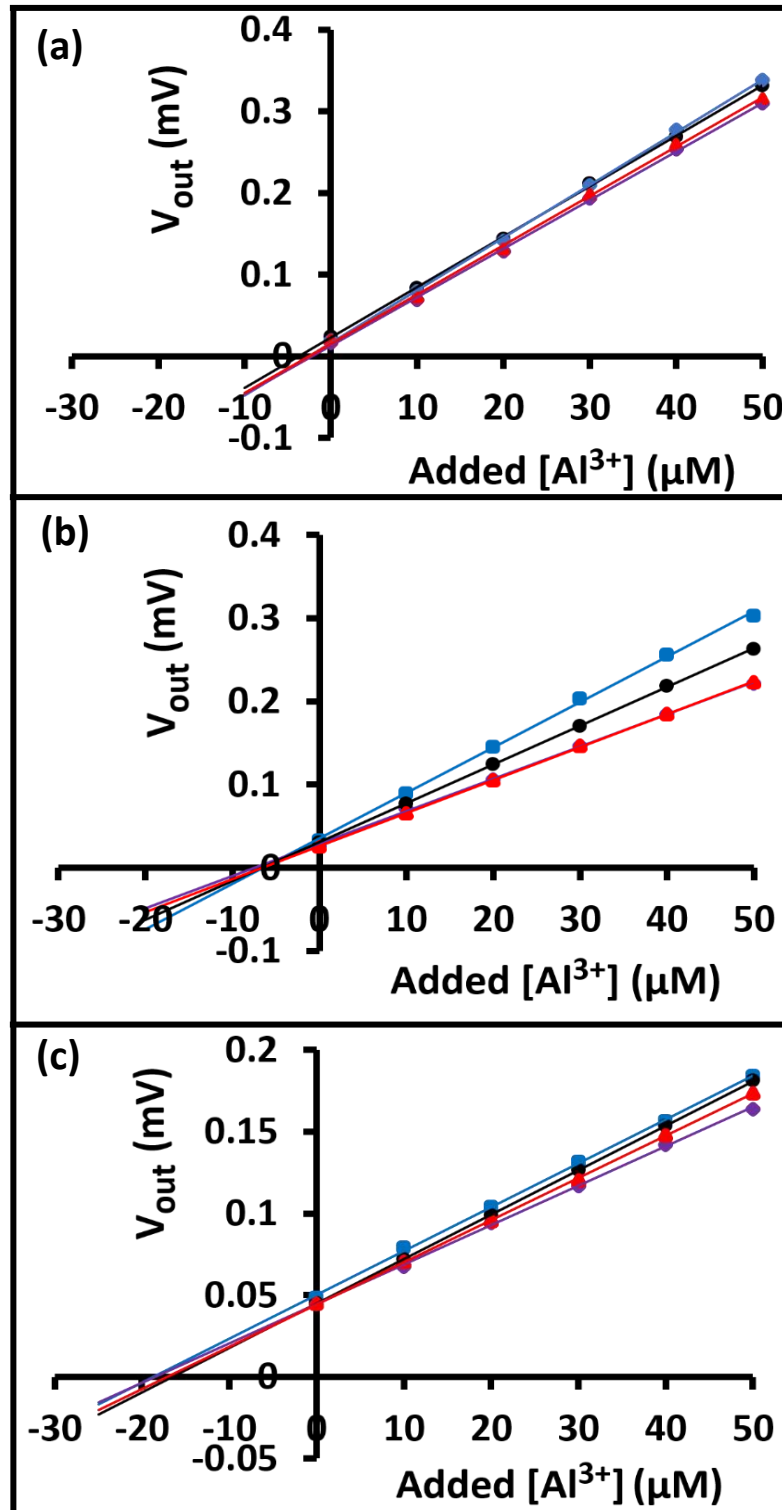


**Figure 7. 6.** The standard addition plots,  $V_{out}$  vs  $c_{add}$ , fitted with straight lines, a.) for sample A b.) for sample B and c.) for sample C. The experiment for each sample was repeated 4 times, but graph a and b show less than 4 lines or 4 experiments because of the overlaying data

The  $\text{Al}^{3+}$  concentration in each unknown sample was determined from the standard addition plots as described in 7.2.7. Table 7.2 summarises all the results and compares them to the actual concentrations, which were revealed after the analysis was completed.

As intended, the standard addition method provides an *in-situ* calibration to account for the small differences between the different fibres, which show as slightly different slopes in the standard addition plots. Nevertheless, the concentrations of samples A, B, and C were determined consistently and repeatedly, with an error similar to the *LoD* of 0.9  $\mu\text{M}$ , independent of the actual magnitude of  $[\text{Al}^{3+}]$ . As the potability limit for  $\text{Al}^{3+}$  is 7.4  $\mu\text{M}$ , we conclude that dissolved NaMSA as used in our instrument is capable of assessing the potability of water with respect to  $\text{Al}^{3+}$ .

**Table 7.2:**

<i>Sample A</i>	<i>Measured concentration [<math>\mu\text{M}</math>]</i>	<i>Actual concentration [<math>\mu\text{M}</math>]</i>
1	3.7	3.85
2	2.6	
3	2.2	
4	2.6	
<i>Sample B</i>	<i>Measured concentration [<math>\mu\text{M}</math>]</i>	<i>Actual concentration [<math>\mu\text{M}</math>]</i>
1	6.4	7
2	6.5	
3	6.6	
4	7.4	
<i>Sample C</i>	<i>Measured concentration [<math>\mu\text{M}</math>]</i>	<i>Actual concentration [<math>\mu\text{M}</math>]</i>
1	18.6	17.3
2	16.6	
3	17.0	
4	18.5	

*Table 7. 2: The results of the standard addition experiments to determine the  $\text{Al}^{3+}$  concentration of samples A, B, C, compared to the actual (calculated) value, which was revealed to the experimenter only after the measurement*

### 7.3.3 Sensor Calibration for ‘on→ off’ F<sup>-</sup> Sensors

Figure 7.7 shows the measured  $V_{out}(c)$  for the titration of solutions of  $[MSA^-:Al^{3+}]$  complex in acidified water of pH = 5, *i.e.* after ‘activation’ of NaMSA by  $Al^{3+}$  as described in section 7.2.5, as function of  $c = [F^-]$  using different cuvettes. Figure 7.7c repeats the experiment shown in Figure 7.7 (a and b) with a NaMSA solution that was aged for two months.

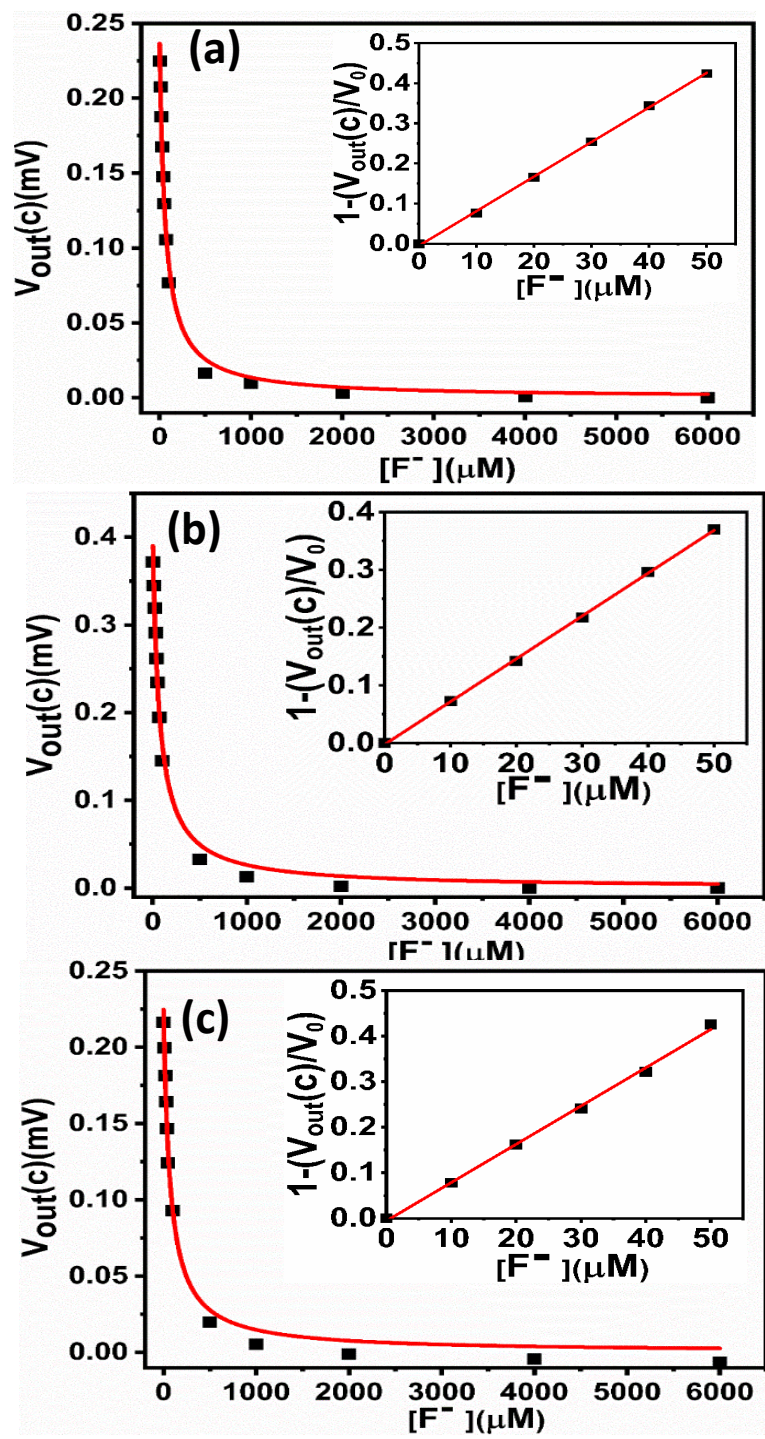


**Figure 7. 7.**  $V_{out}(c)$  as a measure of the fluorescence intensity of NaMSA dissolved in (DI water / HCl), pH = 5, and activated with 50  $\mu M$  of  $Al^{3+}$ , shown against  $F^-$  concentration from 10  $\mu M$  to 6 mM. The solid line is a fit to the data using Eq. 7.3. The insets show the linear regime of  $1-(V_{out}(c)/V_0)$  vs  $F^-$  for concentrations up to 50  $\mu M$ . The three plots are a.) fresh 200  $\mu M$  NaMSA solution as measured in the PMMA cuvette, b.) fresh 200  $\mu M$  NaMSA solution as measured in the stainless steel cuvette, and c.) two months old NaMSA measured in a PMMA cuvette.

Figure 7.7 clearly shows that after ‘activation’ of the NaMSA with  $\text{Al}^{3+}$  to form the  $[\text{MSA}^-:\text{Al}^{3+}]$  complex, this complex then serves as an ‘on  $\rightarrow$  off’ sensor for fluoride ions,  $\text{F}^-$ . NaMSA was previously considered a dye for the detection of  $\text{Al}^{3+}$  that can be recovered by adding high concentrations of  $\text{F}^-$  for de-complexation of  $[\text{MSA}^-:\text{Al}^{3+}]$  by  $\text{F}^-$  [183]. Here we show that NaMSA is in fact a dye suitable for the sensing of either  $\text{Al}^{3+}$ , or  $\text{F}^-$ , whichever is of interest.  $\text{F}^-$  sensitivity can be activated at will, simply by prior addition of  $\text{Al}^{3+}$ , as described in section 7.2.5. Figure 7.7c. shows that once NaMSA has been activated with  $\text{Al}^{3+}$ , it remains active for fluoride sensing even after two months of ageing under ambient conditions.

For quantitative analysis, the response characteristics were fitted to Eq. 7.3;  $LoDs$  were evaluated from the plots according to Eq. 7.4, as shown as insets to Figure 7.7 (a to c), as discussed in section 7.2.7. The results are summarised in table 7.3.

**Table 7.3:**

	$V_0[mV]$	$k [M^{-1}]$	$m [M^{-1}]$	$b$	$\Delta b$	$LoD [\mu M]$
PMMA cuvette 200 $\mu\text{M}$ NaMSA	0.236 $\pm 0.006$	16400 $\pm 1500$	8610 $\pm 10$	-0.0047	0.00322	1.1
Steel cuvette 200 $\mu\text{M}$ NaMSA	0.390 $\pm 0.010$	13800 $\pm 1290$	7410 $\pm 70$	-0.0023	0.00212	0.9
PMMA cuvette aged 200 $\mu\text{M}$ NaMSA	0.225 $\pm 0.006$	14210 $\pm 1470$	8400 $\pm 197$	-0.0084	0.006	2.1

**Table 7.3:** Parameters such as the de-complexation constant  $K$ , slope  $m$ , and  $LoD$  obtained from fitting data in Figure 7.7(a to c) to Eq. 7.4.

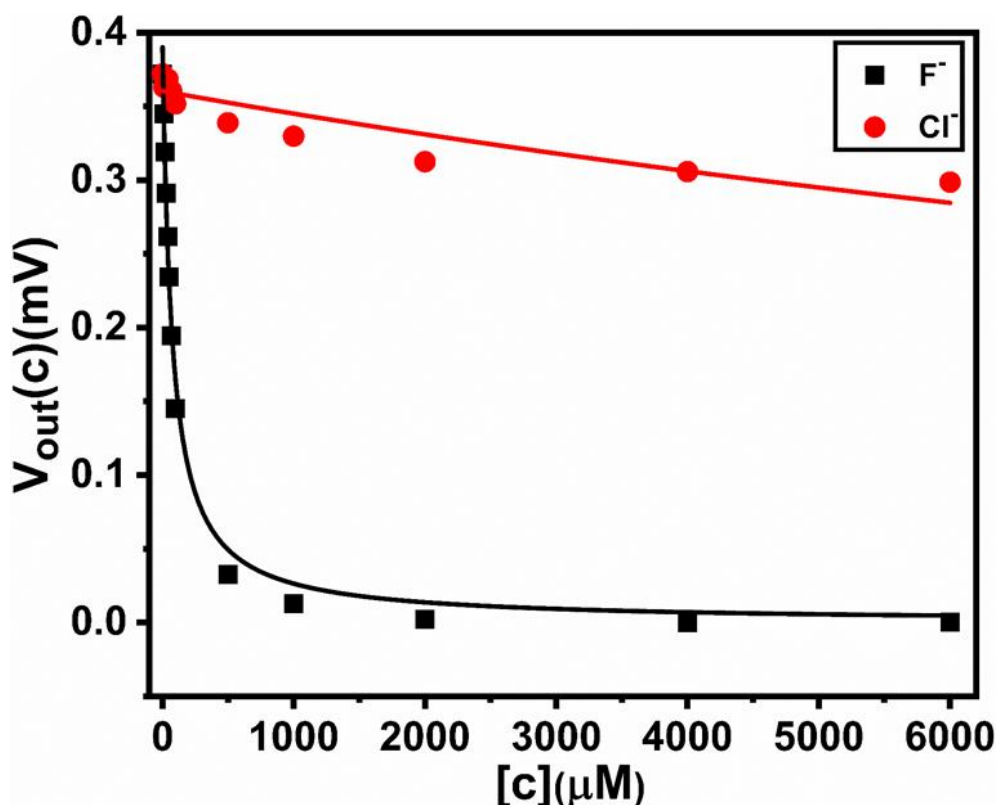
The constant  $k$  shown in table 7.3 is the equilibrium constant for de-complexation of the  $[\text{MSA}^-:\text{Al}^{3+}]$  complex in the presence of  $\text{F}^-$ . Unsurprisingly, this is different from the  $k$  previously determined which describes the complexation of  $\text{MSA}^-$  with  $\text{Al}^{3+}$  in the absence of  $\text{F}^-$ . The de-complexation constant is larger, but again it is similar between different

experimental conditions, as expected. Again, the  $k$  for aged NaMSA solution activated with  $\text{Al}^{3+}$  is similar to that obtained from fresh solution. NaMSA solution is stable for at least 2 months. Also, the use of a reflective (stainless steel) cuvette again improves the  $LoD$  compared with the PMMA cuvette. The  $LoDs$  reported for fresh and aged  $[\text{MSA}^-:\text{Al}^{3+}]$  solution are far below the potability level for  $\text{F}^-$  in drinking water,  $79 \mu\text{M}$  [3]. As long as an excess of  $\text{MSA}^-$  is activated by  $\text{Al}^{3+}$  by its addition into the fluoride-sensitive  $[\text{MSA}^-:\text{Al}^{3+}]$  complex, the solution can be used as a  $\text{F}^-$  sensor with an  $LoD$  well below the potability limit. Note, we have  $c_{1/2} = 1/k \approx 70 \mu\text{M}$ , hence the highest tested  $\text{F}^-$  concentration of  $6 \text{ mM}$  was almost 100 times larger than  $c_{1/2}$ . It is therefore fair to approximate  $V_{out}(c \rightarrow \infty)$  by  $V_{out}(6\text{mM})$ , cf. 7.2.7.

Given the price of the initial morin dye (£72.60 for 10 g) and the yield of 7g NaMSA from 10g morin, each £1 spent on morin dye would provide sufficient solution to fill ~ 4000 cuvettes with  $300\mu\text{L}$  of  $200 \mu\text{M}$  NaMSA solution. We therefore recommend disposal after single use rather than attempting to re-use dye solutions.

#### 7.3.4 Selectivity for Fluoride over Chloride

We have tested the selectivity of the  $[\text{MSA}^-:\text{Al}^{3+}]$  complex as a sensitiser for fluoride by considering chloride as a potential interferant. In Figure 7.8 we compare fluoride and chloride titrations under otherwise identical conditions.



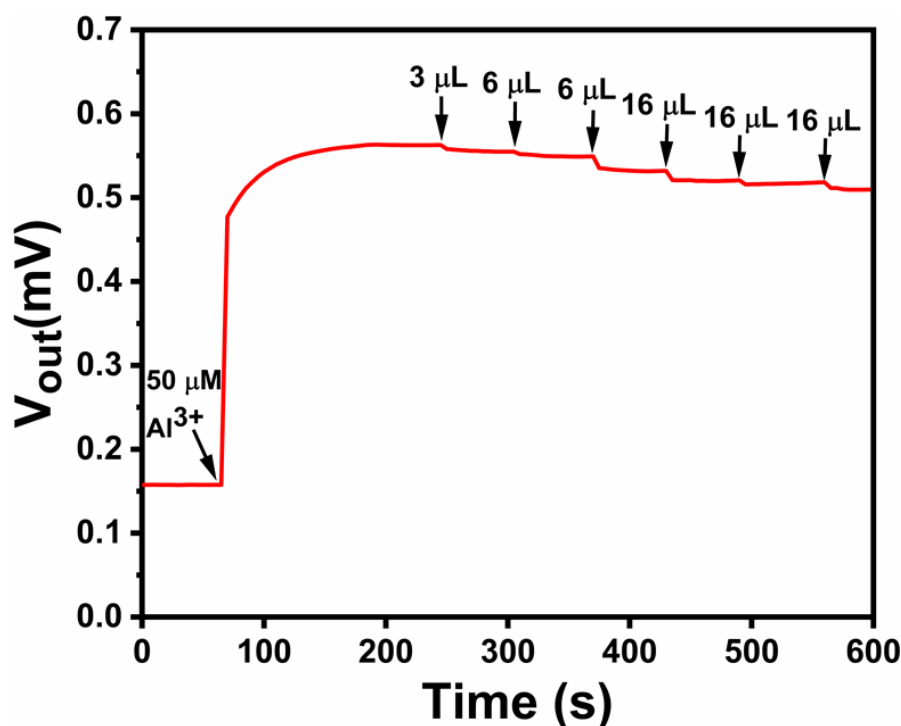
**Figure 7. 8.**  $V_{out}(c)$  as a measure of the fluorescence of 200  $\mu\text{M}$  NaMSA solution in acidified water activated with 50  $\mu\text{M}$  of  $\text{Al}^{3+}$  shown against  $\text{F}^-$  and  $\text{Cl}^-$  concentration, using the PMMA cuvette. The solid lines represent fits to the data according to Eq. 7.3.

Figure 7.8 shows a strong preference of the  $[\text{MSA}^-:\text{Al}^{3+}]$  complex to undergo decomplexation in the presence of  $\text{F}^-$  over  $\text{Cl}^-$ . The (weak) response to  $\text{Cl}^-$  does not fit to the model presented in Eq. 7.3 well, but when forcibly fitted, nevertheless, we find  $k = 44 \text{ M}^{-1}$ , hence selectivity as described previously in Section 2.2.4 and Eq. 2.5 is quantified by  $\log(k(\text{F}^-)/k(\text{Cl}^-)) \approx 2.5$ . More pragmatically, even large amounts of  $\text{Cl}^-$  do not reduce the fluorescence intensity to less than 85% of its original value while  $\text{F}^-$  at the potability limit of 79  $\mu\text{M}$  would reduce the fluorescence to about half of its initial value. Interference from  $\text{Cl}^-$  therefore does not compromise the ability of  $[\text{MSA}^-:\text{Al}^{3+}]$  fluorimetry to assess potability with respect to  $\text{F}^-$ .

### 7.3.5 The Effect of Simultaneous Presence of $\text{F}^-$ and $\text{Al}^{3+}$ on Activated NaMSA

In order to investigate the behaviour of our sensitiser to samples that simultaneously contain fluoride and aluminium, we first activated a 200  $\mu\text{M}$  NaMSA solution with 50  $\mu\text{M}$  of  $\text{Al}^{3+}$ . Then we tested the response of this solution by titrating with a mixed (0.75 mM  $\text{F}^-$  / 0.25 mM

Al<sup>3+</sup>) solution, prepared as described in section 7.2.5. Figure 7.9 shows  $V_{out}$  first increasing under the initial activation of NaMSA solution with Al<sup>3+</sup>, and then its development under titration with the 3:1 mole/mole mixed F<sup>-</sup> / Al<sup>3+</sup> solution.



**Figure 7. 9.**  $V_{out}(mV)$  as a measure of the fluorescence of 200  $\mu M$  NaMSA solution in acidified water. The first arrow indicates NaMSA activation with 50  $\mu M$  Al<sup>3+</sup>, the subsequent arrows indicate the addition of aliquots of (0.75 mM / 0.25 mM) mixed F<sup>-</sup> / Al<sup>3+</sup> solution.

Figure 7.9 shows only a weak response to the addition of mixed 0.75 mM F<sup>-</sup> / 0.25 mM Al<sup>3+</sup> solution. Note that the addition of 63  $\mu L$  of 0.75 mM F<sup>-</sup> / 0.25 mM Al<sup>3+</sup> solution leads to a final concentration of 139.2  $\mu M$  F<sup>-</sup> / 46.4  $\mu M$  Al<sup>3+</sup> in the cuvette. Previously, 100  $\mu M$  F<sup>-</sup> (without any Al<sup>3+</sup>) reduced the fluorescence of an activated NaMSA solution by 66.3% of its initial value as shown in Figure 7.7 (a). While here, 139.2  $\mu M$  of F<sup>-</sup> added in parallel with 46.4  $\mu M$  Al<sup>3+</sup> reduced the fluorescence intensity by only 9.4% of its initial value. On the other hand, the addition of more Al<sup>3+</sup> would be expected to further increase fluorescence intensity, however this is not observed when the Al<sup>3+</sup> is added in a 1:3 ratio with fluoride. When fluoride and aluminium are balanced 3:1, they act to cancel out each other's effect on the fluorescence intensity of a 200  $\mu M$  NaMSA solution activated with 50  $\mu M$  Al<sup>3+</sup>. Such a solution is therefore not suitable for sensing either fluoride or aluminium in samples containing both in (3:1) balanced proportions. It may be possible to sense Al<sup>3+</sup> in mixed Al<sup>3+</sup>/F<sup>-</sup> samples when using

NaMSA that is at first not activated at all with  $\text{Al}^{3+}$ , and to sense  $\text{F}^-$  in mixed  $\text{Al}^{3+}/\text{F}^-$  samples when using NaMSA that is at first ‘fully’ activated with  $\text{Al}^{3+}$  (in the sense of containing an excess of  $\text{Al}^{3+}$  over NaMSA), but this was not explored here. A false negative result may be obtained if both  $\text{Al}^{3+}$  and  $\text{F}^-$  are present in the test sample in the 1:3 ratio (v/v), as their opposing actions cancel each other, this outcome could be avoided in future studies by applying either cation or anion exchange to the sample prior to sensing to remove either the  $\text{Al}^{3+}$  and  $\text{F}^-$  ions (discussed in the future work section 8.2).

### 7.3.6 Comparison to Prior Fluorimetric $\text{Al}^{3+}$ and $\text{F}^-$ Sensors

To assess the quality of our sensors, and in particular our transducer concept, we compare our results for  $k$  and  $LoD$  to previous reports on fluorimetric  $\text{Al}^{3+}$  and  $\text{F}^-$  sensors. A good sensor should have a low  $LoD$ . However, the  $LoD$  is controlled by two factors, by  $k$  which quantifies the ‘strength’ of the analyte / sensitiser interaction (*cf.* the introduction of  $k$  in the context of Eq. 7.1 in section 7.2.7), and the signal-to-noise ratio of the transducer. The transducer’s dimensionless  $FoM$  (as defined in section 2.2.3) separates the contribution of the transducer from the contribution of  $k$ . Table 7.4 summarises  $k$ ,  $LoD$ , and  $FoM$  for a number of fluorimetric sensors for both  $\text{Al}^{3+}$  and  $\text{F}^-$  using different sensitisers and transducers, working in different media.

**Table 7.4:**

No.	Analyte	$k [M^{-1}]$	LoD [M]	FoM	Medium	Ref.
1	Al <sup>3+</sup>	$k=3.3 \times 10^3$	$1 \times 10^{-5}$	30	MeCN	[186]
2	Al <sup>3+</sup>	$k=5 \times 10^3$	$1 \times 10^{-6}$	200	DMF / HEPES	[187]
3	Al <sup>3+</sup>	$k=3.68 \times 10^4$	$1 \times 10^{-6}$	27	MeCN / Water	[188]
4	Al <sup>3+</sup>	$k=1.84 \times 10^4$	$2.3 \times 10^{-7}$	236	Buffer solution	[189]
5	Al <sup>3+</sup>	$k=1 \times 10^5$	$6 \times 10^{-7}$	17	DMSO / Water	[190]
6	Al <sup>3+</sup>	$k=9.87 \times 10^4$	$3 \times 10^{-8}$	337	HEPES buffer	[191]
7	Al <sup>3+</sup>	$k=8.5 \times 10^5$	$1.05 \times 10^{-8}$	112	DMSO / Water	[192]
8	Al <sup>3+</sup>	$k=5 \times 10^6$	$1.35 \times 10^{-9}$	148	DI Water	[193]
9	Al <sup>3+</sup>	$k=2.8 \times 10^3$	$4 \times 10^{-7}$	893	Acidified DI Water	This work
10	F <sup>-</sup>	$k=4.49 \times 10^6$	$1 \times 10^{-9}$	223	HEPES buffer / DMSO	[194]
11	F <sup>-</sup>	$k=4.69 \times 10^4$	$5.8 \times 10^{-7}$	37	MeCN	[195]
12	F <sup>-</sup>	-----	$9 \times 10^{-6}$	-----	DMSO	[196]
13	F <sup>-</sup>	$k=1 \times 10^4$	$2.43 \times 10^{-6}$	41	CHCl <sub>3</sub>	[197]
14	F <sup>-</sup>	$k=1.38 \times 10^4$	$9 \times 10^{-7}$	81	Acidified DI Water	This work

**Table 7. 4:** Performance parameters of different fluorimetric Al<sup>3+</sup> and F<sup>-</sup> sensors. Collated from the literature, and from tables 7.1 and 7.3 for values measured in this work. The abbreviations used for the different media refer to MeCN: Acetonitrile, DMSO: Dimethylsulfoxide, DMF: Dimethylformamide, and CHCl<sub>3</sub>: Chloroform.

We note that a number of reports sensed  $\text{Al}^{3+}$  or  $\text{F}^-$  in aprotic polar organic solvents, *e.g.* acetonitrile (MeCN), chloroform, dimethylsulfoxide (DMSO) or dimethylformamide (DMF), or mixtures of such solvents with water, presumably because the sensitiser was not miscible with water. This rather divorces such research from practical applications such as the testing of drinking water. Also, table 7.4 mostly shows sensitisers for either  $\text{Al}^{3+}$ , or  $\text{F}^-$ , but not for both. The use of water-soluble NaMSA works in aqueous medium without organic additives, and can be adapted to sense both  $\text{Al}^{3+}$  and  $\text{F}^-$ . NaMSA (for Aluminium sensing) and its activated counterpart (for fluoride sensing) provide *LoDs* below the potability limits for both  $\text{Al}^{3+}$  and  $\text{F}^-$ . Therefore, our transducer compares favourably among the sensors working in aqueous medium, since our approach leads to the best *FoM* for both  $\text{Al}^{3+}$  and  $\text{F}^-$  sensing.

#### 7.4 Conclusions

We extend the use of morin or its derivatives as an  $\text{Al}^{3+}$  selective ‘off  $\rightarrow$  on’ fluorescent sensitiser when immobilised in a phase transfer membrane to a morin derivative, NaMSA, dissolved in water, avoiding the need for membrane preparation. A fibre optic transducer to demonstrate  $\text{Al}^{3+}$  detection in drinking water well below the potability limit was developed. The dye is very cheap and its stability in solution over several months was demonstrated. It is possible to reliably quantify the concentration of  $\text{Al}^{3+}$  using the standard addition method. Further, by exposure to fluoride ( $\text{F}^-$ ) anions the  $\text{Al}^{3+}$  cation sensors can be recovered. Here, we also utilise the selective recovery of the dissolved NaMSA-  $\text{Al}^{3+}$  complex by exposure to  $\text{F}^-$  to develop a fully ‘complementary’ sensor for either aluminium cations, or fluoride anions, with *LoDs* below the potability limit for both of these important water pollutants. Dissolved NaMSA works as an ‘off  $\rightarrow$  on’ sensor for  $\text{Al}^{3+}$  cations. In order to become sensitive to  $\text{F}^-$ , the NaMSA must first be ‘activated’ by deliberately adding  $\text{Al}^{3+}$  to form the  $[\text{MSA}^-:\text{Al}^{3+}]$  complex, which then acts as a sensitiser for ‘on  $\rightarrow$  off’ fluorescent sensing of the  $\text{F}^-$  anion. In complementary sensing, the conventional distinction between ‘sensing’ and ‘recovery’ is lifted. We propose that other ion selective dyes with known recovery agents could be used in a similar manner to produce a wide range of low cost complementary ion sensors. The lock-in fibre optic transducer concept developed in this work is recommended as an alternative to conventional spectrofluorimeters, which can demonstrate a higher figure- of- merit at lower footprint.

## Chapter 8: Overall Conclusions and Proposed Future Work

### 8.1 Overall Conclusions

A portable, inexpensive, sensitive fibre optic EW transducer based on lock-in detection, originally designed by Dr Abraham Kirwa [37][38] as a colorimetric transducer for waterborne analyte sensing applications with a low limit of detection (*LoD*), was modified as a part of this work to be used as a fluorimetric transducer, and is described in Chapter 5 and also published in *Talanta* [126]. Moreover, the modified transducer was designed to be versatile, allowing it to be easily adapted for either waterborne or airborne analyte sensing, increasing the range of potential analytes that can be detected. As a part of the modification process, ‘side illumination’ was adopted, as it is a superior excitation mode compared with the evanescent wave. Specifically, as side illumination results in a strong fluorescent signal and very low (negligible) exciting light coupling into the optical fibre, the need for an expensive photodetector and an optical filter were eliminated which greatly reduces the cost. In addition, the transducer developed as a part of this work does not require an optical spectrometer. It also can detect changes in the fluorescence from either a sensitizer film or solution and can be used even when the sensitizer degrades when repeatedly exposed to the exciting light. The versatility of the sensor setup has been proved by DNT detection at very low diluted level in both media. For both the water- and airborne DNT sensors the sensitizer was spray-coated onto the stripped section of an optical fibres before being exposed to various analyte concentrations.

The sensor setup works with these multiple sensitizers for the detection of multiple analytes i.e.  $\text{Cu}^{2+}$ ,  $\text{Al}^{3+}$ ,  $\text{F}^-$  below their potability limits in water. For the detection of waterborne  $\text{Cu}^{2+}$ , the sensitizer (Probe 1 film) was immobilised in a plasticised polyvinyl chloride (PVC) membrane. The sensitised film membrane was dip-coated onto the stripped section of an optical fibre before being exposed to a range of  $\text{Cu}^{2+}$  concentrations. On the other hands, the detection of  $\text{Al}^{3+}$ ,  $\text{F}^-$  was carried out by using water-soluble (NaMSA). I have shown that, by using the complementary recovery ion for established sensitizers, the ion range can be further extended this is probably generic and applicable for all recoverable sensitizers and therefore significantly expands the range of detectable ions. The list of aims in Chapter 1 Section 1.3 have been met except the detection of very toxic ions i.e.  $\text{Hg}^{2+}$ ,  $\text{Pb}^{2+}$ ,  $\text{Cd}^{2+}$  and the detection of explosives by using designated explosives sensitizer, such as “pentiptycene”. The sensing of these ions was not been conducted because they are very toxic and solutions contaminated with them must be disposed according to strict guidelines in a designated container. The detection of explosives

was achieved by using a generic sensitiser i.e. MDMO-PPV instead of designated explosives sensitiser, such as “penttiptycene” because it was not available to us. I believe our transducer with suitable sensitisers can most likely detect these analytes below their allowable level in air or water.

## 8.2 Proposed Future Work

As in all research, the present work is not without its limitations, which could be addressed in future investigations, with some suggestions provided below:

1. Given that MDMO-PPV was shown to degrade considerably under side illumination due to the high intensity of exciting light, exposing the MDMO or other light-sensitive fluorophores to exciting light of a lower intensity will reduce fluorescence degradation when an optimised operational procedure (i.e. short excitation or ‘interrogation’ intervals, separated by longer dark periods) is adopted. In addition, if the absorption band of the fluorophore is broad, it is better to excite the fluorophore with longer wavelength and so reduce the energy per photon and so reduce the fluorescence degradation.

2. The transducer developed as a part of the present study could also be used in conjunction with fluorescent polymers specifically designed and synthesised for capturing nitroaromatic airborne analytes, such as that from the penttiptycene family, as discussed by Swager *et al.* [82]. Swager *et al.* [82] used a photomultiplier-based fluorescence measurement setup and have already shown that such polymers can yield *LoD* of the order of a few parts per trillion. In future studies, there is great potential for improving upon this outcome by adopting the lock-in fibre optic instrument described in this thesis, because it reduces the signal to noise in the measurement. It also allows for a simpler experimental setup without the need for an expensive photomultiplier. It would also be beneficial to use the system developed in this research for the sensing of either airborne or waterborne analytes even if exciting light causes sensitiser degradation, which is a common issue that has been neglected in many extant reports [1][198]. In our system, the fluorescence degradation unrelated to the analyte can be minimised by shortening the pulses of the exciting light. Then we account for the remaining degradation if still existing to have an accurate sensing data.

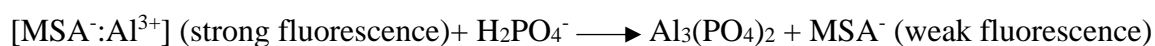
3. The lock-in fibre optic sensor approach described here can also be applied with similar sensitisers that exhibit aggregation-induced emission (AIE) when dissolved in a mixture of organic solvent/non-solvent (usually water), which could be converted into plasticised PVC

membrane films using the approach described in this thesis. This strategy would prevent exposure to harmful organic solvents during analyte sensing experiments. For an example, an Anthracene based 1-(Anthracen-2-yliminomethyl)-naphthalen-2-ol (AIN) has exhibited an AIE characteristic and used as on  $\rightarrow$  off fluorescent sensor for  $\text{Hg}^{2+}$  detection as reported in [199]. Therefore, it has a great potential to be immobilised in a plasticised PVC membrane for the detection of  $\text{Hg}^{2+}$  below its potability limit.

5. Using the methods described here as a starting point, reflective cuvettes with enhanced *LoD* can be developed. The cuvette adopted in the present study reflects only a portion of fluorescent light towards the roughened section of the fibre, which guides the fluorescence to the photodiode (PD), while the remaining fluorescence is dispersed. Thus, in future studies, the cuvette's design can be improved to confine and focus the majority of fluorescent signal onto the optical fibre. The proposed cuvette must contain only three holes with the diameters corresponding to those of the fibre core, the LED cap, and the pipette tip (for analyte titrations), respectively, these design changes would minimise dispersion of the fluorescence.

6. In the present study, it was shown that NaMSA fluorescence is enhanced in the presence of  $\text{Al}^{3+}$  due to the formation of  $[\text{MSA}^-:\text{Al}^{3+}]$  complex, while the fluorescence of partially activated NaMSA is quenched in the presence of  $\text{F}^-$ . However, given that a false negative result may be obtained if both  $\text{Al}^{3+}$  and  $\text{F}^-$  are present in the test sample in the 1:3 ratio (v/v), as their opposing actions cancel each other, this outcome could be avoided in future studies by applying either cation or anion exchange to the sample prior to sensing to remove either the  $\text{F}^-$  or  $\text{Al}^{3+}$  ions. For instance,  $\text{Al}^{3+}$  can be removed by adding dihydrogen phosphate ( $\text{H}_2\text{PO}_4^-$ ) anion to the water sample, whereas commercially available Purolite A520E resin could potentially be used to remove  $\text{F}^-$  [200].

7. Finally, as phosphate can form a strong complex with aluminium which does not readily dissociate unless the pH of the medium is very high [201], an NaMSA solution that is partially or fully activated by aluminium can be used in future investigations as an on  $\rightarrow$  off fluorescence sensor for phosphate anion detection in water. The chemical reaction will be:



### **Published Work during my PhD Unrelated to this Thesis**

Al Baroot, A., **Alshammari, A.** and Grell, M., 2019. Electrochemical gating of a hydrophobic organic semiconductor with aqueous media. *Thin Solid Films*, 669, pp.665-669.

I have prepared acid solutions such as acetic acid and picric acid (PA) in various concentrations. I also have contributed to the discussion of the results including the properties of PA and proofread the first draft of the manuscript.

## References

- [1] R. N. Gillanders, I. D. W. Samuel, and G. A. Turnbull, "A low-cost, portable optical explosive-vapour sensor," *Sensors Actuators, B Chem.*, vol. 245, pp. 334–340, 2017.
- [2] S. Content, W. C. Trogler, and M. J. Sailor, "Detection of nitrobenzene, DNT, and TNT vapors by quenching of porous silicon photoluminescence," *Chem. - A Eur. J.*, vol. 6, no. 12, pp. 2205–2213, 2000.
- [3] F. Edition, "Guidlines for drinking-water quality.," *WHO chronicle*, 2011. [Online]. Available:[http://apps.who.int/iris/bitstream/handle/10665/44584/9789241548151\\_eng.pdf;jsessionid=E52FF5C3E20A4A5D55A7A170FE77A72708?sequence=1](http://apps.who.int/iris/bitstream/handle/10665/44584/9789241548151_eng.pdf;jsessionid=E52FF5C3E20A4A5D55A7A170FE77A72708?sequence=1) (Accessed, 20.06.2020, 2346hrs UK time).
- [4] [http://dwi.defra.gov.uk/stakeholders/legislation/eudir98\\_83\\_EC.pdf](http://dwi.defra.gov.uk/stakeholders/legislation/eudir98_83_EC.pdf) (Accessed, 20.06.2020, 2133hrs UK time).
- [5] [https://www.epa.gov/sites/production/files/2016-06/documents/npwdr\\_complete\\_table.pdf](https://www.epa.gov/sites/production/files/2016-06/documents/npwdr_complete_table.pdf) (Accessed, 20.06.2020, 2133hrs UK time).
- [6] A. O. Ogunfowokan, A. S. Adekunle, B. A. Oyebode, J. A. O. Oyekunle, A. O. Komolafe, and G. O. Omoniyi-Esan, "Determination of Heavy Metals in Urine of Patients and Tissue of Corpses by Atomic Absorption Spectroscopy," *Chem. Africa*, vol. 2, no. 4, pp. 699–712, 2019.
- [7] S. Azimi and Z. Es'haghi, "A Magnetized Nanoparticle Based Solid-Phase Extraction Procedure Followed by Inductively Coupled Plasma Atomic Emission Spectrometry to Determine Arsenic, Lead and Cadmium in Water, Milk, Indian Rice and Red Tea," *Bull. Environ. Contam. Toxicol.*, vol. 98, no. 6, pp. 830–836, 2017.
- [8] S. Veyseh and A. Niazi, "A novel aeration-assisted homogenous liquid-liquid microextraction for determination of thorium and uranium in water and hair samples by inductively coupled plasma-mass spectroscopy," *Talanta*, vol. 147, pp. 117–123, 2016.
- [9] F. Liu, M. Cui, J. Ma, G. Zou, and Q. Zhang, "An optical fiber taper fluorescent probe for detection of nitro-explosives based on tetraphenylethylene with aggregation-induced emission," *Opt. Fiber Technol.*, vol. 36, pp. 98–104, 2017.
- [10] B. Burcu and R. Genç, "Naked eye and smartphone applicable detection of toxic mercury ions using fluorescent carbon nanodots," *Turkish J. Chem.*, vol. 41, no. 6, pp.

- 931–943, 2017.
- [11] M. V. Foguel, X. A. Ton, M. V. B. Zanoni, M. D. P. T. Sotomayor, K. Haupt, and B. Tse Sum Bui, “A molecularly imprinted polymer-based evanescent wave fiber optic sensor for the detection of basic red 9 dye,” *Sensors Actuators, B Chem.*, vol. 218, pp. 222–228, 2015.
- [12] Z. Pan, J. Feng, X. Hu, C. Jia, and X. Huang, “High sensitivity fiber sensor for measurement of Cd<sup>2+</sup> concentration in aqueous solution based on reflective Mach-Zehnder interference with temperature calibration,” *Opt. Express*, vol. 27, no. 22, p. 32621, 2019.
- [13] J. Wang *et al.*, “A terpyridine-based test strip for the detection of Hg<sup>2+</sup> in various water samples and drinks,” *Anal. Methods*, vol. 11, no. 2, pp. 227–231, 2019.
- [14] Y. T. Wang *et al.*, “A colorimetric Pb<sup>2+</sup> chemosensor: Rapid naked-eye detection, high selectivity, theoretical insights, and applications,” *J. Photochem. Photobiol. A Chem.*, vol. 355, pp. 101–108, 2018.
- [15] Y. Tang, Y. Ding, T. Wu, L. Lv, and Z. Yan, “A turn-on fluorescent probe for Hg<sup>2+</sup> detection by using gold nanoparticle-based hybrid microgels,” *Sensors Actuators, B Chem.*, vol. 228, pp. 767–773, 2016.
- [16] R. Singh and G. Das, “Turn-on Pb<sup>2+</sup> sensing and rapid detection of biothiols in aqueous medium and real samples,” *Analyst*, vol. 144, no. 2, pp. 567–572, 2019.
- [17] “World Health Organization”, Mercury and Health. [Online]. Available: <https://www.who.int/news-room/fact-sheets/detail/mercury-and-health> (Accessed, 10.05.2020, 1833hrs UK time).
- [18] “World Health Organization,” *International Programme on Chemical Safety*. [Online]. Available: [https://www.who.int/ipcs/assessment/public\\_health/cadmium/en/](https://www.who.int/ipcs/assessment/public_health/cadmium/en/).
- [19] X. M. Zhao *et al.*, “Distribution and ecological risk assessment of cadmium in water and sediment in Longjiang River, China: Implication on water quality management after pollution accident,” *Chemosphere*, vol. 194, pp. 107–116, 2018.
- [20] S. Nazerdeylami, J. B. Ghasemi, and A. Badiei, “Anthracene modified graphene oxide-silica as an optical sensor for selective detection of Cu<sup>2+</sup> and I<sup>−</sup> ions,” *Int. J. Environ. Anal. Chem.*, vol. 100, no. 6, pp. 686–701, 2020.

- [21] A. K. Manna, K. Rout, S. Chowdhury, and G. K. Patra, "A dual-mode highly selective and sensitive Schiff base chemosensor for fluorescent colorimetric detection of Ni<sup>2+</sup> and colorimetric detection of Cu<sup>2+</sup>," *Photochem. Photobiol. Sci.*, vol. 18, no. 6, pp. 1512–1525, 2019.
- [22] W. Wang *et al.*, "Reusable surface plasmon resonance sensor for rapid detection of Cu<sup>2+</sup> based on modified-chitosan thin film as an active layer," *Sensors Actuators, A Phys.*, vol. 18, no. 6, pp. 1512–1525, 2019.
- [23] Y. Liu *et al.*, "A novel self-assembled nanoprobe for the detection of aluminum ions in real water samples and living cells," *Talanta*, vol. 194, pp. 38–45, 2019.
- [24] Q. Meng, H. Liu, C. Sen, C. Cao, and J. Ren, "A novel molecular probe sensing polynuclear hydrolyzed aluminum by chelation-enhanced fluorescence," *Talanta*, vol. 99, pp. 464–470, 2012.
- [25] J. Zhu *et al.*, "Fluorescence 'On-Off' chemical sensor for ultrasensitive detection of Al<sup>3+</sup> in live cell," *Tetrahedron Lett.*, vol. 61, p. 151893, 2020.
- [26] B. Ke *et al.*, "A fluorescent probe for rapid aqueous fluoride detection and cell imaging," *Chem. Commun.*, vol. 49, no. 25, pp. 2494–2496, 2013.
- [27] X. Sun, Y. Wang, and Y. Lei, "Fluorescence based explosive detection: From mechanisms to sensory materials," *Chem. Soc. Rev.*, vol. 44, no. 22, pp. 8019–8061, 2015.
- [28] K. R. Ghosh, S. K. Saha, and Z. Y. Wang, "Ultra-sensitive detection of explosives in solution and film as well as the development of thicker film effectiveness by tetraphenylethene moiety in AIE active fluorescent conjugated polymer," *Polym. Chem.*, vol. 5, no. 19, pp. 5638–5643, 2014.
- [29] Y. T. Yew, A. Ambrosi, and M. Pumera, "Nitroaromatic explosives detection using electrochemically exfoliated graphene," *Sci. Rep.*, vol. 6, pp. 1–11, 2016.
- [30] B. Prusti and M. Chakravarty, "An electron-rich small AIEgen as a solid platform for the selective and ultrasensitive on-site visual detection of TNT in the solid, solution and vapor states," *Analyst*, vol. 145, no. 5, pp. 1687–1694, 2020.
- [31] B. D. Piorek, S. J. Lee, M. Moskovits, and C. D. Meinhart, "Free-surface microfluidics/surface-enhanced Raman spectroscopy for real-time trace vapor

- detection of explosives,” *Anal. Chem.*, vol. 84, no. 22, pp. 9700–9705, 2012.
- [32] B. Gilbert-López *et al.*, “Detection of multiclass explosives and related compounds in soil and water by liquid chromatography-dielectric barrier discharge ionization-mass spectrometry,” *Anal. Bioanal. Chem.*, vol. 411, no. 19, pp. 4785–4796, 2019.
- [33] F. Novotný, J. Plutnar, and M. Pumera, “Plasmonic Self-Propelled Nanomotors for Explosives Detection via Solution-Based Surface Enhanced Raman Scattering,” *Adv. Funct. Mater.*, vol. 29, no. 33, pp. 1–7, 2019.
- [34] M. Amo-González, S. Pérez, R. Delgado, G. Arranz, and I. Carnicero, “Tandem Ion Mobility Spectrometry for the Detection of Traces of Explosives in Cargo at Concentrations of Parts per Quadrillion,” *Anal. Chem.*, vol. 91, no. 21, pp. 14009–14018, 2019.
- [35] A. S. Chajistamatiou and E. B. Bakeas, “Identification of thiocyanates by Gas Chromatography – Mass Spectrometry in explosive residues used as a possible marker to indicate black powder usage,” *Talanta*, vol. 195, no. 2018, pp. 456–462, 2019.
- [36] K. A. Tuwei, “Self- Referenced Evanescent Wave Sensor for Low Limit of Detection Applications,” University of Sheffield, 2018.
- [37] K. A. Tuwei, N. H. Williams, and M. Grell, “Fibre optic absorbance meter with low limit of detection for waterborne cations,” *Sensors Actuators, B Chem.*, vol. 237, pp. 1102–1107, 2016.
- [38] A. K. Tuwei, N. H. Williams, M. Y. Mulla, C. Di Natale, R. Paolesse, and M. Grell, “‘Rough guide’ evanescent wave optrode for colorimetric metalloporphyrine sensors,” *Talanta*, vol. 164, no. 2016, pp. 228–232, 2017.
- [39] W. R. Seitz, “Chemical Sensors Based on Fiber optics,” *Anal. Chem.*, vol. 56, no. 1, pp. 16–34, 1984.
- [40] J. Burgués, J. M. Jiménez-Soto, and S. Marco, “Estimation of the limit of detection in semiconductor gas sensors through linearized calibration models,” *Anal. Chim. Acta*, vol. 1013, pp. 13–25, 2018.
- [41] Ü. Şengül, “Comparing determination methods of detection and quantification limits for aflatoxin analysis in hazelnut,” *J. Food Drug Anal.*, vol. 24, no. 1, pp. 56–62, 2016.

- [42] T. Ma *et al.*, “Fluorescein-based fluorescent porous aromatic framework for Fe<sup>3+</sup> detection with high sensitivity,” *J. Mater. Chem. C*, vol. 7, no. 8, pp. 2327–2332, 2019.
- [43] V. A. Galievsky, A. S. Stasheuski, and S. N. Krylov, “‘Getting the best sensitivity from on-capillary fluorescence detection in capillary electrophoresis’ – A tutorial,” *Anal. Chim. Acta*, vol. 935, pp. 58–81, 2016.
- [44] A. H. Alshammari, Z. Alqahtani, F. B. Mohd Suah, S. A. Nizar, A. Dunbar, and M. Grell, “Low cost, high sensitivity detection of waterborne Al<sup>3+</sup> cations and F<sup>−</sup> anions via the fluorescence response of a morin derivative dye,” *Anal. Chim. Acta*, vol. 1105, pp. 1–10, 2020.
- [45] G. W. Gokel, W. M. Leevy, and M. E. Weber, “Crown ethers: Sensors for ions and molecular scaffolds for materials and biological models,” *Chem. Rev.*, vol. 104, no. 5, pp. 2723–2750, 2004.
- [46] Z. Alqahtani, N. Alghamdi, and M. Grell, “Monitoring the lead-and-copper rule with a water-gated field effect transistor,” *J. Water Health*, vol. 18, no. 2, pp. 159–171, 2020.
- [47] A. Rouis, M. Echabaane, N. Sakly, I. Bonnamour, and H. Ben Ouada, “Characterization of a sensitive and selective copper optode based on β-ketoimine modified calix[4]arene derivative,” *Mater. Sci. Eng. C*, vol. 46, pp. 125–131, 2015.
- [48] J.-S. Yang and T. M. Swager, “Porous Shape Persistent Fluorescent Polymer Films: An Approach to TNT Sensory Materials.,” *J. Am. Chem. Soc.*, vol. 120, no. 21, pp. 5321–5322, 1998.
- [49] J. Yang and T. M. Swager, “Fluorescent Porous Polymer Films as TNT Chemosensors : Electronic and Structural Effects Fluorescent Porous Polymer Films as TNT Chemosensors : Electronic and Structural Effects,” *J. Am. Chem. Soc.*, vol. 120, no. 46, pp. 11864–11873, 1998.
- [50] A. A. Abdel Aziz, R. G. Mohamed, F. M. Elantabli, and S. M. El-Medani, “A Novel Fluorimetric Bulk Optode Membrane Based on NOS Tridentate Schiff Base for Selective Optical Sensing of Al<sup>3+</sup> Ions,” *J. Fluoresc.*, vol. 26, no. 6, pp. 1927–1938, 2016.
- [51] B. J. Muller, S. M. Borisov, and I. Klimant, “Red- to NIR-Emitting, BODIPY-Based, K<sup>+</sup>-Selective Fluoroionophores and Sensing Materials,” *Adv. Funct. Mater.*, vol. 26,

- no. 42, pp. 7697–7707, 2016.
- [52] F. B. M. Suah and M. Ahmad, “Preparation and characterization of polymer inclusion membrane based optode for determination of  $Al^{3+}$  ion,” *Anal. Chim. Acta*, vol. 951, pp. 133–139, Jan. 2017.
- [53] S. M. Saleh, R. Ali, and I. A. Ali, “A novel, highly sensitive, selective, reversible and turn-on chemi-sensor based on Schiff base for rapid detection of  $Cu(II)$ ,” *Spectrochim. Acta - Part A Mol. Biomol. Spectrosc.*, vol. 183, pp. 225–231, 2017.
- [54] J. A. Broekaert, *Analytical atomic spectrometry with flames and plasmas*. John Wiley & Sons, 2006.
- [55] J. R. Lakowicz, *Principles of Fluorescence Spectroscopy*. Boston, MA: Springer US, 2013.
- [56] N. D. N. Rodrigues and M. Staniforth, “Photophysics of sunscreen molecules in the gas phase: a stepwise approach towards understanding and developing next-generation sunscreens,” *Proc. R. Soc. A Math. Phys. Eng. Sci.*, vol. 472, no. 2195, p. 20160677, 2016.
- [57] E. Terpetschnig and D. M. Jameson, “Fluorescence lifetime,” no. 0, pp. 1–8, 1960.
- [58] G. Book, “Compendium of Chemical Terminology,” *Int. Union Pure Appl. Chem.*, vol. 528, 2014.
- [59] A. R. Young, “Chromophores in human skin,” *Phys. Med. Biol.*, vol. 42, no. 5, p. 789, 1997.
- [60] S. B. Warriar and P. S. Kharkar, “A coumarin based chemosensor for selective determination of  $Cu(II)$  ions based on fluorescence quenching,” *J. Lumin.*, vol. 199, no. March, pp. 407–415, 2018.
- [61] S. Ruan, H. Ebendorff-Heideprié, and Y. Ruan, “Optical fibre turn-on sensor for the detection of mercury based on immobilized fluorophore,” *Measurement*, vol. 121, pp. 122–126, 2018.
- [62] N. Roy, A. Dutta, P. Mondal, P. C. Paul, and T. S. Singh, “A new coumarin based dual functional chemosensor for colorimetric detection of  $Fe^{3+}$  and fluorescence turn-on response of  $Zn^{2+}$ ,” *Sensors Actuators, B Chem.*, vol. 236, pp. 719–731, 2016.

- [63] Y. Fu and N. S. Finney, "Small-molecule fluorescent probes and their design," *RSC Adv.*, vol. 8, no. 51, pp. 29051–29061, 2018.
- [64] A. T. Afaneh and G. Schreckenbach, "Fluorescence Enhancement/Quenching Based on Metal Orbital Control: Computational Studies of a 6-Thienyllumazine-Based Mercury Sensor," *J. Phys. Chem. A*, vol. 119, no. 29, pp. 8106–8116, 2015.
- [65] A. Alvarez, J. M. Costa-Fernández, R. Pereiro, A. Sanz-Medel, and A. Salinas-Castillo, "Fluorescent conjugated polymers for chemical and biochemical sensing," *TrAC - Trends Anal. Chem.*, vol. 30, no. 9, pp. 1513–1525, 2011.
- [66] M. E. Germain and M. J. Knapp, "Optical explosives detection: From color changes to fluorescence turn-on," *Chem. Soc. Rev.*, vol. 38, no. 9, pp. 2543–2555, 2009.
- [67] T. H. Nguyen, T. Sun, and K. T. V Grattan, "A Turn-On Fluorescence-Based Fibre Optic Sensor for the Detection of Mercury," *Sensors*, vol. 19, no. 9, p. 2142, 2019.
- [68] Y. Wang, Z. Liu, J. Sun, X. Liu, M. Pei, and G. Zhang, "A turn-on fluorescence probe for Fe<sup>3+</sup> based-on benzimidazo[2,1- $\alpha$ ]benz[de]isoquinoline-7-one derivatives," *J. Photochem. Photobiol. A Chem.*, vol. 332, pp. 515–520, 2017.
- [69] X. Zhou and X. Zhou, "the Unit Problem in the Thermodynamic Calculation of Adsorption Using the Langmuir Equation," *Chem. Eng. Commun.*, vol. 201, no. 11, pp. 1459–1467, 2014.
- [70] J. J. Davenport, M. Hickey, J. P. Phillips, and P. A. Kyriacou, "A fibre optic fluorescence quenching oxygen partial pressure sensor using PtOEP," *Appl. Opt.*, vol. 55(21), pp. 5603–5609, 2016.
- [71] X. Zhang, Y. Wang, H. Yuan, X. Guo, B. Dai, and X. Jia, "An acid- fluorescence and alkali-colorimetric dual channels sensor for Hg<sup>2+</sup> selective detection by different coordination manners in aqueous media," *J. Photochem. Photobiol. A Chem.*, vol. 373, pp. 12–19, 2019.
- [72] D. Parker and J. A. G. Williams, "Luminescence behaviour of cadmium , lead , zinc , copper , nickel and lanthanide complexes of octadentate macrocyclic ligands bearing naphthyl chromophores," *J. CHEM. soc, Perkin Trans.*, vol. 2, no. 7, pp. 1305–1314, 1995.
- [73] M. Shamsipur, M. Sadeghi, M. Hassan, and H. Sharghi, "Development of a novel fl

- uorimetric bulk optode membrane based on meso -tetrakis ( 2-hydroxynaphthyl ) porphyrin ( MTHNP ) for highly sensitive and selective monitoring of trace amounts of Hg 2 + ions,” *Mater. Sci. Eng. C*, vol. 48, pp. 424–433, 2015.
- [74] P. Ghorai, S. Banerjee, D. Nag, S. Mukhopadhyay, and A. Saha, “Design and synthesis of a novel fl uorescent-colorimetric chemosensor for selective detection of Zn (II) and Cu(II) ions with applications in live cell imaging and molecular logic gate,” *J. Lumin.*, vol. 205, pp. 197–209, 2019.
- [75] Z. Wang, Z. Y. Wang, J. Ma, W. J. Bock, and D. Ma, “Effect of film thickness , blending and undercoating on optical detection of nitroaromatics using fluorescent polymer films,” *Polymer (Guildf)*., vol. 51, no. 4, pp. 842–847, 2010.
- [76] G. He *et al.*, “Pyrene-containing conjugated polymer-based fluorescent films for highly sensitive and selective sensing of TNT in aqueous medium,” *Macromolecules*, vol. 44, no. 12, pp. 4759–4766, 2011.
- [77] F. Chu, G. Tsiminis, N. A. Spooner, and T. M. Monro, “Explosives detection by fluorescence quenching of conjugated polymers in suspended core optical fibers,” *Sensors Actuators, B Chem.*, vol. 199, pp. 22–26, 2014.
- [78] R. N. Gillanders, J. M. E. Glackin, I. A. Campbell, I. D. W. Samuel, and G. A. Turnbull, “Advances in Optical Sensing of Explosive Vapours,” *Proc. 6th Int. Conf. Photonics, Opt. Laser Technol. 2018*), 2018.
- [79] S. K. Basiruddin and S. K. Swain, “Phenylboronic acid functionalized reduced graphene oxide based fl uorescence nano sensor for glucose sensing,” *Mater. Sci. Eng. C*, vol. 58, pp. 103–109, 2016.
- [80] O. Ines and O. S. Wolfbeis, “Optical Sensors for Determination of Heavy Metal Ions,” *Mikrochim. Acta*, vol. 126, no. 34, pp. 177–192, 1997.
- [81] D. A. Olley *et al.*, “Explosive Sensing with Fluorescent Dendrimers : The Role of Collisional Quenching †,” *Chem. Mater.*, vol. 23, no. 3, pp. 789–794, 2011.
- [82] C. J. Cumming *et al.*, “Using novel fluorescent polymers as sensory materials for above-ground sensing of chemical signature compounds emanating from buried landmines,” *IEEE Trans. Geosci. Remote Sens.*, vol. 39, no. 6, pp. 1119–1128, 2001.
- [83] B. M. Omer, “Optical properties of MEH-PPV and MEH-PPV/ [6,6]-Phenyl C61-

- butyric acid 3-ethylthiophene ester thin films,” *Int. J. Org. Electron.*, vol. 2, no. 2, pp. 1–7, 2013.
- [84] P. Wagner, P. Aubert, L. Lutsen, and D. Vanderzande, “Conjugated polymers based on new thienylene – PPV derivatives for solar cell applications,” *Electrochem. commun.*, vol. 4, pp. 912–916, 2002.
- [85] J. C. Sanchez, A. Escobosa, and M. Estrada, “Characterization of Thin Films of Conjugated Polymer (BEHP-PPV) -co-(MEH-PPV) for OLEDs Application,” in *2006 3rd International Conference on Electrical and Electronics Engineering*, 2006, pp. 1–4.
- [86] A. M. Yusufu, A. S. M. M. Noor, N. Tamchek, and Z. Z. Abidin, “MEH-PPV film thickness influenced fluorescent quenching of tip-coated plastic optical fiber sensors,” *Opt. Fiber Technol.*, vol. 39, pp. 21–25, 2017.
- [87] M. D. Woodka, V. P. Schnee, and M. P. Polcha, “Fluorescent Polymer Sensor Array for Detection and Discrimination of Explosives in Water,” *Anal. Chem.*, vol. 82, pp. 9917–9924, 2010.
- [88] C. P. Chang *et al.*, “Fluorescent conjugated polymer films as TNT chemosensors,” *Synth. Met.*, vol. 144, no. 3, pp. 297–301, 2004.
- [89] K. Saxena, P. Kumar, and V. K. Jain, “Fluorescence quenching studies of conjugated polymer poly[2-methoxy-5-(30,70-dimethyloctyloxy)-1,4-phenylenevinylene in the presence of TNT,” *J. Lumin.*, vol. 130, no. 11, pp. 2260–2264, 2010.
- [90] S. Sensfuss *et al.*, “Thienopyrazine-based low-bandgap polymers for flexible polymer solar cells,” *EPJ Appl. Phys.*, vol. 51, no. 3, p. 33204, 2010.
- [91] A. Loudet and K. Burgess, “BODIPY dyes and their derivatives: Syntheses and spectroscopic properties,” *Chem. Rev.*, vol. 107, no. 11, pp. 4891–4932, 2007.
- [92] L. Rose and A. T. A. Jenkins, “The effect of the ionophore valinomycin on biomimetic solid supported lipid DPPTE / EPC membranes,” *Bioelectrochemistry*, vol. 70, pp. 387–393, 2007.
- [93] O. S. Wolfbeis, “Fluorescence-based ion sensing using potential-sensitive dyes,” *Sensors Actuators B*, vol. 29, no. 1–3, pp. 140–147, 1995.

- [94] C. J. Pedersen, "Cyclic Polyethers and Their Complexes with Metal Salts," *J. Am. Chem. Soc.*, vol. 89, no. 26, pp. 7017–7036, 1967.
- [95] P. A. Panchenko, Y. V. Fedorov, and O. A. Fedorova, "Selective fluorometric sensing of Hg<sup>2+</sup> in aqueous solution by the inhibition of PET from dithia-15-crown-5 ether receptor conjugated to 4-amino-1,8-naphthalimide fluorophore," *J. Photochem. Photobiol. A Chem.*, vol. 364, pp. 124–129, 2018.
- [96] L. Lvova *et al.*, "Systematic approach in Mg<sup>2+</sup> ions analysis with a combination of tailored fluorophore design," *Anal. Chim. Acta*, vol. 988, pp. 96–103, 2017.
- [97] Y. C. Hsieh, J. L. Chir, S. T. Yang, S. J. Chen, C. H. Hu, and A. T. Wu, "A sugar-aza-crown ether-based fluorescent sensor for Cu<sup>2+</sup> and Hg<sup>2+</sup> ions," *Carbohydr. Res.*, vol. 346, no. 7, pp. 978–981, 2011.
- [98] L. A. Saari and W. R. Seitz, "Immobilized Morin as Fluorescence Sensor for Determination of Aluminum(III)," *Anal. Chem.*, vol. 55, no. 4, pp. 667–670, 1983.
- [99] V. K. Gupta, A. K. Jain, and G. Maheshwari, "Aluminum(III) selective potentiometric sensor based on morin in poly(vinyl chloride) matrix," *Talanta*, vol. 72, no. 4, pp. 1469–1473, 2007.
- [100] S. M. Z. Al-Kindy, F. O. Suliman, and S. B. Salama, "A sequential injection method for the determination of aluminum in drinking water using fluorescence enhancement of the aluminum-morin complex in micellar media," *Microchem. J.*, vol. 74, no. 2, pp. 173–179, 2003.
- [101] S. Abu Hanifah *et al.*, "A Fluorescence Phosphate Sensor Based on Poly(Glycidyl Methacrylate) Microspheres With Aluminium-Morin," *Malaysian J. Anal. Sci.*, vol. 20, no. 4, pp. 704–712, 2016.
- [102] M. Kopacz, "Quercetin- and Morinsulfonates as Analytical Reagents," *J. Anal. Chem.*, vol. 58, no. 3, pp. 225–229, 2003.
- [103] J. Luo *et al.*, "Aggregation-induced emission of 1-methyl-1,2,3,4,5-pentaphenylsilole," *Chem. Commun.*, vol. 18, p. 1740, 2001.
- [104] K. Kumaravel and G. Vasuki, "Four-component catalyst-free reaction in water: Combinatorial library synthesis of novel 2-amino-4-(5-hydroxy-3-methyl-1H-pyrazol-4-yl)-4H-chromene-3- carbonitrile derivatives," *Green Chem.*, vol. 11, no. 12, pp.

- 1945–1947, 2009.
- [105] M. Pannipara, A. G. Al-Sehemi, A. Irfan, M. Assiri, A. Kalam, and Y. S. Al-Ammari, “AIE active multianalyte fluorescent probe for the detection of Cu<sup>2+</sup>, Ni<sup>2+</sup> and Hg<sup>2+</sup> ions,” *Spectrochim. Acta - Part A Mol. Biomol. Spectrosc.*, vol. 201, pp. 54–60, 2018.
- [106] V. Arora, H. M. Chawla, and S. P. Singh, “Calixarenes as sensor materials for recognition and separation of metal ions,” *Arkivoc*, vol. 2007, no. 2, pp. 172–200, 2007.
- [107] R. E. Gyurcsányi *et al.*, “Direct evidence of ionic fluxes across ion-selective membranes: A scanning electrochemical microscopic and potentiometric study,” *Anal. Chem.*, vol. 73, no. 9, pp. 2104–2111, 2001.
- [108] N. Alghamdi, Z. Alqahtani, and M. Grell, “Sub-nanomolar detection of cesium with water-gated transistor,” *J. Appl. Phys.*, vol. 126, no. 6, p. 064502, 2019.
- [109] M. Wei, X. Li, and M. J. Serpe, “Stimuli-Responsive Microgel-Based Surface Plasmon Resonance Transducer for Glucose Detection Using a Competitive Assay with Concanavalin A,” *ACS Appl. Polym. Mater.*, vol. 1, no. 3, pp. 519–525, 2019.
- [110] S. K. Vashist and P. Vashist, “Recent Advances in Quartz Crystal Microbalance-Based Sensors,” *J. sensors*, vol. 2011, p. 13, 2011.
- [111] A. Rizani *et al.*, “Polyacrylamide coated on quartz crystal microbalance electrodes for highly sensitive sensor of acetic acid,” *Mater. Sci. Forum*, vol. 948 MSF, pp. 254–259, 2019.
- [112] Q. Lin, Y. Fu, P. Chen, T. Wei, and Y. Zhang, “Colorimetric chemosensors designed to provide high sensitivity for Hg<sup>2+</sup> in aqueous solutions,” *Dye. Pigment.*, vol. 96, no. 1, pp. 1–6, 2013.
- [113] S. Bayindir, “A simple rhodanine-based fluorescent sensor for mercury and copper : The recognition of Hg<sup>2+</sup> in aqueous solution , and Hg<sup>2+</sup> /Cu<sup>2+</sup> in organic solvent,” *J. Photochem. Photobiol. A Chem.*, vol. 372, pp. 235–244, 2019.
- [114] X. Ma, D. Wang, Y. Cui, F. Tao, Y. Wang, and T. Li, “Chemical A novel hydrophilic conjugated polymer containing hydroxyl groups : Syntheses and sensing performance for NACs in aqueous solution,” *Sensors Actuators B. Chem.*, vol. 251, pp. 851–857, 2017.

- [115] H. Ma, F. Li, Z. Zhang, and M. Zhang, "Rapid DNT fluorescent films detection with high sensitivity and selectivity," *Sensors Actuators, B Chem.*, vol. 244, pp. 1080–1084, 2017.
- [116] B. Lee, "Review of the present status of optical fiber sensors," *Opt. Fiber Technol.*, vol. 9, no. 2, pp. 57–79, 2003.
- [117] C. Pulido and Ó. Esteban, "Improved fluorescence signal with tapered polymer optical fibers under side-illumination," *Sensors Actuators, B Chem.*, vol. 146, no. 1, pp. 190–194, 2010.
- [118] J. Dunphy, "The fibre-optic choice for the technology has many communications applications in commerce industry," *Data Process.*, vol. 24, no. 5, pp. 26–29, 1982.
- [119] B. E. A. Saleh, M. C. Teich, and Wiley, "Fiber optics," vol. 5, John Wiley & Sons, Inc., 1991, pp. 272–309.
- [120] A. Argyros, "Structure, properties and characteristics of optical fibres," *Handb. Text. Fibre Struct.*, vol. 2, pp. 458–484, 2009.
- [121] G. P. Anderson, J. P. Golden, and F. S. Ligler, "An Evanescent Wave Biosensor- Part I: Fluorescent Signal Acquisition from Step-Etched Fiber Optic Probes," *IEEE Trans. Biomed. Eng.*, vol. 41, pp. 578–584, 1994.
- [122] M. Cui, Y. Zhuang, G. Zou, B. Zhu, and Q. Zhang, "Chemical Fabrication of composite optical fiber taper through 'click' polymerization initiated by evanescent field for sensing," *Sensors Actuators B. Chem.*, vol. 284, pp. 243–249, 2019.
- [123] A. K. Sharma and J. Gupta, "Graphene based chalcogenide fiber-optic evanescent wave sensor for detection of hemoglobin in human blood," *Opt. Fiber Technol.*, vol. 41, no. 2017, pp. 125–130, 2018.
- [124] E. Rodríguez-schwendtner, M. C. Navarrete, N. Díaz-herrera, Ó. Esteban, and A. González-cano, "Chemical Microfiber as light source for exciting fluorescence in a polymer optical fiber," *Sensors Actuators B. Chem.*, vol. 223, pp. 30–34, 2016.
- [125] Claudio Oliveira Egalon, "side illuminated multi point multi parameter optical fibre sensor," United States Patent No. 8,463,083., 2013.
- [126] A. H. Alshammari, A. Kirwa, A. Dunbar, and M. Grell, "Adaptive and sensitive fibre-

- optic fluorimetric transducer for air- and water- borne analytes,” *Talanta*, vol. 199, pp. 40–45, 2019.
- [127] F. KREBS, *Stability and Degradation of Organic Stability and Degradation of Organic and Polymer Solar Cells*. John Wiley & Sons, 2012.
- [128] T. Pruttivarasin, “A robust experimental setup for Johnson noise measurement suitable for advanced undergraduate students,” *Eur. J. Phys.*, vol. 39, p. 065102, 2018.
- [129] S. Watanabe, H. Sugawara, R. Häusermann, T. Okamoto, and J. Takeya, “Remarkably low flicker noise in solution-processed organic single crystal transistors,” *Commun. Phys.*, vol. 1, pp. 1–8, 2018.
- [130] [http://www.anfatec.net/downloads/USBLockIn/USBLockIn250\\_Manual.pdf](http://www.anfatec.net/downloads/USBLockIn/USBLockIn250_Manual.pdf) (Accessed, 20.06.2020, 2158hrs UK time).
- [131] <https://www.thinksrs.com/downloads/pdfs/applicationnotes/AboutLIAs.pdf> (Accessed, 20.06.2020, 2203hrs UK time).
- [132] Texas instruments, Precision High Speed Transimpedance Amplifier OPA380AIDG4 Datasheet, 2007 <https://uk.farnell.com/texas-instruments/opa380aidg4/amp-transimpedance-smd-soic8-380/dp/3118209?st=OPA380> (Accessed, 20.03.2020, 2223hrs UK time).
- [133] [https://www.thorlabs.com/newgrouppage9.cfm?objectgroup\\_id=6845&pn=FT800UMT](https://www.thorlabs.com/newgrouppage9.cfm?objectgroup_id=6845&pn=FT800UMT) (Accessed, 20.04.2020, 2228hrs UK time).
- [134] [https://www.thorlabs.com/newgrouppage9.cfm?objectgroup\\_id=2284&pn=S90R](https://www.thorlabs.com/newgrouppage9.cfm?objectgroup_id=2284&pn=S90R) (Accessed, 18.04.2020, 1628hrs UK time).
- [135] <https://www.thorlabs.com/catalogpages/Obsolete/2015/LFG5P.pdf> (Accessed, 19.04.2020, 1228hrs UK time).
- [136] J. E. Bishop, T. J. Routledge, and D. G. Lidzey, “Advances in Spray-Cast Perovskite Solar Cells,” *Phys. Chem. Lett.*, vol. 9, no. 8, pp. 1977–1984, 2018.
- [137] B. S. Hunter, J. W. Ward, M. M. Payne, J. E. Anthony, O. D. Jurchescu, and D. Anthopoulos, “Low-voltage polymer / small-molecule blend organic thin-film transistors and circuits fabricated via spray deposition,” *Appl. Phys. Lett.*, vol. 106, p. 59\_1, 2015.

- [138] T. J. Routledge, D. G. Lidzey, and A. R. Buckley, "Ultrasonic spray coating as an approach for large-area polymer OLEDs : The influence of thin film processing and surface roughness on electrical performance," *AIP Adv.*, vol. 9, no. 1, p. 015330, 2019.
- [139] Y. Xie, S. Gao, and M. Eslamian, "Fundamental study on the effect of spray parameters on characteristics of P3HT: PCBM active layers made by spray coating," *Coatings*, vol. 5, no. 3, pp. 488–510, 2015.
- [140] D. Vak *et al.*, "Fabrication of organic bulk heterojunction solar cells by a spray deposition method for low-cost power generation," *Appl. Phys. Lett.*, vol. 91, no. 8, p. 081102, 2007.
- [141] T. Carey, C. Jones, F. Le Moal, D. Deganello, and F. Torrisi, "Spray-Coating Thin Films on Three-Dimensional Surfaces for a Semitransparent Capacitive-Touch Device," *ACS Appl. Mater. Interfaces*, vol. 10, pp. 19948–19956, 2018.
- [142] S. Bose, S. S. Keller, T. S. Alstrøm, A. Boisen, and K. Almdal, "Process optimization of ultrasonic spray coating of polymer films," *Langmuir*, vol. 29, no. 23, pp. 6911–6919, 2013.
- [143] A. Boukerika, L. Guerbous, H. Chelef, and L. Benharrat, "Preparation and characterization of bright high quality YAG : Eu<sup>3+</sup> thin films grown by sol – gel dip-coating technique," *Thin Solid Films*, vol. 683, pp. 74–81, 2019.
- [144] M. Al-Hussein *et al.*, "Comparative Study of the Nanomorphology of Spray and Spin Coated PTB7 Polymer : Fullerene Films," *Polym. Eng. Sci.*, vol. 56, no. 8, pp. 889–894, 2016.
- [145] A. Abdellah, D. Baierl, B. Fabel, P. Lugli, G. Scarpa, and T. U. München, "Spray-coating deposition for large area organic thin-film devices," *CRC Press*, vol. 2, pp. 447–450, 2009.
- [146] W. Andrew, *Nanobiomaterials in Hard Tissue Engineering*, William An. Applications of Nanobiomaterials, 2016.
- [147] S. Thomas, Y. Grohens, and Y. B. Pottathara, *Industrial Applications of Nanomaterials*. Elsevier, 2019.
- [148] A. Kulkarni, J. H. Lee, J. Do Nam, and T. Kim, "Thin film-coated plastic optical fiber probe for aerosol chemical sensing applications," *Sensors Actuators, B Chem.*, vol.

- 150, no. 1, pp. 154–159, 2010.
- [149] E. Rodríguez-Schwendtner, M. C. Navarrete, Ó. Esteban, N. Díaz-Herrera., and A. González-Cano, “Fluorescence excitation on tapered polymer optical fibers through microfiber evanescent field,” *24th Int. Conf. Opt. Fibre Sensors*, vol. 9634, p. 96346D, 2015.
- [150] S. Chauhan, N. Punjabi, D. Sharma, and S. Mukherji, “Evanescent wave absorption based S-shaped fiber-optic biosensor for immunosensing applications,” *Procedia Eng.*, vol. 168, pp. 117–120, 2016.
- [151] H. H. Nguyen *et al.*, “Fiber-Optic Detection of Explosives Using Readily Available Fluorescent Polymers,” *Macromolecules*, vol. 42, pp. 921–926, 2009.
- [152] F. Long, M. He, H. C. Shi, and A. N. Zhu, “Development of evanescent wave all-fiber immunosensor for environmental water analysis,” *Biosens. Bioelectron.*, vol. 23, no. 7, pp. 952–958, 2008.
- [153] F. Long *et al.*, “Reusable evanescent wave DNA biosensor for rapid, highly sensitive, and selective detection of mercury ions,” *Biosens. Bioelectron.*, vol. 26, no. 10, pp. 4018–4023, 2011.
- [154] R. A. Abumosa, B. A. Al-asbahi, and M. S. Alsalhi, “Optical Properties and Amplified Spontaneous Emission of Novel MDMO-PPV/C500 Hybrid,” *Polymers (Basel)*, vol. 9, p. 71, 2017.
- [155] P. A. Pella., “Measurement of the vapor pressures of TNT, 2,4-DNT, 2,6-DNT, and EGDN,” *J.chem.thermodynamics*, vol. 9, pp. 301–305, 1977.
- [156] R. B. Cundall, T. F. Palmer, and C. E. C. Wood, “Vapour pressure measurements on some organic high explosives,” *J. Chem. Soc. Faraday Trans. 1 Phys. Chem. Condens. Phases*, vol. 74, pp. 1339–1345, 1978.
- [157] L. M. Besley and G. A. Bottomley, “Vapour pressure of toluence from 273.15 to 298.15 K,” *J. Chem. Thermodyn.*, vol. 6, pp. 577–580, 1974.
- [158] J. M. Phelan and J. L. Barnett, “Solubility of 2,4-Dinitrotoluene and 2,4,6-Trinitrotoluene in Water,” *J. Chem. Eng. Data*, vol. 46, pp. 375–376, 2001.
- [159] E. Turiel, C. Perez-Conde, and A. Martin-Esteban, “Assessment of the cross-reactivity

- and binding sites characterisation of a propazine-imprinted polymer using the Langmuir-Freundlich isotherm,” *Analyst*, vol. 128, no. 2, pp. 137–141, 2003.
- [160] I. S. Kovalev *et al.*, “Fluorescent Detection of 2,4-DNT and 2,4,6-TNT in Aqueous Media by Using Simple Water-Soluble Pyrene Derivatives,” *Chem. - An Asian J.*, vol. 11, no. 5, pp. 775–781, 2016.
- [161] V. Kumar, B. Maiti, M. K. Chini, P. De, and S. Satapathi, “Multimodal Fluorescent Polymer Sensor for Highly Sensitive Detection of Nitroaromatics,” *Sci. Rep.*, vol. 9, no. 1, pp. 1–10, 2019.
- [162] H. Nie, Y. Zhao, M. Zhang, Y. Ma, M. Baumgarten, and K. Müllen, “Detection of TNT explosives with a new fluorescent conjugated polycarbazole polymer,” *Chem. Commun.*, vol. 47, pp. 1234–1236, 2011.
- [163] B. Das *et al.*, “Fluorescein derived Schiff base as fluorimetric zinc (II) sensor via ‘turn on’ response and its application in live cell imaging,” *Spectrochim. Acta - Part A Mol. Biomol. Spectrosc.*, vol. 212, pp. 222–231, 2019.
- [164] L. Li and X. Yang, “The Essential Element Manganese, Oxidative Stress, and Metabolic Diseases: Links and Interactions,” *Oxid. Med. Cell. Longev.*, vol. 2018, p. 11, 2018.
- [165] T. Tang, W. Guo, Y. Zhang, and D. Xu, “A Novel 1,8-Naphthalimide-Based ‘Turn-on’ Fluorescent Sensor for Fe<sup>3+</sup>,” *J. Fluoresc.*, vol. 29, no. 2, pp. 445–450, 2019.
- [166] M. Pannipara, A. G. Al-Sehemi, A. Kalam, A. M. Asiri, and M. N. Arshad, “AIE active turn-off fluorescent probe for the detection of Cu<sup>2+</sup> ions,” *Spectrochim. Acta - Part A Mol. Biomol. Spectrosc.*, vol. 183, pp. 84–89, 2017.
- [167] Y. Nakanishi, S. Iida, H. Ueoka-Nakanishi, T. Niimi, R. Tomioka, and M. Maeshima, “Exploring Dynamics of Molybdate in Living Animal Cells by a Genetically Encoded FRET Nanosensor,” *PLoS One*, vol. 8, no. 3, p. 58175, 2013.
- [168] Y. Li *et al.*, “A BOPHY probe for the fluorescence turn-on detection of Cu<sup>2+</sup>,” *Sensors Actuators, B Chem.*, vol. 235, pp. 33–38, 2016.
- [169] U. S. E. P. Agency and U. Washington, DC, “EPA 2008 Lead and Copper Rule: A Quick Reference Guide.” [Online]. Available: <http://water.epa.gov/drink>.

- [170] A. Mohadesi and M. A. Taher, "Voltammetric determination of Cu(II) in natural waters and human hair at a meso-2,3-dimercaptosuccinic acid self-assembled gold electrode," *Talanta*, vol. 72, no. 1, pp. 95–100, 2007.
- [171] T. W. Lin and S. D. Huang, "Direct and simultaneous determination of copper, chromium, aluminum, and manganese in urine with a multielement graphite furnace atomic absorption spectrometer," *Anal. Chem.*, vol. 73, no. 17, pp. 4319–4325, 2001.
- [172] H. S. Kumbhar and G. S. Shankarling, "Aggregation induced emission (AIE) active  $\beta$ -ketoiminate boron complexes: Synthesis, photophysical and electrochemical properties," *Dye. Pigment.*, vol. 122, pp. 85–93, 2015.
- [173] Y. Wu, X. Wen, and Z. Fan, "An AIE active pyrene based fluorescent probe for selective sensing Hg<sup>2+</sup> and imaging in live cells," *Spectrochim. Acta - Part A Mol. Biomol. Spectrosc.*, vol. 223, p. 117315, 2019.
- [174] International Labour Organization, "promoting jobs, protecting people," <https://www.ilo.org/legacy/english/protection/safework/cis/products/safetytm/solvents.htm>.
- [175] J. R. Albani, *Structure and dynamics of macromolecules: absorption and fluorescence studies*. Elsevier, 2011.
- [176] J. C. Joyner and J. A. Cowan, "Target-directed catalytic metallodrugs," *Brazilian J. Med. Biol. Res.*, vol. 46, no. 6, pp. 465–485, 2013.
- [177] W. Maketon, C. Z. Zenner, and K. L. Ogden, "Removal efficiency and binding mechanisms of copper and copper - EDTA complexes using polyethyleneimine," *Environ. Sci. Technol.*, vol. 42, no. 6, pp. 2124–2129, 2008.
- [178] D. P. Perl and P. F. Good, "Aluminum , Alzheimer ' s Disease , and the Olfactory System "," *Ann. N. Y. Acad. Sci.*, vol. 640, p. 8, 1991.
- [179] M. J. Ahmed, H. Reazul M., A. S. H. Khan, and S. C. Bhattacharjee, "A simple spectrophotometric method for the determination of aluminum in some environmental, biological, soil and pharmaceutical samples using 2-hydroxynaphthaldehydebenzoylhydrazone.," *Eurasian J. Anal. Chem.*, vol. 5, no. 1, pp. 1–15, 2010.
- [180] C. G. Niu, A. L. Guan, G. M. Zeng, Y. G. Liu, and Z. W. Li, "Fluorescence water

- sensor based on covalent immobilization of chalcone derivative,” *Anal. Chim. Acta*, vol. 577, no. 2, pp. 264–270, 2006.
- [181] Y. Çağlar, E. T. Saka, H. Alp, H. Kantekin, Ü. Ocak, and M. Ocak, “A Simple Spectrofluorimetric Method Based on Quenching of a Nickel(II)-Phthalocyanine Complex to Determine Iron (III),” *J. Fluoresc.*, vol. 26, no. 4, pp. 1381–1389, 2016.
- [182] T. Mizuta, K. Sueyoshi, T. Endo, and H. Hisamoto, “Ionic liquid-based dye: A ‘Dyed plasticizer’ for rapid and highly sensitive anion optodes based on a plasticized PVC membrane,” *Sensors Actuators, B Chem.*, vol. 258, pp. 1125–1130, 2018.
- [183] F. B. M. Suah, M. Ahmad, and L. Y. Heng, “Highly sensitive fluorescence optode for aluminium(III) based on non-plasticized polymer inclusion membrane,” *Sensors Actuators, B Chem.*, vol. 201, pp. 490–495, 2014.
- [184] G. R. Bruce and P. S. Gill, “Estimates of Precision in a Standard Additions Analysis,” *J. Chem. Educ.*, vol. 76, no. 6, p. 805, 1999.
- [185] L. Xiong *et al.*, “Sensing in 15 s for aqueous fluoride anion by water-insoluble fluorescent probe incorporating hydrogel,” *Anal. Chem.*, vol. 85, no. 8, pp. 4113–4119, 2013.
- [186] Y. K. Jang, U. C. Nam, H. L. Kwon, I. H. Hwang, and C. Kim, “A selective colorimetric and fluorescent chemosensor based-on naphthol for detection of Al<sup>3+</sup> and Cu<sup>2+</sup>,” *Dye. Pigment.*, vol. 99, no. 1, pp. 6–13, 2013.
- [187] K. B. Kim, D. M. You, J. H. Jeon, Y. H. Yeon, J. H. Kim, and C. Kim, “A fluorescent and colorimetric chemosensor for selective detection of aluminum in aqueous solution,” *Tetrahedron Lett.*, vol. 55, no. 7, pp. 1347–1352, 2014.
- [188] V. P. Singh, K. Tiwari, M. Mishra, N. Srivastava, and S. Saha, “5-[(2-Hydroxynaphthalen-1-yl)methylene]amino]pyrimidine-2,4(1H,3H)-dione as Al<sup>3+</sup> selective colorimetric and fluorescent chemosensor,” *Sensors Actuators, B Chem.*, vol. 182, pp. 546–554, 2013.
- [189] B. In, G. W. Hwang, and K. H. Lee, “Highly sensitive and selective detection of Al(III) ions in aqueous buffered solution with fluorescent peptide-based sensor,” *Bioorganic Med. Chem. Lett.*, vol. 26, no. 18, pp. 4477–4482, 2016.
- [190] Z. Kejkík *et al.*, “Aluminium(III) sensing by pyridoxal hydrazone utilising the chelation

- enhanced fluorescence effect,” *J. Lumin.*, vol. 180, pp. 269–277, 2016.
- [191] J. Y. Xie, C. Y. Li, Y. F. Li, Y. J. Fu, S. X. Nie, and H. Y. Tan, “A near-infrared chemosensor for determination of trivalent aluminum ions in living cells and tissues,” *Dye. Pigment.*, vol. 136, pp. 817–824, 2017.
- [192] D. Sarkar, P. Ghosh, S. Gharami, T. Kumar, and N. Murmu, “A novel coumarin based molecular switch for the sequential detection of Al<sup>3+</sup> and F<sup>-</sup> : Application in lung cancer live cell imaging and construction of logic gate,” *Sensors Actuators B. Chem.*, vol. 242, pp. 338–346, 2017.
- [193] R. Dwivedi *et al.*, “Intracellular application and logic gate behavior of a ‘turn off-on-off’ type probe for selective detection of Al<sup>3+</sup> and F<sup>-</sup> ions in pure aqueous medium,” *Sensors Actuators, B Chem.*, vol. 258, pp. 881–894, 2018.
- [194] M. Selvaraj *et al.*, “On-off-on relay fluorescence recognition of ferric and fluoride ions based on indicator displacement in living cells,” *Anal. Chim. Acta*, vol. 1066, pp. 112–120, 2019.
- [195] B. Bhattacharyya, A. Kundu, N. Guchhait, and K. Dhara, “Anthraimidazoledione Based Reversible and Reusable Selective Chemosensors for Fluoride Ion: Naked-Eye, Colorimetric and Fluorescence ‘ON-OFF,’” *J. Fluoresc.*, vol. 27, no. 3, pp. 1041–1049, 2017.
- [196] J. Y. Xie *et al.*, “A novel colorimetric and fluorescent probe for detecting fluoride anions: From water and toothpaste samples,” *Dye. Pigment.*, vol. 55, no. 7, pp. 4477–4482, 2016.
- [197] D. Thongkum and T. Tuntulani, “Fluoride-induced intermolecular excimer formation of bispyrenyl thioureas linked by polyethylene glycol chains,” *Tetrahedron*, vol. 67, no. 42, pp. 8102–8109, 2011.
- [198] S. Ruan, H. Ebendorff-Heidepriem, Y. Ruan, H. Ebendorff-Heidepriem, and Y. Ruan, “Optical fibre turn-on sensor for the detection of mercury based on immobilized fluorophore,” *Measurement*, vol. 121, pp. 122–126, 2018.
- [199] M. Shyamal, S. Maity, A. Maity, R. Maity, S. Roy, and A. Misra, “Aggregation induced emission based ‘turn-off’ fluorescent chemosensor for selective and swift sensing of mercury (II) ions in water,” *Sensors Actuators, B Chem.*, vol. 263, pp. 347–

- 359, 2018.
- [200] A. Ben Nasr, C. Charcosset, R. Ben Amar, and K. Walha, "Fluoride removal from aqueous solution by Purolite A520E resin: kinetic and thermodynamics study," *Desalin. Water Treat.*, vol. 54, no. 6, pp. 1604–1611, 2015.
- [201] G. Sposito, *The Environmental chemistry of aluminum*. CRC Press, 1995.
- [202] L. H. Jia, Y. Liu, and Y. Z. Li, "Determination of wholesome elements and heavy metals in safflower (*Carthamus tinctorius* L.) from Xinjiang and Henan by ICP-MS/ICP-AES," *J. Pharm. Anal.*, vol. 1, no. 2, pp. 100–103, 2011.
- [203] Y. Yamini and M. Safari, "Modified magnetic nanoparticles with catechol as a selective sorbent for magnetic solid phase extraction of ultra-trace amounts of heavy metals in water and fruit samples followed by flow injection ICP-OES," *Microchem. J.*, vol. 143, no. August, pp. 503–511, 2018.
- [204] S. M. Sorouraddin, "Simultaneous separation and preconcentration of ultra-trace of Cu(II), Pb(II) and Zn(II) in water samples by air-assisted liquid–liquid microextraction prior to determination by graphite furnace atomic absorption spectrometry," *J. Iran. Chem. Soc.*, vol. 13, no. 12, pp. 2219–2227, 2016.
- [205] M. A. Habila, Z. A. Alothman, E. Yilmaz, and M. Soylak, "Activated carbon cloth filled pipette tip for solid phase extraction of nickel(II), lead(II), cadmium(II), copper(II) and cobalt(II) as 1,3,4-thiadiazole-2,5-dithiol chelates for ultra-trace detection by FAAS," *Int. J. Environ. Anal. Chem.*, vol. 98, no. 2, pp. 171–181, 2018.
- [206] L. Liu, X. B. Luo, L. Ding, and S. L. Luo, "Application of Nanotechnology in the Removal of Heavy Metal From Water," in *Nanomaterials for the Removal of Pollutants and Resource Reutilization*, Elsevier Inc., 2018, pp. 83–147.

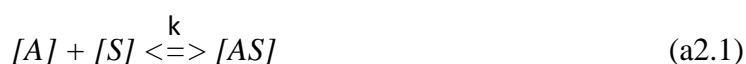
## Appendices

### Appendix I. *LoDs* of Heavy Metals Obtained by the ICP-MS, ICP-AES, GFAAS and FASS techniques.

<i>Heavy Metal</i>	<i>Reported LoDs by different techniques</i>			
	<i>ICP-MS [nM]</i> [202]	<i>ICP-AES</i> [nM] [203]	<i>GFAAS</i> [nM] [204]	<i>FASS</i> [205]
Lead	0.58	4.3	0.12	8.2
Cadmium	0.03	4.45		11.6
Mercury	0.12			
Copper	59	3.15	0.31	31.5
Aluminum	770			
Manganese	9.1	12.7		
Cobalt	0.017	13.6		49.2
Nickel	0.085	13.6		46

### Appendix II. Langmuir Adsorption Isotherm Derivation.

If the chemical reaction between the analyte with known concentration  $[A]$  and the sensitiser  $[S]$  is reversible, the reaction can be expressed as follows:



where  $[AS]$  represents the concentration of the analyte-sensitiser complex.  $k$  is a stability constant that quantifies the interaction strength between the sensitiser and the analyte. The interaction reaches stability when the forward and backward reactions are equal. The forward reaction occurs when analyte molecules bind to the available sites of sensitiser (adsorption).

$$[A] + [B] = k_a [A][S] \quad (\text{a2.2})$$

The backward reaction is when the analytes molecules separate from the sites of sensitiser.

$$[A] + [B] = k_d [AS] \quad (\text{a2.3})$$

At the equilibrium, forward and backward reaction are equal as follows,

$$k_a [A][S] = k_d [AS]$$

$$\theta = \frac{k_a}{k_d} = \frac{[AS]}{[A][S]} \quad (\text{a2.4})$$

The Eq. a2.4 explains the equilibrium between analyte bound on the sensitizer sites and unbound analyte.

The Langmuir equation relies on the number of available sites, which are homogenous, and the analyte concentration. The fraction of bound or occupied sites are expressed in  $\theta$  while the fraction of unoccupied free sites are expressed as  $(1 - \theta)$ .

The rate of adsorption depends on the number of unoccupied sites in the sensitizer's film or solution and the analyte concentration  $c$ . The rate of desorption is dependent on the number of sites occupied by the analyte molecules.

Thus, the adsorption rate  $\propto c (1 - \theta)$  or  $= k_a c (1 - \theta)$  and desorption rate  $\propto \theta$  or adsorption rate  $= k_d \theta$ .

At the equilibrium,  $k_a c (1 - \theta) = k_d \theta$  and can be written as follows:

$$k_a c - k_a c \theta = k_d \theta \quad (\text{a2.5})$$

$$\theta = \frac{k_a c}{k_d + k_a c} \quad (\text{a2.6})$$

When the right hand side of the Eq. a2.6 is divided on the top and bottom by  $k_d$  ( $k_a / k_d = k$  [206]) we get Langmuir Adsorption equation:

$$\theta = \frac{kc}{1 + kc} \quad (\text{a2.7})$$

Eq. a2.7 represents Langmuir adsorption isotherm in a liquid medium and it can be simply written for the gas medium as in Eq. (a2.8).

$$\theta = \frac{ap}{1+ap} \quad (\text{a2.8})$$

where  $p$  = partial pressure (fraction of atmospheric pressure) of the analyte, which is equal to a number fraction (analyte/carrier gas) according to the ideal gas equation and  $(a)$  is stability constant.

### Appendix III. Input Signal Processing via Lock-in Amplifier

$$\sin(A \pm B) = \sin A \cos B \pm \cos A \sin B \quad (\text{a})$$

$$\cos(A \pm B) = \cos A \cos B \mp \sin A \sin B \quad (\text{b})$$

$$\cos A \cos B = \frac{1}{2} \left\{ \cos(A - B) + \cos(A + B) \right\} \quad (\text{c})$$

$$\sin A \cos B = \frac{1}{2} \left\{ \sin(A + B) + \sin(A - B) \right\} \quad (\text{d})$$

$$\sin A \sin B = \frac{1}{2} \left\{ \cos(A - B) - \cos(A + B) \right\} \quad (\text{e})$$

$$\cos A \sin B = \frac{1}{2} \left\{ \sin(A + B) - \sin(A - B) \right\} \quad (\text{f})$$

The trigonometrical identities shown above in Eqs. (a to f) will be used to show how mathematically the lock-in processes the input voltage signal and reject the noise as briefly described earlier in this thesis (chapter 3, Section 3.3). We dedicate the mathematical description to clarify the lock-in amplifier's function in our application. However, the fundamental work of lock-in amplifiers has been previously reported in [130].

The input voltage signal  $V_{sig}$  and the reference signal  $V_L$  are shown in Eq. a3.1 and Eq. a3.2 respectively;

$$V_{sig} = V_{DC} + V_{AC} \sin(\omega_{sig}t + \varphi) + Noise \quad (\text{a3.1})$$

$$V = V_L \sin(\omega_L t) \quad (\text{a3.2})$$

The input voltage is multiplied with the reference voltage as follows;

$$\begin{aligned} V_{sig} \times V &= [V_{DC} + V_{AC} \sin(\omega_{sig}t + \varphi) + Noise] \times [V_L \sin(\omega_L t)] \\ &= V_{DC} V_L \sin(\omega_L t) + \mathbf{V_L V_{AC} \sin(\omega_L t) \sin(\omega_{sig}t + \varphi)} + Noise V_L \sin(\omega_L t) \end{aligned} \quad (\text{a3.3})$$

The highlighted sine functions in Eq. a3.3 can be simplified as;

$V_L V_{AC} \sin(\omega_L t) \sin(\omega_{sig} t + \varphi) = V_L V_{AC} \sin A \sin B$  , where  $A = \omega_L t$  and  $B = \omega_{sig} t + \varphi$

By applying the trigonometrical identity (e), to the Eq. a3.3 we get;

$$= \frac{1}{2} V_L V_{AC} \{ \cos(\omega_L t - (\omega_{sig} t + \varphi)) - \cos(\omega_L t + (\omega_{sig} t + \varphi)) \} \quad (a3.4)$$

The Eq. a3.4 can be rewritten as follows;

$$= \frac{1}{2} V_L V_{AC} \{ \cos((\omega_L - \omega_{sig})t - \varphi) - \cos((\omega_L + \omega_{sig})t + \varphi) \} \quad (a3.5)$$

Assuming  $A1 = (\omega_L - \omega_{sig})t$ ,  $A2 = (\omega_L + \omega_{sig})t$  and  $B = \varphi$ , Eq. a3.5 becomes as expressed below

$$= \frac{1}{2} V_L V_{AC} \{ \cos(A1 - B) - \cos(A2 + B) \} \quad (a3.6)$$

By applying the above trigonometrical identity (b) to the Eq a3.6, we get;

$$= \frac{1}{2} V_L V_{AC} \{ [\cos(\omega_L - \omega_{sig})t \cos \varphi + \sin(\omega_L - \omega_{sig})t \sin \varphi] - \cos[(\omega_L + \omega_{sig})t \cos \varphi - \sin(\omega_L + \omega_{sig})t \sin \varphi] \} \quad (a3.7)$$

By rearranging the a3.7 after opening the brackets, we get;

$$= \frac{1}{2} V_L V_{AC} \{ \cos(\omega_L - \omega_{sig})t \cos \varphi - \cos(\omega_L + \omega_{sig})t \cos \varphi + \sin(\omega_L - \omega_{sig})t \sin \varphi + \sin(\omega_L + \omega_{sig})t \sin \varphi \} \quad (a3.8)$$

When sine  $(\omega_L + \omega_{sig})$  is filtered by the lowpass filter and the  $\sin(\omega_{ref} = \omega_{signal}) = \sin(0) = 0$ , the a3.8 becomes;  $= \frac{1}{2} V_L V_{AC} \cos \varphi \{ \cos((\omega_L - \omega_{sig})t) - \cos(\omega_L + \omega_{sig})t \} \} \quad (a3.9)$

If we apply the Eq. a3.9 to the Eq. a3.3 we get;

$$V_{sig} \times V = \frac{1}{2} V_L V_{AC} \cos \varphi \{ [\cos(\omega_L - \omega_{sig})t - \cos(\omega_L + \omega_{sig})t] \} + [\text{Noise} V_L \sin(\omega_L t)] + [V_{DC} V_L \sin(\omega_L t)] \quad (a3.10)$$

Note that, Eq. a3.10 is shown in Section 3.3 as Eq. 3.5. If the output of digital signal processing (DSP) passes through a lowpass filter (the basic function of lock-in amplifier), all AC signals will be removed including  $\cos \omega_L + \omega_{sig}$  thus Eq. a3.10 becomes as follows;

$$V_{sig} \times V = 1/2 V_L V_{AC} \cos\phi$$

Finally  $V_{sig} \times V$  is integrated over a time  $T$  via lock in amplifier as follows;

$$V_1 = \frac{1}{T} \int_{t-T}^t V_{sig} V dt \tag{a3.11}$$

Where  $T$  is the time constant which the time is taken by the lock-in amplifier to average the input signal.  $V_1$  is the output of DSP after passing through the lowpass filter. The second digital chip in the lock-in amplifier multiplies  $V_{sig}$  with the reference voltage shifted by  $90^\circ$  phase with a similar procedure as outlined above.

$$V = V_L \sin \omega t + 90^\circ \text{ or } V_L \cos \omega t$$

Supporting detail is shown in an appendix (IV).

#### Appendix IV. Block Diagram of the Lock-In (USBLockIn250) Illustrating the Function of the Basic Components.

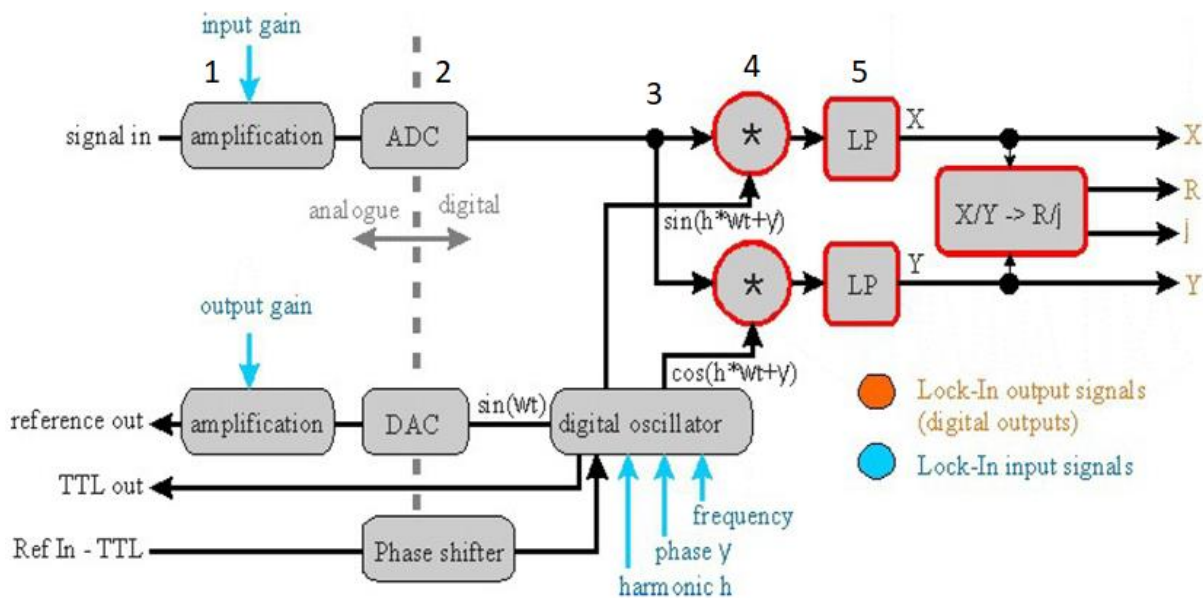


**Figure A1.** This diagram is taken from [130] and already discussed in Chapter 3.

At stage 1: The input signal of the lock-in amplifier is amplified by different factors depending on the chosen gain dynamic. Thus, the signal is amplified by a factor of 100, 10, 1 when the lock-in is set to low, normal, and high dynamic respectively.

At stage 2: The amplified signal is digitized.

At stage 3: The digitized signal is split into two.

At stage 4: One is multiplied with the reference signal while another is multiplied with the reference signal shifted by 90°.

At stage 5: Both pass through the lowpass filter to block all signal whose frequencies deviate from the reference frequency.

The digital lock-in amplifier implemented as part of our sensor displayed the filtered signal to the user into four output channels. Two channels give the real and imaginary parts of the processed output signal as X and Y respectively. The third channel gives the amplitude while the last channel gives the phase.

## Appendix V. Properties of the Used Optical Fibres

(FT800UMT)

### Ø800 µm Core TECS-Clad Multimode Optical Fiber, 0.39 NA ▲

Item #	Wavelength Range	Hydroxyl Content	Core Diameter	Cladding Diameter	Coating Diameter	Core / Cladding	Coating	Stripping Tool	Proof Test	
FT800UMT	300 - 1200 nm	High OH	800 ± 10 µm	830 ± 10 µm	1040 ± 30 µm	Pure Silica / TECS Hard Cladding	Tefzel	<a href="#">M37S46</a>	≥100 kpsi	
FT800EMT	400 - 2200 nm	Low OH								
Item #	NA	Core Index	Cladding Index	Maximum Attenuation @ 808 nm	Bandwidth @ 820 nm	Max Power Capability		Max Core Offset	Bend Radius	Operating Temperature
FT800UMT	0.39	436 nm: 1.466757 589.3 nm: 1.458434 1020 nm: 1.450174	436 nm: 1.406000 589.3 nm: 1.398200 1020 nm: 1.392306	12 dB/km	N/A	16.0 MW	3.2 kW	9 µm	40 mm 80 mm	-65 - 135 °C
FT800EMT		436 nm: 1.467287 589.3 nm: 1.458965 1020 nm: 1.450703	436 nm: 1.406000 589.3 nm: 1.398200 1020 nm: 1.392306	10 dB/km						

Based on your currency / country selection, your order will ship from European warehouse

(FT1500UMT)

### Ø1500 µm Core TECS-Clad Multimode Optical Fiber, 0.39 NA ▲

Item #	Wavelength Range	Hydroxyl Content	Core Diameter	Cladding Diameter	Coating Diameter	Core / Cladding	Coating	Stripping Tool	Proof Test	
FT1500UMT	300 - 1200 nm	High OH	1500 ± 30 µm	1550 ± 31 µm	2000 ± 100 µm	Pure Silica / TECS Hard Cladding	Tefzel	<a href="#">M63S86</a>	≥100 kpsi	
FT1500EMT	400 - 2200 nm	Low OH								
Item #	NA	Core Index	Cladding Index	Maximum Attenuation @ 808 nm	Bandwidth @ 820 nm	Max Power Capability		Max Core Offset	Bend Radius	Operating Temperature
FT1500UMT	0.39	436 nm: 1.466757 589.3 nm: 1.458434 1020 nm: 1.450174	436 nm: 1.406000 589.3 nm: 1.398200 1020 nm: 1.392306	18 dB/km	N/A	56.6 MW	11.3 kW	12 µm	75 mm 150 mm	-65 - 135 °C
FT1500EMT		436 nm: 1.467287 589.3 nm: 1.458965 1020 nm: 1.450703	436 nm: 1.406000 589.3 nm: 1.398200 1020 nm: 1.392306	18 dB/km						

Based on your currency / country selection, your order will ship from European warehouse

These photos are taken from manufacturer's datasheet (Thorlabs) [133].

## Appendix VI. Cooling System

The photo was taken of the lab during the preparation of cooling mixtures before one of the experiments run. Several coils of pipe are running through the cooling medium (ice or ice /salt mixture) maintained into a polyester box. The DNT crystals in a vial are dipped into the same cooling medium that is held in a flask. The gas chamber fitted with the sensitised fibre, all pipes used and the flow rate controller are all shown in the photo.

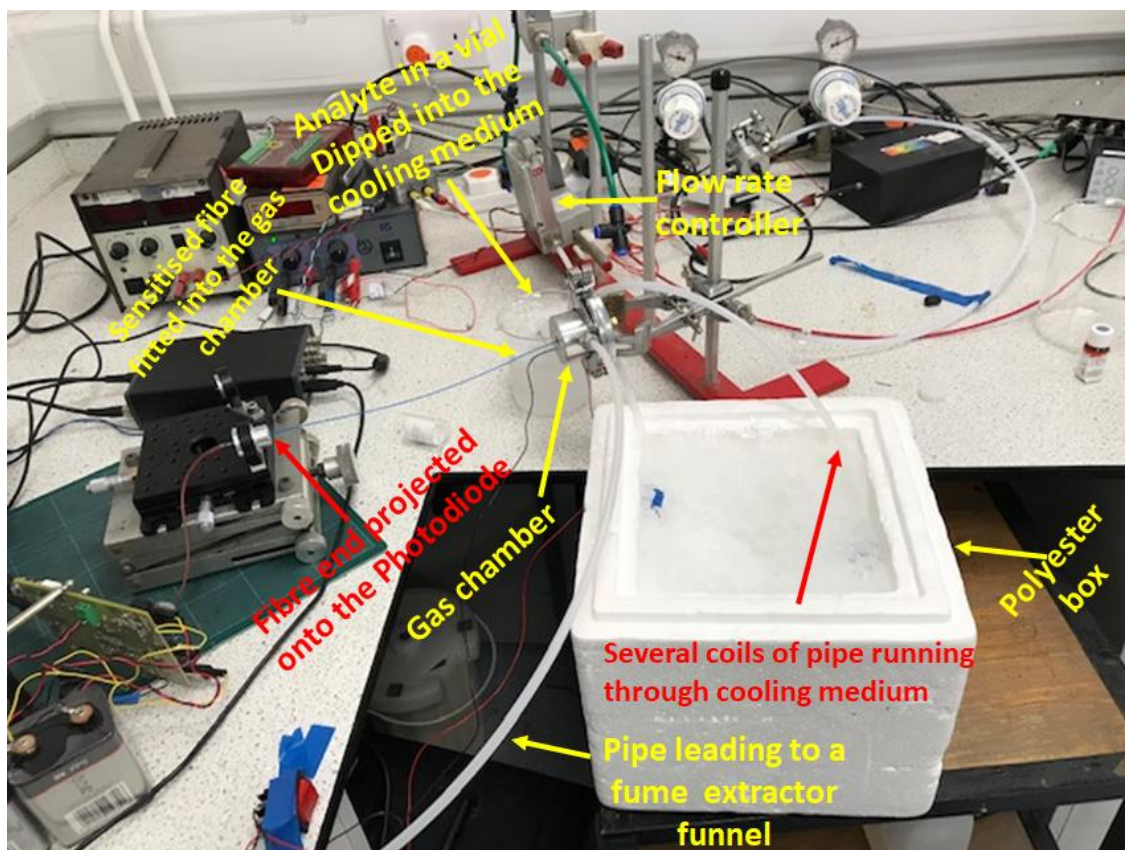
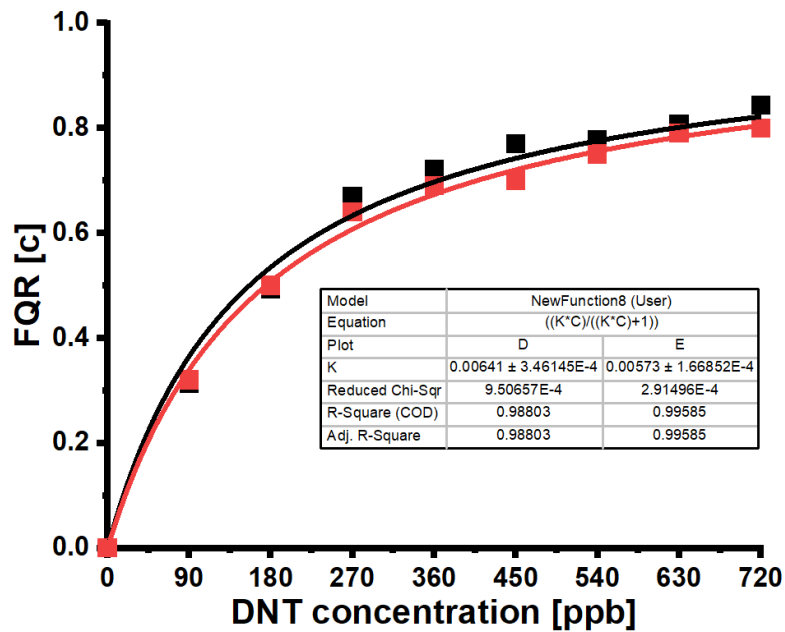


**Figure A2.** Photo of our cooling system and our sensor.

## Appendix VII. Repeatability of DNT Waterborne Sensing Experiments.



## Appendix VIII. Fluorescence Intensity of Thin Film

$V_{out}$  serves as a measure of the fluorescence intensity yielded by the membrane film of 725 nm thickness (as measured by Dektak). At 0.80 mV,  $V_{out}$  is 50% lower than that (1.60 mV) obtained for a 1112 nm thick membrane, as shown in Figure 6.4. Thus, 1112 nm thickness is preferable for a membrane intended for waterborne  $\text{Cu}^{2+}$  sensing.

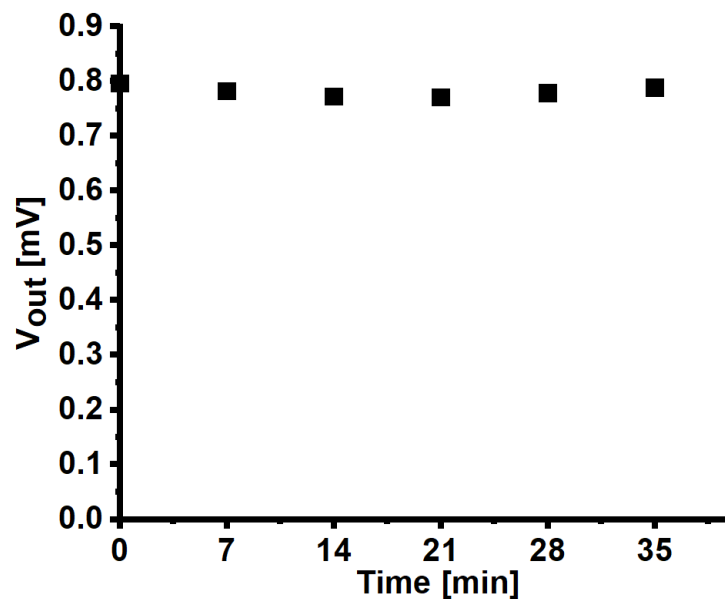


**Figure A1.**  $V_{out}(c)$  vs time, as a measure of the fluorescence intensity obtained from the membrane film coated onto the optical fibre with 725 nm thickness.

**Appendix IX. Repeatability of  $\text{Cu}^{2+}$  sensing experiments.**

$\text{Cu}^{2+}[\mu\text{M}]$	$FQR(c)$ <i>Trial (1)</i>	$FQR(c)$ <i>Trial (2)</i>	$[I_0/I_c]-1$ <i>Trial (1)</i>	$[I_0/I_c]-1$ <i>Trial (2)</i>
1	0.127	0.158	0.145	0.19
2	0.237	0.315	0.31	0.46
3	0.342	0.420	0.52	0.72
4	0.439	0.499	0.78	0.999
6	0.530	0.571	1.13	1.33
8	0.582	0.627	1.39	1.68
10	0.636	0.670	1.75	2.03
12	0.677	0.705	2.09	2.39
14	0.725	0.741	2.63	2.86
16	0.749	0.764	2.98	3.24
18	0.775	0.783	3.45	3.61
20	0.797	0.801	3.94	4.03
22	0.818	0.813	4.49	4.35

The  $\text{Cu}^{2+}$  sensing experiments were replicated and their data ( $FQR$ ) vs  $\text{Cu}^{2+}$  concentration are fitted to Langmuir model.

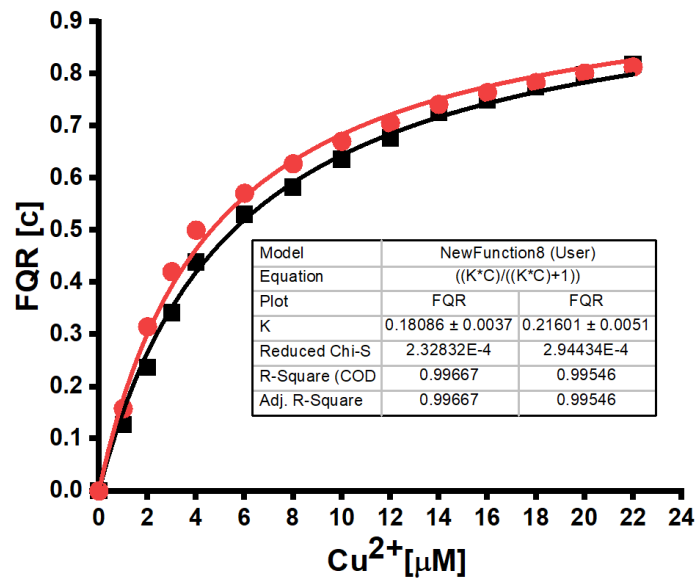


**Figure A2.**  $FQR[c]$  from repeating experiments vs  $\text{Cu}^{2+}$  concentration. Solid lines are fit to Eq. 6.1.

## Appendix X. Copyright Permissions

15/05/2020

Rightslink® by Copyright Clearance Center



RightsLink®



Home

Help

Email Support

Sign in

Create Account



### Adaptive and sensitive fibre-optic fluorimetric transducer for air- and water-borne analytes

Author: Alhulw H. Alshammari, Abraham Kirwa, Alan Dunbar, Martin Grell

Publication: Talanta

Publisher: Elsevier

Date: 1 July 2019

© 2019 Elsevier B.V. All rights reserved.

Please note that, as the author of this Elsevier article, you retain the right to include it in a thesis or dissertation, provided it is not published commercially. Permission is not required, but please ensure that you reference the journal as the original source. For more information on this and on your other retained rights, please visit: <https://www.elsevier.com/about/our-business/policies/copyright#Author-rights>

BACK

CLOSE WINDOW

© 2020 Copyright - All Rights Reserved | Copyright Clearance Center, Inc. | [Privacy statement](#) | [Terms and Conditions](#)  
Comments? We would like to hear from you. E-mail us at [customer@copyright.com](mailto:customer@copyright.com)

15/05/2020

Rightslink® by Copyright Clearance Center



RightsLink®



Home

Help

Email Support

Sign in

Create Account



### Low cost, high sensitivity detection of waterborne Al<sup>3+</sup> cations and F<sup>-</sup> anions via the fluorescence response of a morin derivative dye

Author:

Alhulw H. Alshammari, Zahrah Alqahtani, Faiz Bukhari Mohd Suah, Syaza Atikah Nizar, Alan Dunbar, Martin Grell

Publication: Analytica Chimica Acta

Publisher: Elsevier

Date: 8 April 2020

© 2020 Elsevier B.V. All rights reserved.

Please note that, as the author of this Elsevier article, you retain the right to include it in a thesis or dissertation, provided it is not published commercially. Permission is not required, but please ensure that you reference the journal as the original source. For more information on this and on your other retained rights, please visit: <https://www.elsevier.com/about/our-business/policies/copyright#Author-rights>

BACK

CLOSE WINDOW

© 2020 Copyright - All Rights Reserved | Copyright Clearance Center, Inc. | [Privacy statement](#) | [Terms and Conditions](#)  
Comments? We would like to hear from you. E-mail us at [customer@copyright.com](mailto:customer@copyright.com)

